

ABSTRACT

Title of dissertation: DEVELOPMENT OF A LAGRANGIAN -EULERIAN MODELING FRAMEWORK TO DESCRIBE THERMAL DEGRADATION OF POROUS FUEL PARTICLES IN SIMULATIONS OF WILDLAND FIRE BEHAVIOR AT FLAME SCALE

Mohamed Mohsen Ahmed
Doctor of Philosophy, 2023

Dissertation Directed by: Professor Arnaud Trouv 
Department of Mechanical Engineering

The dynamics of wildland fires involve multi-physics phenomena occurring at multiple scales ranging from sub-millimeter scale representative of small vegetation particles to several kilometers representative of meteorological scales. The objective of this research is to develop an advanced physics-based computational tool for detailed modeling of the coupling between the solid-phase and the gas-phase processes that control the dynamics of flame spread in wildland fire problems. This work focuses on a modeling approach that resolves processes occurring at flame and vegetation scales, i.e., the formation of flammable vapors from the porous biomass vegetation due to pyrolysis, the subsequent combustion of these fuel vapors with ambient air, the establishment of a turbulent flow because of heat release and buoyant acceleration, and the thermal feedback to the solid biomass through radiative and

convective heat transfer. A modeling capability called PBRFoam is developed in this dissertation based on the general-purpose Computational Fluid Dynamics (CFD) library OpenFOAM and an in-house Lagrangian Particle Burning Rate (PBR) model that treats drying, thermal pyrolysis, oxidative pyrolysis, and char oxidation using a one-dimensional porous medium formulation. This modeling capability allows the description of fire spread in vegetation fuel beds comprised of mono- or poly-dispersed porous particles including thermal degradation processes occurring during both flaming and smoldering combustion.

The modeling capability is calibrated for cardboard and pine wood using available micro- and bench-scale experimental data obtained. Then it is applied to simulate the fire spread across the idealized fuel beds made of laser-cut cardboard sticks that have been studied experimentally at the Missoula Fire Sciences Laboratory. The simulations are conducted with prescribed particle and environmental properties (i.e., fuel bed height, fuel bed packing, particle size, moisture content, and wind velocity) that match the experimental conditions. The model is first validated against experimental measurements and observations such as the rate of spread of the fire and the flame residence time. The modeling capability is then used to provide insights into local as well as global behavior at the individual particle level and the fuel bed level with variations of the fuel packing.

The modeling capability is also applied to simulations of fire spread across idealized vegetation beds corresponding to mixed-size cylindrical-shaped sticks of pine wood under prescribed wind conditions. Depending on the particle size distribution, the simulations feature complete fuel consumption with a successful transition

from flaming to smoldering combustion or partial fuel consumption with no or limited smoldering. These simulations show the existence of either a mixed mode of heat transfer through convection and radiation for small particles or a radiation-dominant heat transfer mode for larger particles. The results are interpreted using a novel diagnostic called the Pseudo Incident Heat Flux (PIHF) and 2-D maps that characterize single particle response as a function of the PIHF and the flame residence time.

DEVELOPMENT OF A LAGRANGIAN-EULERIAN MODELING
FRAMEWORK TO DESCRIBE THERMAL DEGRADATION OF
POROUS FUEL PARTICLES IN SIMULATIONS OF WILDLAND
FIRE BEHAVIOR AT FLAME SCALE

by

Mohamed Mohsen Ahmed

Dissertation submitted to the Faculty of the Graduate School of the
University of Maryland, College Park in partial fulfillment
of the requirements for the degree of
Doctor of Philosophy
2023

Advisory Committee:

Professor Arnaud Trouv , Chair/Advisor
Professor James Baeder, Dean's Representative
Dr. Mark Finney
Professor Johan Larsson
Professor Stanislav Stoliarov
Professor Peter Sunderland

© Copyright by
Mohamed Mohsen Ahmed
2023

Dedication

To my dear parents, my lovely sister, my darling Radwa, and our beautiful Nelli.

Acknowledgments

The completion of this Ph.D. dissertation would not have been possible without the generous support and encouragement of so many people, for which I am deeply grateful.

First, I would like to express my deepest gratitude to my advisor, Dr. Arnaud Trouv . His guidance, mentorship, and expertise have been invaluable throughout my research journey. His insightful comments and feedback on my work were instrumental in refining my ideas and improving the quality of my research. I am also grateful for the opportunities he provided me to present my research at conferences and workshops, which helped me gain exposure and build my professional network. His support in securing funding for my research projects was also critical in enabling me to complete my research.

I am also grateful to the faculty members at the University of Maryland who dedicated part of their precious time to serve as an advisory committee for my dissertation. Thanks to Dr. James Baeder, Dr. Johan Larsson, Dr. Stanislav Stoliarov, and Dr. Peter Sunderland for their insightful comments and constructive discussion, which helped me to refine my research.

Special thanks to Dr. Mark Finney from the U.S. Forest Service for allocating some of his valuable time to be on my advisory committee as well as for his ultimate support. I am very thankful to him for sharing the data of his experiments and for the invaluable comments and feedback that he provided at different phases during this project.

I would also like to extend special thanks to Mr. Jason Forthofer from the U.S. Forest Service for the thoughtful and deep discussions we exchanged about model implementation and code development. His guidance was very critical in improving the quality of the computational tools developed in this project.

I would like to acknowledge all my former and present colleagues at the ME and FPE departments especially: Salman Verma, Rui Xu, Yiren Qin, Yujeong Kim, Bouaza Lafdal, Zishanul Hussain, Anagh Dave, Kelliann Lee, Jeffrey Bors and Sofia Le Braddock. I am also grateful to the administrative staff of the FPE department: Christine O'Brien and Nicole Hollywood.

I am thankful for the financial support from the USDA Forest Service, Missoula Fire Sciences Laboratory, with Dr. Mark Finney as Program Manager. I am also thankful for the partial financial support provided by the U.S. National Science Foundation (NSF, CBET Program, Award #1604907) and by FM Global. I would like also to acknowledge the supercomputing resources made available by UMD (<https://www.glue.umd.edu/hpcc>) and by NSF (ACCESS Program, Grant #TG-CTS140046, <https://access-ci.org>).

Finally, I would like to express my deep appreciation to my family. Their ultimate love, encouragement, and support have been my source of strength and inspiration throughout my academic career. Their sacrifices and unwavering belief in my potential have made this accomplishment possible.

Table of Contents

Dedication	ii
Acknowledgements	iii
List of Tables	x
List of Figures	xi
Nomenclature	xxiii
1 Introduction	1
1.1 Wildland fire behavior modeling	2
1.1.1 Scales of wildland fire behavior dynamics	3
1.1.2 Semi-empirical approach to wildfire behavior modeling	5
1.1.3 Physics-based approach to wildfire behavior modeling	6
1.2 Motivation and scope of this dissertation	9
1.3 Literature review of relevant experimental/modeling work in the vegetation-flame scale	10
1.4 Objectives and contributions	13
1.4.1 Objectives	13
1.4.2 Author's contributions	15
1.4.3 Organization	19
2 The Computational Modeling Framework	22
2.1 Overview	22
2.2 Particle Burning Rate (PBR) Model	24
2.2.1 Conservation equations for species/total mass inside the solid phase of an individual particle	29
2.2.2 Rate of change of the particle volume (constant/shrinking/swelling) .	32
2.2.3 Conservation equations for species/total mass inside the gas phase of an individual particle	33
2.2.4 Conservation equation for energy inside an individual particle	35
2.2.5 Outputs of the PBR model	39

2.2.6	Particle burning state	40
2.3	Fuel bed model and the coupled Lagrangian-Eulerian formulation	42
2.3.1	Conservation equations for species/total mass in the gas-phase	43
2.3.2	Conservation equations for momentum in the gas-phase	46
2.3.3	Conservation equation for energy in the gas-phase	46
2.3.4	Radiation transfer in the multiphase fuel bed	47
2.4	Convective transfer model	49
2.5	Drag model and particle motion	52
2.6	Gas-phase homogeneous combustion model	54
2.7	Sub-grid scale turbulence model	57
2.8	Gas-phase radiation absorption and emission model	59
2.8.1	The Prescribed Global Radiant Fraction (PGRF) approach	60
2.8.2	The Weighted-Sum-of-Gray-Gases (WSGG) approach	61
2.9	Soot modeling	63
2.10	Summary	63
3	Verification and Evaluation of the Computational Framework	67
3.1	Overview	67
3.2	Verification tests	68
3.2.1	In-depth heat conduction of solid particles	68
3.2.2	Momentum exchange between the solid- and gas-phases	69
3.2.3	Pressure-velocity coupling inside the fuel bed	72
3.2.4	Radiation absorption and emission inside the fuel bed	74
3.2.5	Smoldering propagation due to radiation penetration	78
3.3	Calibration of the thermal degradation model	80
3.3.1	Micro-scale thermal degradation of pine wood	80
3.3.2	Micro-scale thermal degradation of cardboard	84
3.4	Evaluation of the PBR model against bench-scale experiments	88
3.5	Representative results of complete consumption and the issue of volume change	94
3.6	Summary	99
4	Thermal Feedback in Canonical Pool Fire Configurations	101
4.1	Overview	101
4.2	Medium-scale methanol pool fire	102
4.2.1	Numerical configuration	103
4.2.2	Flame structure	105
4.2.3	Thermal feedback	111
4.3	Turbulent ethylene burner with controlled coflow (FM-Burner)	115
4.3.1	Numerical configuration	116
4.3.2	Flame structure	119
4.3.3	Radiant emissions	123
4.4	Summary	128

5	Simulations of Thermal Degradation of Biomass Particles under Prescribed External Gas Conditions	130
5.1	Overview	130
5.2	Pyrolysis of biomass particles under steady and oscillatory heating conditions	132
5.2.1	Particle response time	134
5.2.2	Response of thick charring particles to radiative heating	134
5.2.3	Response of thick non-charring (shrinking) particles to radiative heating	137
5.2.4	Response of thin non-charring (shrinking) particles to radiative heating	139
5.2.5	Response of thin particles to convective heating	140
5.2.6	Response of thick particles to convective heating	142
5.3	Maps of the pyrolysis and oxidation of porous biomass particles	145
5.3.1	Effect of the particle size	151
5.3.1.1	Maps of small particles (2 mm diameter) heated for a long duration ($\tau_{PIHF} = 120\text{ s}$)	151
5.3.1.2	Maps of large particles (20 mm diameter) heated for a long duration ($\tau_{PIHF} = 120\text{ s}$)	154
5.3.2	Effect of the residence time (τ_{PIHF})	158
5.3.3	Threshold value of the particle core temperature for complete smoldering	160
5.4	Summary	165
6	Simulations of Fire Spread in Engineered Cardboard Fuel Beds	168
6.1	Overview	168
6.2	Numerical configuration	169
6.2.1	Computational domain and fuel bed setup	169
6.2.2	Computational mesh resolution	175
6.2.3	Boundary conditions	177
6.2.4	Sub-models	178
6.2.5	Computational cost	178
6.3	Fire behavior in Burn 53 and Burn 67	179
6.3.1	Flow field at cold flow	179
6.3.2	Flow field during combustion	182
6.3.3	Flame structure	184
6.3.4	Fire intensity and rate of spread	187
6.3.5	Local particle viewpoint	190
6.4	The Pseudo Incident Heat Flux (PIHF)	193
6.5	The flame residence time	194
6.6	Fire behavior variation with the fuel bed packing	197
6.6.1	Global fire behavior	197
6.6.2	Local particle viewpoint	200
6.7	Summary	203

7	Simulations of Fire Spread in Idealized Uniform and Mixed Size Pine Wood Fuel Beds	204
7.1	Overview	204
7.2	Numerical configuration	205
7.2.1	Computational domain and fuel bed setup	207
7.2.2	Computational mesh resolution	209
7.2.3	Boundary conditions	211
7.2.4	Sub-models	212
7.2.5	Computational cost	212
7.3	Fire spread in the uniform fuel bed	212
7.3.1	Global fire behavior	213
7.3.2	The structure of the fire	216
7.3.3	Sensitivity to the grid resolution	217
7.4	Fire spread in the mixed-size fuel patch	224
7.4.1	Variations with the fuel bed height	225
7.4.2	Local gas conditions at mid-elevation of the fuel bed	228
7.4.3	Particle behavior in the wind-dominated fire	231
7.4.4	Particle behavior in the buoyancy-dominated fire	237
7.4.5	The Pseudo Incident Heat Flux (PIHF)	238
7.4.6	Interpretation of the particles' behavior using the quasi-steady 2-D maps	243
7.5	Summary	247
8	Conclusion and Future Directions	249
A	Numerical Algorithms of the Particle Burning Rate Model (PBR)	257
A.1	Discretization of the governing equations	260
A.1.1	Solid-phase mass conservation equations	260
A.1.2	The temperature equation	262
A.1.3	The gas-phase oxygen mass equation	267
A.1.4	The pressure equation	272
A.2	Iterative scheme	275
A.3	Temporal discretization	276
A.4	Deforming mesh and re-meshing capabilities	278
B	Modified Eddy Dissipation Model for Diffusion Controlled Flames	280
B.1	Model derivation	280
B.2	Simulations of two-dimensional laminar counter-flow methane-air flames	284
C	Extension of the LSP Soot Model to LES Framework	287
C.1	Conservation of soot mass	287
C.2	Soot formation and oxidation terms	288
C.3	Closure model for turbulent soot formation and oxidation rates	289
C.4	Integration of the probability density function	291

D Verification of the WSGG Model Implementation in OpenFOAM	292
D.0.1 Radiation configuration 1	293
D.0.2 Radiation configuration 2	294
D.0.3 Radiation configuration 3	295
D.0.4 Radiation configuration 4	297
E Installation of PBRFoam on HPC Clusters and its Parallel Performance	299
E.1 Installation	299
E.2 Parallel Performance	301
Bibliography	303

List of Tables

3.1	Analytical solutions of heat conduction inside solid fuel particles of different geometries, where $\tau = \alpha_s t / \zeta^2$, $\alpha_s = k_s / \rho_s c_s$, T_g the external gas temperature, and $T_{s,i}$ the initial particle temperature.	69
3.2	Calibrated model parameters for pine wood.	85
3.3	Calibrated chemical kinetic parameters for pine wood.	85
3.4	Thermo-physical properties of cardboard.	87
3.5	Chemical kinetic parameters for thermal degradation of cardboard. .	87
5.1	Input parameters of the biomass particles used in the oscillatory heating study.	133
5.2	Ignition and burnout times of particles exposed to quasi-steady (QS) radiative heating and oscillatory radiative heating at 0.1 and 1 Hz. The percentage difference in burnout time is calculated relative to the QS case.	137
5.3	Ignition and burnout times of particles exposed to quasi-steady (QS) convective heating and oscillatory convective heating at 0.1 and 1 Hz. The percentage difference in burnout time is calculated relative to the QS case.	143
6.1	Conditions of Burn 53 and Burn 67.	175
6.2	Characteristics of Burn 53 and Burn 67. A comparison between observed and simulated quantities.	187
7.1	Design parameters of the buoyancy-dominated and wind-dominated line fires in the uniform pine wood fuel bed.	206
7.2	Simulated parameters of the buoyancy-dominated and wind-dominated line fires in the uniform pine wood fuel bed.	216
7.3	Summary of the simulation results corresponding to particles in the mixed-size patch located at $x = 40\text{ m}$, $y = 0.2\text{ m}$, $z = 0$ position. .	242
A.1	Definition of the mesh parameters. In these expressions, A_{rect} is the exposed surface area of rectangular particles, and L_{cyl} is the length of the cylindrical-shaped particles. The subscript C refers to the center of the cell; the subscript R refers to its right-boundary.	259

List of Figures

1.1	Scales of the wildland fire problem. Images sources: Smithsonian's National Zoo & Conservation Biology Institute [3]; Josh Edelson via Getty Images; Greenpeace International [4]; and NASA Earth Observatory [5].	4
1.2	The different classes of CFD models used for simulating wildland fire behavior: combustion solvers resolve dynamics at the vegetation and flame scales; wildfire solvers resolve dynamics at the fireline and geographical scales; atmospheric boundary layers (ABL) solvers resolve dynamics at the meteorological scales.	7
1.3	The larger framework of this project: chain of model development.	10
2.1	A schematic of fire spread in a fuel bed showing the characteristic length-scales of the flame and the different zones identified based on the particle burning state.	42
2.2	Schematic side view of a typical fuel bed showing fuel patches separated by a given distance (left). The computational grid is shown in the background. Each fuel patch is modeled by a collection of mono- or poly-dispersed particles described at the sub-grid level (right). The thermal degradation of each particle is tracked using the PBR solver through the computational grid shown in the inset.	44
2.3	Variation of the convective heat transfer coefficient with: a) wind velocity for particles with different sizes; and b) particle's effective diameter at a wind velocity of 1 m/s.	51
2.4	Variation of drag coefficient with Reynolds number for cylindrical- and rectangular-shaped particles.	53
2.5	Temperature profile of laminar counter-flow diffusion flames under adiabatic conditions obtained from well-resolved simulations using the modified EDM.	58
2.6	Flowchart of the computational modeling framework: the chart of the PBRFoam solver is highlighted in yellow; the chart highlight in gray depicts an interface; the chart of the PBR solver is highlighted in blue.	65
3.1	Temperature evolution inside a semi-infinite rectangular-shaped solid particle. The exposed surface is at $\zeta = 0$	70

3.2	Temperature evolution inside a) cylindrical- and b) spherical-shaped solid particles. The exposed surface is at $\zeta = 0.01 \text{ m}$	70
3.3	Simulations (solid lines) and analytical solution (symbols) of the momentum exchange between solid and gas-phases: a) transient velocity of the solid and the gas-phases, b) momentum of the gas-phase and total momentum of the system (gas+solid).	72
3.4	Comparison between simulations with different grid resolutions (solid lines) and the analytical solution (symbols) of the pressure variation inside a fuel bed.	73
3.5	Simulations with different grid resolutions (solid lines) and analytical solution (symbols) of the radiation absorption by the fuel bed: a) radiation intensity variation with different packing ratios, b) spatial variation of the radiation intensity along the fuel bed length.	76
3.6	Spatial variation of the radiation intensity inside a fuel bed that emits and self-absorbs radiation. The solid lines refer to the numerical simulations, while the symbols refer to the analytical solution. The emission contribution obtained from a case where absorption is neglected is also shown.	77
3.7	Smoldering propagation in idealized charred pine wood bed. The gas-phase is colored by the mass fraction of CO_2 . The fuel bed is colored by a) the percentage mass with red indicating 100% char and blue indicating 100% ash, b) the positive net radiative heat flux indicating heating zones.	79
3.8	Smoldering propagation in idealized charred pine wood bed: a) time evolution of the back and front edges of the smoldering zone; b) smoldering intensity.	81
3.9	Variation of the mass loss rate of a micro-scale pine wood sample with the particle temperature at a) heating rates of 5 and 10 K/min in the inert environment; and b) heating rate of 10 K/min in oxidative environments. Lines: PBR simulations using the kinetic parameters of Lautenberger and Fernandez-Pello [44]. Symbols: the TGA measurements of Ref. [80].	83
3.10	Variation of the mass loss rate of a micro-scale pine wood sample with the particle temperature at a) heating rates of 5 and 10 K/min in the inert environment; and b) heating rate of 10 K/min in oxidative environments. Lines: PBR simulations using the kinetic parameters of Anca-Couce et al. [80]. Symbols: the TGA measurements of Ref. [80].	84
3.11	Evolution of the cardboard particle normalized mass loss rate (top row) and normalized mass (bottom row) with temperature. Comparison of the simulated thermal degradation of cardboard using the calibrated PBR model (solid lines) and the TGA measurements of Refs. [81, 82] (symbols) at a heating rate of 10 K/min in a) 100% N_2 environment, b) 10% O_2 – 90% N_2	89

3.12 Comparison of the simulated heat flow (solid line) and the DSC measurements of Ref. [81] collected at a heating rate of 10 K/min in an inert environment.	90
3.13 Time evolution of the mass loss rate of the 3.8 cm pine wood particle in inert and oxidative environments at a) 25 kW/m^2 and b) 40 kW/m^2 irradiation. Comparison between simulations of the PBR model (lines) and experimental data of Kashiwagi et al. [85] (symbols).	91
3.14 Spatial variation of exposed surface and in-depth temperatures of the 3.8 cm pine wood particle at 40 kW/m^2 irradiation in: a) 100% N_2 , b) 89.5% $N_2 - 10.5\% O_2$, and c) air. Comparison between simulations from the PBR model (lines), experimental data of Kashiwagi et al. [85] (symbols).	93
3.15 Spatial variation of exposed surface temperature and in-depth temperatures of the 3.8 cm pine wood particle at 25 kW/m^2 irradiation in 89.5% $N_2 - 10.5\% O_2$. Comparison between simulations using the PBR model (lines), experimental data of Kashiwagi et al. [85] (symbols).	94
3.16 Predictions, using different grid resolutions, of a) MLR and b) the temperature at 5 mm depth inside the particle under 40 kW/m^2 irradiation in ambient air.	95
3.17 Variation of a 10 mm diameter pine wood particle mass loss rate (a) and mass (b) with time obtained using PBR simulations. The particle is exposed to 60 kW/m^2 radiative flux for 60 s in ambient air flowing at 1 m/s. The vertical dashed line indicates the end of the external heating period.	96
3.18 Two snapshots of spatial profiles of temperature (a) and volume fraction of char and ash (b) inside a 10 mm diameter pine wood particle exposed to 60 kW/m^2 radiative flux for 60 s in ambient air flowing at 1 m/s.	97
3.19 Two snapshots of spatial profiles of oxygen mass fraction (a) and char oxidation reaction rate (b) inside a 10 mm diameter pine wood particle exposed to 60 kW/m^2 radiative flux for 60 s in ambient air flowing at 1 m/s.	98
3.20 Temporal evolution of the volume of 10 mm diameter pine wood particle exposed to 60 kW/m^2 radiative flux for 60 s in ambient air flowing at 1 m/s. The dashed line represents simulations conducted using the char and ash yields listed in Table 3.2. The solid line represents simulations conducted with modified char and ash yields of 0.3 and 0.005, respectively.	99
4.1 A 3-D view of the computational domain of the methanol pool fire (left), and 2-D sections showing an enlarged view of the medium mesh resolution near the fuel pan (right).	103

4.2	A view of the virtual heat flux gauges used in the numerical configuration: a) side view of the computational domain near the burner lip and the gauges; b) top view of the burner surface and the gauges. The gauges are colored in black. The computational domain and the burner surface are colored in red.	106
4.3	Sequence of instantaneous snapshots of the methanol pool flame taken at selected times during a representative instability cycle. The flame is visualized using volume rendering of the high-temperature region (defined as the region where temperatures are larger than 800 K). The time between successive snapshots is 0.06 s and the total duration of the sequence is 0.42 s. The fuel pan and liquid pool surface are colored grey. The simulation was performed with the fine mesh and with PGRF.	108
4.4	Sequence of instantaneous snapshots of the flame-flow configuration taken at selected times during a representative instability cycle and plotted in a central vertical plane. The flame is visualized using isocontours of temperature; the flow is visualized using velocity vectors. The fuel pan and liquid pool are colored white. See the caption of Fig. 4.3.	109
4.5	The power spectrum of the temporal variations of the simulated heat release rate.	110
4.6	Centerline vertical variations of: mean temperature, \bar{T} ; mean vertical velocity, \bar{u} ; mean radial velocity, \bar{v} ; <i>rms</i> temperature, T_{rms} ; <i>rms</i> vertical velocity, u_{rms} ; <i>rms</i> radial velocity, v_{rms} ; cross-correlation between vertical velocity and temperature, $u' T'$. Comparisons between experimental data (symbols) and simulation results obtained with a coarse mesh (dashed blue line), a medium mesh (dash-dotted black line), and a fine mesh (solid red line). Simulations performed with PGRF. The vertical bars denote the uncertainties in the experimental data.	112
4.7	Radial variations of the mean gauge heat flux at 13 mm above the pool surface: (Left) radiative heat flux, $\overline{\dot{q}_{rad}''}$; (Right) total heat flux, $\overline{\dot{q}_{tot}''}$. Comparisons between experimental data (square symbols) and simulations performed with the medium mesh and with PGRF (dashed red line with diamond symbols) or with WSGG (dashed blue line with circle symbols). The vertical bars denote the uncertainties in the experimental data.	113
4.8	Radial variations of the mean radiative heat flux at 13 mm above the pool surface. Comparisons between experimental data (square symbols) and simulations performed with the medium mesh and with the WSGG-Bordbar model (dashed blue line with circle symbols), WSGG-Cassol (solid red line with square symbols), and PMC-LBL (dotted purple line with x symbols). The vertical bars denote the uncertainties in the experimental data.	115

4.9	Comparisons between experimental data (square symbols) and simulations performed with the WSGG-Bordbard model with 36 solid angles (dashed red line with diamond symbols), 64 solid angles (dashed blue line with circle symbols), or 100 solid angles (dotted purple line with square symbols). See the caption of Fig. 4.7.	116
4.10	Photographs of the FM-Burner taken during experiments conducted at different oxygen concentrations [88].	117
4.11	A 3D representation of the computational domain of the FM-Burner (left), and a slice showing the computational mesh near the burner (right).	118
4.12	Contours of the instantaneous and mean values of: the temperature (T and \bar{T}), the mixture fraction (Z and \bar{Z}), and the soot volume fraction (f_v and \bar{f}_v). The white isocontour represents $f_v = 10^{-6}$. The results correspond to the FM-Burner at 20.9% O_2 coflow.	120
4.13	Contours of the instantaneous and mean values of: the volumetric soot formation rate ($\dot{\omega}_{sf}'''$ and $\bar{\omega}_{sf}'''$), and the volumetric soot oxidation rate ($\dot{\omega}_{sf}'''$ and $\bar{\omega}_{sf}'''$). The results correspond to the FM-Burner at 20.9% O_2 coflow.	122
4.14	Radial profiles of mean and <i>rms</i> temperature at different elevations above the fuel surface in the FM-Burner at 20.9% O_2 coflow. Comparison between experiments (symbols) and simulations with PGRF (red dash-dot line), WSGG with gas and soot absorption/emission (blue dashed line), and WSGG with gas radiation only (solid black line).	124
4.15	Radial profiles of mean and <i>rms</i> soot volume fraction at different elevations above the fuel surface of the FM-Burner at 20.9% O_2 coflow. Comparison between experiments (symbols) and simulations with the WSGG model (blue dashed line).	125
4.16	Axial variations of the mean radiative power of the FM-Burner at 20.9% O_2 and 15.2% O_2 concentrations in the coflow. Comparisons between experimental data (symbols) and simulations performed with the PGRF model (dotted red line), the WSGG model with gas and soot contributions (dashed blue line), and the WSGG with gas contribution only (solid black line).	127
4.17	Axial variations of the radiation absorption and emission of the FM-Burner at 20.9% O_2 concentrations in the coflow. The results are estimated using the WSGG model accounting for gas and soot radiation.	127
5.1	Response of a 20 mm-thick charring particle to radiative heating: a) particle surface and core temperatures; b) particle mass loss rate. Comparison between particle response to quasi-steady forcing (QS) (lines with symbols) and oscillatory forcing at $f = 0.1$ Hz or $f = 1$ Hz (lines).	136
5.2	Response of a 20 mm thick non-charring particle to radiative heating: a) particle size; b) particle mass loss rate. See caption of Fig. 5.1.	138

5.3	Response of the 2 <i>mm</i> non-charring particle to radiative heating: a) particle surface and core temperatures; b) particle mass loss rate. See caption of Fig. 5.1.	140
5.4	Response of a 2 <i>mm</i> non-charring particle to convective heating: a) particle surface and core temperatures; b) particle mass loss rate. Comparison between the particle response to quasi-steady forcing (QS) (lines with symbols) and oscillatory forcing by oscillations in T_g at $f = 0.1$ Hz or $f = 1$ Hz (lines).	142
5.5	Response of a 2 <i>mm</i> non-charring particle to convective heating: a) particle surface and core temperatures; b) particle mass loss rate. Comparison between the particle response to quasi-steady forcing (QS) (lines with symbols) and oscillatory forcing by oscillations in both T_g and u_g at $f = 0.1$ Hz or $f = 1$ Hz (lines).	144
5.6	Mass loss rate response of the a 20 <i>mm</i> thick particle to radiative heating: a) non-charring; b) charring. See caption of Fig. 5.5	145
5.7	Response of a 10 <i>mm</i> particle to an external irradiation of $G = 60 \text{ kW/m}^2$ for 60 s, and ambient air flow at $u_g = 1 \text{ m/s}$: a) the net total heat flux; b) the surface and core temperatures; c) the convective heat transfer coefficient; d) the surface emissivity. The duration of the external irradiation is highlighted in red.	148
5.8	Response of a 10 <i>mm</i> particle to an external irradiation of $G = 60 \text{ kW/m}^2$ for 60 s, and ambient air flow at $u_g = 1 \text{ m/s}$: a) the reactions rates of <i>Rd-Rop</i> ; b) the normalized solid constituent mass. The duration of the external irradiation is highlighted in red.	149
5.9	Maps of a 2 <i>mm</i> pine wood particle for $\tau_{\text{PIHF}} = 120 \text{ s}$: a) degree of completion of the drying reaction <i>Rd</i> ; b) degree of completion of the pyrolysis reaction <i>Rp+Rop</i> ; c) degree of completion of the char oxidation reaction <i>Rco</i> . The gray zone indicates $\text{PIHF} < \text{PIHF}_0$	153
5.10	Maps of a 2 <i>mm</i> pine wood particle for $\tau_{\text{PIHF}} = 120 \text{ s}$: a) peak value of the pyrolysis rate; b) pyrolysis duration. The red solid iso-contour depicts the flaming threshold of 1 g/s/m^2 . The gray zone indicates $\text{PIHF} < \text{PIHF}_0$	154
5.11	Maps of a 2 <i>mm</i> pine wood particle for $\tau_{\text{PIHF}} = 120 \text{ s}$: a) the peak particle temperature <i>Rd</i> ; b) the temperature at the core of the particle at $t = \tau_{\text{PIHF}}$. The gray zone indicates $\text{PIHF} < \text{PIHF}_0$	155
5.12	Maps of a 20 <i>mm</i> pine wood particle for $\tau_{\text{PIHF}} = 120 \text{ s}$: a) degree of completion of the drying reaction <i>Rd</i> ; b) degree of completion of the pyrolysis reaction <i>Rp+Rop</i> ; c) degree of completion of the char oxidation reaction <i>Rco</i>	156
5.13	Maps of a 20 <i>mm</i> pine wood particle for $\tau_{\text{PIHF}} = 120 \text{ s}$: a) peak value of the pyrolysis rate; b) pyrolysis duration. The red solid iso-contour highlights the flaming threshold of 1 g/s/m^2	157
5.14	Maps of a 20 <i>mm</i> pine wood particle for $\tau_{\text{PIHF}} = 120 \text{ s}$: a) the peak particle temperature <i>Rd</i> ; b) the temperature at the core of the particle at $t = \tau_{\text{PIHF}}$	158

5.15 Maps of the degree of completion of pyrolysis (left) and the degree of completion of char oxidation (right) for a 2 mm pine wood particle heated for different periods: a) $\tau_{\text{PIHF}} = 5 \text{ s}$, b) $\tau_{\text{PIHF}} = 15 \text{ s}$, and c) $\tau_{\text{PIHF}} = 30 \text{ s}$.	161
5.16 Maps of the particle peak temperature (left), and the particle core temperature at the end of the heating period (right) for a 2 mm pine wood particle heated for different periods: a) $\tau_{\text{PIHF}} = 5 \text{ s}$, b) $\tau_{\text{PIHF}} = 15 \text{ s}$, and c) $\tau_{\text{PIHF}} = 30 \text{ s}$.	162
5.17 Maps of the degree of completion of pyrolysis (left) and the degree of completion of char oxidation (right) for a 20 mm pine wood particle heated for different periods: a) $\tau_{\text{PIHF}} = 15 \text{ s}$, b) $\tau_{\text{PIHF}} = 30 \text{ s}$, and c) $\tau_{\text{PIHF}} = 60 \text{ s}$.	163
5.18 Maps of the particle peak temperature (left), and the particle core temperature at the end of the heating period (right) for a 20 mm pine wood particle heated for different periods: a) $\tau_{\text{PIHF}} = 15 \text{ s}$, b) $\tau_{\text{PIHF}} = 30 \text{ s}$, and c) $\tau_{\text{PIHF}} = 60 \text{ s}$.	164
5.19 Scatter plot of the char oxidation degree of completion against the particle core temperature achieved at the time corresponding to the end of the heating duration τ_{PIHF} .	165
 6.1 Images from the experimental burns of fire spread in cardboard fuel beds conducted at the Missoula Fire Sciences Laboratory (courtesy of Dr. Mark Finney): a) top view of an experiment conducted on an inclined surface, featuring flaming and glowing zones; b) back view of a buoyancy-dominated fire experiment in the wind tunnel (Burn 53), featuring a uniform flame front with peak and trough structures; c) isometric view of the wind-dominated fire in the wind tunnel at high speed (Burn 67), featuring flaming and glowing zones as well as a curved flame front.	170
6.2 Schematic of the wind tunnel facility at Missoula Fire Sciences Laboratory (adapted from Ref. [105]). The dimensions on the image are obtained from private communication with Dr. Mark Finney. The blue dashed box contours the simulated region.	171
6.3 The computational domain used in the simulations of the cardboard fire spread. The fuel bed is colored in yellow.	172
6.4 Variation of the fuel bed packing ratio with the axial spacing between particle arrays.	174
6.5 Contours of the velocity magnitude at the vertical center-plane of the wind tunnel (top slice) and at a horizontal plane at $y = 0.025 \text{ m}$ elevation (bottom slice). The contours correspond to cold flow simulations of a) Burn 53 and b) Burn 67.	180
6.6 Profiles of the mean velocity at different locations in the streamwise direction in a) the low-velocity case (Burn 53), and b) the high-velocity case (Burn 67).	181
6.7 Profiles of the root-mean-square velocity. See the caption of Fig. 6.6.	181

6.8 Streamwise variation of Δy_w^+ in: a) the low-velocity case; b) the high-velocity case. The dashed line represents instantaneous values and the solid line represents mean values. The cardboard fuel bed starts at $x = 0$	182
6.9 Tunnel flow field in the case of wind-dominated fire (Burn 67). Contours of the axial velocity in the tunnel mid-plane. The velocity vectors are scaled by velocity magnitude.	183
6.10 Tunnel flow field in the case of a buoyancy-dominated fire (Burn 53) with a) a prescribed inlet velocity, b) a prescribed total pressure. See the caption of Fig. 6.9.	184
6.11 A 3-D rendering of the simulated fires: a) back view of Burn 53 showing the iso-surface of hot gases at 1000 K and the cardboard particles colored by the mass loss rate (fire spreads into the page); b) isometric view of Burn 67 showing the iso-volume of hot gases $> 550\text{ K}$ and the cardboard particles colored by their surface temperature (fire spreads from left to right).	186
6.12 Global fire behavior of Burn 53 and Burn 67 in terms of a) rate spread, and b) fire line intensity. The dashed lines represent the slope from the measured rate of spread.	188
6.13 Time evolution of the pyrolysis front obtained from simulations with different boundary conditions: a) effect of inlet boundary in Burn 53; b) effect of the side walls on Burn 67.	189
6.14 Time evolution of the pyrolysis front obtained from simulations with the baseline mesh and a refined mesh.	190
6.15 Local viewpoint of the gas conditions in Burn 67 at the top of the particle located at $x = 3\text{ m}$, $z = 0$: a) local gas temperature, b) local gas velocity, c) local oxygen mass fraction; and d) local irradiation. .	192
6.16 The behavior of the particle located at $x = 3\text{ m}$, $z = 0$ in Burn 67: a) particle surface and core temperature, b) particle constituents masses, c) particle mass loss rate; and d) net heat flux at the particle's exposed surface.	193
6.17 The convective and radiation contributions to the pseudo incident heat flux (PIHF) extracted at the top of the fuel bed at $x = 3\text{ m}$, $z = 0$ in a) Burn 53, and b) Burn 67.	195
6.18 Flame residence time based on a) gas temperature, b) particle flaming duration, and c) duration of intense PIHF. The red solid line is a spline fit of the raw data. The vertical dashed blue lines delimit the start and the end of the residence time. The data correspond to the particle located at $x = 3\text{ m}$, $z = 0$ in Burn 67.	196
6.19 A 3-D rendering of the flaming zone variation with the packing ratio β_s . The flaming particles are colored by the gaseous fuel release rate (GFRR) (i.e., the production rate of fuel from the pyrolysis reactions R_p and R_{op}). The hot gases at 1000 K are represented by the white iso-surface.	198

6.20 Variations of the a) fire intensity, b) the flame zone depth, c) the fire rate of spread, and d) the flame height with the fuel bed packing ratio. The symbols represent the simulated cases and the solid line represents a linear fit to the simulated data.	199
6.21 The behavior of 36 particles in Burn 67, starting from $x = 3 \text{ m}$, $z = 0$ and separated by 0.2 m in the x -direction and 0.25 m in the z -direction: a) particle surface temperature, b) normalized particle masses, c) particle state, and d) particle mass loss rate.	201
6.22 Variation of the residence time with the packing ratio: a) the particle flaming and smoldering times, b) the PIHF time, and c) the flame residence time based on the gas temperature. The symbols represent the average of 36 particles, the bars represent the standard deviation, and the solid lines represent linear fit. The dashed blue line represents the experimental fit of Finney et al. [2].	202
7.1 A 3-D view of the computational domain used in the simulations of fire spread in pine wood fuel beds: a) the uniform fuel bed with 2 mm particles ($\beta_s = 0.005$); b) the fuel bed with a patch of mixed small/large particles ($D_p = 2$ and 10 or 20 mm) located at $38 \leq x \leq 42 \text{ m}$ ($\beta_s = 0.0068$ or 0.012).	208
7.2 Propagation of the wind-dominated fire in the uniform bed: a) time evolution of the simulated flame, pyrolysis and smoldering zones (solid and dashed lines) and the estimated spread from Rothermel model (dotted line); b) time evolution of the simulated fire intensity from homogeneous gas-gas reactions (black line) and from heterogeneous solid-gas reactions (blue line).	214
7.3 Global behavior of the buoyancy-dominated fire in the uniform bed at 1 m/s external wind speed. See the caption of Fig. 7.2	215
7.4 Visualization of the wind-dominated fire in the uniform bed: a) isometric view (fire spreads from left to right) of; b) back view of the hot gases only (fire spreads into the page). The hot gases in (a) and (b) are rendered by an iso-volume of $T > 550 \text{ K}$ and colored by the gas temperature. The glowing solid particles in (a) are colored by their surface temperature.	218
7.5 Visualization of the buoyancy-dominated fire in the uniform bed: a) isometric view (fire spreads from left to right) of; b) back view of the hot gases only (fire spreads into the page). The hot gases in (a) and (b) are rendered by an iso-volume of $T > 550 \text{ K}$ and colored by the gas temperature. The glowing solid particles in (a) are colored by their surface temperature.	219
7.6 Visualization of the solid particles colored by their respective burning state. The unburned particles are colored in green, the burned particles are colored in black, the flaming particles are colored red, and the smoldering particles are colored in yellow.	220

7.7	Global fire behavior in the buoyancy-dominated fire predicted using three grid resolutions of the gas-phase: a) pyrolysis front, b) fire intensity from homogeneous gas phase combustion, and c) fire intensity from heterogeneous particle reactions. The particle resolution is fixed at $25 \mu m$	221
7.8	Global fire behavior in the wind-dominated fire predicted using three grid resolutions of the gas-phase. See the caption of Fig. 7.7	222
7.9	Global fire behavior in the buoyancy-dominated fire predicted using three mesh resolutions of the particles. The gas-phase resolution is $10 cm$	223
7.10	Behavior of the particle located $20 m$ downstream of the ignition burner in the buoyancy-dominated fire in terms of a) the temperature at the core of the particle; b) the particle mass. The results are obtained using three mesh resolutions of the particles, and a gas-phase resolution of $10 cm$	224
7.11	Snapshots of the wind-dominated fire while spreading across the mixed-size patch of 2 and $10 mm$ particles. The flame is rendered by an iso-volume of gases at $T_g > 550 K$. The solid particles are colored by their surface temperature.	226
7.12	The variation of a) the core temperature and b) the normalized mass of the lower, middle and upper parts of the $20 mm$ diameter particle located at $x = 40 m, z = 0$ in the mixed-size patch of the wind-dominated fire.	227
7.13	The variation of a) the core temperature and b) the normalized mass of the lower, middle and upper parts of the $10 mm$ diameter particle located at $x = 40 m, z = 0$ in the mixed-size patch of the wind-dominated fire.	228
7.14	External conditions around the particle evaluated at $x = 40 m, y = 0.2 m, z = 0$ position in the wind-dominated fire: a) local gas temperature; b) local irradiation; c) local oxygen mass fraction; d) local gas velocity.	230
7.15	Time variation of the surface and core temperatures of the particles in the mixed-size patch with $2 mm$ and $10 mm$ particles (a, b), and in the mixed-size patch with the $2 mm$ and $20 mm$ particles (c, d). The data correspond to particles located at $x = 40 m, y = 0.2 m, z = 0$ in the wind-dominated fire.	232
7.16	Time variation of the normalized mass loss rate of particles in mixed-size patch of the wind-dominated fire. See caption of Fig. 7.15.	233
7.17	Time variation of the normalized solid constituents masses of particles in mixed-size patch of the wind-dominated fire. See caption of Fig. 7.15.	234
7.18	Spatial distribution of: a) temperature; b) volume fraction of char and ash; c) oxygen mas fraction; d) char oxidation reaction rate inside the $10 mm$ particle located at $x = 40 m, y = 0.2 m, z = 0$ in the mixed-size patch of the wind-dominated fire.	236

7.19	Spatial distributions inside the 20 mm particle. See the caption of Fig. 7.18.	237
7.20	Time variation of the normalized solid constituents masses of particles in the mixed-size patch with 2 mm and 10 mm particles (a, b), and in the mixed-size patch with the 2 mm and 20 mm particles (c, d). The data correspond to particles located at $x = 40 \text{ m}$, $y = 0.2 \text{ m}$, $z = 0$ in the buoyancy-dominated fire.	239
7.21	Time variation of the a) total heat flux, b) convective heat flux, and c) radiative heat flux at the surface of the 2 and 10 mm particles located at $x = 40 \text{ m}$, $z = 0$ in the mixed-size patch of the wind-dominated fire. The heat fluxes are evaluated at mid-elevation.	240
7.22	Time variation of the instantaneous values of the PIHF (black solid line), the moving average (red solid line), and the time integral of the intense PIHF of the 10 mm particle located at $x = 40 \text{ m}$, $y = 0.2 \text{ m}$, $z = 0$ position in the wind-dominated fire.	242
7.23	Time variation of the convective and the radiative components of the PIHF of particles in mixed-size patch of the wind-dominated fire. See caption of Fig. 7.15.	244
7.24	Time variation of the convective and the radiative components of the PIHF of particles in mixed-size patch of the buoyancy-dominated fire. See caption of Fig. 7.20.	245
7.25	Maps of R_{co} degree of completion for 2 mm particles (a,b), 10 mm particles (c,d), and 20 mm particles (e,f). The cross symbol represents conditions from the buoyancy-dominated fire listed in Table 7.3. The circles represent similar conditions from the wind-dominated fire.	246
A.1	One-dimensional computational mesh for particles with: (a) rectangular slab geometry; (b) cylindrical or spherical geometry	258
A.2	Thermal boundary condition at the exposed surface of the particle.	267
A.3	3D rendering of a fuel bed with discrete fuel particles colored by their corresponding time-step during fire spread.	277
B.1	Predictions of the heat release rate per unit surface area of counter-flow methane/air diffusion flames under different mixing conditions.	285
B.2	Profiles of mixture fraction (left) and temperature (right) at the centerline distance between the fuel and oxidizer nozzles for an under-resolved flame using EDM and a well-resolved flame using single-step Arrhenius chemistry.	286
B.3	Scatter of the estimated values of the HRRPUA using a representative value of $\chi_{st} = 1 \text{ s}^{-1}$ in Eq. B.13 .	286
D.1	Comparison between the numerical simulations (lines) and the LBL solution (symbols) of radiation configuration 1.	294
D.2	Comparison between the numerical simulations (lines) and the LBL solution (symbols) of radiation configuration 2.	295

D.3	Comparison between the numerical simulations (lines) and the LBL solution (symbols) of radiation configuration 3	296
D.4	Comparison between the numerical simulations (lines) and the LBL solution (symbols) of radiation configuration 4	298
E.1	Test of the scaling performance of PBRFoam on the HPC cluster Expanse.	302

Nomenclature

Abbreviations

ABL	Atmospheric Boundary Layer
CFD	Computational Fluid Dynamics
DL	Deep Learning
DSC	Differential Scanning Calorimetry
EDM	Eddy Dissipation Model
FMC	Fuel Moisture Content
GFRR	Gaseous Fuel Release Rate
GIS	Geographic Information System
HPC	High Performance Computing
HRR	Heat Release Rate
HRRPUA	Heat Release Rate Per Unit Area
LBL	Line-by-line
LES	Large Eddy Simulation
LSP	Laminar Smoke Point
MaCFP	Measurement and Computation of Fire Phenomena
MLR	Mass Loss Rate
MPI	Message Passing Interface
MRTE	Multiphase Radiative Transfer Equation
PBR	Particle Burning Rate
PDF	Probability Density Function
PGRF	Prescribed Global Radiant Fraction
PIHF	Pseudo Incident Heat Flux
PMC	Photon Monte Carlo
QS	Quasi-steady
RHS	Right Hand Side
ROS	Rate of Spread
TGA	Thermogravimetric Analysis
UMD	University of Maryland
WALE	Wall Adapting Local Eddy-viscosity
WSGG	Weighted-Sum-of-Gray-Gases

Symbols

α	heat diffusivity
β	packing ratio
χ_{rad}	radiant fraction
ΔH	heat of reaction/combustion
Δy_w^+	vertical wall unit
δ	size (half-thickness) of rectangular-shaped particles
δ_{ik}	Kronecker symbol
ΔLES	LES filter size
$\dot{\omega}'''$	volumetric mass reaction rate of gas-phase species/soot
\dot{h}_{th}'''	volumetric rate of heat transfer
\dot{m}'''	solid-phase volumetric mass reaction rate
\dot{m}''	mass flux
\dot{q}_{comb}'''	heat release rate of the gas-phase combustion
\dot{q}_{rad}'''	net radiative power density of the gas-phase
\dot{q}''	heat flux
\dot{Q}_{rad}''	radiative heat flux
\dot{Q}'	fire line intensity
ϵ	emissivity
ϵ_{Turb}	subgrid-scale turbulent dissipation rate
η	mass yield
γ	effective heat conductivity due to pore radiation
κ	radiation absorption coefficient
μ	dynamic viscosity
ν	kinematic viscosity
Ω	radiation solid angle
ω	inverse of periodic time
ϕ	coordinate factor
ψ	porosity
ρ	density
σ	Stefan-Boltzmann constant
σ_p	particle surface area to volume ratio
τ	characteristic time-scale/residence time
τ_w	wall shear stress

Θ	normalized temperature
\tilde{h}_{th}	thermal enthalpy of the gas
ζ	general coordinate
A	pre-exponential factor
A^*	projected surface area of the particle
A_p	the area of the particle's exposed surface
A_{rect}	surface area of rectangular particles
Bi	Biot number
c	heat capacity
C_D	aerodynamic drag coefficient
C_L	aerodynamic lift coefficient
c_p	specific heat at constant pressure
C_A	shape factor
CFL	Courant–Friedrichs–Lewy number
D	mass diffusivity
D_{eff}	effective diameter
E	activation energy
E_m	radiation emission of the gas-phase mixture
E_s	radiation emission of the solid-phase
E_{Rco}	degree of completion of the char oxidation reaction
E_{Rd}	degree of completion of the drying reaction
E_{Rp+Rop}	degree of completion of the pyrolysis reactions
f	frequency
f_i^- , f_i^+	flux across cell's upstream or downstream faces
F_i'''	aerodynamic force vector component (per unit volume)
f_v	soot volume fraction
$F_{D,j}$	component of the aerodynamic drag force
$F_{L,j}$	component of the aerodynamic lift force
FO	Fourier number
G	irradiation
g_i	gravity vector component in index notation
h	heat transfer coefficient
h_f^0	enthalpy of formation
I	radiation intensity

K	permeability
k	thermal conductivity
k_{Turb}	subgrid-scale turbulent kinetic energy
L_{cyl}	length of cylindrical particles
l_{sp}	laminar smoke point height
Le	Lewis number
m	mass
m''_f	fuel loading
n	reactant exponent
N_C	Byram convection number
N_p	number of particles
Nu_D	Nusselt number based on effective diameter
P	presumed probability density function
p	pressure
Pr	Prandtl number
R	radius of cylindrical and spherical particles/ideal gas constant
r	radial coordinate
Re_D	Reynolds number based on effective diameter
S_i^-, S_i^+	surface area of cell's upstream or downstream faces
Sc	Schmidt number
T	temperature
t	time
u	velocity
u_j	velocity vector component in index notation
V	volume
X	volume fraction
x	rectilinear coordinate
x_j	coordinate in index notation
Y	mass fraction
y	rectilinear coordinate
Z	mixture fraction
z	rectilinear coordinate
Z_{st}	stoichiometric mixture fraction

Subscripts

∞	freestream or ambient
a	ash
ad	adiabatic
bed	a control volume of solid vegetation and the gas-phase evaluated at the cell center
C	
c	char
$conv$	convective
ds	dry solid
g	gas
$g \rightarrow s$	gas to solid
hrr	heat release rate
i	cell or face index
k	species/reaction index
L	evaluated at the cell's upstream face
m	mixture of gases
p	particle
R	evaluated at the cell's downstream face
rad	radiative
Rco	char oxidation reaction
Rd	drying reaction
Rop	oxidative pyrolysis reaction
Rp	pyrolysis reaction
s	solid
sf	soot formation
sg	solid to gas
so	soot oxidation
$surf$	evaluated at the particle surface
tot	total
$Turb$	subgrid-scale turbulent quantity
w	evaluated at the wall
ws	wet solid

1 Introduction

Wildland fires are a natural phenomenon that can occur in any region of the world where there is sufficient vegetation (e.g., forest fires, grassland fires, etc.) and a favorable climate (e.g., hot dry weather and high wind conditions). These fires can be caused by unintended actions such as lightning strikes and human activities. Wildland fires also include prescribed burns that intend to clean dense forests and manage the wildland. Uncontrolled wildland fires can spread rapidly, driven by strong winds and/or inclined terrains, and can quickly consume large areas of forest, grassland, or other types of vegetation, and sometimes lead to catastrophic disasters.

The impacts of wildland fire disasters can be severe, including damage to property, loss of wildlife habitat, the displacement of people from their homes, as well as economic losses. According to the National Interagency Fire Center (NIFC) [1], wildfires have increased in occurrence by 223% since 1983, with 68,988 wildfires that burned 7,577,183 acres in the United States (U.S.). In 2022 alone, 4.5 million U.S. homes were identified to be at high or extreme risk of wildfire. Moreover, approximately 4.4 billion U.S. dollars were spent on fire suppression costs in 2021 [1]. In addition to these immediate impacts, wildland fires can also have long-term effects on the environment, including changes to soil fertility and water quality.

The increase in wildland fire risk in recent years is due mainly to: 1) climate change: the rising temperatures and prolonged drought conditions make it easier for fires to ignite and spread quickly; 2) improper land management practices: the accumulation of fuel in many forests makes fires more intense when they occur; and 3) urbanization: the expansion of urban communities to the wildland increases the risk of fires caused by human activities as well as exposes communities at the wildland-urban interface (WUI) to fire risk. As a result of the increasing wildland fire risk, advanced wildland fire behavior modeling tools are critical to help land managers, firefighters, and other responders plan and implement strategies to effectively predict, control, and mitigate wildland fire risks.

This dissertation work is part of a larger research program sponsored by the U.S. Forest Service that aims at developing an advanced dynamical fire spread model in replacement of classical models and an operational tool for the real-time prediction of wildland fires. We describe in the following section the categories of wildland fire behavior models and how the current work compares to existing models and further model developments.

1.1 Wildland fire behavior modeling

Wildland fire behavior refers to the physical and chemical processes that govern the ignition, growth, and spread of wildfires [2]. These processes include the heat transfer from the flame to the vegetation fuel or from a vegetation particle to another within the vegetation fuel bed; the production of flammable vapors due to thermal

degradation of individual fuel particles (known as pyrolysis); the reaction of these flammable vapors with ambient air to release heat, produce luminous turbulent buoyant flames and smoke (known as combustion); the reaction of the charred particles with ambient oxygen (known as glowing or smoldering); and the interaction of the turbulent buoyant flames with the surrounding environment, including the vegetation fuel, topography, and weather. Wildland fire behavior is affected by various factors, including the characteristics of the fuels, such as fuel material, fuel moisture content, and fuel arrangement, as well as weather conditions, such as temperature, humidity, wind speed and direction, and atmospheric turbulence. The topography of the landscape (e.g., flat or sloped terrain) also affects fire behavior, as it can significantly influence the rate of spread of the fire and its direction.

Wildland fire behavior research is critical to understand the complex behavior of wildfires and their interactions with the surrounding environment. The modeling of wildland fire behavior combines various disciplines, including atmospheric science, ecology, physics, and computer science, to develop comprehensive models that can simulate the behavior of wildfires in different environments. These models are essential for developing effective wildfire management strategies, reducing the risk of wildfire damage, and protecting the safety of firefighters and local communities.

1.1.1 Scales of wildland fire behavior dynamics

Before reviewing the approaches to model wildland fire behavior, it is important first to recognize that the dynamics of wildland fires involve multi-physics phenomena

occurring at multiple scales and different length scales are believed to play a role in fire behavior. As shown in Fig. 1.1 the wildland fire behavior can be studied at different scales: the vegetation scale characterized by the geometry of the biomass fuel particles; the flame scales represented by a characteristic flame height and width, as well as the length of the fire line that characterize the combustion and heat transfer processes; the geographical scales that characterize the terrain topography and land cover; and the meteorological scales represented by the depth of the atmospheric boundary layer that characterizes atmospheric conditions.

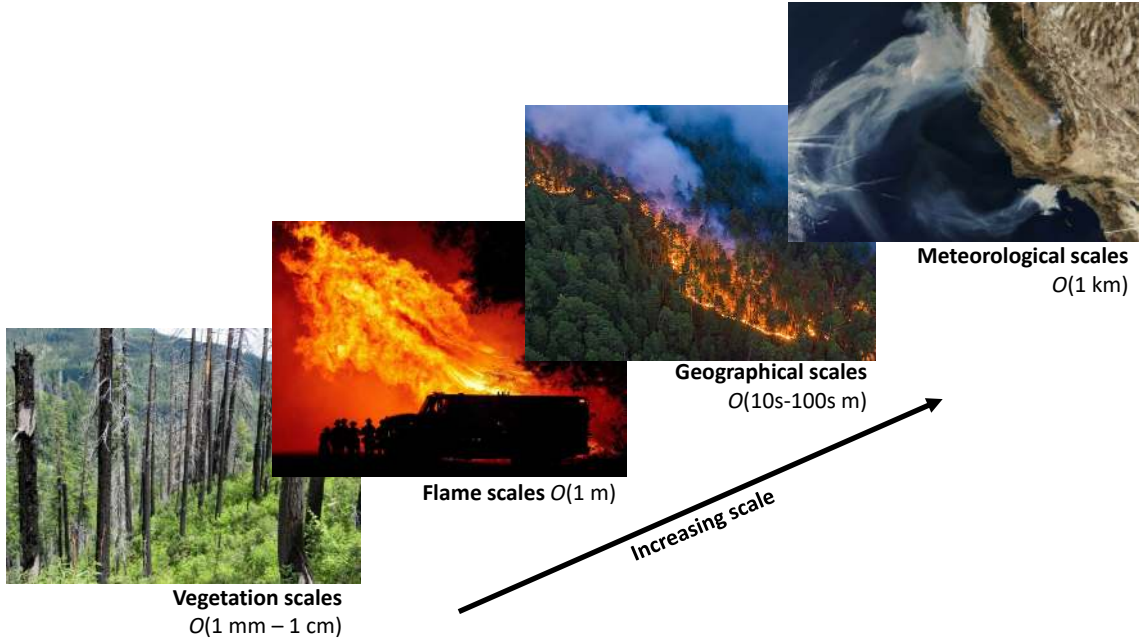


Figure 1.1: Scales of the wildland fire problem. Images sources: Smithsonian's National Zoo & Conservation Biology Institute [3]; Josh Edelson via Getty Images; Greenpeace International [4]; and NASA Earth Observatory [5].

In wildland fire problems, the vegetation scale is on the order of a few millimeters or centimeters; the flames scales are the order of a few meters; the geographical scales

are typically on the order of a few tens or hundreds of meters; and the atmospheric boundary layer is on the order of kilometers. We focus in this dissertation on the wildland fire behavior at the vegetation-to-flame scales.

1.1.2 Semi-empirical approach to wildfire behavior modeling

The first approach to wildland fire behavior modeling uses a semi-empirical technique that combines empirical observations with simplified mathematical equations to describe fire behavior based on input data such as weather conditions, terrain, and fuel load. Details of this approach are outside the scope of this dissertation, but interested readers are invited to review the description of relevant tools such as BEHAVE [6], FARSITE [7], ELMFire [8], and FlamMap [9]). In short, these models rely on a classical empirical model that was proposed by Rothermel in 1972 [10] to estimate the rate of spread of the fire. These models can also use Geographic Information System (GIS) to create maps at regional scales that show areas at risk of wildfire.

There are some limitations and drawbacks to the semi-empirical approach which makes its application in a variety of scenarios questionable [11]. For example, The Rothermel model is based on laboratory-scale observations of certain classes of fuels and may not accurately predict fire behavior under extreme conditions, such as very high winds, extreme slopes, or unusual fuel structures. Moreover, the Rothermel model treats the fuel bed as a uniform entity that burns at a constant rate to complete consumption. However, fire behavior, in reality, can be highly variable

depending on the characteristics of the fuel particles and the spatial heterogeneity of the fuel bed. Therefore, there is a strong interest to replace the Rothermel model with an advanced dynamical model based on physical principles [12].

1.1.3 Physics-based approach to wildfire behavior modeling

The second approach to wildland fire behavior modeling relies on the physical description of the governing processes of fluid dynamics, heat transfer, and combustion. This physics-based approach has potential advantages over the semi-empirical modeling approach, including reducing model-related errors in predictions (by contrast to errors introduced from data or users) and explaining rather than just correlating fire behaviors. Physics-based models are also expected to better describe phenomena outside the range of current semi-empirical models, such as spread/no spread thresholds, acceleration/deceleration, fluctuating wind conditions, discontinuous and heterogeneous fuel beds, and conditions outside current laboratory and field data sets (very strong winds, large flame dimensions, etc.).

The physics-based modeling has the potential to provide detailed information on the interactions between physical phenomena occurring at any of the wildland fire scales by means of Computational Fluid Dynamics (CFD). However, because of computational cost, the domain of application of 3D CFD-based tools is limited to a particular range of scales. Thus, current 3D CFD-based wildland fire models are scale-specific and belong to one of the following three classes (see Fig. 1.2): combustion solvers aimed at describing the coupling between pyrolysis, combustion,

radiation, and flow occurring at the vegetation and flame scales; wildfire solvers aimed at describing the coupling between combustion and flow occurring at the fire line scales and/or geographical scales; and atmospheric boundary layer (ABL) solvers aimed at describing the coupling between combustion and flow occurring at the meteorological scales.

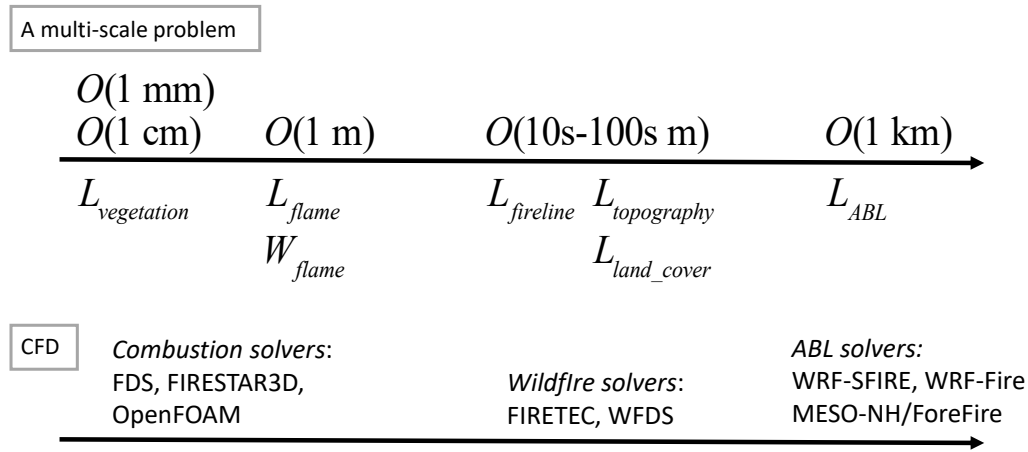


Figure 1.2: The different classes of CFD models used for simulating wildland fire behavior: combustion solvers resolve dynamics at the vegetation and flame scales; wildfire solvers resolve dynamics at the fireline and geographical scales; atmospheric boundary layers (ABL) solvers resolve dynamics at the meteorological scales.

Examples of combustion solvers that have been developed for wildland fire dynamics applications include a group of models known as multiphase models [13–16]. These solvers provide a relatively fine-grained treatment of the fuel bed, the combustion, and the heat transfer processes that are responsible for flame spread. Simulations with these solvers are typically performed in small domains equivalent to a field scale. There are, however, simplifications in existing solvers which we would

like to improve in our modeling approach. Particularly, we would like to include a more sophisticated description of the in-depth thermal degradation processes through a porous medium treatment of the solid fuel. Other examples of combustion solvers include FDS [17] and FireFoam [18]; these solvers are well-established fire modeling tools that are primarily used for building fire applications.

Examples of wildfire solvers include FIRETEC (see Refs. [19–21]) and WFDS (see Ref. [22] and the recent development in Refs. [23, 24]). These solvers provide a coarse-grained treatment of unresolved vegetation-scale and flame-scale processes through a simplified (but physics-based) combustion model. Simulations with these solvers are typically performed in relatively larger domains (e.g., 1 *km* in size).

Examples of atmospheric boundary layer (ABL) solvers that have been developed for wildland fire dynamics applications include WRF-SFIRE and WRF-Fire [25–28], and MESO-NH/ForeFire [29]. These ABL solvers typically provide a macroscopic level treatment of unresolved vegetation-scale, flame-scale, fireline-scale, and geographical-scale processes through a parameterized rate of spread model based on the Rothermel model or simplified physical models of surface fire spread (e.g. [30]), which may have uncertainty in their application to a variety of scenarios. Simulations with ABL solvers are typically performed in arbitrary-size field-scale domains (from a few kilometers to several tens of kilometers and beyond). A strength of ABL solvers is that they are integrated with research-level or operational-level numerical weather prediction capabilities (i.e. WRF and MESO-NH) and therefore incorporate detailed descriptions of the fuel maps, topographic maps, and weather conditions.

1.2 Motivation and scope of this dissertation

As described in the previous section, the existing operational tools rely on simplified semi-empirical models that are questionable, while there is a major challenge in the ability to span a wide range of scales with physics-based models due to the computational burden. Motivated by these challenges, this dissertation work is part of a larger project sponsored by the Missoula Fire Science Laboratory that aims to produce a dynamic physics-based dynamical fire spread model as a replacement for the classical Rothermel model and to deploy this model into an operational tool for real-time wildland fire simulations using Deep Learning (DL) techniques. Figure 1.3 shows the chain of model development in this project. As described in Fig. 1.3, there are three pieces in this project that are connected together. The first piece is a high-fidelity physics-based 3-D solver called PBRFoam that resolves the dynamics of wildland fire behavior at vegetation-flame scale using the Large Eddy Simulations approach (LES). The development of PBRFoam is the main objective of this dissertation and will be discussed in detail in the following chapters. In short, the tool PBRFoam supports the development of the second piece by providing simulation data and detailed diagnostics of the parameters needed to drive the dynamical 1-D fire spread model. For example, we would like to understand how the local gas condition around an individual particle inside a fuel bed varies with the packing of the fuel bed so that a reasonable boundary condition can be set in the dynamic 1-D model. The second piece is a dynamic 1-D fire spread model called LIHTFire [31]. This model aims at providing burning rates, heat transfer, and ignition with explicit

accounting of heterogeneous fuels and time-varying weather. This tool uses the Particle Burning Rate (PBR) model that we developed throughout this dissertation work to describe the thermal degradation of individual fuel particles. It accounts for the coupling between the solid particles and the gas-phase through a set of boundary conditions imposed at the fuel particle surface given estimates of the conditions of the gas-phase around the fuel bed. LIHTFire solves a single 1-D fire line spanning domains of about 50 – 100 m in less than a minute, but this is still considered too slow to be implemented directly in real-time simulations of large fires. This takes us to the third piece which aims at using advanced Artificial Intelligence techniques to embed the fire model LIHTFire inside a Deep Learning (DL) model that accounts for combinations of fuel, weather, and topographical conditions (see Finney et. al. [32]).

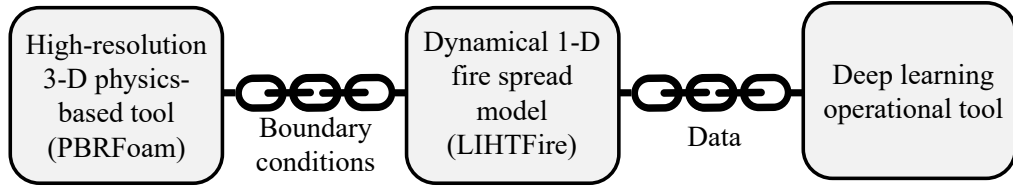


Figure 1.3: The larger framework of this project: chain of model development.

1.3 Literature review of relevant experimental/modeling work in the vegetation-flame scale

As we are interested in developing a computational tool for detailed modeling of wildland fire behavior at the vegetation-flame scale, we present here a literature review of the experimental and modeling efforts that have been carried out to study wildland fire behavior in this regime.

Vogel and Williams [33] found that the rate of flame propagation over horizontal arrays of vertically oriented matchsticks in quiescent air depends on the spacing, the length of the matchsticks, and whether the matchsticks are ignited from the bottom or the top. Wolff et al. [34] investigated fire spread across fuel beds made of arrays of toothpicks of uniform or mixed sizes in a movable ceiling wind tunnel. They identified a relationship between the rate of spread of the fire and the ratio between the wind speed to the fuel loading (i.e., the mass of fuel particles per unit bed area). They also highlighted some important effects in wind tunnel testing of fire spread such as the effect of flow circulation in closed ceiling tunnels, the edge effects, and the inability to obtain an asymptotic one-dimensional fire front. More importantly, they found the burnout time of individual fuel particles to vary linearly with the fuel loading and to be independent of the wind speeds considered in their tests. More recently, Di Cristina et al. [35] identified three regimes of flame spread across discrete wooden dowels under different particle spacing and wind speeds in the range of 2.2 to 3.4 m/s : 1) a continuous flame spread regime at a low spacing in which a flame covers multiple fuel particles; 2) a discrete flame spread regime at a high spacing in which a flame is only attached to an individual particle; 3) a quenching regime at large spacing at which a flame could not be sustained. A more practical technique to experimentally study flame spread in fuel beds comprised of discrete particles at a larger scale was introduced by Finney et al [36]. In these experiments, the fire spread over fuel beds made of laser-cut cardboard of different arrangements was tested in the Missoula wind tunnel at wind speeds up to 1.34 m/s . Similar to the observations made by Wolff et al. [34], these fire spread experiments

showed a linear relationship between the fuel packing ratio and the flame residence time. Using the same experimental technique, He et al. [37, 38] conducted fire spread experiments in a smaller wind tunnel and at wind speeds between 1 and 3.8 m/s. They found that the flame residence time increases linearly with the fuel packing ratio. However, their data suggest that there is also a dependence of the residence time on wind speed.

On the computational modeling side, the studies concerning the fire behavior in fuel beds comprised of discrete particles with different fuel bed characteristics are very limited. For example, Frangieh et al. [39] studied the flame structure of the cardboard fires that have been studied experimentally at the Missoula Fire Sciences Laboratory [36]. They were mainly interested in simulating the coherent flame structure observed in line fires (i.e., the peaks and troughs) using numerical simulations in a wind tunnel and in an open field. Awad et al. [40] conducted 2-D simulations to investigate the fuel moisture content (FMC) threshold for spread and no-spread conditions in grassland fires under different fuel bed loads (i.e., packing) and wind speeds. They found a correlation between the threshold FMC and the Byram number.

In summary, there are a number of studies that aimed at characterizing the burning behavior of discrete fuel particles through experiments of fire spread in idealized fuel beds of thin discrete particles. However, the behavior of fire spread in mixed-size class fuel beds has received little to no examination to this point in the wildland fire literature. Moreover, existing experimental diagnostics and modeling efforts are very limited and there is a need for more studies concerning the burning

behavior in terms of the flame residence time, individual particle response, the degree of fuel consumption, the dependence on fuel bed characteristics such as fuel particle size and packing, the respective weights of radiative and convective heating, and the modes of flaming and smoldering combustion.

1.4 Objectives and contributions

1.4.1 Objectives

The general objective of this project is to develop an advanced computational modeling capability that simulates wildland fire behavior at vegetation and flame scales with detailed descriptions of thermal degradation processes occurring during both flaming and smoldering combustion. Our main focus here is on the development, validation as well as testing of the computational modeling capability in canonical configurations. As described in the previous section, this modeling capability will serve in two ways: 1) providing data for the development of operational tools, and 2) developing our fundamental understanding of the wildland fire behavior through setting the basis for parametric studies and sensitivity analyses.

Our specific objectives in this dissertation are to:

1. develop a particle burning rate (PBR) model that describes the thermal degradation of individual solid biomass/vegetation fuel particles and implement it as an object-oriented C++ tool
2. couple the model into a multiphase solver using an open-source library called

OpenFOAM [41] which allows the utilization of advanced models previously developed in our group at the University of Maryland, as well as an easy implementation of new models

3. validate the model against available experimental measurements and observations
4. simulate flame spread across surrogate vegetation beds comprised of mono-/poly-dispersed particles with prescribed particle and environmental properties (i.e., bed height, surface-to-volume ratio, packing ratio, moisture content, and wind velocity)
5. study the global fire behavior in terms of flame structure, fire intensity, global fuel consumption, and the individual particle response as a function of the fuel packing and the duration of the thermal loading process, and the flame residence time.

On the route to achieve these objectives, there are important intermediate steps discussed in the following chapters. These steps focus primarily on evaluating the ability of the models adopted and developed in this work to accurately describe two main drivers of fire spread: 1) pyrolysis and oxidation of isolated biomass particles at both micro- and bench-scales; 2) heat feedback in canonical fire flames in terms of thermal radiation and flame structure.

1.4.2 Author's contributions

The present work is part of a project sponsored by the U.S. Forest Service that aims at two objectives: 1) developing a dynamical 1-D fire spread model, and 2) studying the wildland fire behavior dynamics through high-fidelity 3-D simulations of spreading line fires in vegetation fuel beds. Past work conducted at the University of Maryland by Dr. Salman Verma [42] on high-fidelity 3-D simulations was focused on studying the structure of non-spreading laboratory-scale line fires produced from stationary gaseous burners in the presence of external wind or on inclined surfaces. On the other hand, the previous version of the dynamical 1-D fire spread model developed by Mr. Jason Forthofer at the Missoula Fire Sciences Laboratory included a particle burning rate (PBR) model that describes only the drying and the pyrolysis of thermally-thick non-porous particles, and it did not account for smoldering combustion.

The present study extends the previous work by developing a model of thermal degradation of porous biomass fuel particles, which includes a description of both flaming and smoldering combustion, that can be implemented in the 1-D dynamical fire spread model as well as in the high-fidelity 3-D simulations of spreading fires.

Several implementations and code development were conducted during this Ph.D. work. The candidate started first by developing an early MATLAB version of the PBR model that was originally created by Dr. Arnaud Trouv  to describe the drying and pyrolysis of thermally-thin as well as thermally-thick rectangular-shaped particles. The candidate extended this MATLAB code to account for the

thermal degradation of 1-D axisymmetric cylindrical- and spherical-shaped particles. The candidate then used this MATLAB code as a stand-alone solver to simulate the unsteady response of charring and non-charring biomass particles (in terms of ignition, mass loss rate, and burnout) when exposed to conditions of the surrounding gas that are fluctuating in time (i.e., surrounding gas temperature, velocity, and irradiance) [43].

Following the work of Lautenberger and Fernandez-Pello [44], the MATLAB version of the PBR model was then further developed by Dr. Arnaud Trouv  and the candidate to account for smoldering combustion by treating the particles as a porous-medium that includes in-depth oxygen diffusion. The candidate used this new solver to generate 2-D maps that describe the burning behavior of individual particles under prescribed thermal loads (Chapter 5).

The candidate created an object-oriented C++ code as stand-alone software for the PBR model of porous biomass particles. The candidate also assisted with the coupling of the C++ PBR code with the dynamical 1-D fire spread model developed by Mr. Jason Forthofer at the Missoula Fire Science Laboratory. The candidate is also the developer of the 3-D multi-phase fluid dynamics solver PBRFoam that is based on the PBR code and the multi-purpose open-source C++ library OpenFOAM [41] (Chapter 2 and Appendix A). The candidate constructed a two-way coupling interface between the Lagrangian particle tracking library of OpenFOAM and the newly developed PBR solver. This interface exchanges information that allows the solid particles to evolve under the given gas-phase conditions and in turn modify the gas-phase by exchanging information about the contribution of the

solid-phase to the mass, momentum, energy, and radiation of the gas-phase. To construct the gas-phase solution algorithm in the PBRFoam solver, the candidate adopted a similar approach to that has been adopted in the well-established fire modeling tool FireFoam developed at FM Global [18], particularly, the description of the pressure-velocity coupling using the PIMPLE algorithm [45].

Additionally, the candidate conducted intermediate model developments and code implementations using the OpenFOAM library toward more accurate fire modeling as part of the Measurement and Computation of Fire Phenomena (MaCFP) working group. These efforts aimed at evaluating the accuracy of different fire modeling approaches in predicting thermal feedback in non-sooting and sooting buoyant turbulent diffusion flames. The candidate developed a modified version of the Eddy Dissipation Model (originally proposed by Magnussen and Hjertag [46]) using laminar diffusion theory to dynamically estimate the rate of fuel consumption based on laminar diffusion in fire regimes where laminar diffusion is dominating over turbulent mixing such as near the flame base (see Appendix B). The candidate also developed and implemented an extension of the Laminar Smoke Point (LSP) soot model (originally proposed by Yao et al. [47]) to account for subgrid-scale turbulent fluctuations in LES description of soot formation and oxidation rates using a probability density function called β -PDF (Appendix C). Furthermore, based on an original code implementation of a Weighted-Sum-of-Gray-Gases (WSGG) framework implemented in the OpenFOAM library by Sikic et al. [48], the candidate implemented a new version that uses a WSGG model proposed by Cassol et al. [49] that accounts for soot radiation (Appendix D).

In terms of model verification and calibration, the candidate conducted a series of benchmark tests to evaluate the accuracy of the implemented models and to check the establishment of a reliable computational framework (Chapter 3).

As part of the MaCFP workshop, the candidate performed Large Eddy Simulations (LES) using FireFoam solver in two configurations that have been identified as target experiments by the MaCFP working group for validation of fire models. The emphasis in these simulations was on evaluating the ability of the EDM combustion model, the Prescribed Global Radiant Fraction model (PGRF), and the WSGG radiation modeling approach to predict thermal feedback in, first, a non-sooting methanol pool fire, then in a sooting ethylene burner (Chapter 4).

Using the newly developed modeling capability (PBRFoam), the candidate performed LES simulations of fire spread in fuel beds made of vertically-oriented engineered cardboard sticks that have been studied experimentally at the Missoula Fire Sciences Laboratory [36] (Chapter 6). The candidate created a C++ script to generate the population of the cardboard particles inside the fuel beds using the given information about the separation distances between arrays of particles. The candidate constructed 3-D configurations of two experimental burns called Burn 53 and Burn 67, as well as 7 configurations corresponding to fuel beds with different particle separation and fuel bed packing. The emphasis in these simulations was on validating the model by comparing the simulated fire behavior in terms of ROS, flame structure, and residence time with available experimental measurements and observations.

The candidate also performed LES simulations of fire spread in surrogate fuel

beds comprised of cylindrical-shaped pine wood particles using PBRFoam. The candidate constructed configurations that have either a uniform fuel bed of the same-size particles or a fuel bed that features a patch of mixed-size particles (Chapter 7). The focus of this study was on studying the degree of consumption of the particles, the respective weights of convective and radiative heating, and the transition from flaming to smoldering combustion.

1.4.3 Organization

In chapter 2, the computational framework is described in detail. The governing equations for the thermal degradation of porous biomass particles are first introduced, followed by a description of the multi-phase formulation that we adopted in our implementation to describe the coupling between the solid biomass particles and the gas-phase. The chapter also provides details of the physical sub-models adopted to describe the convective heat transfer at the surface of the solid particles, the multi-phase radiation transport, the gas-phase combustion, as well as the sub-grid scale turbulence. This chapter is concluded with a summary of the implementation of the computational framework.

In chapter 3, a series of benchmark test cases are presented to verify, calibrate and evaluate the computational modeling framework. This chapter first discusses verification test cases through simplified configurations where analytical solutions can be derived at both the particle level as well as the fuel bed level. Then, the calibration of the thermal degradation model with micro-scale experiments is

discussed. A discussion about the ability of the stand-alone PBR solver to predict thermal degradation of bench-scale experiments is presented, followed by a discussion for representative cases of particles that feature complete consumption (i.e. through smoldering) and particles that feature volume-change (i.e., shrinking or swelling).

Chapter 4 presents numerical studies of flame structure and thermal feedback in two canonical pool fire configurations. This chapter first presents LES results from a medium-scale pool fire that is fueled by a non-sooting ethylene fuel, followed by LES results from a turbulent buoyant flame produced from a circular burner (called the FM-burner) that is fueled by sooting ethylene fuel under controlled coflow conditions.

In chapter 5, a numerical study of the response of the biomass vegetation particles to external heating conditions imposed at their exposed surface is presented. The chapter discusses first the response of a selection of particles, including thin, thick, charring, and/or non-charring particles, in terms of ignition and mass loss rate due to pyrolysis to either steady or oscillatory external gas conditions. Then the chapter presents 2-D maps that characterize the thermal degradation of porous flaming and smoldering particles in terms of the degree of completion of the drying, the pyrolysis, and the char oxidation processes as a function of the external thermal load and the ambient wind.

Chapter 6 focuses on LES simulation results of fire spread in engineered fuel beds made of cardboard sticks that have been studied experimentally at the Missoula Fire Sciences Laboratory. The chapter first discusses the model predictions of the fire behavior against experimental observations of two burns corresponding to a

buoyancy-dominated or a wind-dominated fire regime. The rest of the chapter focuses on fire diagnostics related to the flame residence time and the rate of spread and their variation with the packing of the fuel bed.

Chapter 7 presents LES simulation results of fire spread in idealized fuel beds comprised of vertically-oriented cylindrical-shaped pinewood sticks under two wind speeds corresponding to either a buoyancy-dominated fire or a wind-dominated fire. The chapter discusses first the fire propagation in uniform fuel beds comprised of small particles that are on the order of 1 *mm*-scale. Then, results from fire spread simulations in fuel beds that feature a patch with larger particles (on the order of 1 *cm*-scale) that are added to the smaller ones. The last part of the chapter focuses on an interpretation of the LES results regarding the degree of completion of thermal degradation of the fuel bed using the 2-D maps constructed in chapter 5.

Chapter 8 presents a summary of the work conducted in this dissertation and provides some concluding remarks. The chapter also discusses recommendations and suggestions for a continuation of this work in the future.

2 The Computational Modeling Framework

2.1 Overview

We model the fuel bed as a population of porous particles with different arrangements and with either unique or mixed sizes and geometries. Each porous particle is described as a system with a solid-phase and a gas-phase, which allows for a detailed treatment of the particle-to-external-gas outflow of volatile mass and the external-gas-to-particle diffusion of oxygen mass; this detailed treatment is required to account for in-depth oxidative pyrolysis and char oxidation. We consider here thermally-thick and composition-thick particles featuring in-depth variations of temperature and composition. The particle's geometry can be modeled as rectangular (leaves or sticks), cylindrical (needles or stems), or spherical (embers or firebrands).

This chapter discusses the development and implementation of a Lagrangian Particle Burning Rate (PBR) solver to describe the thermal degradation of individual solid fuel particles, and a coupled multiphase solver to describe the interaction between a solid vegetation fuel bed and the surrounding gases in simulations of wildland fire spread at flame scale.

In terms of exchange of information, the PBR solver uses estimates of the

gas-to-solid heat flux onto a population of particles as input quantities and produces in return estimates of the particle mass, size, and energy as well as the production rate of combustible gaseous volatiles and other gaseous products inside the fuel bed as output quantities to the coupled multiphase solver. More precisely, the input quantities to the PBR model are:

$$\dot{q}_{g \rightarrow s}'' = h(T_{g,\infty} - T_{p,surf}) + \epsilon_{p,surf}(G - \sigma T_{p,surf}^4) \quad (2.1)$$

and

$$\dot{m}_{g \rightarrow s,O_2}'' = h_{mass}(Y_{g,O_2,\infty} - Y_{g,O_2,surf}) \quad (2.2)$$

where h is the convective heat transfer coefficient, $T_{g,\infty}$ the external gas temperature in the vicinity of the particle under consideration, $T_{p,surf}$ the temperature of the exposed surface of that particle, $\epsilon_{p,surf}$ the particle surface emissivity (treated as an opaque solid), G the averaged radiation heat flux incident on the particle external surface (G designates the irradiation due to distant hot sources, e.g., the flame, the plume, other particles, etc., as well as the irradiation due to ambient gas), σ the Stefan-Boltzmann constant, h_{mass} is the convective mass transfer coefficient $h_{mass} = (h/\bar{c}_{p,g})$ with $\bar{c}_{p,g}$ the heat capacity of the gas at constant pressure, where $Y_{g,O_2,\infty}$ is the mass fraction of oxygen in the external gas in the vicinity of the particle, and where $Y_{g,O_2,surf}$ is the mass fraction of oxygen gas at the exposed surface of the particles.

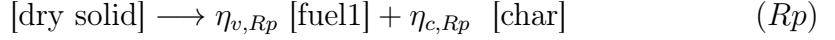
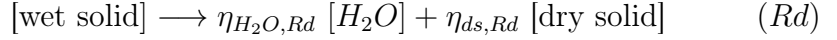
In the expression for $\dot{q}_{g \rightarrow s}''$, the input quantities are the external gas temperature $T_{g,\infty}$, the convective heat transfer coefficient h (treated through Nusselt-number-correlations as a function of the external flow velocity and temperature, $u_{g,\infty}$ and

$T_{g,\infty}$ and the irradiation G . In the expression for $\dot{m}_{g \rightarrow s, O_2}''$, the input quantity is the external oxygen mass fraction in the gas in the vicinity of the particle $Y_{g,O_2,\infty}$. These quantities are functions of spatial location inside the fuel bed, i.e., presumably functions of both the distance along the direction of fire spread and the vertical elevation. We refer to these quantities as "external gas conditions" and we describe their variations using the coupled multiphase formulation described in section 2.3.

2.2 Particle Burning Rate (PBR) Model

Thermal degradation of individual solid fuel particles exposed to the external gas conditions is tracked individually in space and time following a Lagrangian viewpoint. In a one-way coupled formulation, the external gas conditions are imposed, and the model calculates the time-dependent response of the fuel particle to the heat loading from the gaseous environment. In a two-way coupled formulation, the external gas conditions (i.e., composition, velocity, temperature, and radiation) are updated with terms representing the effects of the fuel particles. The description of the fuel particle model presented in this section applies to both one-way and two-way coupled formulations.

We follow the work of Lautenberger and Fernandez-Pello [44, 50] by describing the fuel particle as a matrix of pores featuring a solid-phase and a gas-phase. We consider each porous particle to experience four heterogeneous (gas/solid) reactions: a drying reaction (Rd); a thermal pyrolysis reaction (Rp); an oxidative pyrolysis reaction (Rop); and a char oxidation reaction (Rco):



where $\eta_{H_2O,Rd}$ and $\eta_{ds,Rd}$ are the mass yields of water vapor and dry solid in reaction Rd , respectively, $\eta_{H_2O,Rd} + \eta_{ds,Rd} = 1$, where $\eta_{v,Rp}$ and $\eta_{c,Rp}$ are the mass yields of volatile and char in reaction Rp , respectively, $\eta_{v,Rp} + \eta_{c,Rp} = 1$, where $\eta_{O_2,Rop}$ is the oxygen-to-dry-solid mass ratio, and $\eta_{v,Rop}$ and $\eta_{c,Rop}$ are the mass yields of volatile and char in reaction Rop , respectively, $\eta_{v,Rop} + \eta_{c,Rop} = 1 + \eta_{O_2,Rop}$, and where $\eta_{O_2,Rco}$ is the oxygen-to-char mass ratio, and $\eta_{CO_2,Rco}$ and $\eta_{a,Rco}$ are the mass yields of CO_2 and ash in reaction Rco , respectively, $\eta_{CO_2,Rco} + \eta_{a,Rco} = 1 + \eta_{O_2,Rco}$.

Note that these reactions are written per unit kg of the reactant.

Consistent with the model proposed in Ref. [44], we do not differentiate between the char products of the thermal and oxidative reactions Rp and Rop . While the gaseous fuel produced from Rp and Rop may have different chemical compositions noted as [fuel1] and [fuel2], we use a single lumped chemical species with an average heat of combustion to represent the external gas-phase combustion of these two fuels (see section 2.6). Note that, we focus here on the heterogeneous reactions that produce fuel for gaseous combustion and implicitly assume that this fuel will burn externally, i.e., outside of the particles. Therefore, the homogeneous (gas/gas) reactions that may take place inside the particle pores are ignored.

The composition of the solid-phase of the particle is described in terms of the following four mass fractions:

$$Y_{s,ws} = \frac{m_{s,ws}}{m_s}; Y_{s,ds} = \frac{m_{s,ds}}{m_s}; Y_{s,c} = \frac{m_{s,c}}{m_s}; Y_{s,a} = \frac{m_{s,a}}{m_s} \quad (2.3)$$

where m is the mass, the subscript s refers to the solid-phase, and where the subscripts ws , ds , c , and a refer to the wet solid, dry solid, char, and ash, respectively. We have by definition: $(Y_{s,ws} + Y_{s,ds} + Y_{s,c} + Y_{s,a}) = 1$.

At the initial time, the composition of the particle is assumed uniform, and its moisture content (FMC) is expressed as the ratio of the mass of water vapor divided by the mass of dry solid obtained after the drying reaction Rd . In other words, the water vapor yield $\eta_{H_2O,Rd}$ is considered as an input quantity related to the moisture content:

$$\eta_{H_2O,Rd} = \frac{\text{FMC}}{1 + \text{FMC}} \quad (2.4)$$

We follow the work of Khan et al. [51] and we consider the properties of the wet solid to be dependent on the moisture content through the following relations:

$$\rho_{ws,bulk} = \rho_{ds,bulk} \times (1 + \text{FMC}) \quad (2.5)$$

$$c_{ws,bulk} = c_{ds,bulk} \times (1 + 2.1 \times \text{FMC}) \quad (2.6)$$

$$k_{ws,bulk} = k_{ds,bulk} \times (1 + 5 \times \text{FMC}) \quad (2.7)$$

where c and k are the heat capacity and thermal conductivity, respectively.

In the following, we adopt the approach proposed in Ref. [50] and treat the particle as a porous medium featuring a solid phase and a gas phase (i.e., the particle is considered as a matrix of pores). The proportions of solid and gas inside the

particle are described through a porosity variable, noted $\bar{\psi} = V_g/V_p$, where V_p is the total volume of the particle ($V_p = V_s + V_g$), and where the subscript g refers to the gas-phase occupying the pores of the particle. Neglecting the contribution of the gases to the total particle's mass (i.e. $m_g \ll m_s$), we write the bulk mass density of the particle as

$$\bar{\rho}_{bulk} = \frac{m_s}{V_s + V_g} = \frac{m_s}{V_s} \times \frac{V_s}{V_s + V_g} = \bar{\rho}_s \times (1 - \bar{\psi}) \quad (2.8)$$

Following the approach proposed in Ref. [50], we introduce special values of the porosity obtained for reference particle compositions (i.e., reference states): ψ_k is the value taken by $\bar{\psi}$ for the vector composition $Y_{s,i} = \delta_{ik}$ with δ_{ik} the Kronecker symbol. In this framework, ψ_{ws} designates the porosity of a solid particle in its original state, i.e., with moisture and no char and no ash; ψ_{ds} designates the porosity of a particle after drying and prior to pyrolysis and char oxidation, i.e., with no moisture, no char and no ash; ψ_c designates the porosity of a char particle after drying and pyrolysis, and prior to char oxidation, i.e., with no virgin solid (wet or dry) and no ash; and ψ_a designates the porosity of an ash particle after drying, pyrolysis and char oxidation, i.e., with no virgin solid and no char. The parameters (ψ_{ws} , ψ_{ds} , ψ_c , and ψ_a) are simply treated as input data to the model.

Consider one of the reference states of the particle introduced above, $Y_{s,i} = \delta_{ik}$, $k = ws, ds, c$ or a . Assume a particle with a solid mass $m_{s,k}$. This particle occupies a volume ($V_{s,k} + V_{g,k}$) that can be calculated as a function of the mass density $\rho_{s,k}$, the porosity ψ_k and the mass $m_{s,k}$:

$$V_{s,k} + V_{g,k} = \frac{V_{s,k} + V_{g,k}}{V_{s,k}} \times \frac{V_{s,k}}{m_{s,k}} \times m_{s,k} = \frac{1}{1 - \psi_k} \times \frac{1}{\rho_{s,k}} \times m_{s,k} \quad (2.9)$$

The bulk mass density of the particle (in its reference state k) is expressed as

$$\rho_{k,bulk} = \frac{m_{s,k}}{V_{s,k} + V_{g,k}} = \rho_{s,k} \times (1 - \psi_k) \quad (2.10)$$

Note that in this expression, the contribution of the gaseous mass $m_{g,k}$ has been neglected, $m_{g,k} \ll m_{s,k}$. The porosity ψ_k is treated as a pseudo material property and the linear relationship between total (solid and gas) volume occupied by a species k and the mass of that species is assumed to hold for any particle containing k :

$$V_{s,k} + V_{g,k} = \frac{m_{s,k}}{\rho_{k,bulk}} = \frac{m_{s,k}}{\rho_{s,k} (1 - \psi_k)} \quad (2.11)$$

Let us now consider a particle with an arbitrary composition characterized by $(Y_{s,ws}, Y_{s,ds}, Y_{s,c}, Y_{s,a})$ and a solid mass m_s . We introduce volume fraction variables defined as the ratio of the total (solid and gas) volume occupied by species k divided by the total volume occupied by the particle:

$$\begin{aligned} X_k &= \frac{V_{s,k} + V_{g,k}}{V_s + V_g} = \frac{(m_{s,k}/\rho_{k,bulk})}{V_s + V_g} = \frac{(Y_{s,k} \times m_s/\rho_{k,bulk})}{V_s + V_g} \\ &= \frac{Y_{s,k}}{\rho_{k,bulk}} \times \frac{m_s}{V_s + V_g} = \frac{Y_{s,k}}{\rho_{k,bulk}} \times \bar{\rho}_{bulk} \end{aligned} \quad (2.12)$$

We can write:

$$X_k = \frac{\bar{\rho}_{bulk}}{\rho_{k,bulk}} \times Y_{s,k} = \frac{\bar{\rho}_s \times (1 - \bar{\psi})}{\rho_{s,k} \times (1 - \psi_k)} \times Y_{s,k} \quad (2.13)$$

and

$$\bar{\rho}_{bulk} = \sum_{k=ws,ds,c,a} \rho_{k,bulk} X_k = \left(\sum_k \frac{Y_{s,k}}{\rho_{k,bulk}} \right)^{-1} \quad (2.14)$$

$$\bar{\psi} = \sum_k \psi_k X_k = 1 - \frac{\bar{\rho}_{bulk}}{\bar{\rho}_s} \quad (2.15)$$

In the following, we will use the volume fraction (X_k) instead of the mass fraction (Y_k) to characterize the particle composition with the understanding that these variables contain information on the solid-phase composition as well as information on the solid/gas proportion. In the general case with drying, thermal/oxidative pyrolysis, and char oxidation, the composition vector $X_k = (X_{ws}, X_{ds}, X_c, X_a)$ is variable and evolves with time t and distance ζ across the particle. The variations in the particle composition are calculated through the mass conservation equations presented in the next section.

Finally, we note that if the reactions occur without a net change in the total volume of the particle, $V_p = V_s + V_g = \text{constant}$, then there are relationships that hold between the bulk mass densities and the species yields. For instance, if reaction Rp occurs at constant volume, then we have:

$$\rho_{c,bulk} = \eta_{c,Rp} \rho_{ds,bulk} \quad (2.16)$$

The issue of volume change will be further discussed in section [2.2.2](#).

2.2.1 Conservation equations for species/total mass inside the solid phase of an individual particle

Let us consider an elementary control volume noted dV inside a given porous (solid/gas) particle. The particle is discretized into an ensemble of computational cells introduced to describe variations of heat and mass in the direction normal to the exposed surface of the particle. In that case, dV denotes the volume of a given computational cell such that $\int_{V_p} dV = V_p$. The reader can refer to appendix [A](#) for a

detailed description of the particle's geometry and computational grid.

We write the mass conservation equations for the wet solid, dry solid, char, and ash inside dV as follows:

$$\begin{aligned}\frac{\partial}{\partial t}(\rho_{ws,bulk} X_{ws} dV) &= -\dot{m}_{Rd}''' dV \\ \frac{\partial}{\partial t}(\rho_{ds,bulk} X_{ds} dV) &= \eta_{ds,Rd} \dot{m}_{Rd}''' dV - \dot{m}_{Rp}''' dV - \dot{m}_{Rop}''' dV \\ \frac{\partial}{\partial t}(\rho_{c,bulk} X_c dV) &= \eta_{c,Rp} \dot{m}_{Rp}''' dV + \eta_{c,Rop} \dot{m}_{Rop}''' dV - \dot{m}_{Rco}''' dV \\ \frac{\partial}{\partial t}(\rho_{a,bulk} X_a dV) &= \eta_{a,Rco} \dot{m}_{Rco}''' dV\end{aligned}\quad (2.17)$$

where \dot{m}_{Rd}''' , \dot{m}_{Rp}''' , \dot{m}_{Rop}''' and \dot{m}_{Rco}''' are the volumetric mass reaction rates for the drying, thermal pyrolysis, oxidative pyrolysis, and char oxidation reactions, respectively.

Using the classical Arrhenius model, we write:

$$\begin{aligned}\dot{m}_{Rd}''' dV &= \left(\frac{\rho_{ws,bulk} X_{ws} dV}{(\rho_{ws,bulk} X_{ws} dV)_\Sigma} \right)^{n_{Rd}} (\rho_{ws,bulk} X_{ws} dV)_\Sigma \times A_{Rd} \exp\left(\frac{-E_{Rd}}{RT_p}\right) \\ \dot{m}_{Rp}''' dV &= \left(\frac{\rho_{ds,bulk} X_{ds} dV}{(\rho_{ds,bulk} X_{ds} dV)_\Sigma} \right)^{n_{Rp}} (\rho_{ds,bulk} X_{ds} dV)_\Sigma \times A_{Rp} \exp\left(\frac{-E_{Rp}}{RT_p}\right) \\ \dot{m}_{Rop}''' dV &= \left(\frac{\rho_{ds,bulk} X_{ds} dV}{(\rho_{ds,bulk} X_{ds} dV)_\Sigma} \right)^{n_{Rop}} (\rho_{ds,bulk} X_{ds} dV)_\Sigma \\ &\quad \times \left(\frac{Y_{g,O_2}}{Y_{g,O_2,air}} \right)^{n_{O_2,Rop}} \times A_{Rop} \exp\left(\frac{-E_{Rop}}{RT_p}\right) \\ \dot{m}_{Rco}''' dV &= \left(\frac{\rho_{c,bulk} X_c dV}{(\rho_{c,bulk} X_c dV)_\Sigma} \right)^{n_{Rco}} (\rho_{c,bulk} X_c dV)_\Sigma \\ &\quad \times \left(\frac{Y_{g,O_2}}{Y_{g,O_2,air}} \right)^{n_{O_2,Rco}} \times A_{Rco} \exp\left(\frac{-E_{Rco}}{RT_p}\right)\end{aligned}\quad (2.18)$$

where A , E , and n are the pre-exponential factors, activation energies, solid-phase reactant exponents, and gas-phase oxygen exponents associated with reactions

Rd - Rco , where T_p is the particle temperature (we assume here local thermal equilibrium and T_p designates both the local temperature in the solid and gas-phases of the particle, $T_p = T_s = T_g$), where Y_{g,O_2} designates the mass fraction of gaseous oxygen inside the gas-phase (i.e., the pores) of the particle, and where we use the following time-integrated quantities:

$$(\rho_{ws,bulk} X_{ws} dV)_\Sigma = (\rho_{ws,bulk} X_{ws} dV)_{t=0} \quad (2.19)$$

$$(\rho_{ds,bulk} X_{ds} dV)_\Sigma = (\rho_{ds,bulk} X_{ds} dV)_{t=0} + \int_0^t (\eta_{ds,Rd} \dot{m}_{Rd}''' dV) dt \quad (2.20)$$

$$(\rho_{c,bulk} X_c dV)_\Sigma = (\rho_{c,bulk} X_c dV)_{t=0} + \int_0^t (\eta_{c,Rp} \dot{m}_{Rp}''' dV + \eta_{c,Rop} \dot{m}_{Rop}''' dV) dt \quad (2.21)$$

In the expressions of the chemical reaction rates, the values of A , E , and n are external input parameters that are determined using calibration tests against micro-scale measurements through Thermogravimetric Analysis (TGA) [52] (see chapter 3).

We construct the conservation equation for the total particle mass by adding Eqs. 2.17 as follows:

$$\frac{\partial}{\partial t} (\rho_{bulk} dV) = -\dot{m}_{sg}''' dV \quad (2.22)$$

where

$$\dot{m}_{sg}''' = (1 - \eta_{ds,Rd}) \dot{m}_{Rd}''' + (1 - \eta_{c,Rp}) \dot{m}_{Rp}''' + (1 - \eta_{c,Rop}) \dot{m}_{Rop}''' + (1 - \eta_{a,Rco}) \dot{m}_{Rco}''' \quad (2.23)$$

2.2.2 Rate of change of the particle volume (constant/shrinking/swelling)

By dividing Eqs. 2.17 by the corresponding mass density, respectively, and by adding the resulting equations, we get an evolution equation for the elementary volume dV :

$$\frac{\partial}{\partial t}(dV) = -\dot{V}_{sg}''' dV \quad (2.24)$$

where

$$\begin{aligned} \dot{V}_{sg}''' &= \left(\frac{1}{\rho_{ws,bulk}} - \frac{\eta_{ds,Rd}}{\rho_{ds,bulk}} \right) \dot{m}_{Rd}''' + \left(\frac{1}{\rho_{ds,bulk}} - \frac{\eta_{c,Rp}}{\rho_{c,bulk}} \right) \dot{m}_{Rp}''' \\ &\quad + \left(\frac{1}{\rho_{ds,bulk}} - \frac{\eta_{c,Rop}}{\rho_{c,bulk}} \right) \dot{m}_{Rop}''' + \left(\frac{1}{\rho_{c,bulk}} - \frac{\eta_{a,Rco}}{\rho_{a,bulk}} \right) \dot{m}_{Rco}''' \end{aligned} \quad (2.25)$$

This equation shows that the total volume of the particle does not change provided that $\eta_{ds,Rd} = \rho_{ds,bulk}/\rho_{ws,bulk}$, $\eta_{c,Rp} = \eta_{c,Rop} = \rho_{c,bulk}/\rho_{ds,bulk}$, and $\eta_{a,Rco} = \rho_{a,bulk}/\rho_{c,bulk}$.

Sines the bulk mass density of any solid constituent is related to its solid mass density and porosity ($\rho_{k,bulk} = \rho_{s,k}(1 - \psi_k)$), we can see from the relations above that an evolution at constant volume requires a change in the mass density of the solid-phase, a change in the porosity of the particle, or a combination of both. In general, the particle expands or contracts to a finite size. In the special case of a non-charring material, $\eta_{c,Rp} = \eta_{c,Rop} = 0$ and $\dot{m}_{Rco}''' = 0$, the particle completely vaporizes and its size, δ or R_p , decreases to 0.

While the coupled fire spread simulations presented in this dissertation are limited to particles with constant volume change, the computational solver can handle the volume change using a deforming mesh and a re-meshing capability (see section

[A.4](#) in appendix [A](#)). Additionally, representative scenarios of thermal degradation of isolated particles with and without volume change are presented in chapter [3](#) to demonstrate this effect.

2.2.3 Conservation equations for species/total mass inside the gas phase of an individual particle

Let us consider again an elementary control volume dV located inside a porous particle. We write mass conservation equations for gaseous oxygen mass inside dV as follows:

$$\begin{aligned} \frac{\partial}{\partial t} (\bar{\rho}_g Y_{g,O_2} \bar{\psi} dV) + \frac{1}{\phi} \frac{\partial}{\partial \zeta} (\phi \dot{m}_{\zeta}'' Y_{g,O_2}) dV \\ = \frac{1}{\phi} \frac{\partial}{\partial \zeta} \left(\phi \bar{\psi} \bar{\rho}_g \bar{D}_g \frac{\partial Y_{g,O_2}}{\partial \zeta} \right) dV - \eta_{O_2,Rop} \dot{m}_{Rop}''' dV - \eta_{O_2,Rco} \dot{m}_{Rco}''' dV \quad (2.26) \end{aligned}$$

where $\bar{\rho}_g$ is the gas-phase mass density, Y_{g,O_2} the oxygen mass fraction in the gas-phase, and \bar{D}_g a mass diffusivity coefficient. The formulation is one-dimensional and ζ designates the coordinate normal to the exposed surface of the particle, $0 \leq \zeta \leq \delta$ (rectangular slabs) or $0 \leq \zeta \leq R_p$ (cylindrical- or spherical-shaped particles); $\zeta = 0$ is the location of the center of the particle; $\zeta = \delta$ or $\zeta = R_p$ is the location of the exposed surface. The second term on the left-hand side of Eq. [2.26](#) represents the transport of oxygen mass by convection: \dot{m}_{ζ}'' designates the convective mass flux in the direction normal to the exposed surface of the particle; for a rectangular shape, $\zeta = x$ and $\phi = 1$; for a cylindrical shape, $\zeta = r$ and $\phi = r$; and for a spherical shape, $\zeta = r$ and $\phi = r^2$. The first term on the right-hand side of Eq. [2.26](#) represents the transport of oxygen mass by molecular diffusion. The second and third terms on the

right-hand side of Eq. 2.26 are the volumetric rates of oxygen mass consumption due to the heterogeneous reactions R_{op} and R_{co} , respectively.

We consider the gas-phase mass diffusivity \bar{D}_g as input data, and assume unity Schmidt numbers, i.e., we treat \bar{D}_g as being equal to the dynamic viscosity of the gas, $\bar{D}_g = \nu_g$.

Equation 2.26 also requires a boundary condition at the particle surface:

$$\left(\bar{\psi} \bar{\rho}_g \bar{D}_g \frac{\partial Y_{g,O_2}}{\partial \zeta} \right)_{surf} = \dot{m}_{g \rightarrow s, O_2}'' \quad (2.27)$$

where the left-hand-side is the oxygen mass flux due to diffusive transport occurring inside the porous particle and evaluated at the exposed surface, and where the right-hand-side is the gas-to-solid oxygen mass flux due to both convective and diffusive mass transfer from the surrounding gas (based on the external gas condition described in Eq. 2.2).

The boundary condition at the center of the particle is simply:

$$\left(\frac{\partial Y_{g,O_2}}{\partial \zeta} \right)_{\zeta=0} = 0 \quad (2.28)$$

We can also write a mass conservation equation for the gas mass inside dV :

$$\frac{\partial}{\partial t} (\bar{\rho}_g \bar{\psi} dV) + \frac{1}{\phi} \frac{\partial}{\partial \zeta} (\phi \dot{m}_\zeta'') dV = +\dot{m}_{sg}''' dV \quad (2.29)$$

As expected from mass conservation considerations, the right-hand sides of Eqs. 2.22 and 2.29 are identical in magnitude and have opposite signs.

Equation 2.29 is turned into an equation for pressure. First, we invoke Darcy's law that describes the flow in porous media as a function of the pressure gradient:

$$\dot{m}_\zeta'' = -\frac{\bar{K}}{\nu_g} \times \frac{\partial p}{\partial \zeta} \quad (2.30)$$

where \bar{K} is the permeability and p is the pressure. For \bar{K} , we treat the permeability as a weighted average of values obtained for reference compositions and treated as pseudo material properties:

$$\bar{K} = \sum_{k=ws,ds,c,a} K_k X_k \quad (2.31)$$

where K_k is the value of the permeability of the solid constituent k and is treated as an external input parameter.

Next, using the ideal gas law we obtain an evolution equation for pressure inside the particle:

$$\frac{\partial}{\partial t} \left(\frac{M_g}{RT_g} p \bar{\psi} dV \right) = \frac{1}{\phi} \frac{\partial}{\partial \zeta} \left(\phi \frac{\bar{K}}{\nu_g} \frac{\partial p}{\partial \zeta} \right) dV + \dot{m}_{sg}''' dV \quad (2.32)$$

The solution of Eq. 2.32 provides a description of the variations of the convective mass flux inside the particle, \dot{m}_ζ'' .

The corresponding boundary conditions at the exposed surface and at the center of the particle are:

$$p_{surf} = p_\infty , \quad \left(\frac{\partial p}{\partial \zeta} \right)_{\zeta=0} = 0 \quad (2.33)$$

where p_∞ is the external ambient pressure.

2.2.4 Conservation equation for energy inside an individual particle

Let us consider again an elementary control volume dV located inside a porous particle. We can write a temperature equation for the solid-phase inside dV , as follows

$$\bar{\rho}_s \bar{c}_s (1 - \bar{\psi}) \frac{\partial T_s}{\partial t} dV = \frac{1}{\phi} \frac{\partial}{\partial \zeta} ((1 - \bar{\psi}) \bar{k}_s \phi \frac{\partial T_s}{\partial \zeta}) dV + \dot{q}_{hrr}''' dV + \dot{q}_{gs}''' dV \quad (2.34)$$

where \bar{c}_s is the heat capacity, \bar{k}_s the heat conductivity and T_s the temperature of the solid-phase. The first term on the right-hand side of the temperature equation represents the transport of heat by conduction; this term can also include transport by radiation across the pores of the particle. The second term on the right-hand side of the temperature equation is the volumetric rate of heat consumption/production due to the heterogeneous reactions (moisture evaporation, thermal/oxidative pyrolysis, and char oxidation). The third term on the right-hand side of the temperature equation is the volumetric rate of heat transfer between the gas and solid-phases.

The volumetric rate of heat consumption/production is expressed as:

$$\begin{aligned} \dot{q}_{hrr}''' &= (1 - \eta_{ds,Rd}) \dot{m}_{Rd}''' \Delta H_{Rd} + (1 - \eta_{c,Rp}) \dot{m}_{Rp}''' \Delta H_{Rp} \\ &\quad + (1 - \eta_{c,Rop}) \dot{m}_{Rop}''' \Delta H_{Rop} + (1 - \eta_{a,Rco}) \dot{m}_{Rco}''' \Delta H_{Rco} \end{aligned} \quad (2.35)$$

where ΔH_{Rd} is the heat of drying (per unit mass of water evaporated), ΔH_{Rp} and ΔH_{Rop} the heats of the thermal and oxidative pyrolysis reactions (per unit mass of gas produced), and ΔH_{Rco} the heat of the char oxidation reaction (per unit mass of gas produced). In this expression, the heats of reaction are positive (negative) when the corresponding reaction is exothermic (endothermic). These heats of reaction are typically obtained using Differential Scanning Calorimetry (DSC) analysis of the heat flow in micro-scale samples [53] (see chapter 3 for the values of these input parameters adopted in this dissertation).

We can also write a temperature equation for the gas-phase inside dV , as follows:

$$\bar{\rho}_g \bar{c}_{p,g} \bar{\psi} \frac{\partial T_g}{\partial t} dV + \dot{m}_\zeta'' c_{p,g} \frac{\partial T_g}{\partial \zeta} dV = \frac{1}{\phi} \frac{\partial}{\partial \zeta} (\phi \bar{\psi} \bar{k}_g \frac{\partial T_s}{\partial \zeta}) dV - \dot{q}_{gs}''' dV \quad (2.36)$$

where \bar{k}_g the heat conductivity. The second term on the left-hand side of the temperature equation represents the transport of heat by convection. The first term on the right-hand side of the temperature equation represents the transport of heat by conduction. The second term on the right-hand side of the temperature equation is the volumetric rate of heat transfer between the gas and solid-phases (this term has an opposite sign in the equations for T_s and T_g).

We assume a local thermal equilibrium, $T_s = T_g$, and denote T_p the local solid/gas temperature. By combining the equations for T_s and T_g presented above, one gets:

$$(\bar{\rho}_s \bar{c}_s (1 - \bar{\psi}) + \bar{\rho}_g \bar{c}_{p,g} \bar{\psi}) \frac{\partial T_p}{\partial t} dV + \dot{m}_\zeta'' \bar{c}_{p,g} \frac{\partial T_p}{\partial \zeta} dV = \frac{1}{\phi} \frac{\partial}{\partial \zeta} \left(((1 - \bar{\psi}) \bar{k}_s + \bar{\psi} \bar{k}_g) \phi \frac{\partial T_p}{\partial \zeta} \right) dV + \dot{q}_{hrr}''' dV \quad (2.37)$$

This equation describes the transport of heat across the porous particle and is coupled to the mass conservation equation 2.17 through the source term \dot{q}_{hrr}''' as well as through the specification of the thermal properties of the particle, $(\bar{\rho}_s \bar{c}_s)$ and \bar{k}_s . Equation 2.37 provides in turn the space-time variations of the particle temperature that determine the rates of evaporation, pyrolysis, and char oxidation across the particle.

In Eq. 2.37, the solid-phase thermal properties, $(\bar{\rho}_s \bar{c}_s)$ and \bar{k}_s , are simply calculated as weighted averages of the corresponding properties of individual species,

using volume fractions as weight coefficients:

$$\begin{aligned}\bar{\rho}_s \bar{c}_s (1 - \bar{\psi}) &= \bar{\rho}_{bulk} \bar{c}_s = \sum_{k=ws,ds,c,a} (\rho_{k,bulk} c_{s,k}) X_k \\ \bar{k}_s (1 - \bar{\psi}) &= \sum_{k=ws,ds,c,a} k_{s,k} X_k\end{aligned}\quad (2.38)$$

where $c_{s,k}$ and $k_{s,k}$ are input data to the model and are temperature-dependent such that

$$\begin{aligned}c_{s,k} &= c_{0,k} \left(\frac{T_p}{T_0}\right)^{n_{c,k}} \\ k_{s,k} &= k_{0,k} \left(\frac{T_p}{T_0}\right)^{n_{k,k}} + \gamma_k \sigma T_p^3\end{aligned}\quad (2.39)$$

where $c_{0,k}$, $n_{c,k}$, T_0 , $k_{0,k}$, $n_{k,k}$ and γ_k are prescribed model coefficients and where the γ_k -term represents an effective heat conductivity due to pore radiation (γ_k is in units of length). We also estimate the gas-phase thermal properties $\bar{c}_{p,g}$ and \bar{k}_g inside the particle pores using tabulated temperature-dependent data [54].

Equation 2.37 requires a boundary condition at the particle surface:

$$\left(((1 - \bar{\psi}) \bar{k}_s + \bar{\psi} \bar{k}_g) \frac{\partial T_p}{\partial \zeta} \right)_{surf} = \dot{q}_{g \rightarrow s}'' \quad (2.40)$$

where the left-hand-side is the heat flux due to conduction (and possibly due to radiation across the pores) occurring inside the porous particle and evaluated at the exposed surface, and where the right-hand-side is the gas-to-solid heat flux due to both convective and radiative heat transfer from the surrounding gas (based on the external gas condition described in Eq. 2.1):

The boundary condition at the center of the particle is simply:

$$\left(\frac{\partial T_p}{\partial \zeta} \right)_{\zeta=0} = 0 \quad (2.41)$$

2.2.5 Outputs of the PBR model

As shown in the previous sections, the PBR model calculates the spatial and temporal variations of the solid particle's constituents, the solid particle's temperature as well as the oxygen concentration and the pressure inside the solid particle's pores in response to the gas-to-solid heat flux $\dot{q}_{g \rightarrow s}''$ and oxygen mass flux $\dot{m}_{g \rightarrow s, O_2}''$. A quantity of interest that is commonly used in the literature is the total mass loss rate of the particle (MLR, in units of kg/s), which we calculate as:

$$\text{MLR} = \int_{V_p} \dot{m}_{sg}''' dV \quad (2.42)$$

with

$$\dot{m}_{sg}''' = (1 - \eta_{ds,Rd})\dot{m}_{Rd}''' + (1 - \eta_{c,Rp})\dot{m}_{Rp}''' + (1 - \eta_{c,Rop})\dot{m}_{Rop}''' + (1 - \eta_{a,Rco})\dot{m}_{Rco}''' \quad (2.43)$$

The model also provides the mass production (or consumption) rates of gaseous species (*i.e.*, water vapor (H_2O), oxygen (O_2), carbon dioxide (CO_2), and gaseous fuel (noted as *fuel*)) due to reactions *Rd-Rco* as follows:

$$\begin{aligned} \dot{m}_{s,H_2O} &= \int_{V_p} (1 - \eta_{ds,Rd})\dot{m}_{Rd}''' dV \\ \dot{m}_{s,fuel} &= \int_{V_p} ((1 - \eta_{c,Rp})\dot{m}_{Rd}''' + (1 - \eta_{c,Rop})\dot{m}_{Rop}''') dV \\ \dot{m}_{s,CO_2} &= \int_{V_p} (1 + \eta_{O_2,Rco} - \eta_{a,Rco})\dot{m}_{Rco}''' dV \\ \dot{m}_{s,O_2} &= -\dot{m}_{g \rightarrow s, O_2}'' A_p \end{aligned} \quad (2.44)$$

where A_p is the area of the particle's exposed surface.

As noted earlier, we assume in the above expressions that the combustible volatiles produced from reactions Rp and Rop are similar and are lumped into a single chemical species. We also assume that the oxidation of char in Rco does not produce any flammable gaseous fuel that can burn outside the particle, and if any flammable gaseous products are produced during this process (e.g., CO), they are assumed to be completely consumed within the particle pores.

2.2.6 Particle burning state

In order to track the state of each individual particle during thermal degradation, we developed different criteria based on the particle's instantaneous composition, size, the rate of production of gaseous fuel, and the particle's heat release rate. We describe the state of the particle as follows:

- Drying: the particle is losing moisture, and some pyrolysis gas may be emitted but it is below the set threshold for flaming ignition [55], such that

$$(X_{ws}|_{\zeta=0} > 0.1\%) \quad \text{and} \quad (\dot{m}_{s,fuel}/A_p < 1 \text{ g/m}^2/\text{s})$$

- Pyrolyzing: the particle is dry, and some pyrolysis gas may be emitted but it is below the set threshold for flaming ignition, such that

$$(X_{ds}|_{\zeta=0} > 99.9\%) \quad \text{and} \quad (\dot{m}_{s,fuel}/A_p < 1 \text{ g/m}^2/\text{s})$$

- Flaming: the particle is releasing pyrolysis gas at a rate higher than the ignition threshold, and charring could also be occurring, such that

$$(\dot{m}_{s,fuel}/A_p \geq 1 \text{ g/m}^2/\text{s})$$

- Charring: the particle has some residual dry solid, but insignificant amounts of pyrolysis gas are being released and insignificant oxidation is occurring, such that

$$(X_c|_{\zeta=0} > 0.1\%) , (\dot{m}_{s,fuel}/A_p < 1 \text{ g/m}^2/\text{s}) \text{ and } (\dot{q}_{hrr} \leq 0)$$

- Glowing: the particle has some char, and it may have some residual dry solid but insignificant amounts of pyrolysis gas are being released, and significant oxidation is occurring

$$(X_c|_{\zeta=0} > 0.1\%) , (\dot{m}_{s,fuel}/A_p < 1 \text{ g/m}^2/\text{s}) \text{ and } (\dot{q}_{hrr} > 0)$$

- Ashed: charring and pyrolysis rates are insignificant and the particle is mostly composed of ash

$$(X_a|_{\zeta=0} > 99.9\%)$$

While the ashed particles may collapse due to structural failure and contribute to some boundary layer heat transfer and drag, we remove these ashed particles from the calculation.

- Consumed: the particle is completely consumed to an insignificant size relative to its initial size

$$(\delta_p/\delta_{p,0} < 0.01) \text{ or } (R_p/R_{p,0} < 0.01)$$

Note that in this case, the particle is completely removed from the system and no further calculations of this particle are carried out.

The above criteria are also used to identify different zones of the fuel bed in fire spread simulations (see Fig 2.1). The state of each particle is tracked and the

front and back edges of the drying, pyrolysis, and smoldering fronts are identified based on the corresponding state of the rearmost and the foremost particles in the spread direction. Note that the flame front is identified based on the heat release rate of the homogeneous gas-phase reaction.

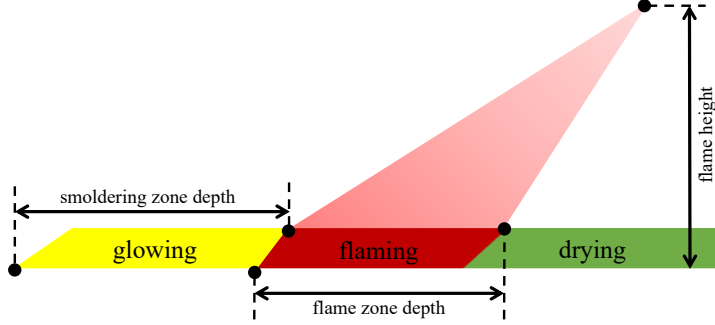


Figure 2.1: A schematic of fire spread in a fuel bed showing the characteristic length-scales of the flame and the different zones identified based on the particle burning state.

2.3 Fuel bed model and the coupled Lagrangian-Eulerian formulation

In order to describe gas-solid mass, momentum, and energy exchanges in simulations of fire spread across a set of fuel patches comprised of discrete porous fuel particles under ambient air conditions and for a given terrain, we developed PBRFoam, a finite-volume Large Eddy Simulation (LES) solver that couples the PBR model presented in the previous section with the open-source C++ library OpenFOAM [41]. The PBRFoam solver leverages various features from the OpenFOAM library such as the flexibility to implement and build new models using object-oriented inheritance, the existence of various discretization schemes and iterative algorithms, the advanced

meshing capabilities (structured/unstructured polyhedral mesh), and the massively parallel computing capability using Message Passing Interface (MPI) technique. These features include mesh generation, boundary conditions, discretization schemes, and matrix solvers. The structure of the computational solver is described in section 2.10.

The PBRFoam solver adopts a coupled multiphase formulation following the work proposed by Porterie et al. [13] and Morvan and Dupuy [14, 15]. We use here a low Mach number formulation of the Favre-filtered reactive-radiative Navier-Stokes equations. We write the conservation statements for a control volume, hereinafter referred to as “*bed*”, comprised of solid particles and gases per unit total volume of the bed, $V_{bed} = (V_{s,bed} + V_{g,bed})$, where $V_{s,bed}$ designates the volume occupied by the population of particles inside the control volume V_{bed} and $V_{g,bed}$ designates the corresponding volume occupied by the gas. A schematic of a typical fuel bed is presented in Fig. 2.2.

2.3.1 Conservation equations for species/total mass in the gas-phase

We write for the conservation of total mass:

$$\frac{\partial}{\partial t} (\bar{\rho}(1 - \beta_s)) + \frac{\partial}{\partial x_j} (\bar{\rho}(1 - \beta_s)\tilde{u}_j) = \dot{m}_{s,bed}''' \quad (2.45)$$

where $\bar{\rho}$ is the mass density of the gas, $\bar{\rho} = (m_g/V_{g,bed})$, and where \tilde{u}_j the gas flow velocity in the x_j direction.

For clarity, we introduce the quantity X_p which represents the volume fraction occupied by a specific class of particles in a fuel bed comprised of poly-dispersed

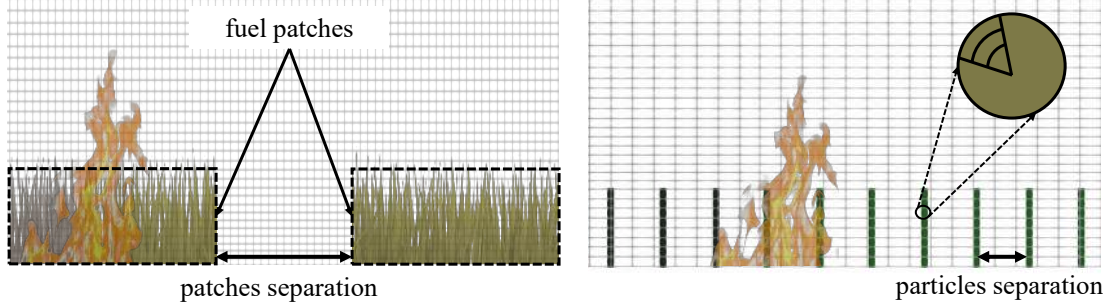


Figure 2.2: Schematic side view of a typical fuel bed showing fuel patches separated by a given distance (left). The computational grid is shown in the background. Each fuel patch is modeled by a collection of mono- or poly-dispersed particles described at the sub-grid level (right). The thermal degradation of each particle is tracked using the PBR solver through the computational grid shown in the inset.

particles:

$$X_p = V_p / V_{bed} \quad (2.46)$$

The packing ratio of the fuel bed can then be constructed from

$$\beta_s = \frac{\sum_{\text{particles}} V_p}{V_{bed}} = \sum_{\text{particles}} X_p \quad (2.47)$$

Using the previous expression, we write:

$$\begin{aligned} \dot{m}_{s,bed}''' &= \frac{1}{V_{bed}} \sum_{\text{particles}} \int_{V_p} \dot{m}_{sg}''' dV \\ &= \sum_{\text{particles}} \left(X_p \frac{\int_{V_p} \dot{m}_{sg}''' dV}{V_p} \right) \end{aligned} \quad (2.48)$$

Similarly, we write for the conservation of chemical species mass:

$$\begin{aligned} \frac{\partial}{\partial t} (\bar{\rho}(1 - \beta_s) \tilde{Y}_k) + \frac{\partial}{\partial x_j} (\bar{\rho}(1 - \beta_s) \tilde{u}_j \tilde{Y}_k) \\ = \frac{\partial}{\partial x_j} (\bar{\rho}(1 - \beta_s)(D_k + D_{Turb}) \frac{\partial \tilde{Y}_k}{\partial x_j}) + \dot{m}_{s,k,bed}''' + \dot{\omega}_k''' \end{aligned} \quad (2.49)$$

where \tilde{Y}_k is the mass fraction of (gaseous) species k , $\tilde{Y}_k = (m_{k,g}/m_g)$, D_k and D_{Turb} the mass diffusivity of species k due to molecular transport and to subgrid-scale turbulent convective transport, respectively, where $\dot{m}_{s,k,bed}'''$ is the mass production/consumption of species k due to drying, pyrolysis and/or char oxidation, and ω_k''' the mass production/consumption of species k due to homogeneous (gas-phase) combustion.

Using the previous section, we write:

$$\begin{aligned}\dot{m}_{s,k,bed}''' &= \frac{1}{V_{bed}} \sum_{particles} \int_{V_p} \dot{m}_{s,k}''' dV \\ &= \sum_{particles} \left(X_p \frac{\int_{V_p} \dot{m}_{s,k}''' dV}{V_p} \right)\end{aligned}\quad (2.50)$$

where $\dot{m}_{s,k}'''$ designates the mass production/consumption of species k (due to drying, pyrolysis, and/or char oxidation) for an individual particle.

In Eq. 2.49, we neglect differential diffusion, we assume that the molecular diffusivities of all species are equal (i.e., equidiffusivity) and we assume a unity Schmidt number

$$Sc = \frac{\nu_k}{D_k} = \frac{\nu_m}{D_m} = 1 \quad (2.51)$$

where ν_k is the kinematic viscosity of species k , D_m the molecular diffusivity of the mixture, and where ν_m is the kinematic viscosity of the mixture of gases.

We model the kinematic viscosity of the mixture, ν_m , using Sutherland's model

$$\mu_m = A_0 \frac{\sqrt{T}}{1 + T_0/T} \quad (2.52)$$

where $\nu_m = \mu_m / (\bar{\rho}(1 - \beta_s))$, $A_0 = 1.67212 \times 10^{-6} \text{ kg/m.s.K}^{0.5}$, and $T_0 = 170.672 \text{ K}$.

2.3.2 Conservation equations for momentum in the gas-phase

We write for conservation of momentum in the x_i direction:

$$\begin{aligned} \frac{\partial}{\partial t} (\bar{\rho}(1 - \beta_s) \tilde{u}_i) + \frac{\partial}{\partial x_j} (\bar{\rho}(1 - \beta_s) \tilde{u}_j \tilde{u}_i) \\ = \frac{\partial}{\partial x_j} (\bar{\rho}(1 - \beta_s) (\nu_m + \nu_{Turb}) (\frac{\partial \tilde{u}_i}{\partial x_j} + \frac{\partial \tilde{u}_j}{\partial x_i} - \frac{2}{3} \delta_{ij} \frac{\partial \tilde{u}_k}{\partial x_k})) \\ - \frac{\partial}{\partial x_i} ((1 - \beta_s) \bar{p}) + \bar{\rho}(1 - \beta_s) g_i + F_i''' \end{aligned} \quad (2.53)$$

where ν_{Turb} is the kinematic viscosity due to subgrid-scale turbulent convective transport, where \bar{p} is the gas pressure, g_i the gravity acceleration in the x_i direction, and where F_i''' is the aerodynamic force (per unit volume) due to the solid particles (see section 2.5 for additional details). The conservation statement is again written per unit volume of fuel bed, $V_{bed} = (V_{g,bed} + V_{s,bed})$.

2.3.3 Conservation equation for energy in the gas-phase

We write for the conservation of energy:

$$\begin{aligned} \frac{\partial}{\partial t} (\bar{\rho}(1 - \beta_s) \tilde{h}_{th}) + \frac{\partial}{\partial x_j} (\bar{\rho}(1 - \beta_s) \tilde{u}_j \tilde{h}_{th}) \\ = \frac{\partial}{\partial x_j} (\bar{\rho}(1 - \beta_s) (\alpha_m + \alpha_{Turb}) \frac{\partial \tilde{h}_{th}}{\partial x_j}) + \dot{q}_{comb}''' + \dot{q}_{rad}''' + \dot{h}_{th}''' \\ + \dot{m}_{s,bed}''' \tilde{h}_{th,surf} \end{aligned} \quad (2.54)$$

where \tilde{h}_{th} is the thermal enthalpy of the gas, α_m and α_{Turb} the heat diffusivity due to molecular transport and to subgrid-scale turbulent convective transport, respectively, where \dot{q}_{comb}''' the heat release rate associated with homogeneous (gas-phase) combustion, \dot{q}_{rad}''' the net radiative power density in the gas-phase due to

radiation absorption and emission (scattering effects are neglected), and \dot{h}_{th}''' the volumetric rate of (convective and radiative) heat transfer between the gas and the solid particles. The last term on the right-hand side of Eq. 2.54 represents the energy gain in the gas-phase associated with the addition of vapor mass due to drying, pyrolysis, and char oxidation; in the expression of that term, $\tilde{h}_{th,surf}$ is the thermal enthalpy of the vapors taken at the release conditions, i.e., at the particle surface conditions; note that it is not clear whether this term plays any significant role in the overall heat transfer. The gas-phase heat release rate \dot{q}_{comb}''' and the net radiative power density \dot{q}_{rad}''' are computed from the gas-phase combustion model and the radiation model discussed in the following.

In Eq. 2.54, we obtain thermal diffusivity of the mixture α_m assuming a unity Lewis number

$$Le = \frac{\alpha_m}{D_m} = 1 \quad (2.55)$$

The expression for \dot{h}_{th}''' in Eq. 2.54 is:

$$\begin{aligned} \dot{h}_{th}''' &= \frac{1}{V_{bed}} \sum_{particles} (-\dot{q}_{g \rightarrow s}'' A_p) \\ &= \sum_{particles} \sigma_p X_p \left(-h(\tilde{T} - T_{p,surf}) - \epsilon_{p,surf}(G - \sigma T_{p,surf}^4) \right) \end{aligned} \quad (2.56)$$

where σ_p is the surface area to volume ratio of an individual solid particle.

2.3.4 Radiation transfer in the multiphase fuel bed

We adopt the Multiphase Radiative Transfer Equation (MRTE) proposed by Consalvi et al. [56] to account for the radiation absorption and emission by the solid

fuel particles and by the hot gases. We write the MRTE as follows:

$$\frac{d}{ds} ((1 - \beta_s)I) = (1 - \beta_s)\kappa_m \left(\frac{\sigma \tilde{T}^4}{\pi} - I \right) + \sum_{particles} \left(\frac{\sigma_p X_p \epsilon_{p,surf}}{4} \left(\frac{\sigma T_{p,surf}^4}{\pi} - I \right) \right) \quad (2.57)$$

where κ_m is the Planck mean absorption coefficient due to the mixture of gas species and soot inside the fuel bed, T the gas temperature, and $T_{p,surf}$ the characteristic surface temperature of the particles. The first term on the RHS of Eq. 2.57 corresponds to radiation emission and absorption by gas species and soot (note that subgrid-scale turbulence-radiation interactions are neglected); the second term corresponds to radiation emission and absorption by the solid particles.

From the MRTE we can approximate the characteristic radiation length scale of a fuel bed as $((1 - \beta_s)\kappa_m + \sum_{particles} \sigma_p X_s \epsilon_{p,surf}/4)^{-1}$. This length scale must be resolved by the computational grid.

The expression for \dot{q}_{rad}''' in Eq. 2.37 comes from the integration over angular space of the source/sink terms appearing in the MRTE:

$$\dot{q}_{rad}''' = (1 - \beta_s)\kappa_m \left(\int_{4\pi} Id\Omega - 4\sigma \tilde{T}^4 \right) + \sum_{particles} \frac{\sigma_p X_s \epsilon_{p,surf}}{4} \left(\int_{4\pi} Id\Omega - 4\sigma T_{p,surf}^4 \right) \quad (2.58)$$

Also, the irradiation incident on the solid fuel particles G is obtained from

$$G = \left(\int_{4\pi} Id\Omega \right) / 4 \quad (2.59)$$

From the previous section, we re-write the expression of \dot{h}_{th}''' as

$$\dot{h}_{th}''' = - \sum_{particles} (\sigma_p X_p) \times h \left(\tilde{T} - T_{p,surf} \right) - \sum_{particles} (\sigma_p X_p \epsilon_{p,surf}) \times \left(\frac{\int_{4\pi} Id\Omega}{4} - \sigma T_{p,surf}^4 \right) \quad (2.60)$$

Interestingly, the radiative contributions of solid particles in the expressions for \dot{q}_{rad}''' and \dot{h}_{th}''' cancel out and we obtain:

$$\dot{q}_{rad}''' + \dot{h}_{th}''' = (1 - \beta_s)\kappa_m \left(\int_{4\pi} I d\Omega - 4\sigma \tilde{T}^4 \right) - \sum_{particles} (\sigma_p X_p \epsilon_{p,surf}) \times h \left(\tilde{T} - T_{p,surf} \right) \quad (2.61)$$

with the first term on the RHS representing the radiation contribution from the hot gases and soot to the energy of the multiphase control volume (i.e., the fuel bed), and the second term on the RHS representing the contribution of convective heating/cooling from the solid particles. See section 2.8 for additional details about the treatment of the radiation terms.

2.4 Convective transfer model

The convective heat and mass transfer between an individual solid fuel particle and the external gas surrounding it is modeled through the convective heat transfer coefficient h and the convective mass transfer coefficient $h_{mass} = (h/\bar{c}_{p,g})$. These coefficients are obtained from empirical correlations for the Nusselt number under no blowing conditions:

$$h_0 = Nu_D \frac{k_g}{D_{eff}} \quad (2.62)$$

where h_0 is the convective heat transfer coefficient under no blowing condition, Nu_D is the Nusselt number, D_{eff} the effective diameter of the particle (for rectangular-shaped particles, $D_{eff} = 2\delta \times 2/\sqrt{\pi}$, while for cylindrical- and spherical-shaped particles, $D_{eff} = 2R_p$).

For rectangular- and cylindrical-shaped particles, we use a comprehensive

empirical correlation developed by Churchill and Bernstein [57] for applications to convective heat transfer over cylinders and valid over a wide range of Reynolds numbers:

$$Nu_D = \frac{h \times D_{eff}}{k_g} = 0.3 + \frac{0.62 \times Re_D^{0.5} \times Pr^{1/3}}{\left(1 + \left(\frac{0.4}{Pr}\right)^{2/3}\right)^{1/4}} \left(1 + \left(\frac{Re_D}{282000}\right)^{5/8}\right)^{4/5} \quad (2.63)$$

where Pr is the Prandtl number of the external gas surrounding the particle, Re_D the Reynolds number, $Re_D = (\bar{\rho}u_g D_{eff}/\nu_g)$, with u_g the flow velocity of the external gas ($u_g = \sqrt{(\tilde{u}_j - u_{s,j})(\tilde{u}_j - u_{s,j})}$), and where k_g and ν_g are the temperature-dependent thermal conductivity and kinematic viscosity of the external gas, calculated at the film temperature $(T_{g,\infty} + T_{p,surf})/2$ using tabulated data [54]. Figure 2.3 shows the variation of the convective heat transfer coefficient h calculated using Eq. 2.63 at different gas velocities and particle diameters. These plots highlight the strong variation of h with the particle's effective diameter such that smaller particles tend to heat (and cool) much faster than larger ones.

For spherical-shaped particles, we use an empirical correlation developed by Whitaker [58] for applications to convective heat transfer over spheres and valid over a wide range of Reynolds numbers:

$$Nu_D = 2 + \left(0.4 Re_D^{0.5} + 0.06 Re_D^{2/3}\right) \times Pr^{0.4} \left(\frac{\mu_g}{\mu_s}\right)^{0.25} \quad (2.64)$$

where μ_s is the dynamic viscosity of the external gas surrounding the particle evaluated at the surface temperature using tabulated data [54]. All other properties are evaluated at the gas temperature.

We modify the convective transfer coefficient to account for the blowing effect due to outflowing volatiles through a Couette approximation [50]. We write the

convective transfer coefficient at blowing conditions as:

$$h = \frac{\dot{m}_{surf}'' \bar{c}_{p,g}}{\exp(\dot{m}_{surf}'' \bar{c}_{p,g}/h_0) - 1} \quad (2.65)$$

where \dot{m}_{surf}'' is the flow at the surface of the particle which is obtained from the pressure gradient at the particle's surface using Darcy's law (Eq. 2.30).

It should be noted that there might be some uncertainties in the choices of the heat transfer coefficient due to many factors such as the orientation of each particle inside the fuel bed with respect to the flow direction and the particle-to-particle interactions. For example, as presented in a recent work by Mueller et al. [59], the bed-average heat transfer coefficient can be lower than that of an isolated particle by 11% to 25%.

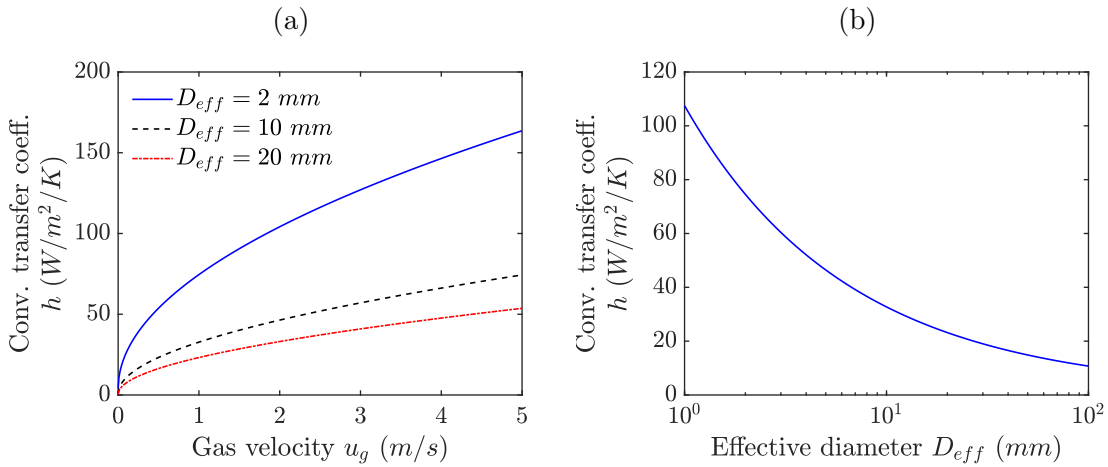


Figure 2.3: Variation of the convective heat transfer coefficient with: a) wind velocity for particles with different sizes; and b) particle's effective diameter at a wind velocity of 1 m/s .

2.5 Drag model and particle motion

As described in the previous section, the drag force inside the fuel bed due to the presence of solid particles requires a description of the drag coefficient. Similar to the heat transfer coefficient, the drag coefficient of a particle inside a fuel bed can differ from that of an isolated particle. There is a very limited number of studies about fuel bed drag in the wildland fire community (e.g., Ref. [60]), but there are more data on vegetation hydrodynamics [61–64]).

In this work, we describe the particle's drag coefficient using Reynold's dependent empirical correlations (see Fig. 2.4). The drag coefficients of isolated cylinders and spheres are described as follows [54]:

$$C_D|_{\text{cylinder}} = \begin{cases} 100/Re_D^{0.7} & \text{if } Re_D \leq 1 \\ \frac{10(0.6+0.4Re_D^{0.8})}{Re_D} & \text{if } 1 < Re_D < 1000 \\ 1 & \text{if } Re_D \geq 1000 \end{cases} \quad (2.66)$$

$$C_D|_{\text{sphere}} = \begin{cases} 24/Re_D & \text{if } Re_D \leq 1 \\ \frac{24(0.85+0.15Re_D^{0.687})}{Re_D} & \text{if } 1 < Re_D < 1000 \\ 0.44 & \text{if } Re_D \geq 1000 \end{cases} \quad (2.67)$$

We use a constant value of the drag coefficient for rectangular-shaped particles ($C_D \approx 2$) which we find to represent the drag from various arrangements of groups of rectangular particles under conditions of interest.

In the case of movement of the solid fuel particle (e.g., firebrands), we consider

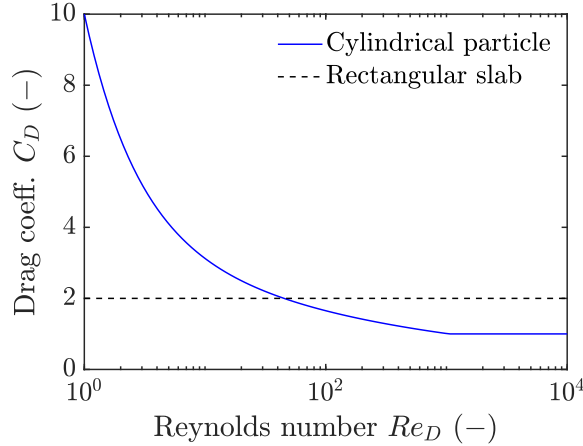


Figure 2.4: Variation of drag coefficient with Reynolds number for cylindrical- and rectangular-shaped particles.

an additional equation for the particle's momentum. We write the momentum balance of each moving particle as

$$\frac{d}{dt}(u_{s,j}) = \frac{F_{D,j}}{m_s} + \frac{F_{L,j}}{m_s} + g_j \quad (2.68)$$

where $u_{s,j}$ is the solid particle's velocity in j direction, $F_{D,j}$ and $F_{L,j}$ are the drag and lift forces generated by the solid particle, and where g_j is the gravitational acceleration in j direction.

We use the classical aerodynamic expressions for the lift and drag force and we write

$$\begin{aligned} F_{L,j} &= \frac{1}{2} C_L \bar{\rho} (1 - \beta_s) A_p^* |\tilde{u}_j - u_{s,j}| \times (\tilde{u}_j - u_{s,j}) \\ F_{D,j} &= \frac{1}{2} C_D \bar{\rho} (1 - \beta_s) A_p^* |\tilde{u}_j - u_{s,j}| \times (\tilde{u}_j - u_{s,j}) \end{aligned} \quad (2.69)$$

where C_L and C_D are the lift and drag coefficients, respectively, and A_p^* the projected surface area of the particle. We further write $A_p^* = C_A \times A_p$, where C_A is a shape

factor (for a rectangular-shaped particle, $C_A = 1$; for a cylindrical-shaped particle, $C_A = 1/\pi$; for a spherical-shaped particle, $C_A = 1/4$).

In the general case of moving and stationary particles, the expression for the aerodynamic force in Eq. 2.53 is

$$F_j''' = \frac{1}{V_{bed}} \sum_{particles} -(F_{L,j} + F_{D,j}) \quad (2.70)$$

For fuel beds composed of stationary particles, the aerodynamic force per unit volume of the fuel bed becomes

$$F_j''' = - \sum_{particles} \left(\sigma_p X_p C_D \frac{C_A}{2} \bar{\rho} \sqrt{\tilde{u}_k \tilde{u}_k} \times \tilde{u}_j \right) \quad (2.71)$$

2.6 Gas-phase homogeneous combustion model

As described earlier, due to a lack of data about the chemical composition of the combustible gaseous volatiles produced from thermal and oxidative pyrolysis reactions (*R_p* and *R_{op}*), we use a lumped chemical species to represent the gaseous fuel and we use a global combustion equation to describe its reaction with ambient air. Following the work of Ritchie et al. [65], we assume that the gaseous fuel has a composition of $C_{3.4}H_{6.2}O_{2.5}$ (molecular weight of 87.096 g/mol). This surrogate fuel has an average heat of combustion (ΔH_c) that is selected based on the average heat of combustion of the gaseous volatiles obtained from experimental techniques such as Micro-scale Combustion Calorimetry (MCC) [66]. We write the global combustion equation as follows:



The Eddy Dissipation Model (EDM) [46] is adopted in most computational fire models because it is often assumed that the combustion is primarily controlled by turbulent mixing. However, because there are laminar regions in many fire flames, such as near the base of the flame where the flame starts as laminar and then transitions into turbulence due to buoyancy, the application of the EDM as is might not be appropriate. In order to correctly capture the heat release rate in these laminar flames, we developed a modified version of the EDM in which we use laminar diffusion flame theory to determine the characteristic time-scale of laminar diffusion. This modified model allows the blend between laminar or turbulent mixing based on the minimum of the characteristic time-scales of laminar diffusion and turbulent mixing in a particular region. The reader is invited to refer to appendix B for more details about this model. In short, we calculate the gas-phase heat release rate term in Eq. 2.54 from

$$\dot{q}_{comb}''' = \frac{\bar{\rho}(1 - \beta_s)}{\tau_{EDM}} \times \min \left(\tilde{Y}_F, \frac{\tilde{Y}_{O_2}}{r_s} \right) \times \Delta H_c \quad (2.73)$$

where \tilde{Y}_F and \tilde{Y}_{O_2} are the (gas-phase) mass fractions of fuel and oxygen, r_s the stoichiometric oxygen-to-fuel mass ratio, and where τ_{EDM} is the characteristic time-scale of the combustion process which we model as

$$\tau_{EDM} = \min(\tau_{Diff}, \tau_{Turb}) \quad (2.74)$$

The turbulent mixing time-scale τ_{Turb} is obtained from

$$\tau_{Turb} = \frac{k_{Turb}}{\epsilon_{Turb}} \quad (2.75)$$

where k_{Turb} is the subgrid-scale turbulent kinetic energy and ϵ_{Turb} is the subgrid-scale

turbulent dissipation rate. These subgrid-scale quantities are computed using the subgrid-scale turbulence models described later in section 2.7.

We model the diffusion time-scale as

$$\frac{1}{\tau_{Diff}} = C_{Diff} \frac{D_g}{\Delta_{LES}^2} \quad (2.76)$$

where C_{Diff} is a model parameter that depends on the LES filter size Δ_{LES} (see appendix B).

We now turn to discuss the thermochemical properties of the combustible gaseous volatiles and other gaseous species. We use the JANAF-Chemkin polynomials [67, 68] to determine thermochemical properties such as molecular weight, heat capacity, enthalpy of formation, etc. These properties are, however, unknown for the combustible gaseous volatiles of thermal and oxidative pyrolysis. We follow again the work of Ritchie et al. [65], and we assume that the surrogate fuel $C_{3.4}H_{6.2}O_{2.5}$ has the same heat capacity as C_7H_{16} . Since we know the heat of combustion of the surrogate fuel $C_{3.4}H_{6.2}O_{2.5}$ from experimental measurements of the gas-phase combustion of gaseous volatiles of thermal and oxidative pyrolysis, we did a reverse calculation to determine the fuel enthalpy of formation:

$$\begin{aligned} \Delta H_c &= H_{prod} - H_{react} \\ &= N_{CO_2} h_{f,CO_2}^0 + N_{H_2O} h_{f,H_2O}^0 - N_{fuel} h_{f,C_{3.4}H_{6.2}O_{2.5}}^0 \end{aligned} \quad (2.77)$$

where N_i are the stoichiometric coefficients determined from Eq. 2.72.

Using a simplified energy balance between reactants and products and an average heat capacity of products at 1200K, and assuming that $\Delta H_c = 14.3MJ/kg$,

one can use hand calculations to find that the adiabatic flame temperature at a constant pressure of this surrogate fuel is approximately 1862 K .

A more elaborate estimate of the adiabatic flame temperature is obtained from simulations of a counter-flow diffusion flame using the modified version of the EDM. Figure 2.5 shows the adiabatic flame temperatures of the surrogate fuel ($C_{3.4}H_{6.2}O_{2.5}$) with two different heats of combustion corresponding to gaseous volatiles produced from thermal degradation of cardboard ($\Delta H_c = 14.3 \text{ MJ/kg}$) and pine wood ($\Delta H_c = 15.6 \text{ MJ/kg}$), and methane (CH_4) in the mixture fraction space (see Appendix B for more details). The simulation shows a peak flame temperature of approximately 1700 K for $C_{3.4}H_{6.2}O_{2.5}$, and approximately 2250 K for CH_4 under adiabatic conditions. In general, we anticipate the peak flame temperature of wildland fire flames to be much lower than common hydrocarbon fuels, under the same radiation conditions, because the combustible gaseous volatiles of fuel has a low heat of combustion $\approx 10 - 20 \text{ MJ/kg}$, while most common hydrocarbon fuels have a heat of combustion in the range of $\approx 40 - 50 \text{ MJ/kg}$.

2.7 Sub-grid scale turbulence model

Although our objective is to use fine-grained LES, the sub-grid scale turbulence modeling is important because it provides the turbulence mixing time-scale, which is required to model the gas-phase combustion process, in addition to the unresolved convective and thermal transport.

We model the sub-grid scale turbulent convective and thermal transport, D_{Turb}

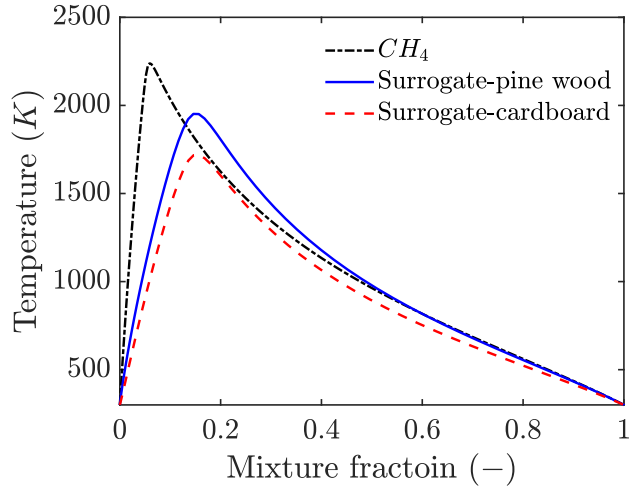


Figure 2.5: Temperature profile of laminar counter-flow diffusion flames under adiabatic conditions obtained from well-resolved simulations using the modified EDM.

and $D_{th,Turb}$, as follows:

$$D_{Turb} = D_{th,Turb}$$

$$\frac{\nu_{Turb}}{D_{th,Turb}} = Pr_{Turb} = 0.5 \quad (2.78)$$

where Pr_{Turb} is the turbulent Prandtl number.

In order to calculate the turbulent viscosity, ν_{Turb} , and the time-scale associated with turbulent mixing, τ_{Turb} , the PBRFoam solver leverages various subgrid-scale turbulence models implemented in the native OpenFOAM library. In particular, we adopt in this work the Wall Adapting Local Eddy-viscosity (WALE) model proposed by Nicoud and Ducros [69] and the Dynamic k-Equation model proposed by Kim and Menon [70].

In the WALE model, the turbulent viscosity, ν_{Turb} , is calculated from an

algebraic expression based on the square of the velocity gradient tensor [69], and the subgrid-scale turbulent kinetic energy k_{Turb} is calculated from

$$k_{Turb} = \left(\frac{\nu_{Turb}}{C_k \Delta_{LES}} \right)^2 \quad (2.79)$$

where C_k is a model coefficient ($C_k = 0.094$), and Δ_{LES} is the LES filter width ($\Delta_{LES} = (\Delta_x \Delta_y \Delta_z)^{(1/3)}$).

In the Dynamic k-Equation model, a transport equation for k_{Turb} is solved to calculate k_{Turb} [70], then the turbulent viscosity is calculated from Eq. 2.79.

Lastly, the turbulent mixing time-scale used in the combustion model is constructed from

$$\tau_{Turb} = \frac{k_{Turb}}{\epsilon_{Turb}} = \frac{1}{C_e} \frac{\Delta_{LES}}{k_{Turb}^{1/2}} \quad (2.80)$$

where C_e is a model coefficient ($C_e = 1.048$).

2.8 Gas-phase radiation absorption and emission model

We now turn to discuss the modeling choices for the radiation absorption/emissions of the gas-phase. We assume that the participating medium of the gas-phase radiation is primarily a mixture of CO_2 , H_2O , and soot. Note that although soot may exist in a solid-phase, we still group soot to the gas-phase mixture for simplicity and for avoiding confusion with the solid fuel particles.

Let us re-arrange the MRTE (i.e., Eq. 2.57) as follows

$$\frac{d}{ds} ((1 - \beta_s) I) = -((1 - \beta_s) \kappa_m + \kappa_s) I + (1 - \beta_s) \kappa_m \frac{\sigma \tilde{T}^4}{\pi} + \frac{1}{4\pi} (E_m + E_s) \quad (2.81)$$

Here we write

$$\kappa_s = \sum_{\text{particles}} \sigma_p X_p \epsilon_{p,\text{surf}} / 4 \quad (2.82)$$

as the absorption coefficient of the solid fuel particles inside the fuel bed, and

$$E_s = \sum_{\text{particles}} \sigma_p X_p \epsilon_{p,\text{surf}} \sigma T_{p,\text{surf}}^4 \quad (2.83)$$

as the radiation emission of the solid fuel particles inside the fuel bed. We introduce an additional term (E_m) that allows for alternative modeling choices of the radiation absorption/emission from the gas-phase mixture as shown in the following.

2.8.1 The Prescribed Global Radiant Fraction (PGRF) approach

In the first modeling choice, we assume that the radiation absorption and emission effects of the gas and soot mixture inside the flame zone (i.e., the region where $\dot{q}_{\text{comb}}''' > 0$) are linearly proportional to the heat release rate of the flame through a prescribed empirical radiant fraction χ_{rad} (i.e. the fraction of the energy released by homogeneous gas-phase combustion that is lost to the surroundings due to thermal radiation transport). We lump this radiation into an emission term E_m , such that:

$$E_m = \chi_{\text{rad}} \dot{q}_{\text{comb}}''' \quad \text{and} \quad \kappa_m = 0 \quad \text{if} \quad \dot{q}_{\text{comb}}''' > 0 \quad (2.84)$$

while outside the flame zone (i.e., the region where $\dot{q}_{\text{comb}}''' = 0$), the radiation absorption/emission effects of that region are accounted for by the Plank mean absorption coefficient

$$\kappa_m = p_{CO_2} \kappa_{CO_2} + p_{H_2O} \kappa_{H_2O} \quad (2.85)$$

where p_{CO_2} and p_{H_2O} are the partial pressures of CO_2 and H_2O , respectively, and where κ_{CO_2} and κ_{H_2O} are the temperature-dependent Plank mean absorption coefficients of CO_2 and H_2O , respectively, which are deduced from polynomial curve fits determined using RADCAL data [71, 72]. Note that this approximation assumes that soot completely oxidizes within the flame zone and it does not contribute to radiation outside the flame zone.

2.8.2 The Weighted-Sum-of-Gray-Gases (WSGG) approach

In the second modeling choice, we consider the WSGG approach proposed by Modest [73], and we divide the MRTE (Eq. 2.81) into a certain number of bands (J) such that:

$$\begin{aligned} \frac{d}{ds} ((1 - \beta_s) I) &= \sum_{j=1}^J \left[\frac{d}{ds} ((1 - \beta_s) I_j) \right] \\ &= - \sum_{j=1}^J \left[(1 - \beta_s) \kappa_{m,j} I_j + \frac{\kappa_s}{J} I_j \right] \\ &\quad + \sum_{j=1}^J \left[(1 - \beta_s) \kappa_{m,j} a_{m,j} \frac{\sigma \tilde{T}^4}{\pi} \right] + \sum_{j=1}^J \left[\frac{1}{4\pi} \frac{E_m + E_s}{J} \right] \end{aligned} \quad (2.86)$$

where I_j is the radiation intensity of band j , $\kappa_{m,j}$ the absorption coefficient of band j , $a_{m,j}$ a weighting coefficient ($\sum_{j=1}^J a_{m,j} = 1$), and where $E_m = 0$.

From the previous equation, we can deduce the MRTE for each band j :

$$\begin{aligned} \frac{d}{ds} ((1 - \beta_s) I_j) &= - \left[(1 - \beta_s) \kappa_{m,j} I_j + \frac{\kappa_s}{J} I_j \right] \\ &\quad + (1 - \beta_s) \kappa_{m,j} a_{m,j} \frac{\sigma \tilde{T}^4}{\pi} + \frac{1}{4\pi} \frac{E_s}{J} \end{aligned} \quad (2.87)$$

Equation 2.87 is solved J times for I_j , then a summation is taken over all bands

to deduce the total radiation intensity I .

In order to obtain each band's absorption and weighting coefficients, $\kappa_{m,j}$ and a_j , the superposition method is commonly used in WSGG modeling for mixtures of multiple participants, such that

$$\begin{aligned}\kappa_{m,j} &= \kappa_{CO_2/H_2O,j} + \kappa_{soot,j} \\ a_{m,j} &= a_{CO_2/H_2O,j} \times a_{soot,j}\end{aligned}\tag{2.88}$$

where $\kappa_{CO_2/H_2O,j}$ and a_{CO_2/H_2O} are the absorption and weighting coefficients of CO_2/H_2O , respectively in band j , and where $\kappa_{soot,j}$ the $a_{soot,j}$ are the absorption and weighting coefficients of soot in band j . To get the values of these quantities, we use either the model provided by Bordbar et al. [74] for mixtures composed of CO_2 and H_2O only, or the model provided by Cassol et al. [49] for mixtures composed of CO_2 , H_2O and soot. The model of Bordbar requires $J = 5$ bands (4 bands for CO_2/H_2O mixture and one transparent band), and it does not account for soot radiation. The model of Cassol et al. requires at least $J = 9$ bands (4 bands for CO_2/H_2O mixture, 2 bands for soot, and one transparent band), and it accounts for soot radiation which requires a description of the evolution of the soot volume fraction in the mixture (see next section).

Although the WSGG model is generally viewed as a more elaborate model than the PGRF approach, we consider it less favorable in the present study due to its computational burden associated with solving at least additional $(J - 1)$ equations. Therefore, we adopt the PBRF approach in the coupled fire spread simulations presented in this dissertation. However, in order to evaluate this choice, we present

in chapter 4 a comparison between the estimated radiation field in canonical fire configurations in non-sooting and sooting flames obtained using the PGRF or the WSGG approach.

2.9 Soot modeling

We adopted at an early phase of this dissertation a soot model based on the Laminar Smoke Point (LSP) soot model of Yao et al. [47] to evaluate the predictions of the radiation modeling choices in sooting flames. Detailed modeling and quantification of soot and smoke production in wildland fires are beyond the scope of this dissertation. Interested readers in our preliminary effort to extend the LSP concept to LES formulation are invited to see appendix C for more details.

2.10 Summary

This chapter presents a new modeling capability that accounts for the coupling between processes occurring in the solid-phase, during the thermal degradation of solid biomass vegetation, and the in the gas-phase during fire propagation. The modeling capability is based on the general-purpose C++ library OpenFOAM and an in-house C++ solver of the PBR model that treats drying, thermal pyrolysis, oxidative pyrolysis, and char oxidation using a one-dimensional porous medium formulation that allows descriptions of thermal degradation processes occurring during both flaming and smoldering combustion. A flowchart that summarizes the computational modeling framework described in this chapter is described in Fig.

[2.6](#). The reader is invited to view Appendix [A](#) for more details about the numerical algorithms and Appendix [E](#) for code compiling and parallel performance.

In short, a stand-alone C++ solver of the PBR model is developed to track the thermal degradation of porous biomass vegetation particles. Each individual porous particle is discretized into a set of 1-D control volumes representing rectangular-, cylindrical- or spherical-shaped particles. The governing equations of mass, momentum, and energy conservation inside each control volume (described in section [2.2](#)) are solved iteratively using an implicit approach that treats convection and diffusion through a second-order, Crank-Nicolson method and chemical reaction through a first-order, backward Euler method. This solver features an adaptive time-stepping technique (for speed, stability, and robustness), as well as a deforming and re-meshing capability (for swelling or shrinking particles).

Also, a coupled Lagrangian-Eulerian solver called PBRFoam is developed to solve the governing equations of the gas-phase (described in section [2.3](#)). The PBRFoam solver is constructed using the OpenFOAM library and uses the PIMPLE algorithm [\[45\]](#) to handle the pressure-velocity coupling in the conservation equations (see Fig. [2.6](#)). The PIMPLE algorithm is a blend of the Semi-Implicit Method for Pressure-Linked Equations (SIMPLE) and the Pressure-Implicit with Splitting of Operators (PISO) algorithms [\[45\]](#), and it has been applied in many of the OpenFOAM-based compressible low Mach-number solvers including the well-established fire modeling solver FireFoam [\[18, 75\]](#). The PBRFoam solver utilizes the discretization schemes readily available in the OpenFOAM library to solve the gas-phase governing equations. In particular, we use an implicit scheme called “Backward Differentiation

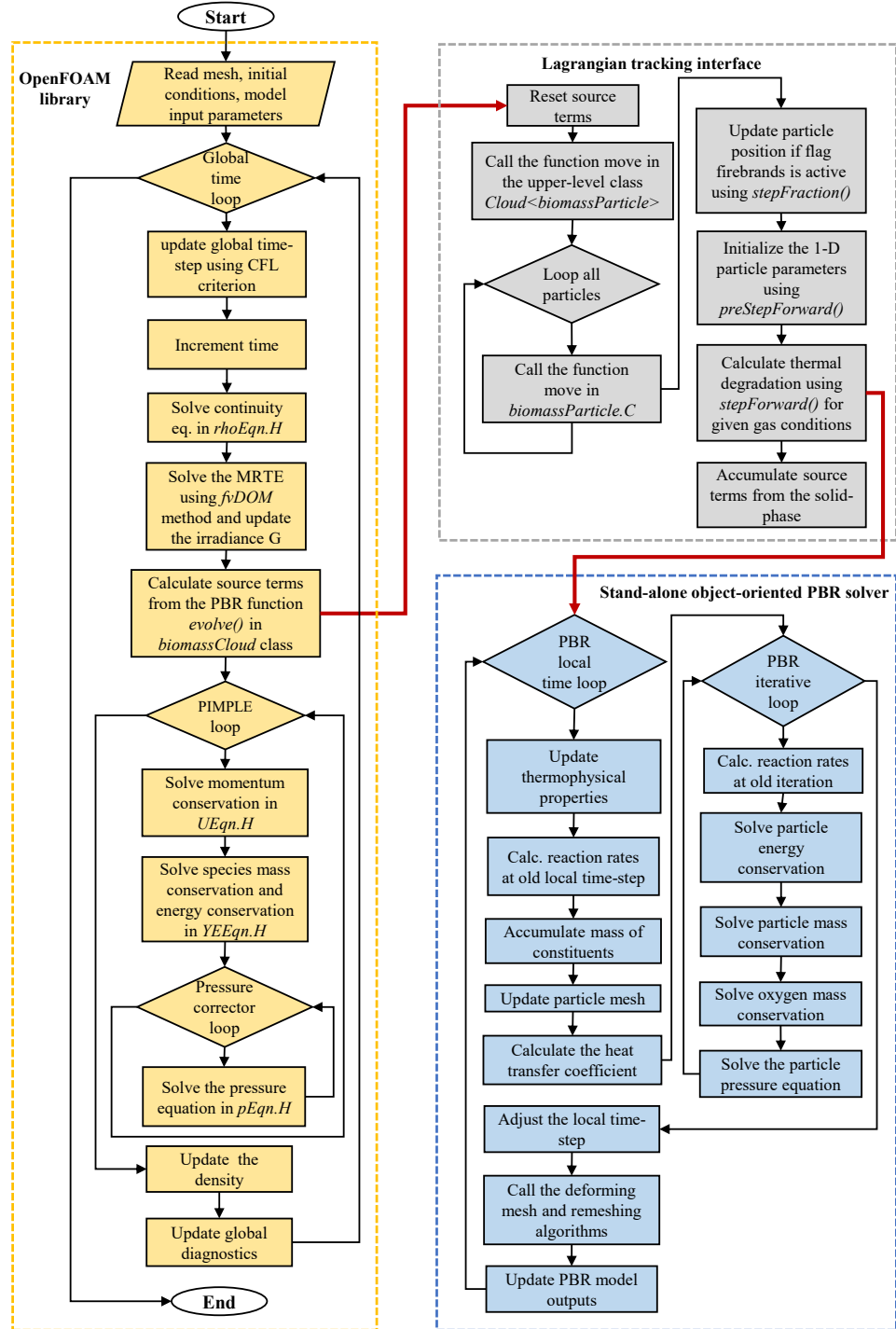


Figure 2.6: Flowchart of the computational modeling framework: the chart of the PBRFoam solver is highlighted in yellow; the chart highlight in gray depicts an interface; the chart of the PBR solver is highlighted in blue.

Formula" (BDF) for time integration and we use a Total Variation Diminishing (TVD) scheme (or more precisely a scheme that satisfies the Convection Boundedness Criterion) called *limitedLinear* for spatial discretization of the convection terms. We also use the finite volume Discrete Ordinate Method (fvDOM) to solve the MRTE by decomposing the angular space into a finite number of solid angles. More details about the discretization schemes and the matrix solvers that are included in the OpenFOAM library can be found in the official OpenFOAM foundation repository [41] as well as in Refs. [42, 45, 76, 77].

3 Verification and Evaluation of the Computational Framework

3.1 Overview

This chapter has four sections. The first section presents verification tests of the 1-D implementation of the rectangular-shaped particles as well as the axisymmetric cylindrical- and spherical-shaped solid biomass particles, particularly the solution of the in-depth diffusion of heat. The first section also presents verification of the coupled Lagrangian-Eulerian interface through simulations of simplified configurations where analytical solutions of momentum and radiation exchange between the solid-phase and the gas-phase are obtained.

The second section presents first a calibration of the thermal degradation model using experimental data obtained from micro-scale Thermogravimetric Analysis (TGA) of cardboard and pine wood. The choice of cardboard is because the fire spread over laser-cut cardboard fuel beds has been studied experimentally at the Missoula Fire Sciences laboratory and there are measurements and observations that we can compare our simulations to. The choice of pine wood is because of the availability of bench-scale experimental measurements that can be used to evaluate

the PBR model for thermally-thick composition-thick samples that feature both pyrolysis and char oxidation, and also because pine wood has been studied in a similar work by Lautenberger and Fernandez-Pello [44].

In the third section of this chapter, we present an evaluation of the PBR model at a larger scale through simulations of a bench-scale cone-calorimeter experiment of a thick pine wood slab in an inert and oxidative environment. This allows us to evaluate the modeling capability to capture the pyrolysis and smoldering processes.

Lastly, we present in the fourth section a representative result of the in-depth degradation of a thick particle that features complete consumption and a transition from flaming to smoldering. We also discuss the issue of the particle's volume change during thermal degradation and its relationship to the input parameters of the model.

3.2 Verification tests

3.2.1 In-depth heat conduction of solid particles

We present here verification tests of the heat conduction in one-dimensional rectangular-, cylindrical- and spherical-shaped solid particles using the PBR code. In the case of rectangular-shaped particles, a 6 *cm* thick particle is exposed to ambient gas at 900 *K* and at a convective rate of 90 *W/m*²/*K*. In the case of cylindrical- and spherical-shaped particles, the radius of each particle is 1 *cm* and the particle is exposed to ambient gas at 900 *K* at a convective rate of 25.2 *W/m*²/*K*. All particles have a mass density of 663 *kg/m*³, a heat capacity of 2520 *J/kg/K* and a conductivity of 0.126 *W/m/K*. The simulations use a grid resolution of $\Delta\zeta = 100 \mu\text{m}$.

The particle's energy conservation is verified by comparing the temperature evolution inside the particles with the analytical solutions of heat conduction in a semi-infinite solid, a solid cylinder, and a solid sphere. The analytical solutions are listed in Table 3.1. Figures 3.1 and 3.2 show the temperature distributions inside the particle at different times obtained using the PBR solver (solid lines) and the analytical solution (symbols). The results show that the numerical model correctly resolves the time evolution of the temperature distribution inside the three different geometries considered.

Table 3.1: Analytical solutions of heat conduction inside solid fuel particles of different geometries, where $\tau = \alpha_s t / \zeta^2$, $\alpha_s = k_s / \rho_s c_s$, T_g the external gas temperature, and $T_{s,i}$ the initial particle temperature.

Geometry	Analytical solution [78]
Semi-infinite rectangle	$\frac{T_s - T_{s,i}}{T_g - T_{s,i}} = 1 - \text{erf}\left(\frac{\zeta}{2\sqrt{\alpha_s}}\right)$ $- \exp\left(\frac{h\zeta}{k_s} + \frac{h^2 \alpha_s}{k_s^2}\right) \left(1 - \text{erf}\left(\frac{\zeta}{2\sqrt{\zeta}} + \frac{h\sqrt{\alpha_s}}{k_s}\right)\right)$
Cylinder	$\frac{T_s - T_g}{T_{s,i} - T_g} = A_1 \exp(-\lambda_1^2 \tau) J_0\left(\frac{\lambda_1 \zeta}{R_p}\right), \quad \lambda_1 = 1.5995, \quad A_1 = 1.3384$
Sphere	$\frac{T_s - T_g}{T_{s,i} - T_g} = A_1 \exp(-\lambda_1^2 \tau) \frac{\sin\left(\frac{\lambda_1 \zeta}{R_p}\right)}{\frac{\lambda_1 \zeta}{R_p}}, \quad \lambda_1 = 2.0288, \quad A_1 = 1.4793$

3.2.2 Momentum exchange between the solid- and gas-phases

In this test, we consider an infinitely long fuel bed exposed to a stream-wise airflow at an initial velocity $u_0 = 10 \text{ m/s}$. The fuel bed is comprised of pine wood slabs with a bulk mass density of $\rho_{s,bulk} = 361 \text{ kg/m}^3$. The total number of particles

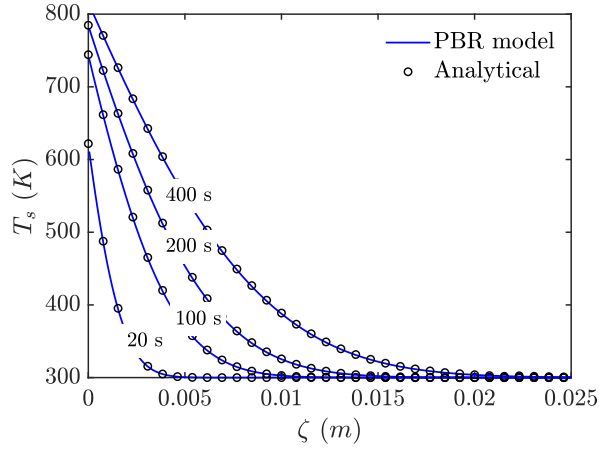


Figure 3.1: Temperature evolution inside a semi-infinite rectangular-shaped solid particle. The exposed surface is at $\zeta = 0$.

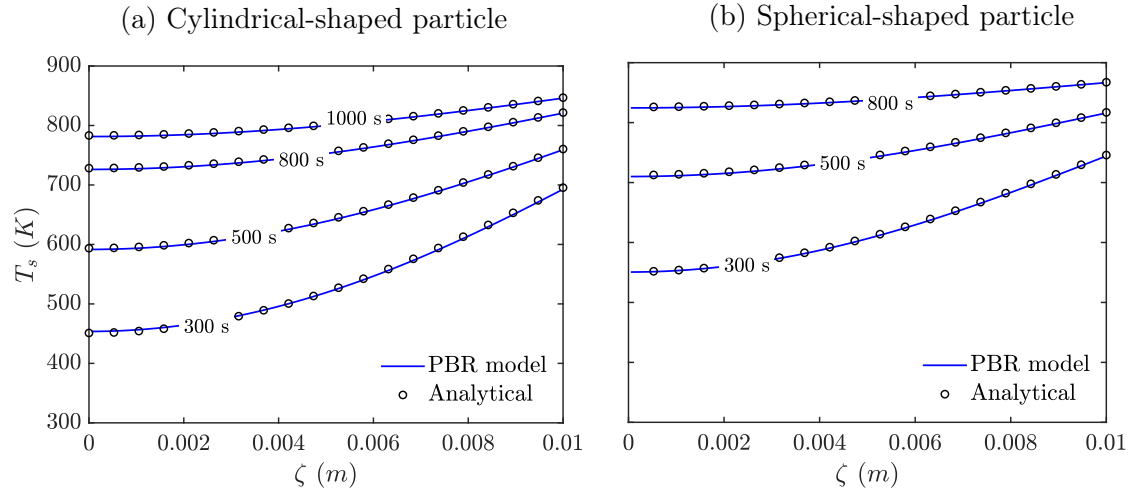


Figure 3.2: Temperature evolution inside a) cylindrical- and b) spherical-shaped solid particles. The exposed surface is at $\zeta = 0.01 \text{ m}$.

in the fuel bed is $N_p = 1000$. The particles are 10 mm thick with a surface area of 10 mm^2 . The particles are initially stationary but they are allowed to move due to the momentum exchange with the stream-wise flow. The drag coefficient of the particles is constant ($C_D = 10$).

If we ignore gravity and turbulence, the problem can be represented by a one-dimensional configuration (with activities in the streamwise direction and no activities in all the other directions). We use periodic boundary conditions in the streamwise direction to mimic an infinitely long fuel bed. Following the FDS Verification Guide [79], we can write the analytical solution of the unsteady momentum equations of the gas and the particles as follows:

$$\begin{aligned}\tilde{u} &= u_p + \frac{u_0}{1 + C_1 u_0 t} \\ u_p &= \frac{1}{2} \frac{C_2}{C_1} \left(u_0 - \frac{u_0}{1 + u_0 C_1 t} \right)\end{aligned}\quad (3.1)$$

where

$$C_1 = \frac{1}{2} \left(\frac{N_p C_D A_p^*}{V_p} + C_2 \right), \quad C_2 = \frac{\bar{\rho} C_D A_p^*}{m_s} \quad (3.2)$$

Figure 3.3 presents a comparison between the numerical simulations and the analytical solution in terms of the velocity and the momentum of the solid and the gas-phases. The plots show that the simulations are able to correctly predict the analytical solution. As shown in Fig. 3.3a, the solid particles' velocity increases with time due to the momentum exchange with the gas-phase, while the gas-phase velocity decreases. As time goes by, the solid particles achieve a steady state velocity equal to $\frac{1}{2}(C_2/C_1)u_0$. Figure 3.3b shows that despite the momentum exchange, the total momentum of the system (i.e., the solid particles + gas-phase) is conserved at a constant amount. In conclusion, this verification case shows the capability of the PBRFoam solver to model moving solid particles such as showers of embers and firebrands.

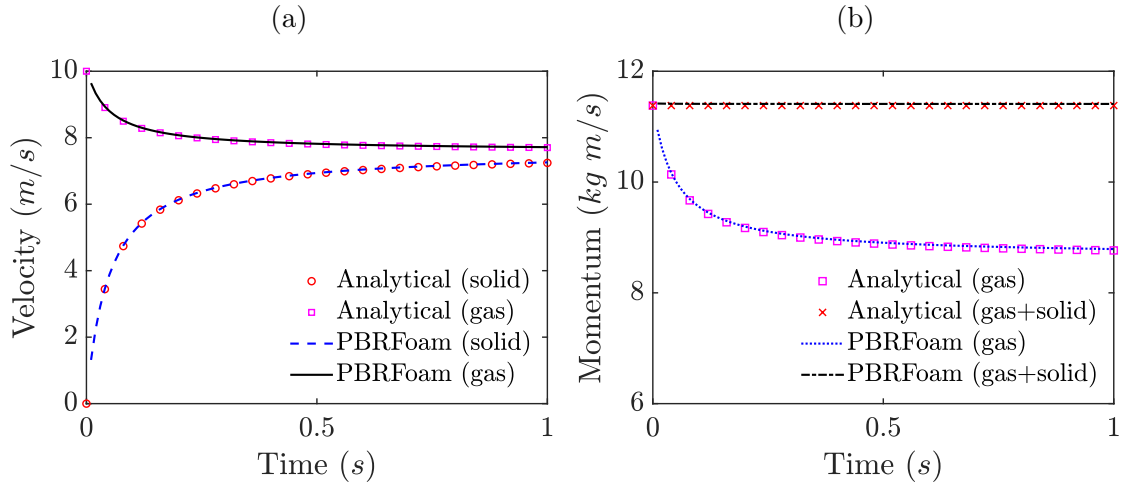


Figure 3.3: Simulations (solid lines) and analytical solution (symbols) of the momentum exchange between solid and gas-phases: a) transient velocity of the solid and the gas-phases, b) momentum of the gas-phase and total momentum of the system (gas+solid).

3.2.3 Pressure-velocity coupling inside the fuel bed

This verification test aims at verifying the pressure variation inside the fuel bed due to the change in the gas flow velocity associated with the fuel bed drag. We consider a 4 m long tunnel with an arbitrary width and height. The stream-wise velocity in the tunnel is $u_\infty = 5\ m/s$. A 1 m long fuel bed comprised of pine wood cylinders packed at $\beta_s = 0.0031$ is placed at the center of the tunnel. The pine wood cylinders have a 1 mm radius, and a drag coefficient of $C_D = 2$.

Let us ignore gravity and variations in the lateral directions. Then the system can be treated as one-dimensional, and the analytical solution of the gas-phase

momentum equations yields a pressure gradient of

$$\frac{d\bar{p}}{dx} = -\frac{1}{2}\bar{\rho} C_D C_A \beta_s \sigma_p u_\infty^2 \quad (3.3)$$

A comparison between the simulations and the analytical solution of the pressure variation inside the fuel bed is presented in Fig. 3.4. The graph shows simulation results obtained using a coarse and a fine grid resolution of the multiphase fuel bed: 10 cm and 5 cm, respectively. The results of the coarse grid resolution show a slight deviation from the analytical solution in the gauge pressure upstream of the fuel bed. The maximum error in the gauge pressure at this grid resolution is 6%. The finer grid resolution is able to predict the pressure variation with a maximum error of only 2%. These results suggest that the pressure-velocity coupling may require a careful design of the fine computational grid to minimize the numerical errors.

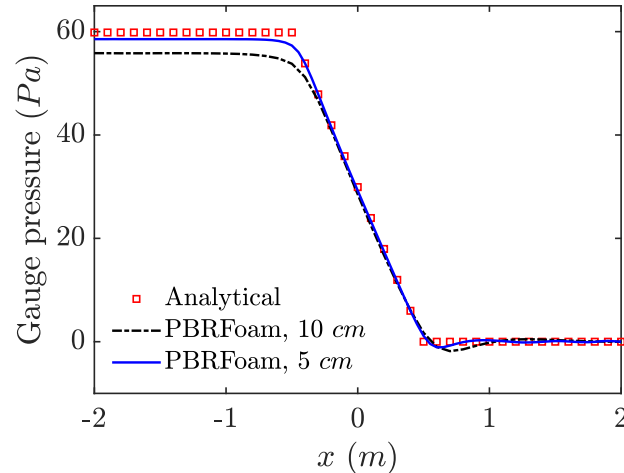


Figure 3.4: Comparison between simulations with different grid resolutions (solid lines) and the analytical solution (symbols) of the pressure variation inside a fuel bed.

3.2.4 Radiation absorption and emission inside the fuel bed

The absorption and emission of thermal radiation inside the multiphase fuel bed are very critical in wildland fire phenomena such as during flameless smoldering propagation where the dominant source of heat transfer is through particle-to-particle radiation. This verification case aims at evaluating the ability of the MRTE (Eq. 2.81) to correctly calculate the variation of the radiation intensity inside the fuel bed due to absorption and emission effects.

Let us assume a one-dimensional domain that has a length of 4 m . A 1 m long fuel bed is centered at the center of the domain (i.e., at $x = 0$). The fuel bed is comprised of 1 mm spherical particles with surface emissivity $\epsilon_{p,surf} = 0.757$. For simplicity, the particles are treated as passive objects that do not heat up nor thermally degrade (i.e., the particle's temperature and composition are constant). Also, the absorption and emission of the gas-phase are ignored.

First, we consider a case where the solid particles absorb thermal radiation from an external source. We assume that one of the boundaries of the domain is a black body that emits radiation at $T_0 = 1273\text{ K}$, while the other boundary is a black body at 0 K . We fix the temperature of the solid particles and the background gases at 0 K . We pack the particles at different packing ratios to check their effect on radiation absorption. The largest packing ratio that we consider is $\beta_s = 0.004$, which corresponds to a radiation length-scale of $\sim 0.44\text{ m}$. The analytical solution

of the MRTE under these conditions is

$$I(x) = I_0 \exp\left(-\frac{\kappa_s \Omega}{J} x\right) \quad (3.4)$$

where $I_0 = \sigma T_0^4 / \pi$, $\Omega = 2\pi$ and $J = \Omega$.

A comparison between this analytical solution and the numerical solution of the MRTE obtained using a range of grid resolutions (between 5 and 50 cm) is shown in Fig. 3.5. Figure 3.5a shows the change of the radiation intensity behind the fuel bed (i.e. at $x = 0.5m$) at different packing ratios. As indicated in the analytical solution, the radiation intensity behind the fuel bed decreases with the increase of the packing ratio due to an increased radiation absorption by the solid particles. The results of the simulations conducted with fine grid resolution show very good agreement with the analytical solution. Simulations with coarser grid resolution (20 and 50 cm) show some deviation from the analytical solution. The maximum deviation occurs with the 50 cm grid resolution in the highest packing ratio ($\beta_s = 0.004$) where the radiation length-scale is comparable to the grid resolution. The axial profile of the radiation intensity at this packing ratio is shown in Fig. 3.5b. It is clearly seen that the 50 cm resolution under-resolves the radiation intensity profile leading to the largest error in the radiation intensity behind the fuel bed. We conclude that a grid resolution of 10 – 20 cm is appropriate to resolve the radiation intensity variation inside the fuel bed for different packing ratios up to $\beta_s = 0.004$.

We now consider a case where the fuel bed emits and self-absorbs thermal radiation at the same time. We set the surface temperature of the particles at $T_{p,surf} = 1000 K$, and we set the boundaries of the domain at 0 K. Again, the

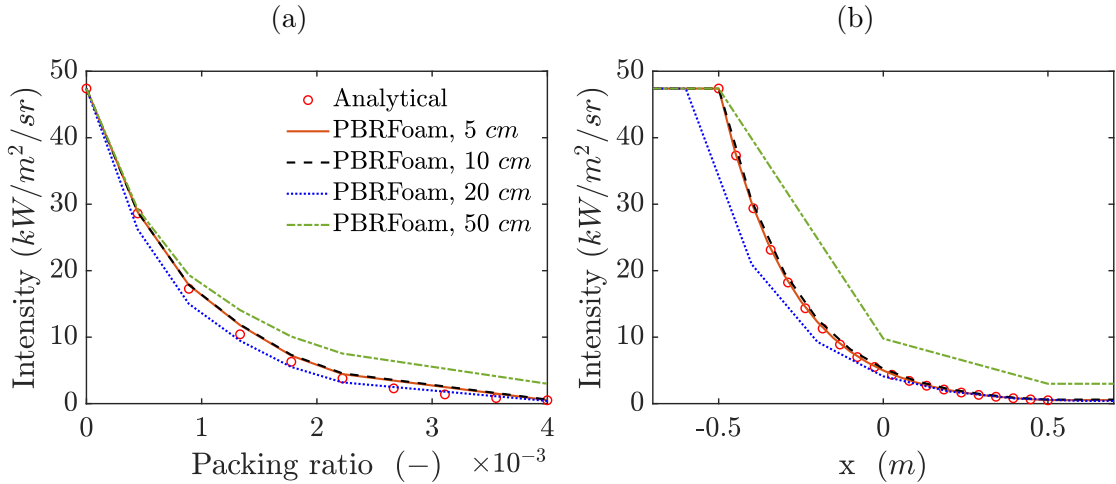


Figure 3.5: Simulations with different grid resolutions (solid lines) and analytical solution (symbols) of the radiation absorption by the fuel bed: a) radiation intensity variation with different packing ratios, b) spatial variation of the radiation intensity along the fuel bed length.

particles are not allowed to thermally degrade and their temperature is kept constant.

In this case, the analytical solution of the MRTE is

$$I(x) = \frac{\sigma T_{p,surf}^4}{\pi} \left(\exp\left(\frac{\kappa_s \Omega}{J} x\right) - 1 \right) \exp\left(-\frac{\kappa_s \Omega}{J} x\right) \quad (3.5)$$

where $\Omega = 2\pi$ is the solid angle and $J = \pi$ is the magnitude of the direction vector.

Figure 3.6 shows the axial variation of the radiation intensity inside the fuel bed obtained from the analytical solution and the numerical simulation of this configuration. The emission contribution to the radiation intensity obtained from a case where absorption is neglected is also plotted in Fig. 3.6. The figure shows that the numerical simulation is able to correctly describe both emission and absorption and is matching the analytical solution. It can be seen from the results that the

emission contribution is linearly increasing with the axial direction inside the fuel bed due to the accumulation of radiation emission from each individual particle. However, due to self-absorption, the net radiation intensity shows much lower values in the axial direction. The net intensity reached behind the fuel bed is 4 times lower than the emission contribution. Note that in a real case of thermally degradable particles, the temperature of the particles is allowed to change to respond to thermal radiation. Thus, the net effect of the absorption and emission might be different from what is shown in this simple case.

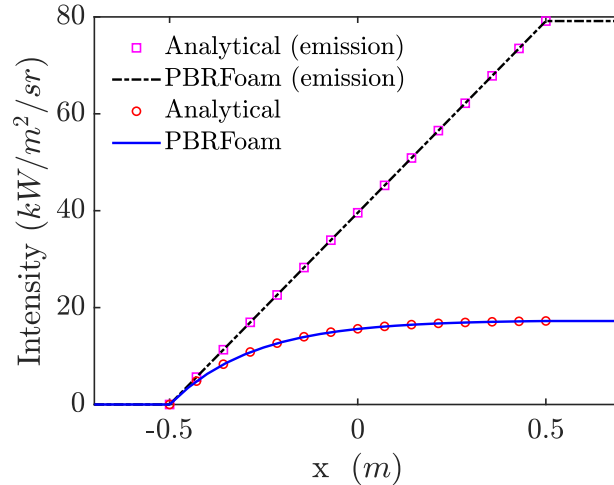


Figure 3.6: Spatial variation of the radiation intensity inside a fuel bed that emits and self-absorbs radiation. The solid lines refer to the numerical simulations, while the symbols refer to the analytical solution. The emission contribution obtained from a case where absorption is neglected is also shown.

3.2.5 Smoldering propagation due to radiation penetration

As an extension to the previous case, we simulate here an idealized case of smoldering propagation in a fuel bed made of charred pine wood sticks. The objective of this test case is to evaluate the ability of the radiation penetration inside the fuel bed (due to radiative emissions from glowing particles) to provide a self-sustained propagating smoldering front.

We consider here a 2-D computational domain that is 50 m long and 3 m high. A fuel bed is inserted at 2 m from the domain left side and extends to a length of 48 m . The fuel bed is comprised of cylindrical-shaped charred pine wood particles with a radius of 1 mm . The fuel bed height is $\delta_{bed} = 0.4 m$. The particles are distributed inside the fuel bed such that a packing ratio of $\beta_s = 0.005$ is achieved. The properties of the char, as well as the kinetics of the char oxidation reaction (R_{co}), are obtained from pine wood calibration shown later in this chapter.

The domain has initially stagnant air at ambient temperature. A wind is imposed from the left side of the domain at a speed of 1 m/s which supplies oxygen to the fuel bed at the ambient air level. The bottom of the domain is treated as an adiabatic no-slip wall. The top and the right boundaries are treated as open boundaries. Ignition is achieved using a 0.5 m long hot plate that is placed underneath the fuel bed and is activated for 10 seconds. The gas-phase radiation is deactivated as we focus here on the radiation penetration inside the fuel bed from particle to particle only.

Figure 3.7 shows the contours of the normalized particle mass, the mass fraction

of CO_2 produced from the char oxidation reaction, and the positive net radiative heat flux that indicates the heating zone. We see in Fig. 3.7a the smoldering reaction zone that converts all the charred particles into ash. This zone is driven solely by radiation from the hot particles to the unburned ones. The net radiative heat flux reaches $30\ kW/m^2$ in the preheat zone upfront of the smoldering zone.

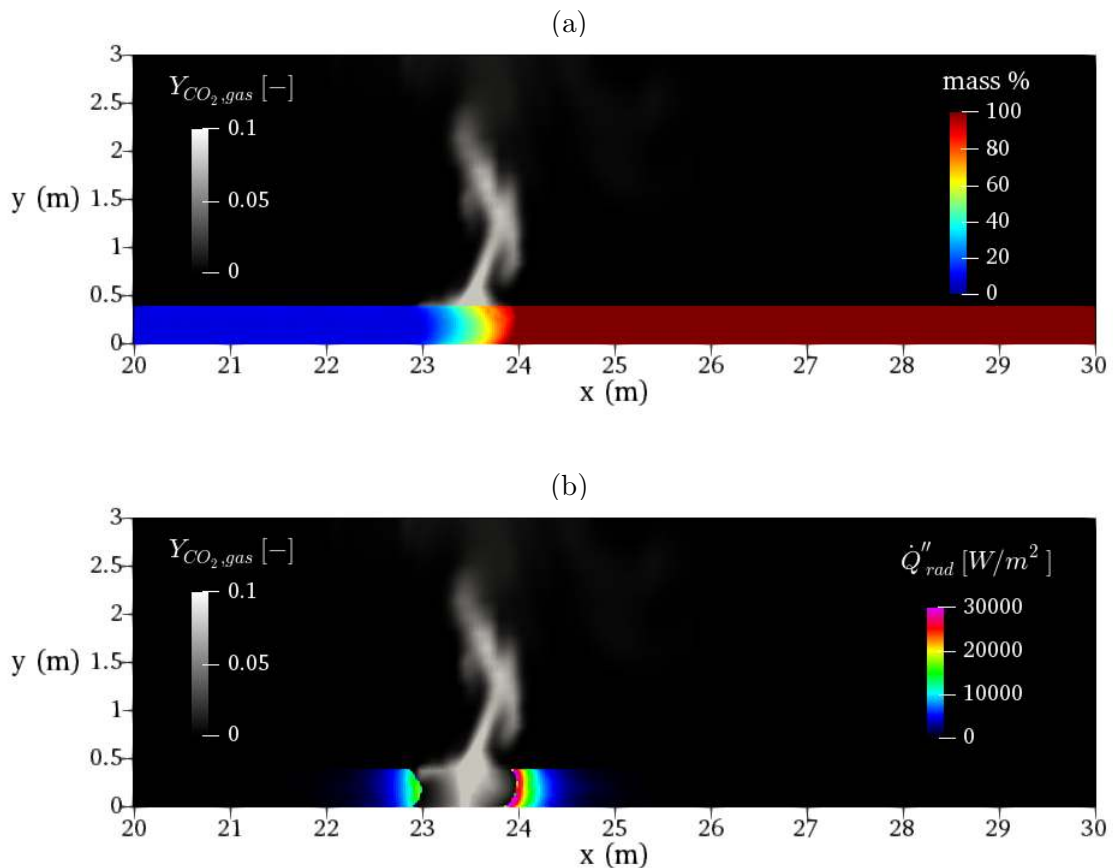


Figure 3.7: Smoldering propagation in idealized charred pine wood bed. The gas-phase is colored by the mass fraction of CO_2 . The fuel bed is colored by a) the percentage mass with red indicating 100% char and blue indicating 100% ash, b) the positive net radiative heat flux indicating heating zones.

The rate of spread of this reaction zone and its intensity are shown in Fig. 3.8. These plots show that the model is able to achieve a steady rate of spread of the smoldering zone $ROS_{smoldering}$ with the absence of any external heat source, and the model is able to transfer some of the heat released from the exothermic oxidative reaction (Rco) to the unburned charred particles through radiation. The model estimates the smoldering rate of spread as $ROS_{smoldering} = 0.096 \text{ m/s}$. Figure 3.8 also shows that a mean intensity of $\dot{Q}'_{smoldering} = 491 \text{ kW/m}$ is achieved. Using Byram's expression, the theoretical intensity of the smoldering fire can be calculated from:

$$\dot{Q}'_{theoretical} = m''_{fuel} \times ROS_{smoldering} \times \Delta H_{Rco} \quad (3.6)$$

where m''_{fuel} is the combustible fuel loading calculated from

$$m''_{fuel} = (1 - \eta_{ash}) \times \rho_p \times \beta_s \times \delta_{bed} \quad (3.7)$$

The theoretical intensity estimated from the above expression is $\dot{Q}'_{theoretical} = 487 \text{ kW/m}^2$. The difference between the simulated intensity and the one estimated using Byram's expression is 0.8% which is acceptable.

3.3 Calibration of the thermal degradation model

3.3.1 Micro-scale thermal degradation of pine wood

The chemical kinetic parameters and the material properties of pine wood have been calibrated previously by Lautenberger and Fernandez-Pello [44] using optimization techniques to fit bench-scale experimental measurements of thick samples.

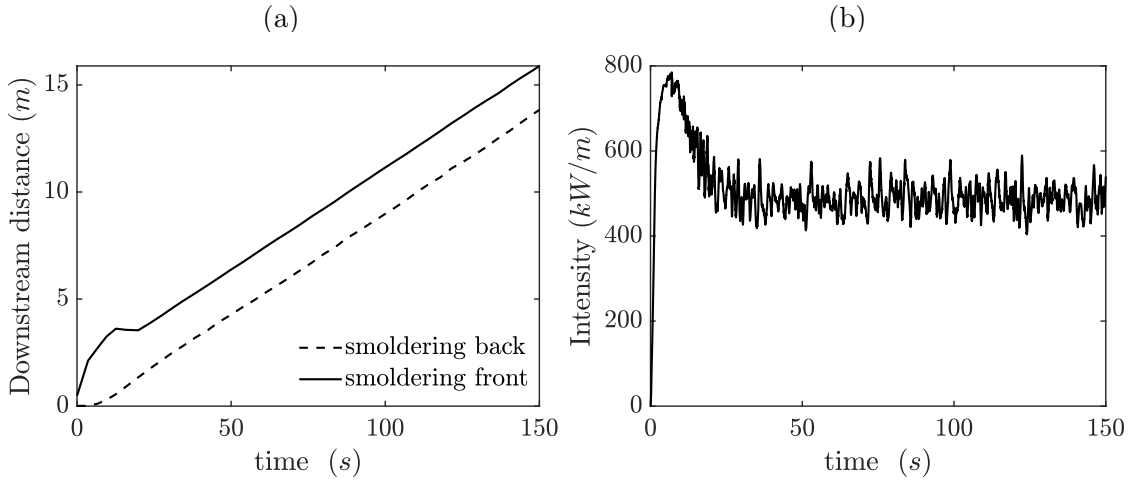


Figure 3.8: Smoldering propagation in idealized charred pine wood bed: a) time evolution of the back and front edges of the smoldering zone; b) smoldering intensity.

However, it is not known whether the chemical kinetic parameters of the pyrolysis and oxidative reactions R_p - R_{co} are able to reproduce the behavior of micro-scale samples similar to that obtained in TGA measurements. We evaluate in this section these chemical kinetic parameters using micro-scale simulations of the TGA experiments.

In the TGA experiments, a micro-scale particle is placed inside a well-controlled enclosure that heats at a controlled rate. The heat transfer to the micro-scale particle is infinitely fast such that the temperature of the enclosure and the temperature of the particle are in equilibrium. The mass of the particle, the temperature of the enclosure, and the released volatiles are monitored in these techniques. In order to simulate these experiments, we consider a thin rectangular particle with a thickness of $20 \mu m$ that is exposed to convective heating with $h = 10^5 W/m^2/K$. We impose an external gas temperature that increases linearly in time at a rate obtained from the experimental setup. We consider an initial moisture of about 2% of the initial

particle mass.

We first performed simulations using the PBR model with the input parameters of Ref. [44] to check the model predictions of the micro-scale measurements of pine wood samples conducted by Anca-Couce et al. [80]. Figure 3.9a shows a comparison between the mass loss rates predicted using the PBR model with the chemical kinetic parameters of Lautenberger and Fernandez-Pello [44] against the experimental data of Anca-Couce et al. [80] obtained at two heating rates of 5 and 10 K/min in nitrogen environments. A similar comparison at a heating rate of 10 K/min but in two oxidative environments with oxygen concentrations of 4.3 % O_2 and 20.5 % O_2 is shown Fig. 3.9b. The data shown in Figs. 3.9a and 3.9b show that there is a large discrepancy between the model predictions and the experimental measurements which suggests that the kinetic parameters of Ref. [44] can not describe thermal degradation of pine wood at micro-scale.

We also performed a similar set of simulations but with the chemical kinetic parameters of the pyrolysis and oxidative reactions (i.e., R_p , R_{op} and R_{co}) taken from Ref. [80] while keeping the drying reaction and the material properties of pine wood similar to those of Ref. [44]. The results in Figs. 3.10a show that the pyrolysis reaction (R_p) achieves much better agreement with the experiments at the two simulated heating rates than that obtained using the kinetics of Ref. [44]. A similar comparison at a heating rate of 10 K/min but in two oxidative environments with oxygen concentrations of 4.3 % O_2 and 20.5 % O_2 is shown in Fig. 3.10b. The calibrated model results show a very good agreement with experimental data in the temperature range where the pyrolysis reaction (R_p) is still dominating (i.e., 450 -

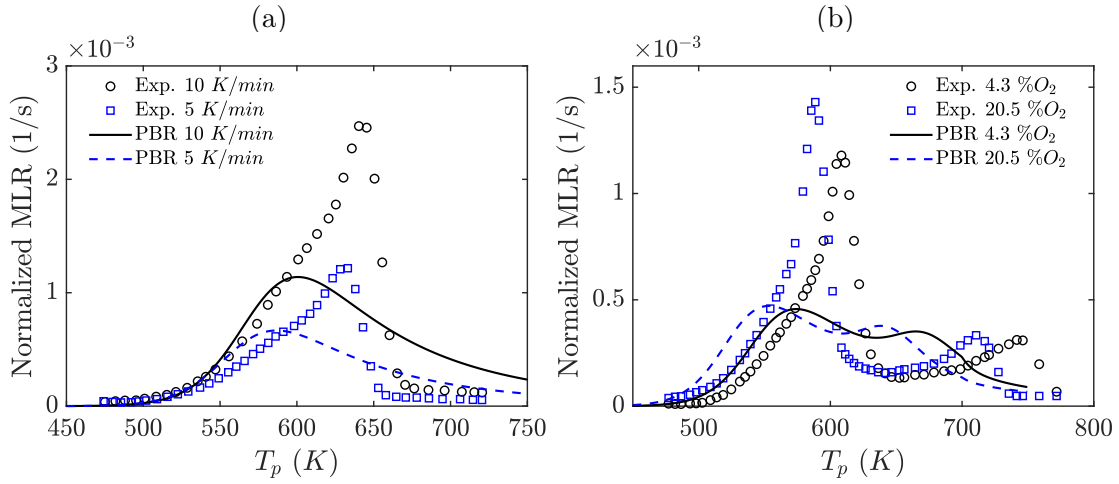


Figure 3.9: Variation of the mass loss rate of a micro-scale pine wood sample with the particle temperature at a) heating rates of 5 and 10 K/min in the inert environment; and b) heating rate of 10 K/min in oxidative environments. Lines: PBR simulations using the kinetic parameters of Lautenberger and Fernandez-Pello [44]. Symbols: the TGA measurements of Ref. [80].

600 K). The calibrated model results show a deviation from experimental data in the temperature range between 600 and 650 K where some intermediate reaction steps may exist before the temperature range 700-800 K where the agreement between the simulations and the experimental data improves.

This calibration exercise shows that the baseline choice of the kinetic parameters of the pyrolysis and oxidative reactions is not adequate at the micro-scale despite showing good results at bench-scale simulations as presented in Ref. [44]. Therefore, to avoid such discrepancies between micro- and bench-scale tests, we decide to use the kinetics of Ref. [80]. A summary of the calibrated model parameters for pine wood simulations is provided in Tables 3.2 and 3.3.

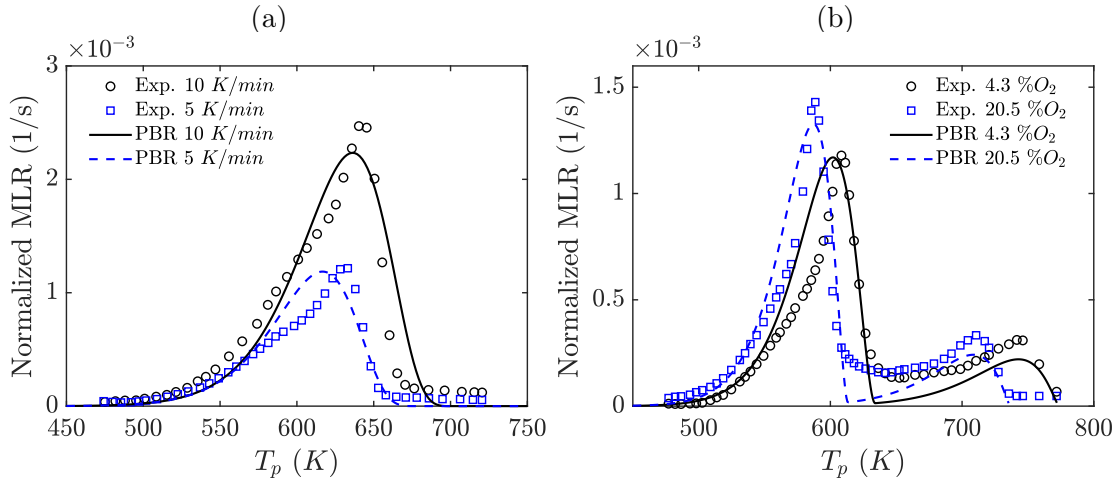


Figure 3.10: Variation of the mass loss rate of a micro-scale pine wood sample with the particle temperature at a) heating rates of 5 and 10 K/min in the inert environment; and b) heating rate of 10 K/min in oxidative environments. Lines: PBR simulations using the kinetic parameters of Anca-Couce et al. [80]. Symbols: the TGA measurements of Ref. [80].

3.3.2 Micro-scale thermal degradation of cardboard

To calibrate the PBR model for cardboard, we consider here the experiments of McKinnon et al. [81] and Semmes et al. [82] that were performed on micro-scale cardboard samples using TGA and DSC techniques. In order to obtain the chemical kinetic parameters of the pyrolysis and oxidative reactions (R_p , R_{op} , and R_{co}) corresponding to cardboard, we attempt to utilize the Sequential Quadratic Programming (SQP) algorithm to perform a constrained nonlinear optimization [83] to achieve the best fit to the TGA data. We consider the chemical kinetic parameters of the moisture evaporation process to be independent of the solid particle material,

Table 3.2: Calibrated model parameters for pine wood.

Property	Value	Reference
$\rho_{ds,bulk}$ (kg/m^3)	361	[50]
ψ_{ds} (-)	0.0744	[50]
c_{ds} ($J/kg/K$)	$1664(T_p/300)^{0.66}$	[50]
k_{ds} ($W/m/K$)	$0.176(T_p/300)^{0.594}$	[50]
γ_{ds} (m)	0	[50]
ϵ_{ds} (-)	0.759	[50]
K_{ds} (m)	10^{-10}	[50]
$\rho_{c,bulk}$ (kg/m^3)	73	calculated ($\eta_c = 0.2022$)
ψ_c (-)	0.8128	calculated ($= 1 - \rho_{c,bulk}/\rho_s$)
c_c ($J/kg/K$)	$1219(T_p/300)^{0.283}$	[50]
k_c ($W/m/K$)	$0.065(T_p/300)^{0.435}$	[50]
γ_c (m)	3.3×10^{-3}	[50]
ϵ_c (-)	0.957	[50]
K_c (m)	10^{-10}	[50]
$\rho_{a,bulk}$ (kg/m^3)	5.7	calculated ($\eta_a = 0.07808$)
ψ_a (-)	0.9854	calculated ($= 1 - \rho_{a,bulk}/\rho_s$)
c_a ($J/kg/K$)	$1244(T_p/T)^{0.315}$	[50]
k_a ($W/m/K$)	$0.058(T_p/300)^{0.353}$	[50]
γ_a (m)	6.4×10^{-3}	[50]
ϵ_a (-)	0.955	[50]
K_a (m)	10^{-10}	[50]

Table 3.3: Calibrated chemical kinetic parameters for pine wood.

Reaction	A (s^{-1})	E_a (J/mol)	n (-)	n_{O_2} (-)	ΔH (kJ/kg)
<i>Rd</i>	4.29×10^3	43.8×10^3	0.99	0	-2410
<i>Rp</i>	2.1878×10^6	105×10^3	0.87	0	-533
<i>Rop</i>	524.8075×10^6	127×10^3	0.63	0.72	994
<i>Rco</i>	3.5481×10^6	124×10^3	0.56	0.68	37700

and we take the kinetics of the drying reaction Rd from Ref. [50].

Following the work of Fiola et al. [84], we aim to minimize the following error:

$$\text{Error} = \frac{0.6}{\text{MLR}_{\max,\text{exp}}} \sqrt{\frac{\sum_i^N (\text{MLR}_{i,\text{exp}} - \text{MLR}_{i,\text{PBR}})^2}{N}} + \frac{0.4}{m_{\max,\text{exp}}} \sqrt{\frac{\sum_i^N (m_{i,\text{exp}} - m_{i,\text{PBR}})^2}{N}} \quad (3.8)$$

where MLR_{exp} and MLR_{PBR} are the mass loss rate obtained from the experimental TGA data and the PBR model, respectively, and where $m_{i,\text{exp}}$ and $m_{i,\text{PBR}}$ are their corresponding mass.

We first conducted the minimization process of Eq. 3.8 using simulations in an inert environment to obtain the chemical reaction parameters of thermal pyrolysis reaction (Rp). Then, we use these reaction parameters to conduct a second minimization of Eq. 3.8 but using simulations conducted in oxidative environments to obtain the chemical parameters of the oxidative reactions (Rop) and (Rco). Thermo-physical properties of cardboard used in the optimization process are listed in Table 3.4. The calibrated values of the chemical kinetic parameters for the thermal degradation of cardboard are listed in Table 3.5.

The results of thermal degradation of micro-scale cardboard particles under a heating rate of 10 K/min , obtained using the proposed chemical kinetic parameters are presented in Fig. 3.11. Figure 3.11a shows the time evolution of the particle's mass and mass loss rate normalized by the initial mass due to thermal pyrolysis in an inert environment. The model shows a very good agreement with the experimental

Table 3.4: Thermo-physical properties of cardboard.

Property	Value	Reference
$\rho_{ds,bulk}$ (kg/m^3)	520	[81, 82]
ψ_{ds} (-)	0.0744	[50]
c_{ds} ($J/kg/K$)	1800	[81, 82]
k_{ds} ($W/m/K$)	0.1	[81, 82]
γ_{ds} (m)	0	[50]
ϵ_{ds} (-)	0.7	[81, 82]
K_{ds} (m)	10^{-10}	[50]
$\rho_{c,bulk}$ (kg/m^3)	104	calculated ($\eta_c = 0.2$)
ψ_c (-)	0.8149	calculated ($= 1 - \rho_{c,bulk}/\rho_s$)
c_c ($J/kg/K$)	1300	[81, 82]
k_c ($W/m/K$)	$0.00405(T_p/300)^{0.3}$	[81, 82]
γ_c (m)	3.3×10^{-3}	[50]
ϵ_c (-)	0.85	[81, 82]
K_c (m)	10^{-10}	[50]
$\rho_{a,bulk}$ (kg/m^3)	21.6944	calculated ($\eta_a = 0.2086$)
ψ_a (-)	0.9614	calculated ($= 1 - \rho_{a,bulk}/\rho_s$)
c_a ($J/kg/K$)	1300	[81, 82]
k_a ($W/m/K$)	$0.00405(T_p/300)^{0.3}$	[81, 82]
γ_a (m)	6.4×10^{-3}	[50]
ϵ_a (-)	0.85	[81, 82]
K_a (m)	10^{-10}	[50]

Table 3.5: Chemical kinetic parameters for thermal degradation of cardboard.

Reaction	A (s^{-1})	E_a (J/mol)	n (-)	n_{O_2} (-)	ΔH (kJ/kg)
<i>Rd</i>	4.29×10^3	43.8×10^3	0.99	0	-2410
<i>Rp</i>	1.2589×10^8	12.086×10^4	1.617	0	-210
<i>Rop</i>	1.2885×10^{12}	16.3901×10^4	2.0	0.7839	0
<i>Rco</i>	1.1168×10^{49}	66.9432×10^4	1.049	2.0	32900

data of McKinnon et al. [81] with a maximum deviation of 5%, calculated using Eq. 3.8. Figure 3.11b shows the particle response to the presence of oxygen at 10% concentration. The first peak in the MLR curve corresponds to thermal pyrolysis, while the second peak corresponds to oxidative reactions (R_{op} and R_{co}). The second peak is comparable to the first peak but occurs in a much narrower temperature range which indicates the stiffness of the oxidative reactions. Overall, the model is able to predict the experimental data of Semmes et al. [82] within 6% deviation according to Eq. 3.8.

Figure 3.12 shows a comparison between the PBR predictions of the particle's heat flow (the energy transferred to the particle as a function of the heat capacity and the heat of reactions) and the DSC experimental measurements of McKinnon et al. [81] obtained at a heating rate of 10 K/min in nitrogen. The discrepancy between the experimental data and the simulations from 300 to 350 K is attributed to the transient heating rate which ramps from 0 to 10 K/min in a finite time. There is a very good agreement in the heat flow between 400 K and 500 K , but there is a shift of $\approx 50 K$ in the peak heat flow which is deemed acceptable. Note that our thermal pyrolysis reaction (R_p) is endothermic, therefore, the slight dip in the heat flow at the end of the pyrolysis process is not accounted for.

3.4 Evaluation of the PBR model against bench-scale experiments

We aim here to evaluate the PBR model through simulations of bench-scale thermally-thick composition-thick pine wood particles. These simulations correspond

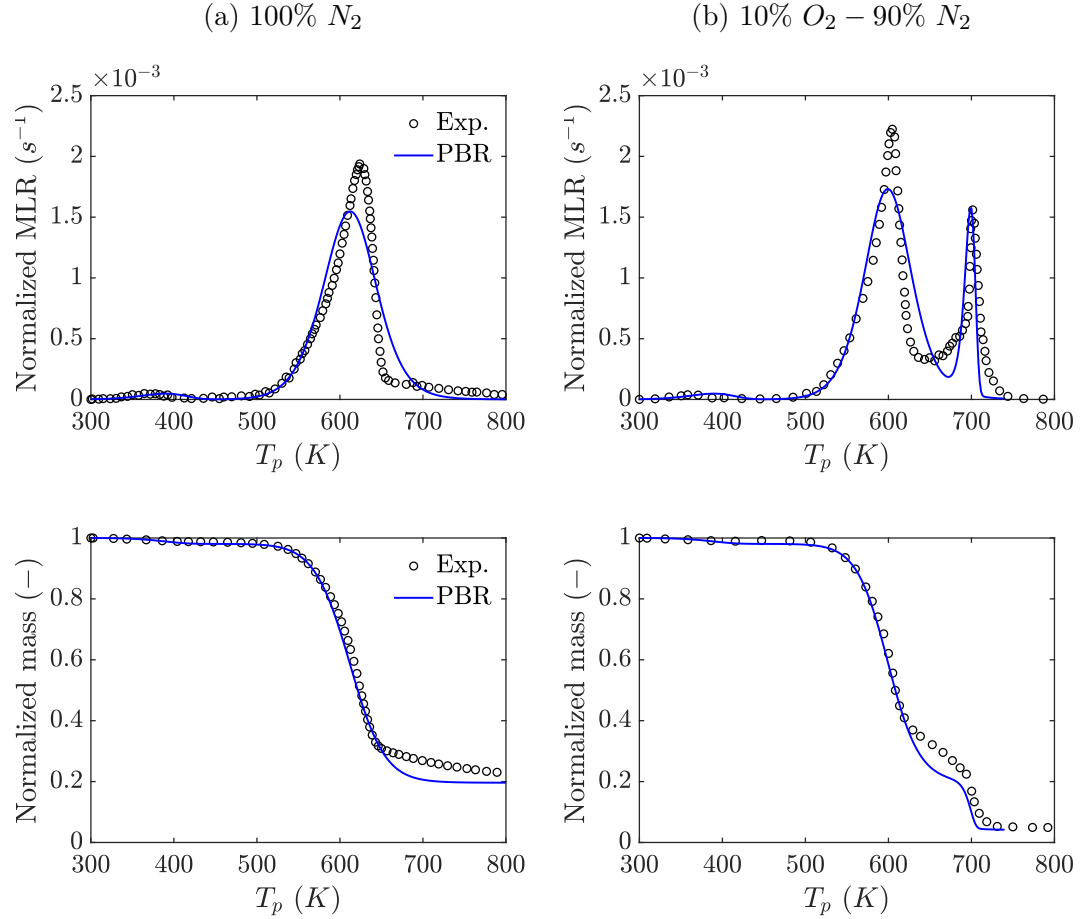


Figure 3.11: Evolution of the cardboard particle normalized mass loss rate (top row) and normalized mass (bottom row) with temperature. Comparison of the simulated thermal degradation of cardboard using the calibrated PBR model (solid lines) and the TGA measurements of Refs. [81, 82] (symbols) at a heating rate of 10 K/min in a) 100% N_2 environment, b) 10% O_2 – 90% N_2 .

to the experiments of Kashiwagi et al. [85]. In these simulations, a 3.8 cm thick pine wood slab is placed in a well-controlled environment at different nitrogen-oxygen concentrations of (100% N_2 – 0% O_2), (80% N_2 – 10% O_2) and (79% N_2 – 21% O_2). The particle's top surface is exposed to different irradiation intensities (25 and

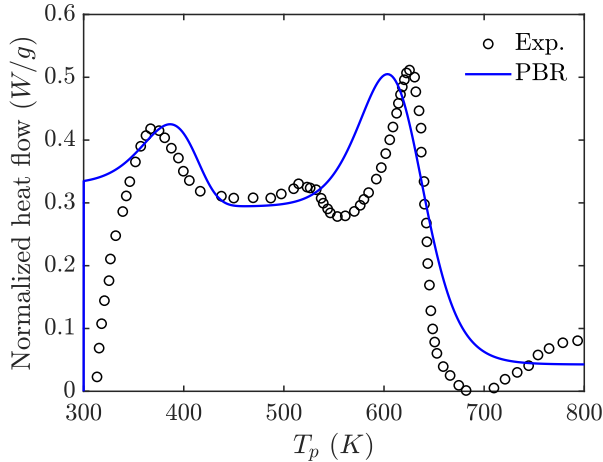


Figure 3.12: Comparison of the simulated heat flow (solid line) and the DSC measurements of Ref. [81] collected at a heating rate of $10\text{ K}/\text{min}$ in an inert environment.

40 kW/m^2), while the particle's bottom surface is isolated. The flow speed around the particle is estimated to be 1 m/s , which results in a convective transfer rate of $\approx 12\text{ W/m}^2/\text{K}$ estimated by the convective heat transfer model presented in section 2.4.

Figures 3.13a and 3.13b present a comparison between the simulated and measured mass loss rates of the particle at irradiation intensities of 25 and 40 kW/m^2 , respectively. Each of the two figures reveals a significant effect of oxygen present on the MLR, which results in an increase in the MLR of about 2 to 4 times when moving from a nitrogen environment to an air environment. This increase in the MLR is due to two factors. First, the increase in the particle temperature due to exothermic oxidative reactions promotes the rate of the consumption of the dry solid mass due to thermal pyrolysis reaction (R_p). Then, the oxidative reactions (R_{op}

and R_{co}) allow for additional consumption of the particle's char mass resulting in an overall increase in the total mass loss rate.

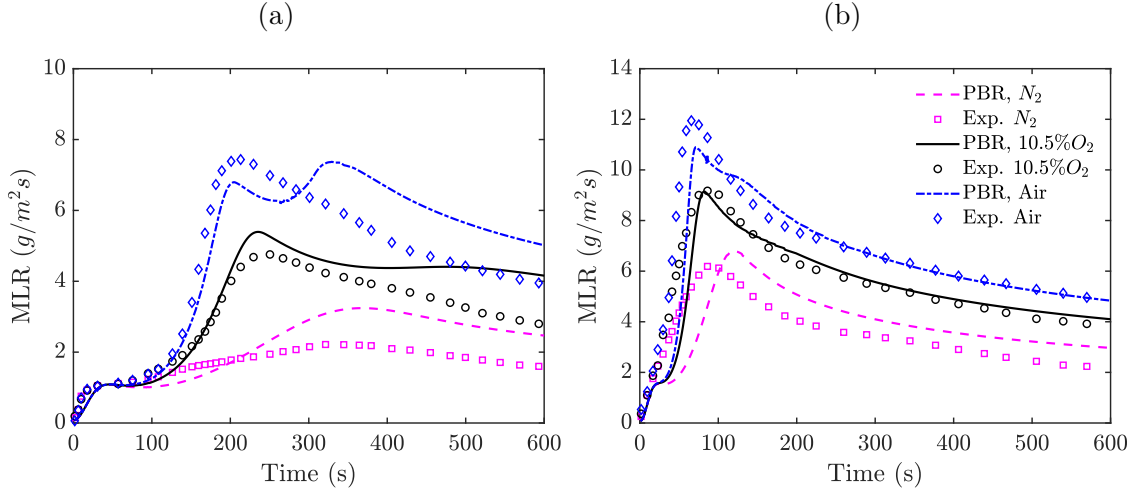


Figure 3.13: Time evolution of the mass loss rate of the 3.8 cm pine wood particle in inert and oxidative environments at a) 25 kW/m^2 and b) 40 kW/m^2 irradiation. Comparison between simulations of the PBR model (lines) and experimental data of Kashiwagi et al. [85] (symbols).

Figures 3.13a and 3.13b suggest that the PBR is able to very well capture the increase in the MLR associated with the presence of oxygen. The simulation results show an acceptable agreement with the experimental measurements in the case of low irradiation intensity (25 kW/m^2) despite some quantitative differences. A much better agreement is achieved at the higher irradiation intensity (40 kW/m^2). Some of the discrepancies between the simulated and measured results are attributed to uncertainties associated with the complexity of the flow conditions around the particle rather than the chemical kinetics of the reactions. These conditions are responsible for convective cooling at the surface of the particle as well as the diffusion of oxygen

into the particle. We believe that the flow condition may have less impact on the particle's behavior at high irradiation intensities rather than at lower irradiation intensities due to the quick response of the particle to high heating conditions.

The time variation of the temperature at the particle's exposed surface, and at 5 mm and 10 mm below the exposed surface is monitored during the thermal degradation process. Figure 3.14 shows the simulated and measured temperatures in the case of an irradiation intensity of 40 kW/m^2 and under different environments. First, the plots show a very good agreement between the simulations and the experimental measurements. Second, we can see a large difference in the temperature at the three considered locations during the entire duration which indicates that the particle is thermally-thick. Also, the overall temperature at the three locations is seen to increase steadily when moving from the nitrogen environment to the air due to the heat generated from the oxidative reactions. The peak temperature achieved in the nitrogen environment is $\sim 800\text{ K}$, while the peak temperature achieved in the air is $\sim 950\text{ K}$. Figure. 3.15 shows a similar comparison at an irradiation intensity of 25 kW/m^2 . The simulated particle temperatures still show very good agreement with experimental data at this heating condition. Note that there are changes in the slope of the time variation of the temperature in both the experimental measurements and the simulations presented in Figs. 3.14 and 3.15. These changes are due to the thermal degradation process and its corresponding changes in the composition and the thermophysical properties of the solid.

We end this section with a verification check of the grid resolution choice. Figure 3.16 presents the MLR and the 5 mm depth temperature obtained using

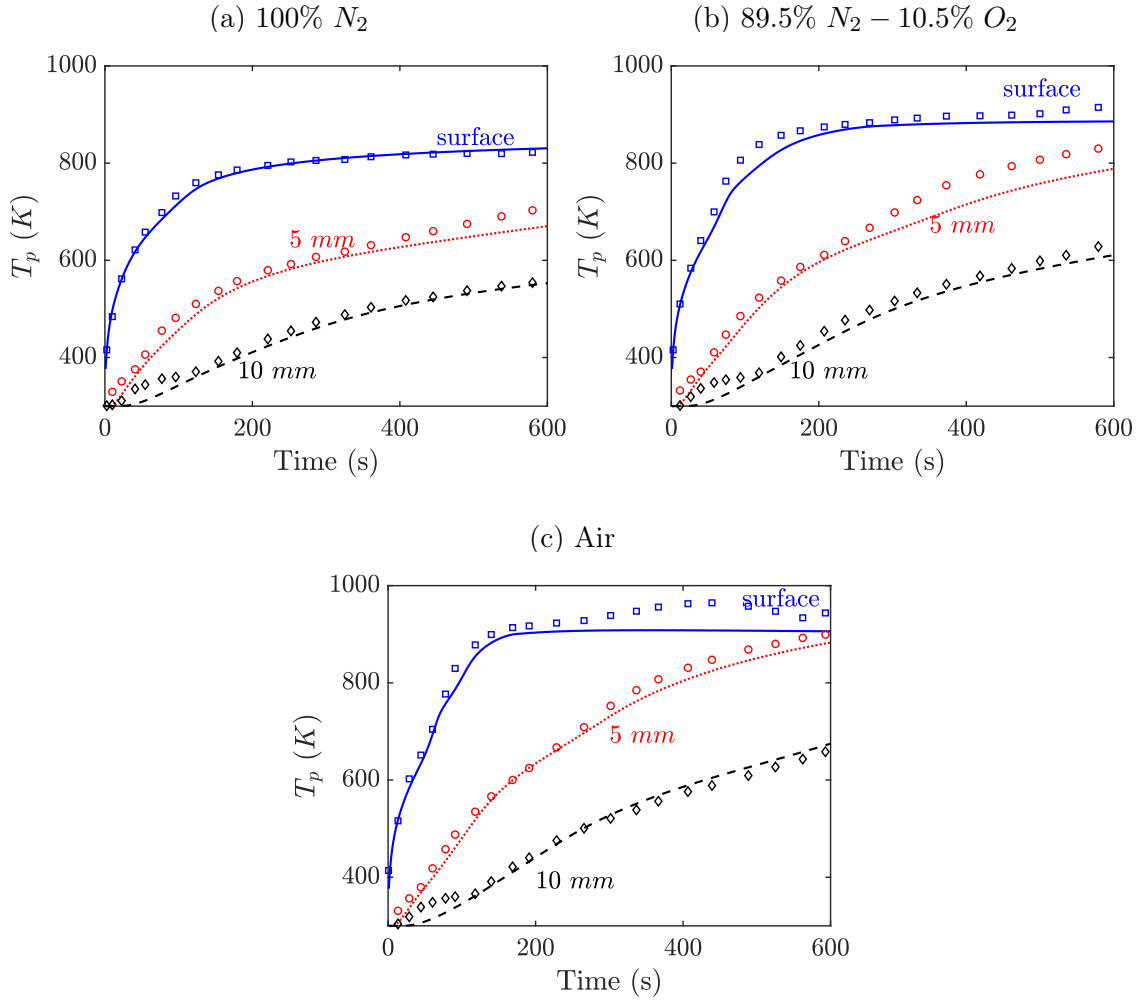


Figure 3.14: Spatial variation of exposed surface and in-depth temperatures of the 3.8 cm pine wood particle at 40 kW/m^2 irradiation in: a) 100% N_2 , b) 89.5% N_2 – 10.5% O_2 , and c) air. Comparison between simulations from the PBR model (lines), experimental data of Kashiwagi et al. [85] (symbols).

simulations with three grid resolutions: $20 \mu\text{m}$, $100 \mu\text{m}$ and $500 \mu\text{m}$. The number of grid cells corresponding to these resolutions is 1900, 380, and 76 cells, respectively. We do not observe any significant difference between the results of the 20 and $100 \mu\text{m}$ resolutions. However, the results of the $500 \mu\text{m}$ show numerical oscillations in the

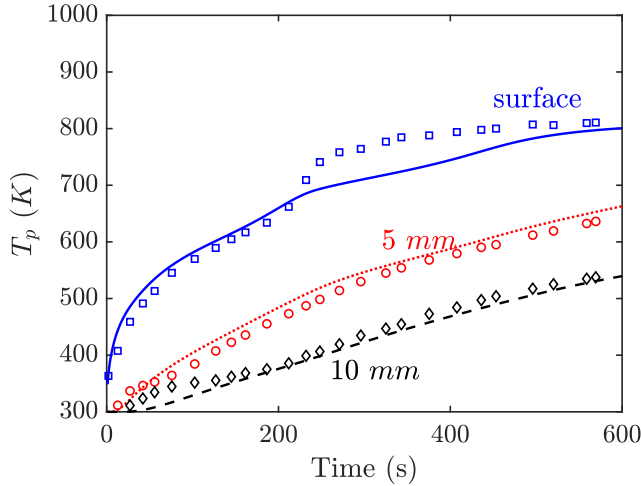


Figure 3.15: Spatial variation of exposed surface temperature and in-depth temperatures of the 3.8 cm pine wood particle at $25\text{ }kW/m^2$ irradiation in $89.5\% N_2 - 10.5\% O_2$. Comparison between simulations using the PBR model (lines), experimental data of Kashiwagi et al. [85] (symbols).

MLR. This test suggests that the baseline choice of $100\text{ }\mu m$ resolution adopted in this section provides an appropriate number of grid cells required to correctly capture the spatial variations inside the particle. Note that simulations with higher particle temperature where the particle transitions from flaming to smoldering may still require grid resolution finer than $100\text{ }\mu m$ (see section 3.5).

3.5 Representative results of complete consumption and the issue of volume change

We present here representative results of the PBR model corresponding to a 10 mm diameter cylindrical-shaped pine wood particle heated for only 60 seconds at

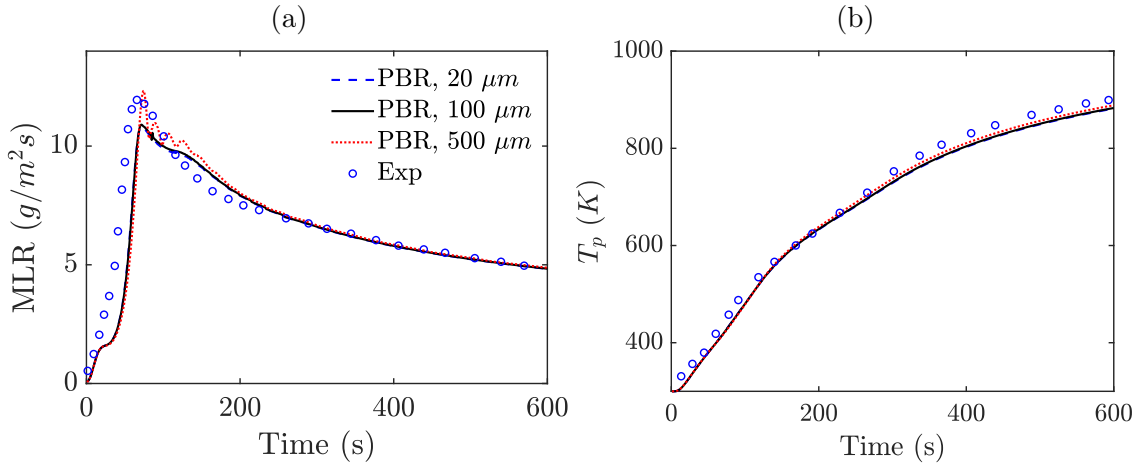


Figure 3.16: Predictions, using different grid resolutions, of a) MLR and b) the temperature at 5 mm depth inside the particle under 40 kW/m² irradiation in ambient air.

a level of $G = 60 \text{ kW/m}^2$ irradiance flux. After 60 seconds, the irradiance flux drops to its ambient value. The particle is exposed to ambient air flowing at a velocity of $u_g = 1 \text{ m/s}$. The particle is resolved with a grid resolution of $10 \mu\text{m}$.

Figure 3.17a shows the time evolution of the mass loss rate of the simulated particle. We see from the mass loss rate of this simulated particle the existence of two phases: a first phase that corresponds to pyrolysis that is sustained by the external heat coming into the particle; and a second phase that corresponds to smoldering combustion that is self-sustained and continues even when the external heating is stopped. This simulation represents a case where a transition from flaming combustion to smoldering combustion is achieved. As a result, the particle is completely consumed to ash as indicated in the mass consumption curve in Fig. 3.17b.

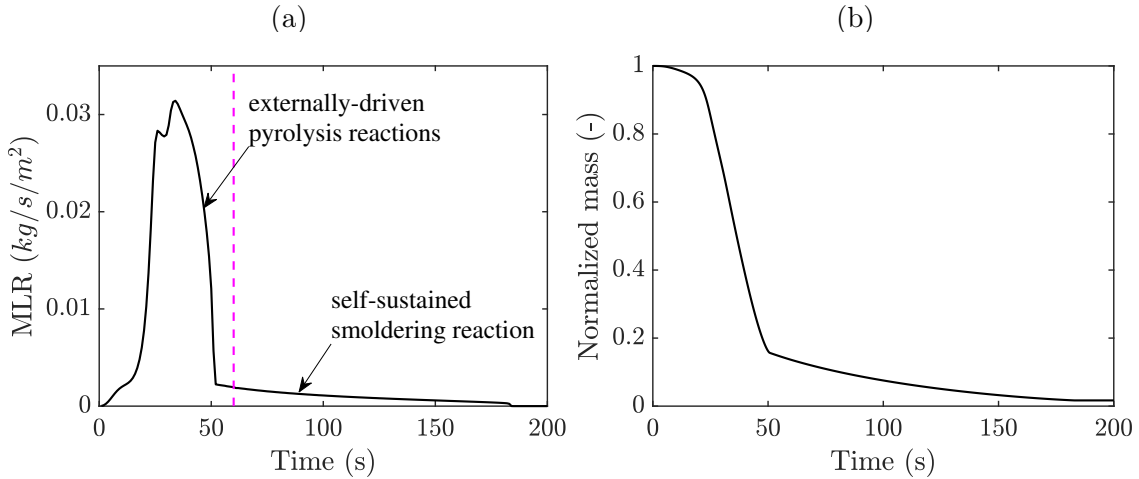


Figure 3.17: Variation of a 10 mm diameter pine wood particle mass loss rate (a) and mass (b) with time obtained using PBR simulations. The particle is exposed to 60 kW/m^2 radiative flux for 60 s in ambient air flowing at 1 m/s . The vertical dashed line indicates the end of the external heating period.

Figures 3.18a and 3.18b show two different snapshots of the details of the temperature profile and the volume fractions of char and ash across the particle radius. As seen in Fig. 3.18a, the particle achieves at $t = 50 \text{ s}$ (just before the external heating is stopped) a temperature level of about 850 K at its core and about 1150 K near its exposed surface. After the external heating is removed, the particle is able to self-heat due to exothermic oxidative reactions. At $t = 135 \text{ s}$, the core temperature increases to above 1000 K while the surface of the particle loses heat to ambient air. Figure 3.18b shows the spatial profiles of char and ash at the $t = 50$ and 135 s . These profiles show the displacement of the char oxidation reaction from the particle surface to the core of the particle. This region is the region where char is transformed into ash. Note that at $t = 50 \text{ s}$, the volume fraction of char at the

particle core is below 1 indicating incomplete pyrolysis at that time.

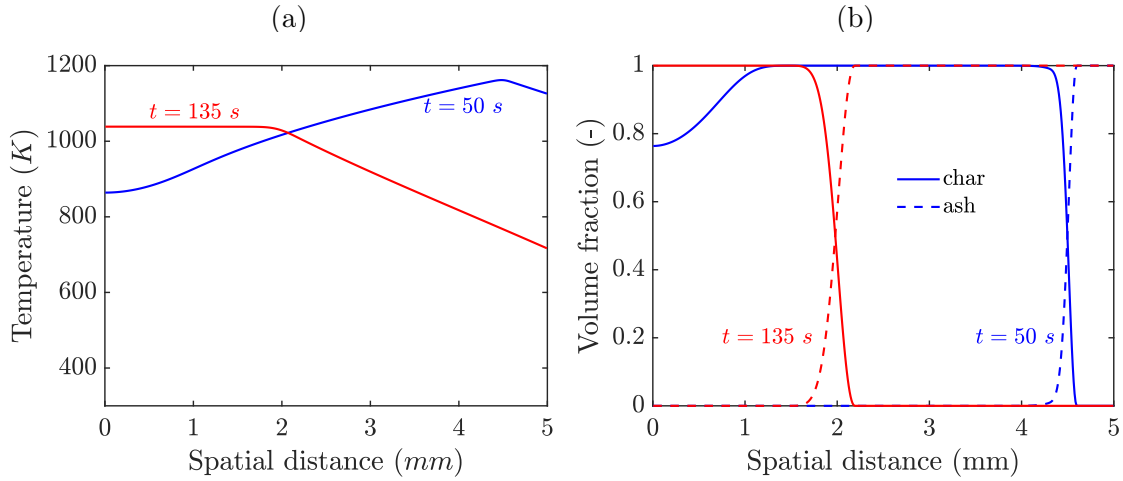


Figure 3.18: Two snapshots of spatial profiles of temperature (a) and volume fraction of char and ash (b) inside a 10 mm diameter pine wood particle exposed to 60 kW/m^2 radiative flux for 60 s in ambient air flowing at 1 m/s.

Figure 3.19a shows the distribution of oxygen inside the porous particle. At the initial time, the particle pores are filled with ambient oxygen. As the pyrolysis reaction evolves, the particle blows flammable gaseous volatiles to the ambient, and the interior of the particle is filled by flammable gaseous fuel. Thus, at $t = 50\text{ s}$, the oxygen mass fraction inside the particle is zero except near the surface where some oxygen is diffused from external ambient air through the particle surface. At $t = 135\text{ s}$, more oxygen has diffused into the particle. Figure 3.19b shows the spatial profiles of the char oxidation reaction rate at $t = 50$ and 135 s . Our first observation from these profiles is that the char oxidation reaction is oxygen-diffusion limited because there is no oxygen in the core of the particle and all oxygen that diffuses into the particle is consumed by the char oxidation reaction. Our second observation

is that the thickness of the char oxidation zone is very thin compared to the particle size. At the start of the char oxidation reaction, this thickness is on the order of 0.1 mm which indicates the need for sub-millimeter grid resolution in the PBR model.

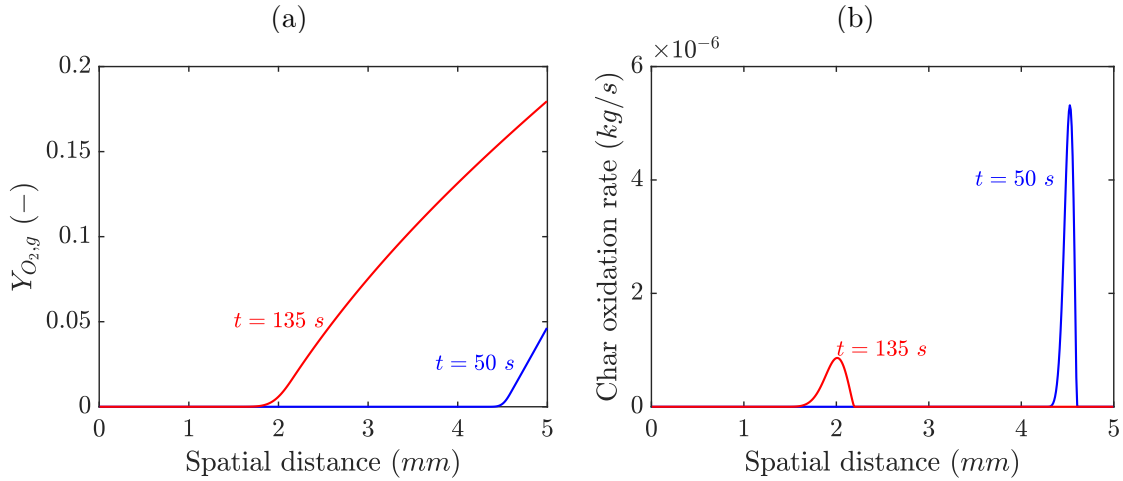


Figure 3.19: Two snapshots of spatial profiles of oxygen mass fraction (a) and char oxidation reaction rate (b) inside a 10 mm diameter pine wood particle exposed to 60 kW/m^2 radiative flux for 60 s in ambient air flowing at 1 m/s .

We now consider a case where the particle volume changes during thermal degradation. Recall from section 2.2.2 that the variation of the particle volume during thermal degradation is dependent on the residual yield and their mass density (e.g., char yield and char mass density) as well as the porosity of the particle. These input parameters can be adjusted such that thermal degradation is achieved at either variable or constant volume. We attempt here to verify the capability of the model to simulate the thermal degradation of swelling and/or shrinking particles. We performed a simulation of the 10 mm pine wood particle discussed in the previous

paragraphs but with different char and ash yields than those listed in Table 3.2. Figure 3.20 shows the time variation of the particle diameter during thermal degradation with the baseline char and ash yields (Table 3.2) and modified char and as yields of $\eta_{c,Rp} = \eta_{c,Rop} = 0.3$ and $\eta_{a,Rco} = 0.005$. These results are consistent with Eq. 2.24 since the particle undergoes swelling as $\eta_{c,Rp} > \rho_{c,bulk}/\rho_{ds,bulk}$, and the particle undergoes shrinking as $\eta_{a,Rco} < \rho_{a,bulk}/\rho_{c,bulk}$.

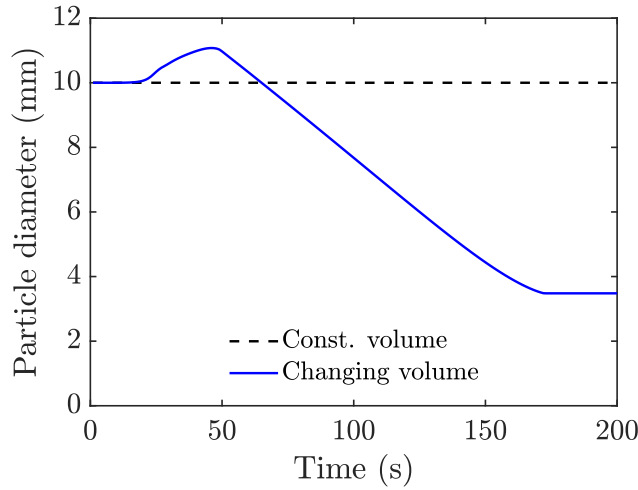


Figure 3.20: Temporal evolution of the volume of 10 mm diameter pine wood particle exposed to 60 kW/m^2 radiative flux for 60 s in ambient air flowing at 1 m/s . The dashed line represents simulations conducted using the char and ash yields listed in Table 3.2. The solid line represents simulations conducted with modified char and ash yields of 0.3 and 0.005, respectively.

3.6 Summary

This chapter presented a series of test cases to verify the developed models using simplified configurations where exact analytical solutions can be obtained. These

tests included a verification of the in-depth heat conduction in thick rectangular-, cylindrical- and spherical-shaped solids, a verification of the momentum exchange between the gas-phase and the solid fuel bed, a verification of the pressure-velocity coupling through examining the pressure drop inside the solid fuel bed, a verification of the multi-phase radiative transfer by examining the radiation absorption and emission in solid fuel beds, and lastly a verification of the in-depth radiation heat transfer inside the fuel bed and the model capability to simulate a self-sustained smoldering front driven solely by particle-to-particle radiation.

This chapter also provided a series of calibration tests of the thermal degradation model for cardboard and for pine wood using simulations of micro-scale TGA experiments in inert and oxidative environments, followed by an evaluation of the PBR model's ability to predict thermal degradation of thick samples by comparing the model predictions to a well-established bench-scale experiment of thick pine wood slab that is radiatively heated in controlled inert and oxidative environments.

Lastly, the chapter discussed a representative simulation using the PBR model of a thick particle, that exhibits a transition from flaming to smoldering as well as complete consumption, by presenting profiles of the temporal and the spatial evolution of quantities of interest. The chapter also discussed the ability of the PBR model to simulate particles that feature a volume change (i.e., swelling or shrinking) and the impact of the choice of the model inputs on this behavior.

4 Thermal Feedback in Canonical Pool Fire Configurations¹

4.1 Overview

Pool fire configurations are used for fundamental studies of the structure of open fires, including studies of the complex interactions that take place between the buoyancy-driven turbulent flow, the non-premixed combustion processes occurring inside the flame region, and the air entrainment and possible additional low-temperature chemistry occurring in the plume/smoke region. Pool fires have important features such as transitions from laminar to fully developed turbulent flow, a transition from convection- to radiation-dominated heat transfer at the pool surface; and in the case of hydrocarbon sooty fuels, a transition from sooting (non-smoking) to smoking conditions. Because of these features, and from a modeling perspective, the study of pool fires is viewed as an intermediate but essential step towards modeling of more complex fire configurations that feature fire spread over solid fuel as discussed in the following chapters.

We focus in this chapter on evaluating the ability of the gas-phase combustion and radiation models to predict thermal feedback in two canonical pool fires configura-

¹Parts of this chapter are taken from the publication by Ahmed and Trouv  [86]

tions that have been recently adopted by the “IAFSS Working Group on Measurement and Computation of Fire Phenomena” (the MaCFP Working Group) [87, 88] among other target experiments recommended for validation of computational fire models. In particular, we would like to compare the predictions of the radiation field obtained using either the simple PGRF model or using more elaborate models such as the WSGG or the Line-By-Line (LBL) models against those obtained from experimental measurements. We would like also to evaluate the sensitivity of the results to the choice of the angular resolution of the radiation field.

4.2 Medium-scale methanol pool fire

The first configuration corresponds to a medium-scale methanol pool fire that features a moderately-turbulent flow, a gas-to-liquid heat transfer dominated by radiation, and a non-sooting flame. This configuration was previously studied experimentally by different groups at the University of Waterloo in Canada [89] and at the National Institute of Standards and Technology (NIST) in the U.S. [90, 91].

In this configuration, a 30 cm diameter circular pan is placed at a certain position above the floor such that the pool surface is located at an elevation equal to one pool diameter. The lip height of the fuel pan is constant and equals 1 cm in Refs. [89, 91] and 0.5 cm in Ref. [90]. The heat release rate of the methanol pool fire is 21.3 kW in Ref. [89] and 19.2 kW in Ref. [91]. The global radiant fraction averaged over various studies is 0.22 ± 0.02 [91].

The experimental database in Ref. [89] includes simultaneous measurements

of the temperature and vertical/radial flow velocity obtained with fine-wire thermocouples. The experimental database in Refs. [90, 91] includes measurements of the radiative and total heat fluxes near the pool surface obtained with water-cooled gauges.

4.2.1 Numerical configuration

As shown in Fig. 4.1, the computational domain is cylindrical-shaped, has a diameter of 150 cm, and a height of 173 cm. The inner diameter of the fuel pan is 30.5 cm. The fuel pan is radially centered inside the computational domain and is vertically placed so that the elevation of the liquid pool surface is $z = 30$ cm. The burner rim is modeled as a 1-cm-thick solid ring with a lip height equal to 1 cm.

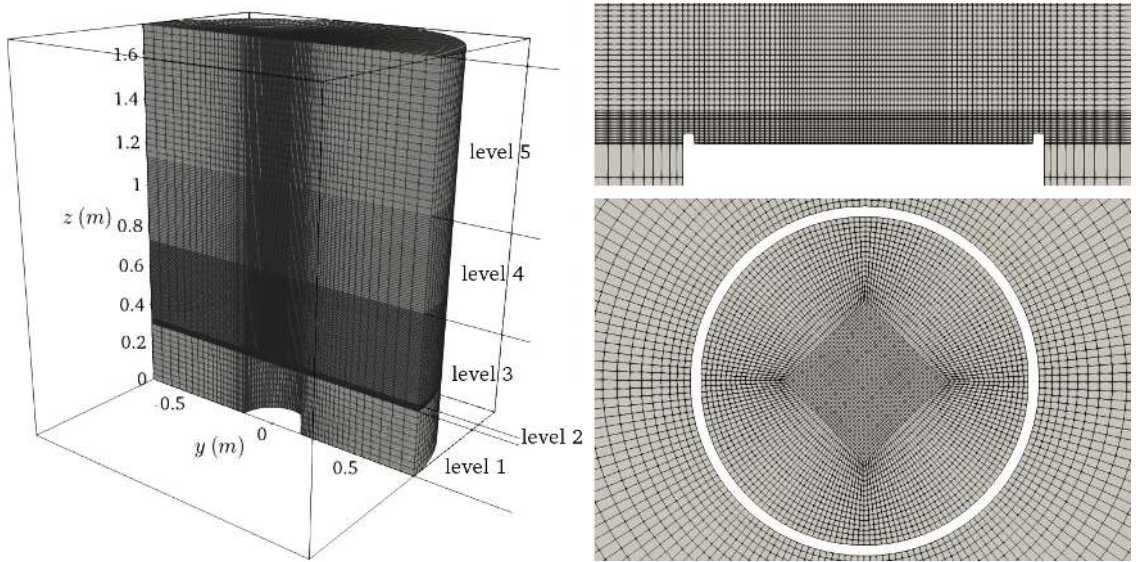


Figure 4.1: A 3-D view of the computational domain of the methanol pool fire (left), and 2-D sections showing an enlarged view of the medium mesh resolution near the fuel pan (right).

We consider three different multi-block structured meshes denoted by coarse, medium, and fine. The coarse mesh resolution varies from 5 mm at the pool surface, 10 mm in the flame zone, and 60 mm far downstream. The medium mesh resolution varies between 2 mm at the pool surface, 5 mm in the flame zone, and 30 mm far downstream. The fine mesh resolution varies between 1 mm at the pool surface, 2.5 mm in the flame zone, and 30 mm far downstream. The total number of computational cells is 7.7 million (fine mesh), 1.5 million (medium mesh), and 0.185 million (coarse mesh). Our baseline choice of angular space resolution is 64 solid angles. We also show the sensitivity of the solution to this choice by presenting simulations with 36 and 100 solid angles, applied to the medium mesh resolution configuration.

Regarding the boundary conditions, the pool surface is treated as an inflow boundary with a baseline value of the prescribed mass flow rate of methanol vapors corresponding to the conditions of Ref. [89] (i.e., a fuel evaporation rate of $\approx 1.067\text{ g/s}$). The methanol vapors are released at the boiling temperature, 337.8 K . The simulation that discusses the flame structure uses a heat of combustion (per unit mass of fuel) equal to 21105 kJ/kg ; the corresponding value of the total heat release rate is 22.6 kW . The study of thermal feedback includes a modified configuration that is more representative of the conditions reported in Ref. [91]: a fuel evaporation rate of $\approx 0.963\text{ g/s}$, a heat of combustion of 19940 kJ/kg and a heat release rate of 19.2 kW . In all simulations, the pan sidewalls are modeled as no-slip adiabatic solid walls, and the side and bottom boundaries of the computational domain are treated as surfaces with open flow conditions.

In order to compare simulation results to the experimental measurements of the total heat flux made in Ref. [91], several virtual gauges are inserted into the numerical configuration and are positioned at the exact same vertical and radial location where heat flux gauges are placed in the experiments. The gauges are positioned at 13 mm elevation above the pool surface (see Fig. 4.2). In the following, we will use the same virtual gauges to also compare simulation results to the experimental measurements of the radiative heat flux made in Ref. [90]. The virtual gauges occupy one grid cell and are treated as no-slip isothermal solid walls at the temperature equivalent to the water-cooled heat flux gauges in the experiments, which is close to 60°C . In order to limit disturbances, the virtual gauges are staggered and distributed along various radial lines as shown in Fig. 4.2. The virtual gauges record the net vertical heat flux received on their upper surface.

We present below simulation results obtained using the two modeling options of gas-phase radiation described in chapter 2: the PGFR approach with a radiant fraction of 0.22 and the WSGG approach. For all simulations presented in this chapter, we use the EDM for combustion and the dynamic k-Equation model for subgrid-scale turbulence.

4.2.2 Flame structure

The simulations feature a typical turbulent pool flame characterized by a mean flame height of approximately 0.6 m and peak combustion intensities in the flame base region. Consistent with experimental observations, the simulations also feature

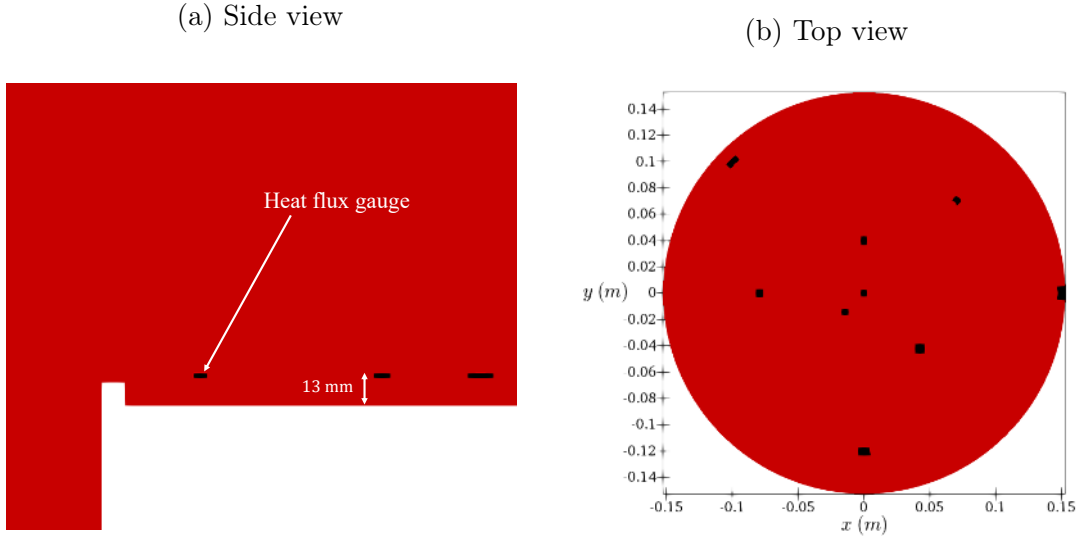


Figure 4.2: A view of the virtual heat flux gauges used in the numerical configuration:
 a) side view of the computational domain near the burner lip and the gauges; b) top view of the burner surface and the gauges. The gauges are colored in black. The computational domain and the burner surface are colored in red.

a strongly unstable flame. Figure 4.3 shows a 3-D visualization of the flame using volume rendering of the temperature field. The snapshots are taken at different times to show the time evolution of the flame structure. Figure 4.4 presents corresponding information on the structure of the flow field in a two-dimensional central vertical plane at the same selected times already used in Fig. 4.3. As shown in these figures, the flame is characterized by: the cyclic formation of quasi-axisymmetric perturbations along the flame surface that are first formed at the burner rim ($t = 0$); the growth of these perturbations into a vortex ring that moves vertically upward and radially inward ($t = 0.06, 0.12, 0.18$ s); the evolution of the vortex ring into a “bouquet” of three-dimensional thermal plumes ($t = 0.24, 0.30$ s); and the subsequent merging of

the thermal plumes near the center of the pool followed by rapid vertical acceleration and necking of the flame ($t = 0.36, 0.42$ s). This instability is buoyancy-driven and in the fire literature, is generally designated as a puffing instability [89, 92, 93]. The frequency of the simulated puffing instability determined from the power spectrum of the temporal variations of the simulated heat release rate shown in Fig. 4.5 is ~ 2.4 Hz and is close to the 2.8 Hz frequency reported in the experiments [89, 92]. Significant cycle-to-cycle variations are observed and the instability is not truly periodic.

We now turn to a discussion of the characteristic length scales of the pool fire. Figures 4.3 and 4.4 show that the unstable flame features the intermittent presence of large toroidal vortices of diameter D as well as that of small vortex structures, thermal plumes, and a boundary layer flame. The size of the vortex ring at formation time is on the order of 1 cm (see Fig. 4.4 at $t = 0$ and $t = 0.42$ s and at $r \approx 15$ cm); the vertical thickness of the intermittent boundary layer flame is also on the order of 1 cm (see Fig. 4.4 at $t = 0.30, 0.36$ s and at $5 \leq r \leq 15$ cm). This analysis suggests that a grid resolution of millimeter-scale is adequate.

We now briefly discuss the sensitivity of the flame structure, in terms of temperature and velocity fields, to the computational grid resolution. Figure 4.6 presents comparisons between the measured and simulated centerline vertical variations of the mean and *rms* values of temperature, and vertical and radial velocities, as well as the mean values of the cross-correlation between vertical velocity and temperature. In the simulations, mean quantities are obtained by performing time-averaging; *rms* quantities correspond to the grid-resolved amplitudes of the fluctuations (because

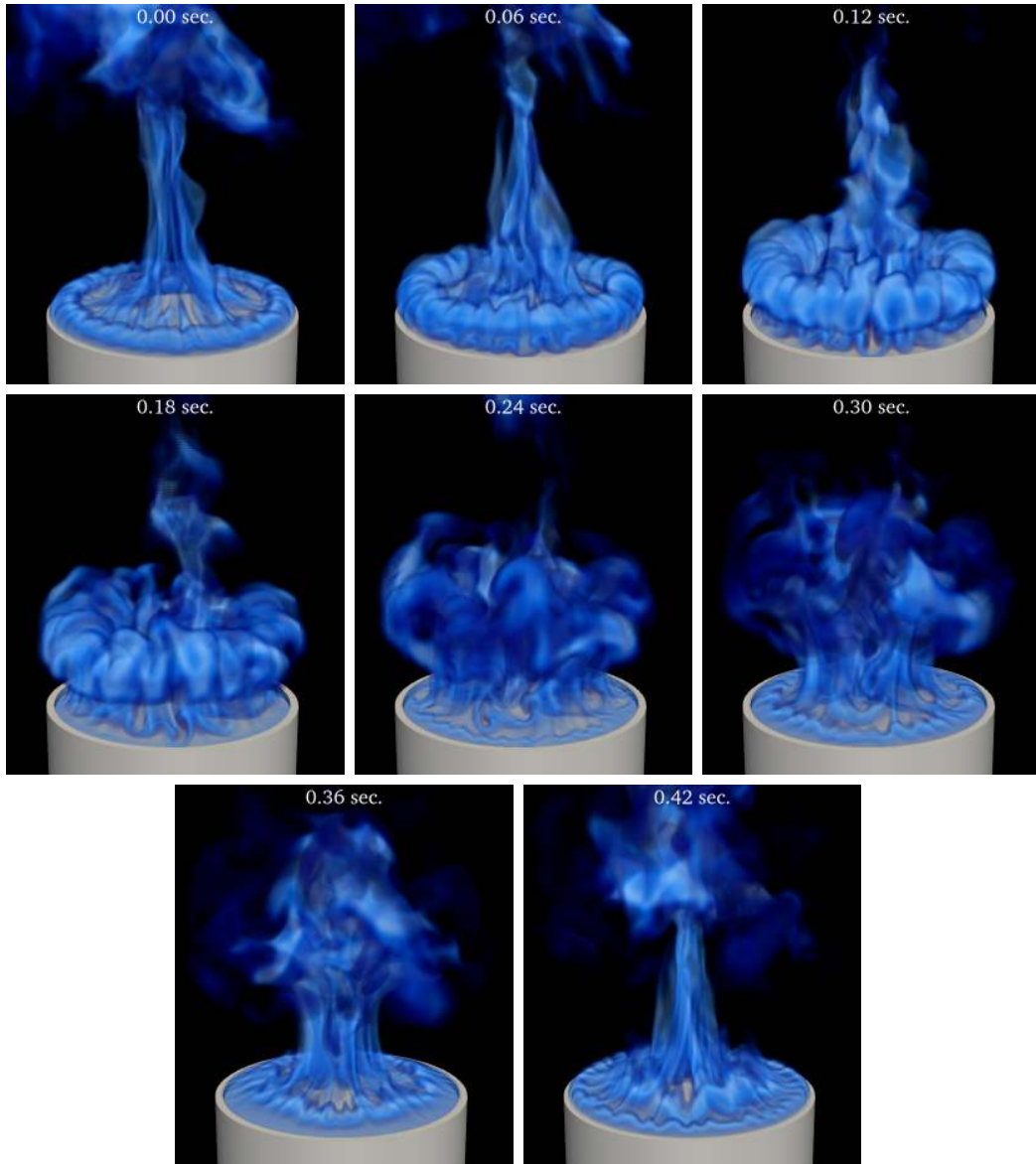


Figure 4.3: Sequence of instantaneous snapshots of the methanol pool flame taken at selected times during a representative instability cycle. The flame is visualized using volume rendering of the high-temperature region (defined as the region where temperatures are larger than 800 K). The time between successive snapshots is 0.06 s and the total duration of the sequence is 0.42 s. The fuel pan and liquid pool surface are colored grey. The simulation was performed with the fine mesh and with PGRF.

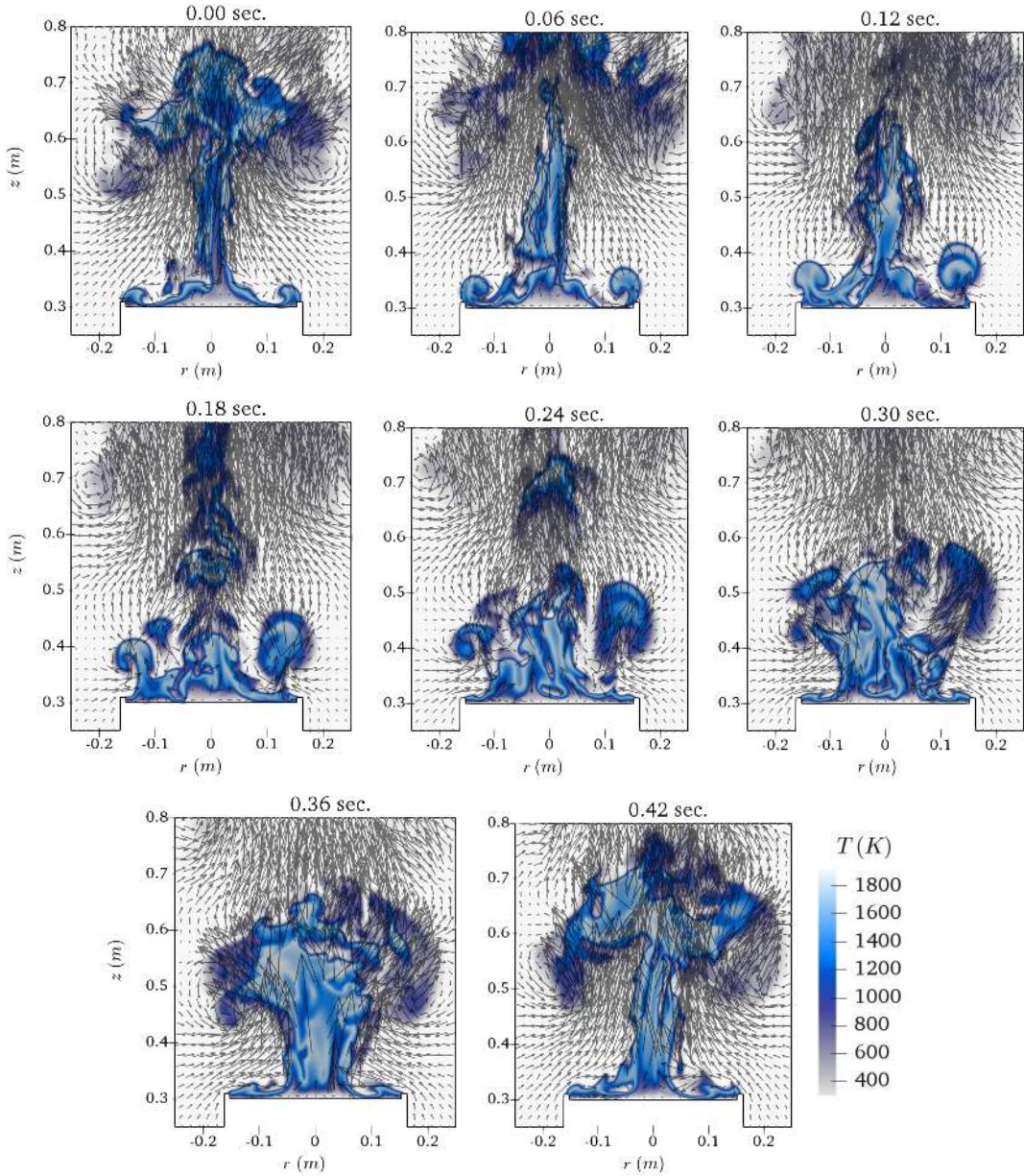


Figure 4.4: Sequence of instantaneous snapshots of the flame-flow configuration taken at selected times during a representative instability cycle and plotted in a central vertical plane. The flame is visualized using isocontours of temperature; the flow is visualized using velocity vectors. The fuel pan and liquid pool are colored white. See the caption of Fig. 4.3.

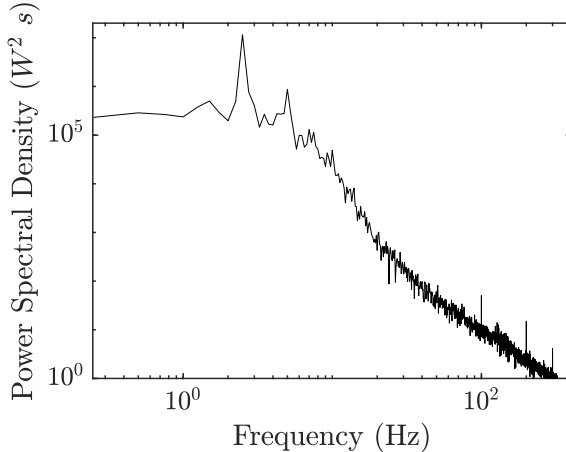


Figure 4.5: The power spectrum of the temporal variations of the simulated heat release rate.

the present LES simulations are well-resolved, the contributions of subgrid scales are neglected and these quantities are interpreted as estimates of the true *rms* values). Experimental data are taken from Ref. [89]. In the plots, we adopt the notations of the MaCFP Working Group [87] and use u and v to denote the vertical (axial) and horizontal (radial) components of the flow velocity, respectively; we also use z_p as a measure of vertical distance from the pool surface.

The plots in Fig. 4.6 show that the discrepancies between experimental data and simulation results are reduced as one goes from coarse to medium spatial resolution. The differences between simulations performed with the medium and fine meshes are very small, which suggests that the solutions may be grid-converged. The plots also suggest that the overall level of accuracy achieved in the simulations with medium and fine resolution is good despite some discrepancies such as: the mean temperature which is slightly under-estimated at low elevations (by approximately 100 K at

$z_p \leq 10 \text{ cm}$); the *rms* temperature which is overestimated at high elevations (by up to 150 K at $z_p \geq 10 \text{ cm}$); the *rms* radial velocity which is under-estimated (by a factor 2 at $z_p \leq 10 \text{ cm}$); the vertical-velocity-temperature correlation which is overestimated at high elevations ($z_p > 20 \text{ cm}$). Some of these discrepancies may be attributed to the simplified description of a constant and uniform fuel evaporation rate which may require a more elaborate description (i.e., as a function of temporal and spatial variations of thermal feedback). Note that in the simulations of flame spread presented later, we account for such spatial and temporal variations of the rate of production of gaseous fuel as the thermal feedback to the fuel bed changes.

4.2.3 Thermal feedback

Figure 4.7 presents comparisons between the measured and simulated radial variations of the mean gauge heat flux evaluated at 13 mm above the liquid pool surface. Experimental data for the total heat flux, $\overline{\dot{q}''_{tot}}$, are taken from Ref. [91]. Experimental data for the radiative heat flux, $\overline{\dot{q}''_{rad}}$, are taken from Ref. [90]; note that these data are obtained at 7 mm above the liquid pool surface. In Fig. 4.7, simulated values correspond to results obtained at medium resolution using either the PGRF radiation modeling approach or the WSGG approach with the formulation of Bordbar et al. [74].

We see in Fig. 4.7 that the simulations qualitatively capture the radial variations of the mean total heat flux from high values at the pool center to low values near the pool edge. The simulation results and the experimental measurements show a peak

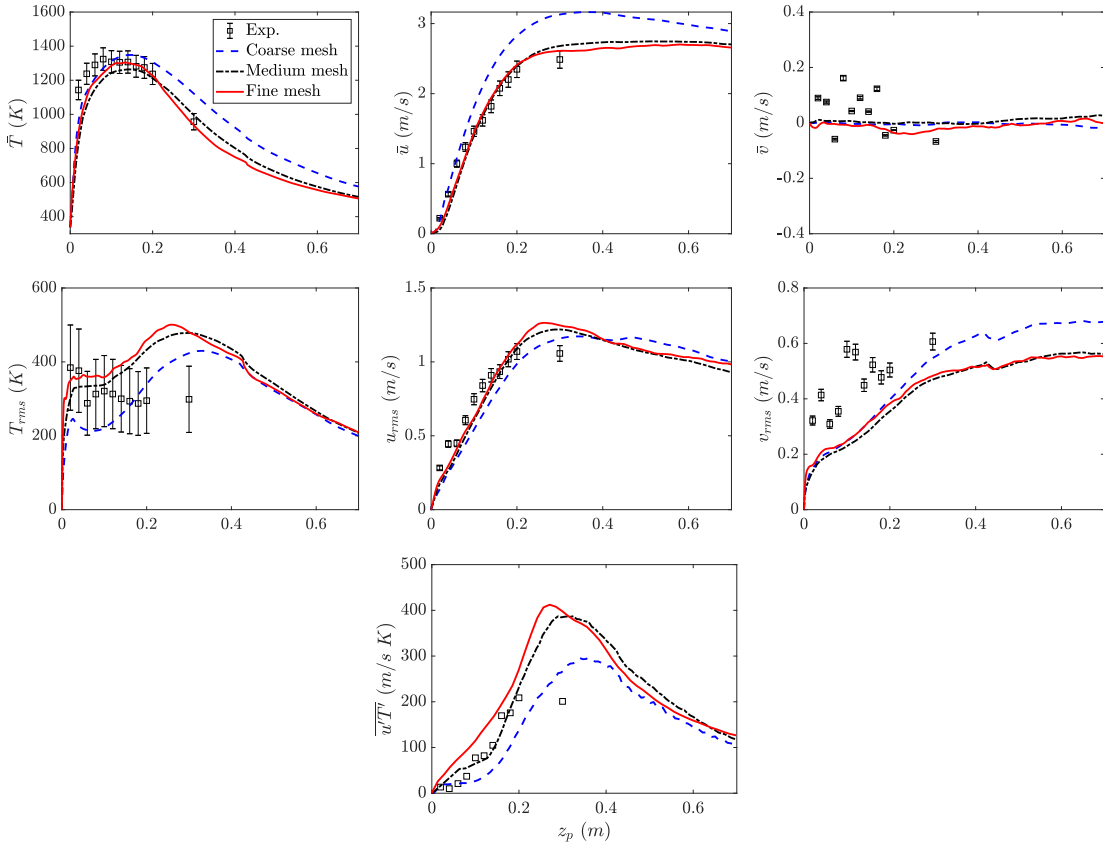


Figure 4.6: Centerline vertical variations of: mean temperature, \bar{T} ; mean vertical velocity, \bar{u} ; mean radial velocity, \bar{v} ; rms temperature, T_{rms} ; rms vertical velocity, u_{rms} ; rms radial velocity, v_{rms} ; cross-correlation between vertical velocity and temperature, $u' \bar{T}'$. Comparisons between experimental data (symbols) and simulation results obtained with a coarse mesh (dashed blue line), a medium mesh (dash-dotted black line), and a fine mesh (solid red line). Simulations performed with PGRF. The vertical bars denote the uncertainties in the experimental data.

value of the total heat fluxes occurring at an off-center location because the intensity of convective heat transfer is related to the magnitude of the radial velocity and because by symmetry, this intensity remains small at the pool center. The simulations

with the WSGG approach agree well with the experimental measurements of the radiative heat flux with a peak value at the center. The simulation with PGRF slightly overestimates the radiative heat flux and predicts a peak occurring at an off-center location. We also find that the intensity of the thermal feedback obtained from both PGRF and WSGG simulations is within the experimental uncertainty of the total and radiative heat fluxes except for the locations close to the burner rim. A reasonable estimate of the relative error in predictions of the mean total gauge heat flux, $\overline{\dot{q}''_{tot}}$, is $\approx 30\%$. The discrepancy near the burner edge may be due to the treatment of the burner rim as an adiabatic boundary which leads to overestimating the gas temperature in the vicinity of the burner rim.

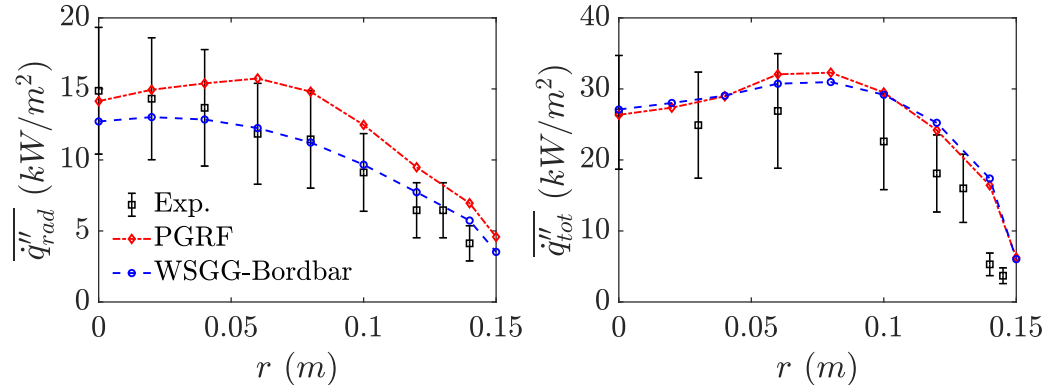


Figure 4.7: Radial variations of the mean gauge heat flux at 13 mm above the pool surface: (Left) radiative heat flux, \dot{q}''_{rad} ; (Right) total heat flux, \dot{q}''_{tot} . Comparisons between experimental data (square symbols) and simulations performed with the medium mesh and with PGRF (dashed red line with diamond symbols) or with WSGG (dashed blue line with circle symbols). The vertical bars denote the uncertainties in the experimental data.

Figure 4.8 compares the simulated radiative heat flux obtained using the WSGG approach with the formulation of Cassol et al. [49] (WSGG-Cassol) to the experimental data of Ref. [90]. We also include additional simulation results obtained using a higher-fidelity approach based on a Photon Monte Carlo and a line-by-line spectral model (PMC-LBL) [94]. These results are obtained by running the PMC-LBL radiation solver only using 20 time snapshots of the temperature, pressure, and mass fractions of CO_2 and H_2O obtained at 0.12s. interval from the simulation previously conducted using the WSGG-Bordbar model. These snapshots capture the change in the solution during the puffing cycle as well as cycle-to-cycle variations. The results obtained using the WSGG-Cassol model are very similar to those obtained using the WSGG-Bordbar model, and both are in very good agreement with the higher fidelity PMC-LBL simulations and the experimental data.

We also performed a sensitivity study on the choice of the angular resolution of the radiation field. Figure 4.9 shows a comparison between the radiative gauge heat flux obtained from simulations with 32, 64, or 100 radiation solid angles. These simulations are performed using the WSGG-Bordbar model. The results suggest that all three resolutions are able to qualitatively predict the radiative and total heat fluxes as in the experimental measurements. The relative error in the radiative heat flux between the 36 and 64 solid angles is $\approx 23\%$, while the relative error between 64 and 100 solid angles is $\approx 8\%$. This result suggests that an appropriate resolution of the angular space should be at least 64 solid angles.

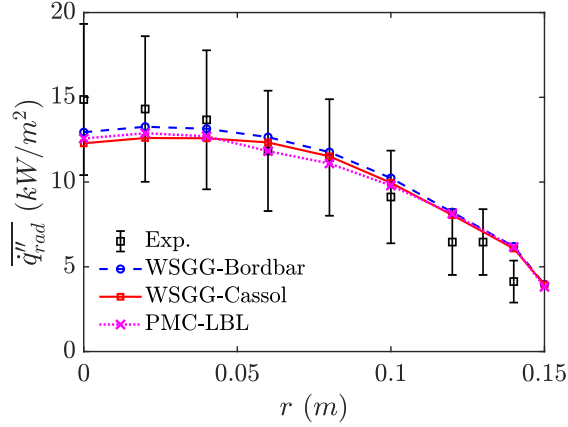


Figure 4.8: Radial variations of the mean radiative heat flux at 13 *mm* above the pool surface. Comparisons between experimental data (square symbols) and simulations performed with the medium mesh and with the WSGG-Bordbar model (dashed blue line with circle symbols), WSGG-Cassol (solid red line with square symbols), and PMC-LBL (dotted purple line with x symbols). The vertical bars denote the uncertainties in the experimental data.

4.3 Turbulent ethylene burner with controlled coflow (FM-Burner)

The second configuration corresponds to a circular burner that features a sooting turbulent ethylene flame in a controlled coflow at different oxygen levels (see Fig. 4.10). The burner has an inner diameter of 13.7 *cm* and an outer diameter of 15.2 *cm* and is placed inside a controlled enclosure at approximately 13 *cm* above a sand bed that provides a controlled coflow. The burner is water-cooled at 25°C. The flow rate of ethylene is 0.318 *g/s* which provides a theoretical heat release rate of ~ 15 *kW*. The controlled coflow provides different oxygen concentrations including normal air, 16.8%, and 15.2% oxygen by volume in nitrogen (i.e., oxygen mass

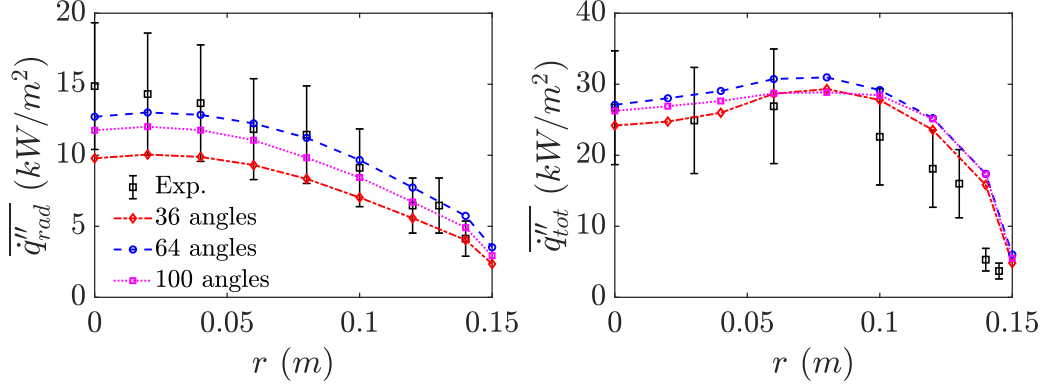


Figure 4.9: Comparisons between experimental data (square symbols) and simulations performed with the WSGG-Bordbard model with 36 solid angles (dashed red line with diamond symbols), 64 solid angles (dashed blue line with circle symbols), or 100 solid angles (dotted purple line with square symbols). See the caption of Fig. 4.7.

fractions of 0.231, 0.187, and 0.17, respectively). This configuration was studied experimentally at FM Global and is known as the FM-Burner in the MaCFP working group [88, 95–97]. The experimental database in Refs. [95, 97] provides measurements of radiant power distribution and temperature profiles at different elevations above the burner, and the experimental database of Ref. [96] provides measurements of soot volume fraction obtained using laser-induced incandescence (LII) technique.

4.3.1 Numerical configuration

Figure 4.11 shows the computational domain used in the simulations of the FM-Burner. The computational domain has a square base of $1.2 \times 1.2 \text{ m}^2$, and a height of 1.8 m. The burner is placed at 13 cm elevation above the domain base, and has a diameter of 13.7 cm. As shown in Fig. 4.11, the computational

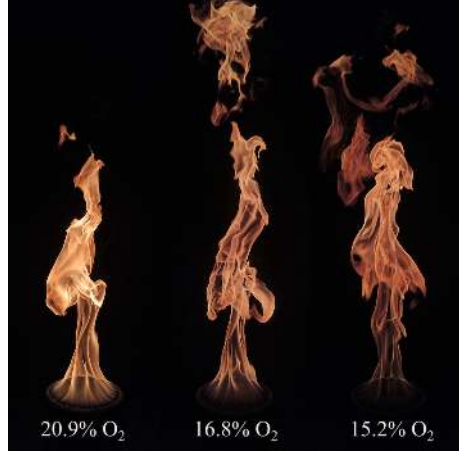


Figure 4.10: Photographs of the FM-Burner taken during experiments conducted at different oxygen concentrations [88].

grid has multi-block quadrilateral cells with two refinement zones. The size of the computational grid cells in the far field is 4 cm , while the size of the computational grid cells in the second refinement zone is 0.5 cm . The first refinement zone has a radius of 0.25 m and extends from the base of the domain to 1.2 m elevation. The second refinement has a radius of 0.15 m and extends from 0.1 m to 0.7 m elevations. A mesh refinement with 0.5 cm grid cell size is also included around the sidewalls of the burner.

Regarding the boundary conditions, an inflow at a constant velocity of 0.041 m/s is imposed at the bottom boundary with concentrations of O_2 and N_2 selected according to the experimental coflow condition. The side walls of the domain are treated as no-slip adiabatic walls. The top boundary is treated as an open boundary condition. The burner surface is treated as an advective-diffusive isothermal boundary with a flow rate of ethylene at 0.318 kg/s and 353 K . This results in a theoretical heat release rate of $\sim 15\text{ kW}$ for a heat of combustion of 47.17 MJ/kg .

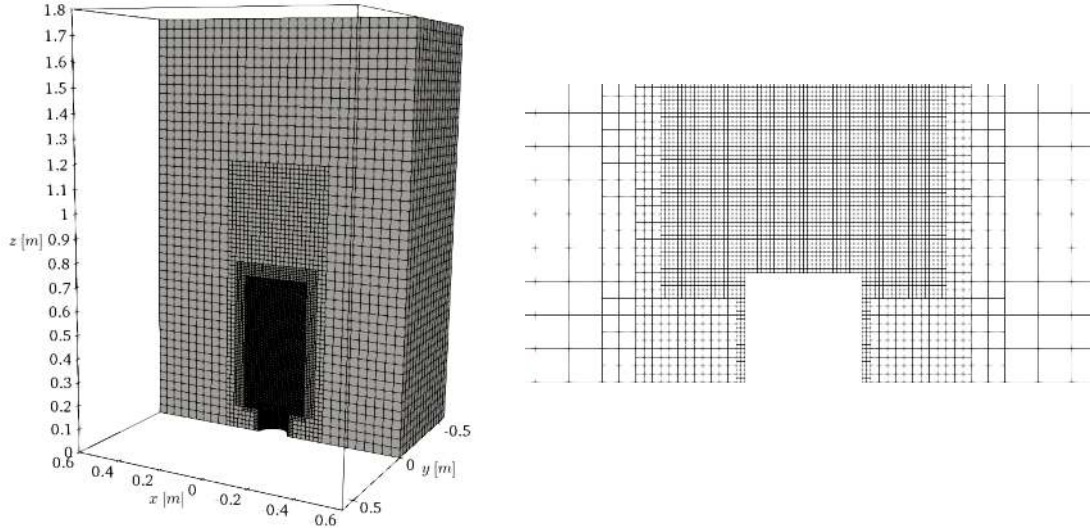


Figure 4.11: A 3D representation of the computational domain of the FM-Burner (left), and a slice showing the computational mesh near the burner (right).

Note that this theoretical heat release rate assumes complete combustion of the fuel, which may not be the case for heavily sooting flames.

Our primary objective here is to evaluate the capability of the two radiation modeling approaches (PGRF and WSGG) to predict the measured radiant power distribution of this sooting flame. Our secondary objective is to evaluate the LES version of the LSP soot model presented in appendix C by comparing our predictions of the mean and *rms* values of the soot volume fraction to experimental measurements. We present below simulations conducted using the WSGG approach for gas and soot radiation where the LSP soot model is employed. We also include simulations performed using the PGRF approach with the experimental value of the global radiant fraction obtained from Ref. [95] (0.34 in the case of 20.9% O_2 coflow and 0.22 in the case of 15.2% O_2 coflow). Note that the soot model is not needed and is not invoked in the simulations with the PGRF model.

4.3.2 Flame structure

Figure 4.12 displays the instantaneous and mean contours of temperature, mixture fraction and soot volume fraction at the center plane, obtained from the simulation with the WSGG model of the FM-Burner at 20.9% O_2 . Our first observation from these contours is that the overall flame structure is consistent with the experimental photographs in which a weakly turbulent necking region exists at the base of the flame (from the burner surface to a height equal to approximately one burner diameter), followed by a transition to a buoyant turbulent structure. The second observation is that the instantaneous temperature is high and reaches a maximum of $\sim 1800 - 2000\ K$ at several locations at both low and high elevations above the burner. Due to flame intermittency, the mean temperature is much lower than the instantaneous temperature (generally below 1300 K) except near the vicinity of the burner where it reaches higher values of up to $\sim 1600\ K$ indicating much lower flame intermittency.

Consistent with experimental measurements, the simulations show a peak value of the instantaneous soot volume fraction of $\sim 10\ ppm$. The corresponding experimental measurements of Ref. [96] show a peak instantaneous value of soot volume fraction of $\sim 8\ ppm$ and our predictions are not far from the measurements. Another important result from the simulations is that all soot is oxidized within the flame and no smoke is found to exit from the flame tip. This is consistent with experimental observations, and suggests that the application of the LSP modeling approach is adequate here.

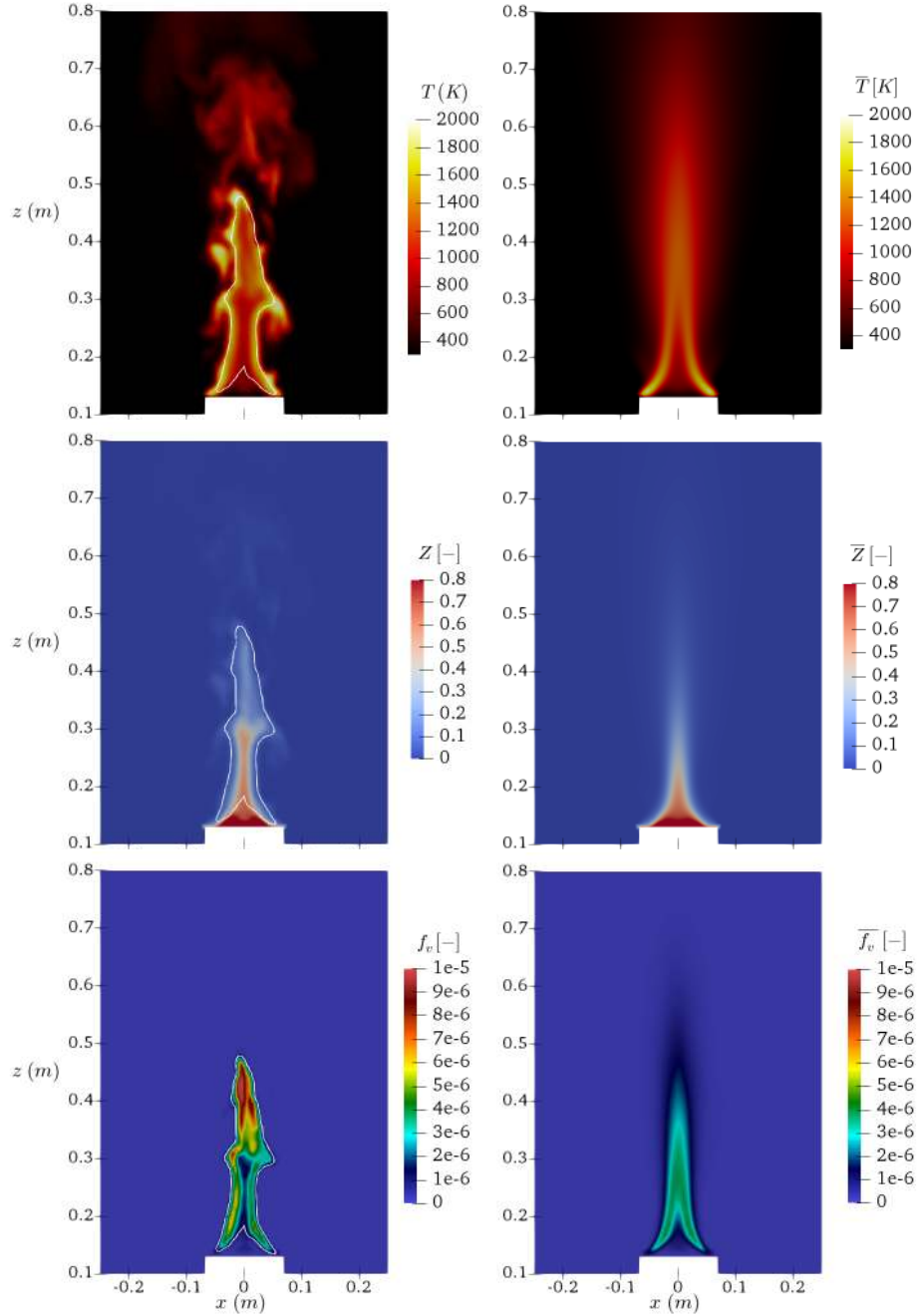


Figure 4.12: Contours of the instantaneous and mean values of: the temperature (T and \bar{T})), the mixture fraction (Z and \bar{Z})), and the soot volume fraction (f_v and \bar{f}_v)). The white isocontour represents $f_v = 10^{-6}$. The results correspond to the FM-Burner at 20.9% O_2 coflow.

Figure 4.13 shows the instantaneous and the mean contours of the volumetric soot formation and oxidation rates. We see from these contours that the region of activity is on the order of one grid cell (i.e., $0.5 - 1\text{ cm}$). However, the experimental observations of Ref. [96] suggest that soot exists in very thin filaments on the order of $\sim 1\text{ mm}$ (the zone of formation and oxidation is believed to be less than 1 mm-thick). This suggests that the soot formation and oxidation rates are not resolved by the LES grid and the predicted soot field may be very sensitive to the choices made in the subgrid-scale modeling of the soot formation and oxidation rates. As mentioned earlier, accurate predictions of the soot field are outside the scope of this dissertation, and our main focus is on evaluating the predictions of thermal feedback.

In order to do a quantitative comparison with experimental measurements, we present the radial profiles of the mean and *rms* values of temperature at different heights above the burner in Figs. 4.14. The plots show additional simulation results obtained using the PGRF model and the WSGG model where soot is not modeled (i.e. WSGG with radiation contribution of gases only). It can be seen from the radial profiles of temperatures that the measured and simulated values are in good agreement for both the WSGG and the PGRF cases. The WSGG approach considering only the contribution of gases overpredicts the mean temperature by $100 - 400\text{ K}$. This suggests that radiation is underestimated in the absence of soot absorption/emission. On the other hand, all simulations overpredict the *rms* of temperature. Simulations with PGRF and WSGG show a $100 - 200\text{ K}$ increase in the temperature *rms* at some radial locations. The discrepancy in the *rms* temperature may be attributed to the turbulence-radiation interaction which is

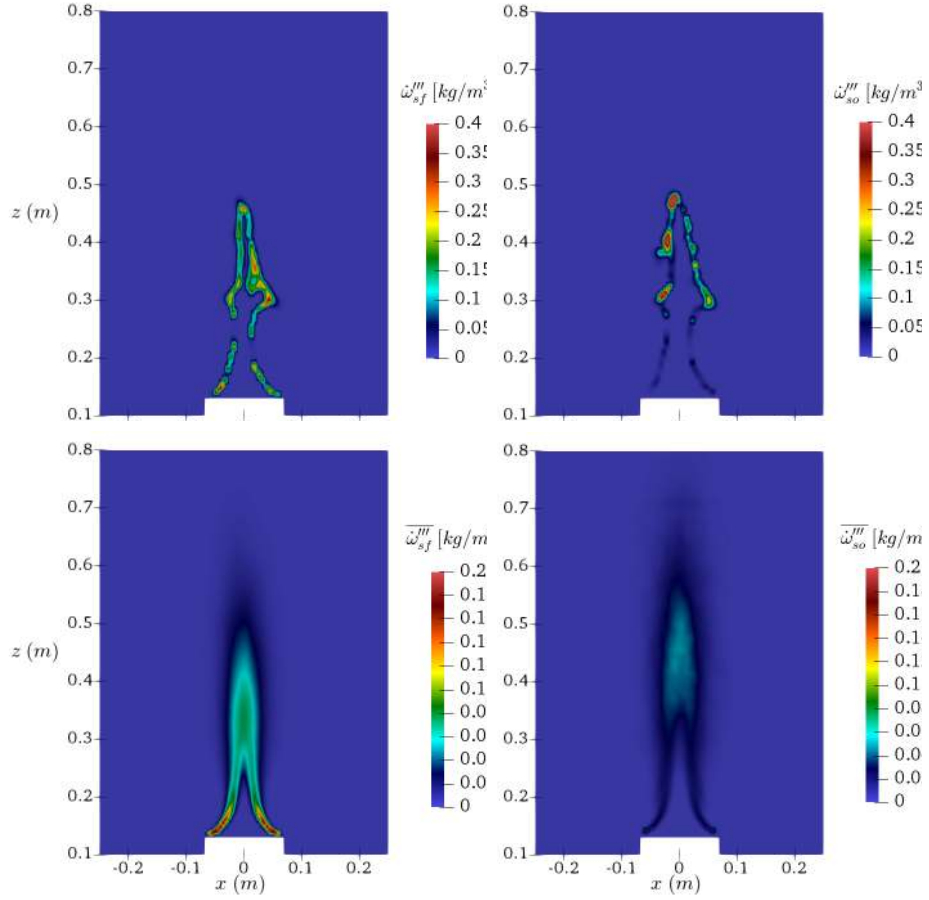


Figure 4.13: Contours of the instantaneous and mean values of: the volumetric soot formation rate ($\dot{\omega}_{sf}'''$ and $\overline{\dot{\omega}_{sf}'''}$), and the volumetric soot oxidation rate ($\dot{\omega}_{so}'''$ and $\overline{\dot{\omega}_{so}'''}$). The results correspond to the FM-Burner at 20.9% O_2 coflow.

ignored in our models. Note that radiation intensity and soot formation/oxidation rates vary non-linearly with temperature, and vice-versa.

Figure 4.15 shows the profiles of the mean and the *rms* of the soot volume fraction obtained from experimental measurements and from the simulations with the WSGG model. The results show that the simulations overpredict these quantities near the centerline of the burner (by up to factor 5) and underpredict them when moving toward the burner edge. We believe that at low elevations (i.e. $< 1 D$) the

flame base is weakly turbulent, and the use of the β – PDF model (which is mainly dependent on turbulent fluctuations) to estimate unresolved subgrid-scale quantities may not be appropriate. Thus, an alternative way to correct the volumetric soot formation/oxidation rates for under-resolved simulations is needed (perhaps an idea similar to that presented in appendix B for estimating the combustion heat release rate in under-resolved simulations is needed).

4.3.3 Radiant emissions

We now turn to discuss thermal radiation from this sooting flame. In terms of global quantities, the simulations using WSGG radiation and LSP soot models predict that 28% (20.9%) of the total heat release of the flame (i.e., 15 kW) is due to soot oxidation at 20.9% O_2 (15.2%) coflow condition. The simulation results also suggest that radiation absorption by combustion products (i.e., H_2O , CO_2 , and soot) is equivalent to 17% of the total heat release rate, with soot contributing 4% of radiation absorption. The radiation emission due to combustion products is estimated to be 51% of the total heat release rate with soot contributing 18% of radiation emission. Overall, the estimated net radiant fraction (i.e., emission-absorption) is 0.33 (0.28) at 20.9% O_2 (15.2%) coflow condition, compared to an experimental value of 0.34 (0.22).

Figure 4.16 presents the vertical distribution of the radiation power per unit surface area of horizontal planes above the burner surface. These distributions are shown at 20.9% and 15.2% O_2 concentrations in the coflow. From a qualitative

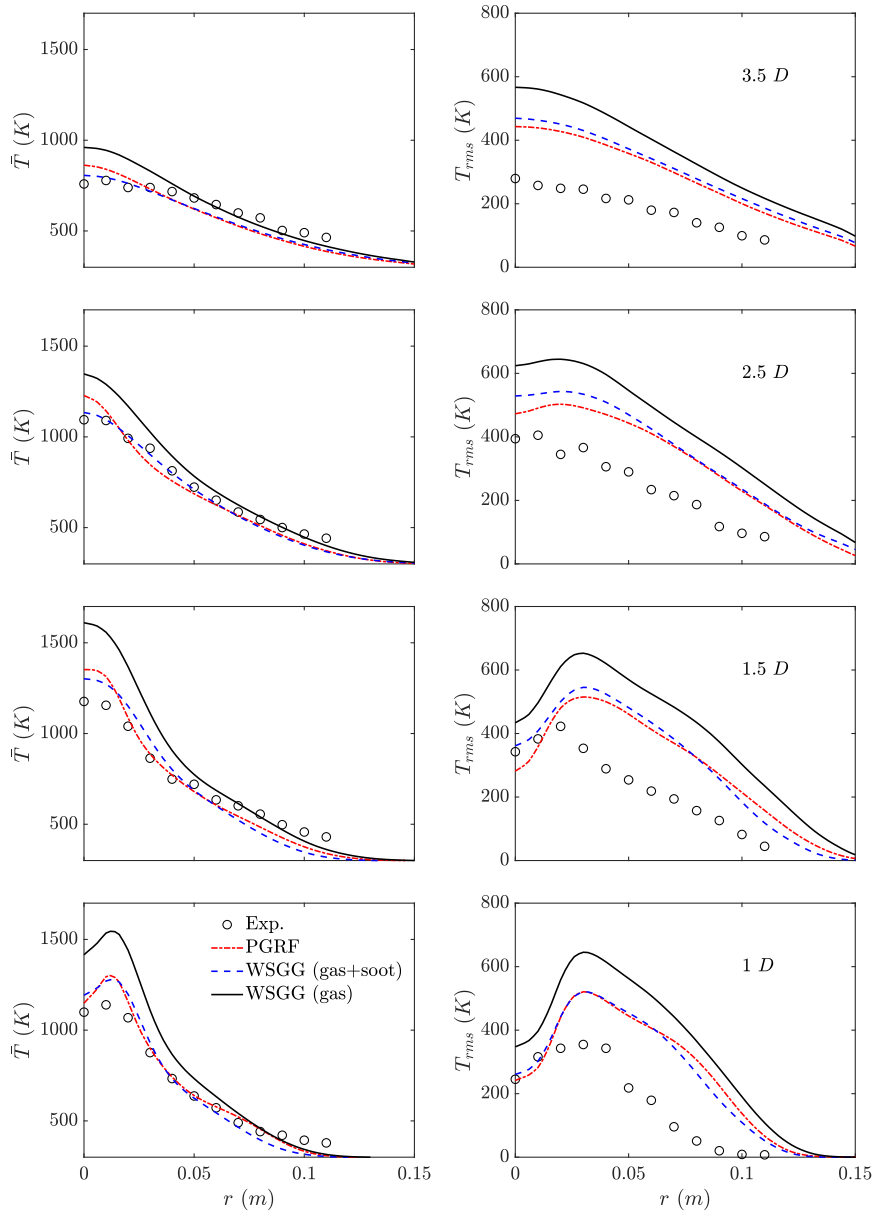


Figure 4.14: Radial profiles of mean and *rms* temperature at different elevations above the fuel surface in the FM-Burner at 20.9% O_2 coflow. Comparison between experiments (symbols) and simulations with PGRF (red dash-dot line), WSGG with gas and soot absorption/emission (blue dashed line), and WSGG with gas radiation only (solid black line).

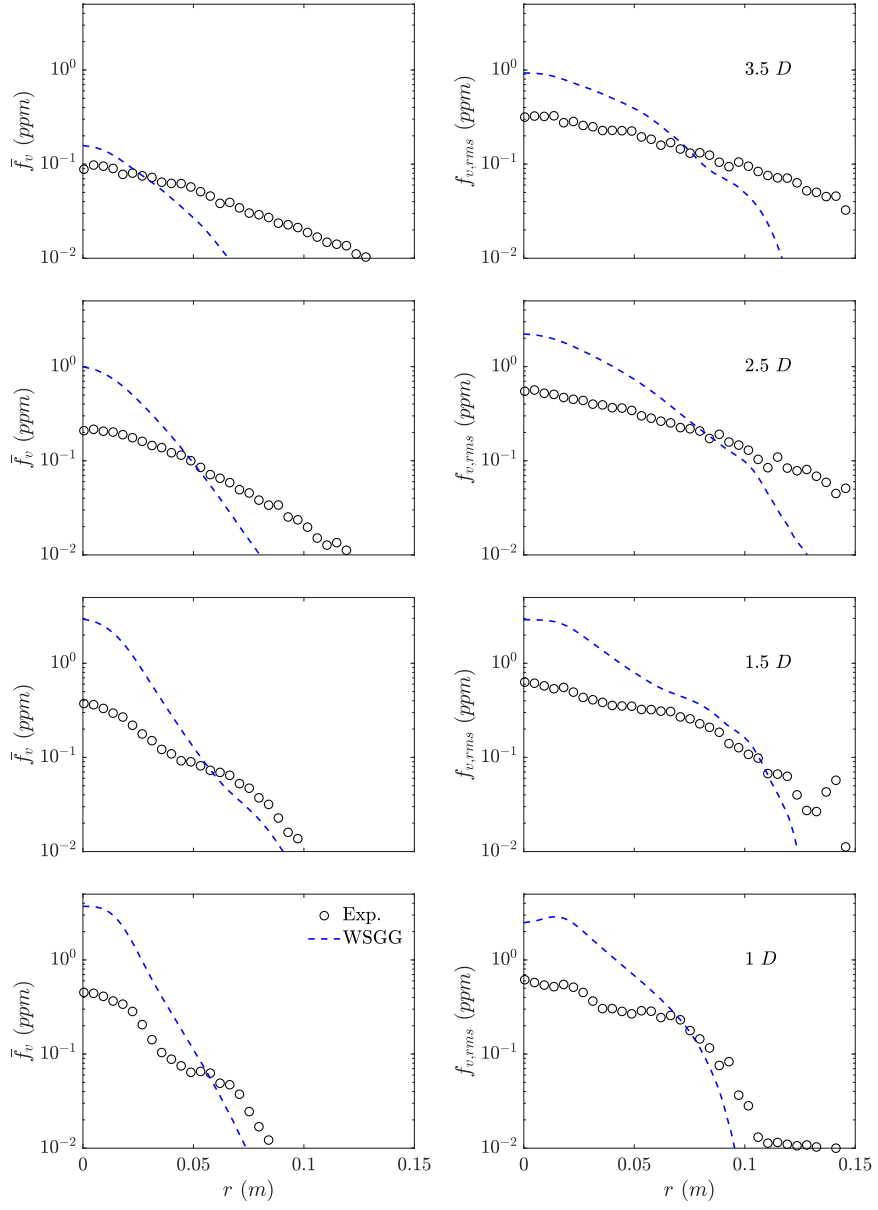


Figure 4.15: Radial profiles of mean and *rms* soot volume fraction at different elevations above the fuel surface of the FM-Burner at 20.9% O_2 coflow. Comparison between experiments (symbols) and simulations with the WSGG model (blue dashed line).

perspective, the simulation results obtained with PGRF and WSGG models show a behavior similar to experimental data in which the radiation power exhibits a short decline when moving slightly upward from the burner surface followed by a rapid increase to a peak value at about 0.3 m above the surface (equivalent to $\sim 2\text{ D}$), then followed by a gradual decline when moving to higher elevations. We believe that the increase in the radiation power at 0.3 m elevation is correlated with the tip of the necking region (see Fig. 4.10) where the flame shows a puffing behavior. The simulations results obtained with the PGRF model and the WSGG model (with gas and soot contributions) show fair agreement with experimental measurements in the case of $20.9\%O_2$ coflow and are off by a maximum of $\sim 25\%$. A better agreement is seen in the case with reduced oxygen.

To understand the source of discrepancies, we performed simulations with the WSGG model where we do not account for the contribution of soot to the radiation field (the black solid line in Fig. 4.16a). We notice that the model significantly under-predicts the radiation power in this case, which suggests that a large portion of the radiation field is attributed to soot emissions. Furthermore, Figure 4.17 shows that, with the WSGG model that accounts for soot radiation, the radiation emission as well as absorption are significantly large near the base of the flame which correspond to over-estimated soot volume fractions in this region (see Fig. 4.15). These data suggest the need for further development of the soot modeling approach which is beyond the scope of this dissertation and is left for future work.

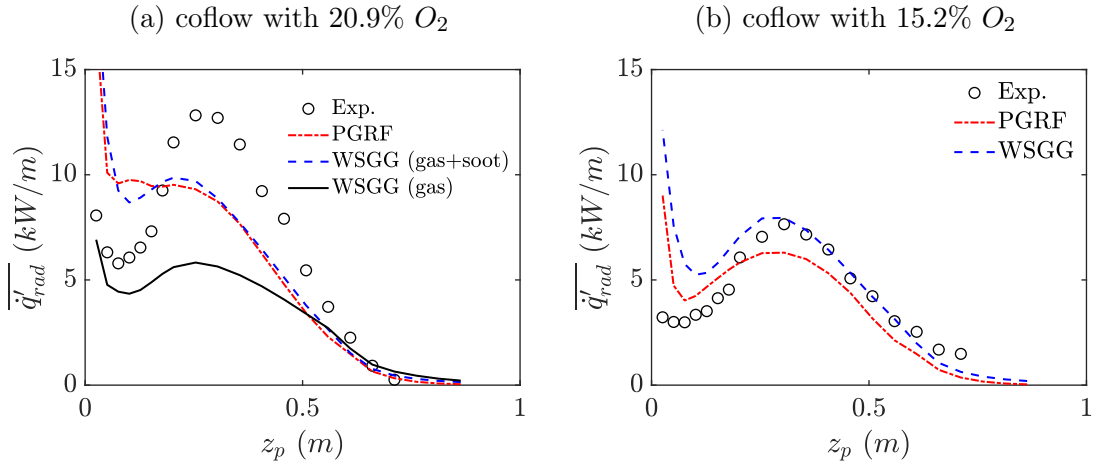


Figure 4.16: Axial variations of the mean radiative power of the FM-Burner at 20.9% O_2 and 15.2% O_2 concentrations in the coflow. Comparisons between experimental data (symbols) and simulations performed with the PGRF model (dotted red line), the WSGG model with gas and soot contributions (dashed blue line), and the WSGG with gas contribution only (solid black line).

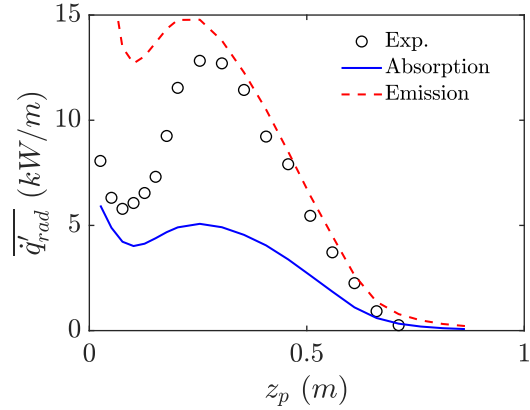


Figure 4.17: Axial variations of the radiation absorption and emission of the FM-Burner at 20.9% O_2 concentrations in the coflow. The results are estimated using the WSGG model accounting for gas and soot radiation.

4.4 Summary

This chapter presented comparisons between experimental data and simulation of two canonical configurations that have been identified by the MaCFP working group as target cases for validating fire models. The configurations correspond to a non-sooting methanol pool fire and a sooting buoyancy-driven turbulent ethylene burner. The main objective of this chapter was on evaluating the accuracy of the combustion and radiation models to predict the flame structure and the radiant emissions in these non-sooting and sooting flames.

In terms of flame structure, temperature fields, and thermal feedback, the numerical results are found to range from fair to very good agreement with experimental measurements. In particular, the results related to a quantification of the thermal feedback are of particular interest in the present study. The results suggest that the thermal feedback is estimated within 25% error using the PGRF modeling approach in non-sooting and sooting flames. The simulations with WSGG show a significant dependence on soot radiation which suggest the need for accurate estimations of the soot field. The results also suggest the need for more accurate modeling of soot at the subgrid level where soot formation/oxidation rates are strongly under-resolved by LES grid cells.

In summary, given the complexity associated with soot modeling and the computational burden associated with the WSGG model, and since the PGRF predictions seem to be very close to that of the WSGG where both are within an acceptable deviation from the experimental measurements, we will move forward

with the PGRF approach as our baseline radiation modeling choice in the spreading fire configurations presented later in this dissertation.

5 Simulations of Thermal Degradation of Biomass Particles under Prescribed External Gas Conditions¹

5.1 Overview

Biomass vegetation particles play a crucial role in the behavior and spread of wildland fires as they are the primary fuel source for these fires. During fire propagation, the heat is transferred from the hot gases surrounding the particles, in the form of either convection, radiation, or a mix of both, to the exposed surface of the biomass vegetation particles. The response of the biomass vegetation particles to this external heating depends on many factors, including the duration of this heating period, the intensity of the heat load, the size of the particle, and the ambient wind speed. Moreover, due to the unsteady turbulent nature of wildland fires, the biomass vegetation fuel is exposed to conditions that may be fluctuating over time, and it is not clear whether these fluctuating conditions have strong effects on the particle behavior as opposed to steady conditions that represent the time-average values of the fluctuations. We use in this chapter the stand-alone PBR model to characterize the response of the biomass vegetation particles to prescribed external

¹Parts of this chapter are taken from the publication by Ahmed and Trouvé [43]

heating conditions that are approximated to represent conditions similar to those found in wildland fires.

The first part of this chapter focuses on the pyrolysis of charring and non-charring biomass particles under steady and oscillatory radiative or convective heat fluxes. The heat fluxes are characterized by sinusoidal oscillations of the irradiance, the gas temperature, and/or the gas velocity. The objective here is to study whether the particle response is going to be affected by the presence of oscillations in external gas conditions. We aim to identify conditions in which oscillations are observed in the particle's temperature and mass loss rate, and to identify the significance of these oscillations on the global particle behavior in terms of ignition and burnout times.

In the second part of this chapter, we focus on the pyrolysis and the oxidation of char in porous biomass particles. We present 2-D maps to characterize the burning behavior of different size particles under a range of intensity and duration of the incident heat fluxes as well as a range of ambient wind speeds. Our objective here is to understand the effects of heating or cooling and the increase or decrease of the oxygen supply to the particles on the ignition and the degree of complete combustion of the particles. Our specific objective is to identify conditions at which the particles ignite, release enough flammable fuel for flaming combustion, self-sustain their combustion after the heat load is removed, and successfully transition from flaming combustion to smoldering combustion.

5.2 Pyrolysis of biomass particles under steady and oscillatory heating conditions

We consider here two separate cases corresponding to radiative heating or convective heating. We apply these conditions to two extreme scenarios of either a particle that features complete charring at constant volume or a particle that features shrinkage and complete gasification without charring. We also consider thick rectangular-shaped particles that are 20 mm thick ($\delta = 10 \text{ mm}$), as well as thin particles that are 2 mm thick ($\delta = 1 \text{ mm}$).

For simplicity, we focus our analysis on the burning behavior in terms of pyrolysis only. Thus, all particles considered in this section are assumed to be dry and non-porous. The particle material properties and the kinetic parameters of the pyrolysis reaction R_p are adopted from Ref. [98]. A summary of the input parameters used in this study is listed in Table 5.1.

The oscillations of the local gas temperature, T_g , local gas velocity, u_g , and the irradiation flux, G , are characterized by cosine functions of time with a given amplitude and frequency:

$$T_g = T_{g,m} - T_{g,a} \cos(\omega t) ; \quad u_g = u_{g,m} - u_{g,a} \cos(\omega t) \\ \text{and} \quad G = G_m - G_a \cos(\omega t) \quad (5.1)$$

where subscripts m and a refer to the mean value and the amplitude of the oscillations, respectively, where also $\omega = 2\pi f$, with f the frequency of the oscillations. We assume that oscillations in the local gas temperature and irradiation are independent, and

Table 5.1: Input parameters of the biomass particles used in the oscillatory heating study.

Quantity	Value
$\rho_{ds,bulk}$ (kg/m^3)	663
$\rho_{c,bulk}$ (kg/m^3)	132.6
k_{ds}, k_c ($W/m/K$)	0.126
c_{ds}, c_c ($J/kg/K$)	2520
$\epsilon_{ds}, \epsilon_c$ (-)	0.9
A_{Rp} ($1/s$)	5.25×10^7
E_{Rp} (J/mol)	1.256×10^5
n_{Rp} (-)	1
ΔH_{Rp} (kJ/kg)	0
$\eta_{c,Rp}$ (-)	0 or 0.2

we study each case separately. In the radiative forcing case, $T_{g,m} = 300 K$, $T_{g,a} = 0$, and $u_{g,m} = u_{g,a} = 0$; in the convective forcing case, $G_m = G_a = 0$, and $\epsilon_{p,surf} = 0$.

We simulate cases corresponding to particles exposed to either oscillatory radiative forcing by ($G_m = G_a = 80 kW/m^2$), particles exposed to oscillatory convective forcing by oscillations in the gas temperature only ($T_{g,m} = 700 K, T_{g,a} = 400 K, u_{g,m} = 1 m/s$, and $u_{g,a} = 0$), or particles exposed to oscillatory convective forcing by oscillations in both the gas temperate and the gas velocity ($T_{g,m} = 700 K, T_{g,a} = 400 K, u_{g,m} = 1 m/s$, and $u_{g,a} = 1 m/s$). We select oscillations at low or high frequencies ($f = 0.1$ or 1 Hz), and particles that are either charring and at constant volume ($\eta_{c,Rp} = 0.2$) or shrinking and non-charring ($\eta_{c,Rp} = 0$). The selected values for $G_m, G_a, T_{g,m}, T_{g,a}$ and f are chosen based on reported field measurements [99–102]; the selected values for $u_{g,m}$ and $u_{g,a}$ are educated guesses.

5.2.1 Particle response time

From a simplified theoretical analysis of thermally-thin particles, we find that the parameter ($\omega\tau_p$) is a controlling factor in the particle response to an oscillatory heat flux, where τ_p is the characteristic particle response time. In the case of convective heating, $\tau_p = (\rho_p c_p \delta / h)$; in the case of radiative heating, $\tau_p = (\rho_p c_p \delta / h_t)$, where $h_t = h + h_{rad}$ with $h_{rad} \approx 4\epsilon_p \sigma T_p^3$. Lower (higher) frequencies will result in larger (smaller) fluctuations in T_p . And cases with large (small) values of h or h_t will result in larger (smaller) fluctuations in T_p . This analysis can be extended to the case of thermally-thick particles, with some modification. The characteristic response time of thick particles is $\tau_p = (k_p \rho_p c_p / h^2)$ in the case of convective heating, and $\tau_p = (k_p \rho_p c_p / h_t^2)$ in the case of radiative heating (note that these estimates consider properties at the particle surface and essentially measure the particle response at the exposed surface). Also, the temperature fluctuations are limited to a region located at the exposed surface and are otherwise damped in the depth of the particle; an estimate of the thickness of the surface region where temperature fluctuations are significant is $\delta_{oscillation} = \sqrt{2(k_p/\rho_p c_p)/\omega}$ (see Refs. [43, 103]).

5.2.2 Response of thick charring particles to radiative heating

Figure 5.1 shows the overall response of a thick charring particle to oscillatory radiative heating. Figure 5.1a presents the corresponding time variations of the temperature, T_p , evaluated at both the surface ($x = \delta$) and center of the particle ($x = 0$), for $f = 0.1$ and 1 Hz. The plots also include results obtained in the

corresponding case without heat flux oscillations. We first note that the magnitude of the surface oscillations is larger in the lower frequency case. This effect can be explained by a comparison of time scales as discussed earlier: the calculations suggest that for this case, $\tau_p = (k_p \rho_p c_p / h_t^2)$ is of order 1 s; thus, for $f = 0.1$ Hz, $(\omega \tau_p) \approx 0.6$, and for $f = 1$ Hz, $(\omega \tau_p) \approx 6$, which corresponds to much-reduced amplitudes (the earlier discussion suggests that the amplitude of fluctuations decrease when the parameter $(\omega \tau_p)$ increases).

Figure 5.1a shows that the center of the particle does not exhibit any oscillation. This may be explained by the fact that oscillations are only present in a limited region close to the exposed surface, i.e., for $(\delta - \delta_{oscillation}) \leq x \leq \delta$. In the present case, $\delta_{oscillation} = \sqrt{2(k_p/\rho_p c_p)/\omega}$ is smaller than δ and the center of the particle remains quasi-steady.

Figure 5.1b presents the corresponding time variations of the MLR. The data presented in Fig. 5.1b are of great interest since the pyrolysis MLR is a measure of the rate of supply of fresh fuel for the combustion process. We see that the MLR features oscillations for a limited time only: after this initial period, MLR relaxes to a quasi-steady behavior. This finding can be explained by the displacement of the thin pyrolysis reaction zone that migrates from the surface of the particle to its center; when the location of the pyrolysis reaction zone is at a distance to the surface greater than $\delta_{oscillation}$, pyrolysis takes place in a region that is free of temperature oscillations and MLR becomes quasi-steady. Figure 5.1b shows that in the case $f = 0.1$ Hz, MLR oscillations are present for $t \leq 200$ s, while in the case $f = 1$ Hz, MLR oscillations are present for $t \leq 50$ s. The difference in behavior

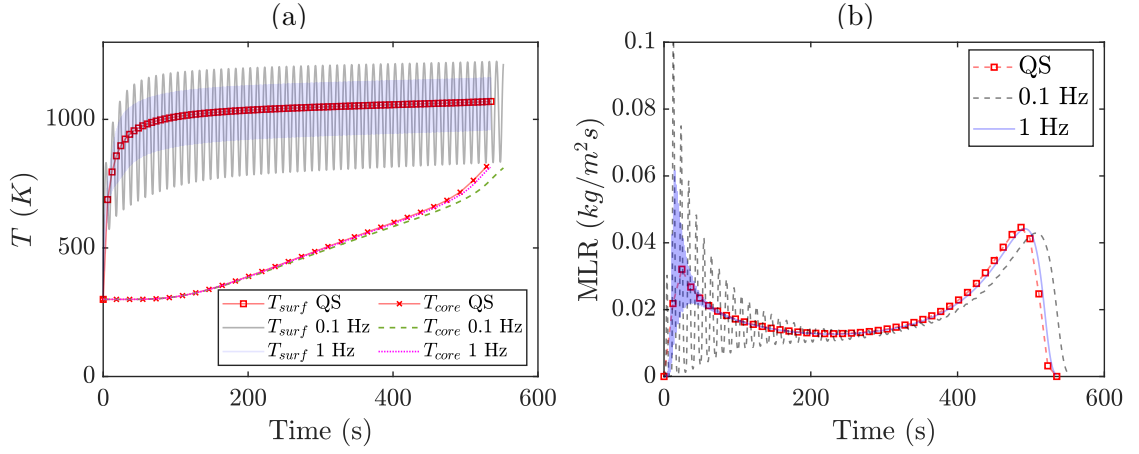


Figure 5.1: Response of a 20 mm -thick charring particle to radiative heating: a) particle surface and core temperatures; b) particle mass loss rate. Comparison between particle response to quasi-steady forcing (QS) (lines with symbols) and oscillatory forcing at $f = 0.1 \text{ Hz}$ or $f = 1 \text{ Hz}$ (lines).

when changing the oscillation frequency is explained by the difference in the size of the surface region where temperature fluctuations are significant: the thickness $\delta_{oscillation} = \sqrt{2(k_p/\rho_p c_p)/\omega}$ is reduced by a factor 3.2 when going from $f = 0.1 \text{ Hz}$ to $f = 1 \text{ Hz}$.

A numerical evaluation of the ignition and burnout times for this case is summarised in Table 5.2. Overall, we find that the thick charring particle exposed to oscillatory radiative heating corresponds to a quasi-linear response in which the net effect of oscillations remains small and the mean particle behavior is well represented by a simulation without heat flux oscillations.

Table 5.2: Ignition and burnout times of particles exposed to quasi-steady (QS) radiative heating and oscillatory radiative heating at 0.1 and 1 Hz. The percentage difference in burnout time is calculated relative to the QS case.

Case	Frequency (Hz)	Ignition time (s)	Burnout time (s)	Difference in burnout time (%)
Thick charring	QS	12.2	529.1	0
	0.1	2.7	552.3	+4
	1	7.3	534.4	+1
Thick non-charring	QS	8.1	158.1	0
	0.1	2.5	162.1	+3
	1	6.4	162.3	+3
Thin non-charring	QS	7.3	16.4	0
	0.1	2.5	14.1	-14
	1	6.3	16.4	0

5.2.3 Response of thick non-charring (shrinking) particles to radiative heating

Figure 5.2 presents results of a 20 mm-thick non-charring particle exposed to oscillatory radiative heating, for $f = 0.1$ and 1 Hz, and $\eta_c = 0$. In contrast to the charring particle, the particle is now shrinking in size, and the particle half-thickness approaches zero at burnout time ($\delta \approx 0$).

Many of the features observed in the charring particle case are also present in this case. Compared to the charring particle, this case features larger values of MLR

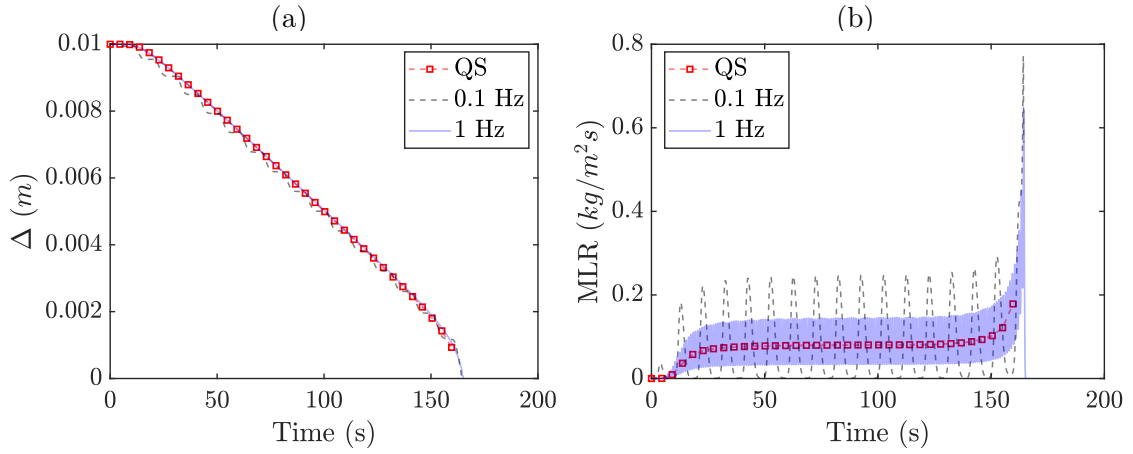


Figure 5.2: Response of a 20 mm thick non-charring particle to radiative heating: a) particle size; b) particle mass loss rate. See caption of Fig. 5.1.

and shorter burnout times. The larger values of MLR and shorter burnout times are typical of pyrolysis in non-charring materials: in contrast to charring materials in which the pyrolysis region migrates to the particle center and is therefore exposed to temperatures lower than those at the surface, in non-charring materials the pyrolysis region remains at the surface and is always exposed to the highest temperatures found in the particle.

Furthermore, it is seen that in contrast to the charring particle, oscillations in MLR here are present during the entire burning phase. This result may be explained by the location of the pyrolysis region: the pyrolysis region remains at the exposed surface of the particle, i.e., at the location of maximum amplitude in temperature fluctuations. The same argument also explains why the amplitude of MLR fluctuations is larger in the non-charring particle than in the charring particle case.

Overall, while details are different, we find that similar to the charring particle case, the non-charring particle corresponds to a quasi-linear response in which the net effect of oscillations remains small.

5.2.4 Response of thin non-charring (shrinking) particles to radiative heating

We now turn to much thinner particles with a thickness of 2 mm . Figure 5.3 presents results in the case of oscillatory radiative heating, for $f = 0.1$ and 1 Hz, and $\eta_c = 0$. Consistent with the thicker particles presented in the two previous cases, the time evolution of the particle temperature shown in Fig. 5.3a features oscillations at a higher magnitude in the case of 0.1 Hz than in the case of 1 Hz. We also see that there is a spike in the temperature oscillations near burnout as the particle shrinks. This is because as the particle size (δ) approaches 0, its response time takes decreasing values ($\tau_p = \rho_p c_p \delta / h_t$) and it becomes more sensitive to oscillations in the incident irradiance which oscillates from ambient to 160 kW/m^2 .

Figures 5.3b present the time variations of the MLR of these thin particles. The MLR displays strong oscillatory behavior and we see some limited non-linear effects (in which the net effect of oscillations is significant and the mean particle behavior is not well represented by a simulation without heat flux oscillations). As a result of stronger fluctuations in the 0.1 Hz case, the burnout time is modified by $\sim 14\%$ as shown in Table 5.2.

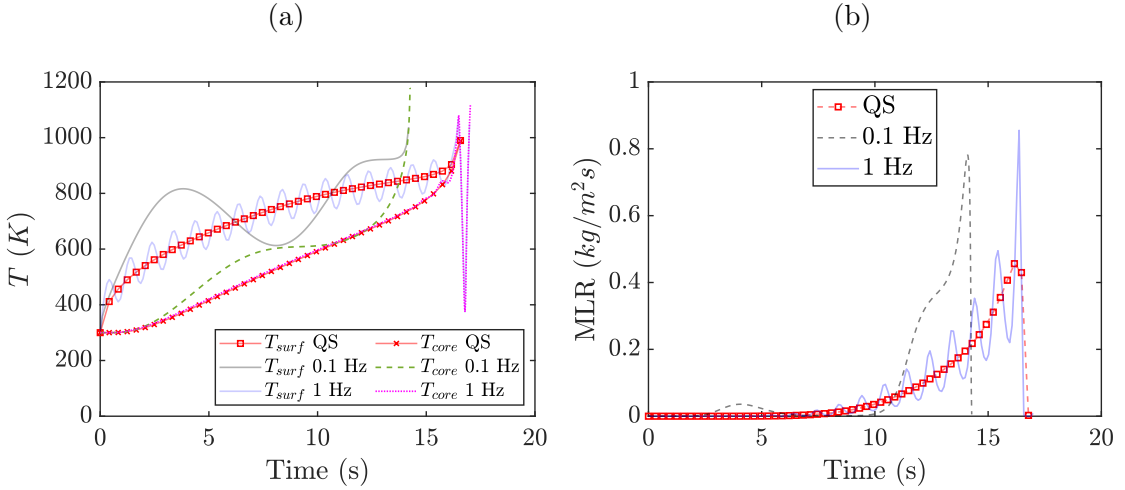


Figure 5.3: Response of the 2 mm non-charring particle to radiative heating: a) particle surface and core temperatures; b) particle mass loss rate. See caption of Fig. 5.1.

5.2.5 Response of thin particles to convective heating

In contrast to all previous cases, oscillations in the rate of gas-to-solid heat transfer now come from oscillations in the temperature (and possibly the velocity) of the gas surrounding the particle.

We first discuss a scenario of a thin non-charring particle (thickness = 2 mm and $\eta_c = 0$) exposed to oscillatory gas temperate only. Figure 5.4a presents the corresponding time variations of the particle temperature evaluated both at the surface and center of the particle. Similar to the previous cases, we see oscillations in the particle temperature at both frequencies, with a smaller amplitude in the high-frequency case. These oscillations in the particle temperature fluctuate around the corresponding particle temperature obtained at quasi-steady heating. Also, the

amplitude of the oscillations increases in time as the particle approaches burnout. This effect may be explained by considering the particle response time introduced earlier ($\tau_p = \rho_p c_p \delta / h$). As the thickness of the particle approaches 0, the particle size δ takes decreasing values, the heat transfer coefficient, h , takes increasing values, and the particle response time takes decreasing values. Under those conditions, the particle gradually evolves towards the fast-response regime in which the amplitude of the fluctuations is maximum.

Figure 5.4b presents the corresponding time variations of the MLR. The amplitude of the MLR oscillations increases in time as a consequence of the growing oscillations in the particle temperature. A numerical evaluation of the ignition and burnout times for this case is shown in Table 5.3. We see some non-linear effects in the presence of fluctuations as the burnout time is modified by up to 50%.

We now turn to the scenario where the oscillations in the convective heat flux are due to oscillations in both T_g and u_g . Figure 5.5a presents the time variations of T_p , evaluated at both the surface and the center of the particle. The main features of the temperature curves in the cases with oscillatory convective heating are similar to those of the previous case in which oscillations exist at in the particle surface temperature with higher amplitude at the lower frequency case. However, compared to the quasi-steady case without oscillation, we see that due to the augmentation of the rate of heat transfer provided by the fluctuations in both h and T_g , the particle achieves higher temperatures.

Figure 5.5b presents the corresponding time variations of MLR. These plots show strong non-linear effects and show in particular that in the presence of oscillations,

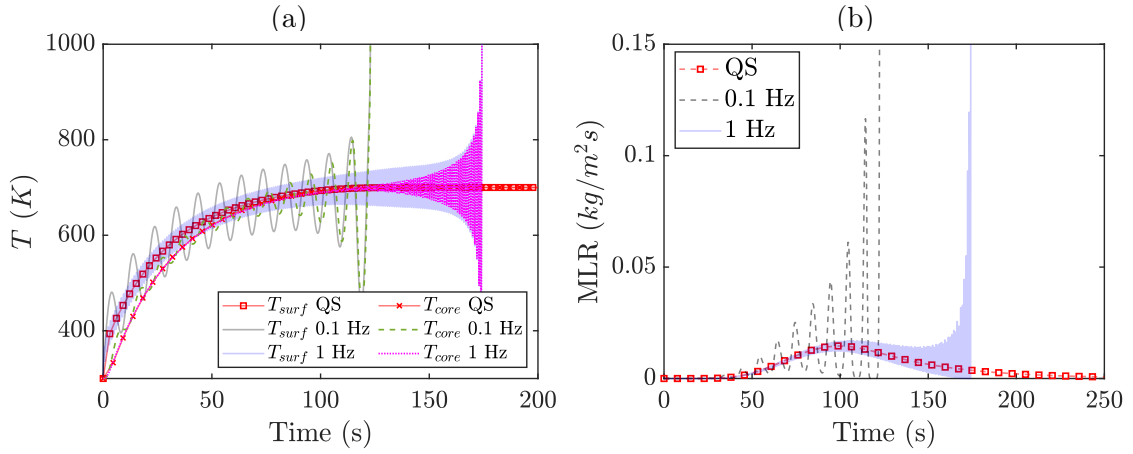


Figure 5.4: Response of a 2 mm non-charring particle to convective heating: a) particle surface and core temperatures; b) particle mass loss rate. Comparison between the particle response to quasi-steady forcing (QS) (lines with symbols) and oscillatory forcing by oscillations in T_g at $f = 0.1$ Hz or $f = 1$ Hz (lines).

the ignition and burnout times are significantly reduced and the peak MLR value is significantly increased. These effects are explained by the augmented heat transfer due to the fluctuations in h and T_g . A numerical evaluation of the ignition and burnout times for the different simulations considered in this case is presented in Table 5.3. In short, this case shows strong non-linear effects: in the presence of fluctuations, the burnout time is decreased by up to 70%.

5.2.6 Response of thick particles to convective heating

In contrast to the previous case, this case corresponds to much thicker particles exposed to oscillatory convective heating due to fluctuations in T_g and u_g . Figures 5.6 present the time variations of MLR in the case of oscillatory convective heating, for

Table 5.3: Ignition and burnout times of particles exposed to quasi-steady (QS) convective heating and oscillatory convective heating at 0.1 and 1 Hz. The percentage difference in burnout time is calculated relative to the QS case.

Case	Frequency (Hz)	Ignition time (s)	Burnout time (s)	Difference in burnout time (%)
Thin non-charring oscillatory T_g only	QS	56.3	222.0	0
	0.1	43.5	112	-50
	1	54.5	142.2	-36
Thin non-charring oscillatory T_g, u_g	QS	56.3	222.0	0
	0.1	32.1	62.7	-72
	1	33.3	63.2	-72
Thick non-charring oscillatory T_g, u_g	QS	1485.1	2227.7	0
	0.1	834.3	1412.5	-37
	1	869.3	1398.1	-37
Thick charring oscillatory T_g, u_g	QS	1591.2	2837.6	0
	0.1	903.8	1801.2	-37
	1	933.5	1776.8	-37

$f = 0.1$ and 1 Hz, thickness = 20 mm and $\eta_c = 0$ (non-charring particles) or $\eta_c = 0.2$ (charring particles). Both cases use velocity fluctuations, $u_{g,a} = 1$ m/s. The MLR features growing oscillations in time, a feature that is similar to that found in thin particles presented in the previous case. Also similar to the case of radiative heating of charring particles, the MLR in this convective heating case features oscillations for a limited time only. As shown in table 5.3, consistent with observations made in thin particles, in the presence of oscillations in the convective heat flux, the ignition and burnout times are significantly reduced and the peak MLR value is significantly increased.

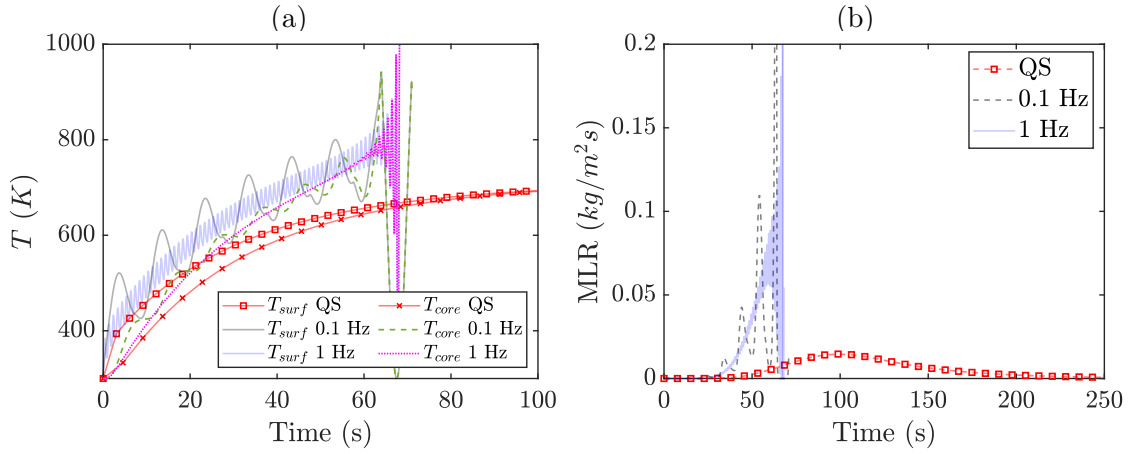


Figure 5.5: Response of a 2 mm non-charring particle to convective heating: a) particle surface and core temperatures; b) particle mass loss rate. Comparison between the particle response to quasi-steady forcing (QS) (lines with symbols) and oscillatory forcing by oscillations in both T_g and u_g at $f = 0.1$ Hz or $f = 1$ Hz (lines).

To summarise this section, the results of the numerical simulations suggest that the particles experience a quasi-linear response in the case of fluctuating irradiation (or fluctuating local gas temperature only). This linear response means that the effects of oscillations can essentially be ignored, even when temperature and mass loss rate oscillations are strong. And the mean particle behavior is well represented by a simulation without oscillations in the external heating conditions. However, some non-linear response is obtained in the case of unsteady convective heating (when the local gas velocity fluctuates in phase with the local gas temperature). This non-linear response leads to a net effect of the oscillations in the form of an augmented heat transfer, higher temperatures, higher values of the fuel mass loss rate, and shorter burnout times, and the particle behavior may be misrepresented if

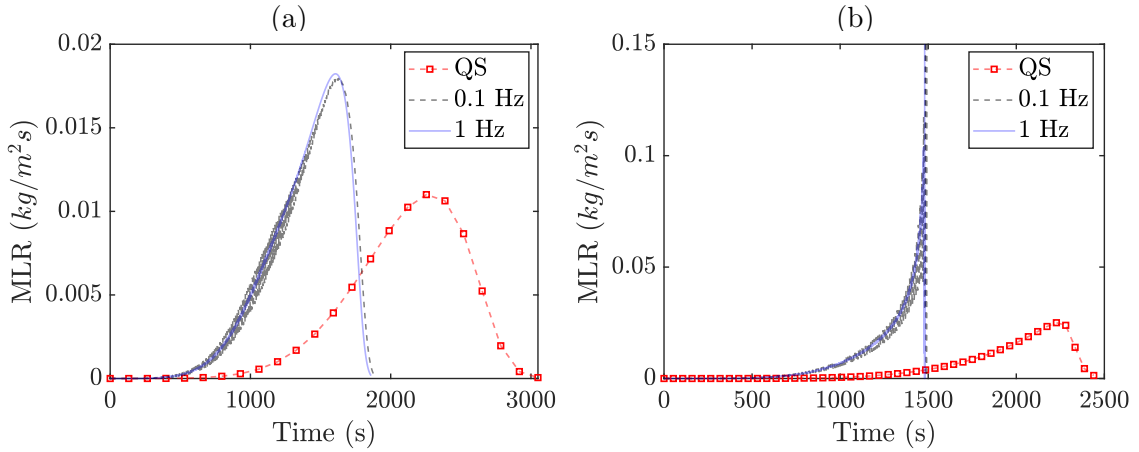


Figure 5.6: Mass loss rate response of the a 20 mm thick particle to radiative heating; a) non-charring; b) charring. See caption of Fig. 5.5

the unsteady convective heating is ignored.

5.3 Maps of the pyrolysis and oxidation of porous biomass particles

This section presents 2-D maps that characterize the thermal degradation of porous biomass particles under prescribed heating conditions. These characteristics are discussed in terms of the degree of completion of the drying, thermal and oxidative pyrolysis, and char oxidation reactions (Rd - Rco), the rate of production of gaseous fuel, and the peak particle temperature. Our objective is to identify conditions in which the particles can ignite and produce sufficient gaseous fuel for flaming combustion, and conditions in which the particle transition from flaming to a partial or complete smoldering combustion.

We consider in this section cylindrical-shaped porous particles made of the pine wood described in Chapter 3. The particles are imagined to be immersed in a

spreading flame that passes across the particle and heats it for a certain duration known as the residence time. We focus here on residence time defined as the time at which the particle is being heated by external convection or radiation or a combination of both.

First, let us consider a 10 mm diameter particle exposed to an external irradiation of $G = 60\text{ kW/m}^2$ for a duration of 60 s that mimics a flame residence time. After 60 s , the external irradiation drops to the ambient value of $G = G_0 = \sigma T_{g,0}^4$, where $T_{g,0} \approx 300\text{ K}$. The particle is also exposed to ambient air flowing at $u_g = 1\text{ m/s}$ and $T_{g,\infty} = 300\text{ K}$ for its lifetime. Note that during the flame spread, the oxygen level in the vicinity of the particle may fluctuate between ambient level to zero because of the turbulent flames produced from the homogeneous gas-phase reaction between the pyrolysis fuel and the ambient oxygen. Therefore, this assumption is viewed as the extreme case in which the particle can always have access to oxygen. The variation of oxygen concentration in the vicinity of the particle during the flame spread will be discussed in the following chapters.

Figure 5.7 shows the response of this 10 mm particle in terms of the time variation of the net total heat flux ($\dot{q}_{g \rightarrow s}'' = h(T_{g,\infty} - T_{p,surf}) + \epsilon_{p,surf}(G - \sigma T_{p,surf}^4)$), the surface and core temperatures, the convective heat transfer coefficient (h), and the particle surface emissivity ($\epsilon_{p,surf}$). The corresponding time evolution of the reaction rates of *Rd-Rco*, as well as the normalized mass of solid constituents (i.e., wet solid, dry solid, char, and ash), are shown in Fig. 5.8. As shown in Fig. 5.7, the net total heat flux displays variations in the magnitude as well as the sign. These variations are dependent not only on the imposed external gas conditions (which are

constant in this case), but also on the response of the particle surface temperature ($T_{p,surf}$) as well as the instantaneous values of the local heat transfer coefficient (h) and the particle surface emissivity ($\epsilon_{p,surf}$). Note that the changes in the slope of the time variation of the temperature are due to the changes in the composition and the thermophysical properties of the solid associated with the thermal degradation process. Note also that the variations of h here are mainly due to the blowing of gases from the particle to the surrounding and partially due to changes in the particle surface temperature, and the variations of $\epsilon_{p,surf}$ are due to the formation of a char or ash layer at the particle surface.

The results presented in Fig. 5.8 show that the drying and the pyrolysis reactions are stopped during the first 60 s when the external heat source existed, and the particle is converted from wet solid to dry solid and from dry solid to char. The char oxidation reaction, however, is self-sustained after the external heat source is removed. The degree of completion of these processes needs rigorous evaluation as they may vary according to the magnitude and duration of the external heat source.

Because of the variations of the net total heat flux with the particle response, this quantity can not be used directly as a global metric to compare the behavior of different particles. Therefore, we developed a novel diagnostic called the Pseudo Incident Heat Flux (PIHF), which determines the amount of external heat load that a particle is exposed to during a certain time. The PIHF depends mainly on the external gas conditions, and partially on the particle size through the heat transfer coefficient h . It also includes information on both the convective and the radiative contributions. Hence, it can be used to interpret the response of particles with

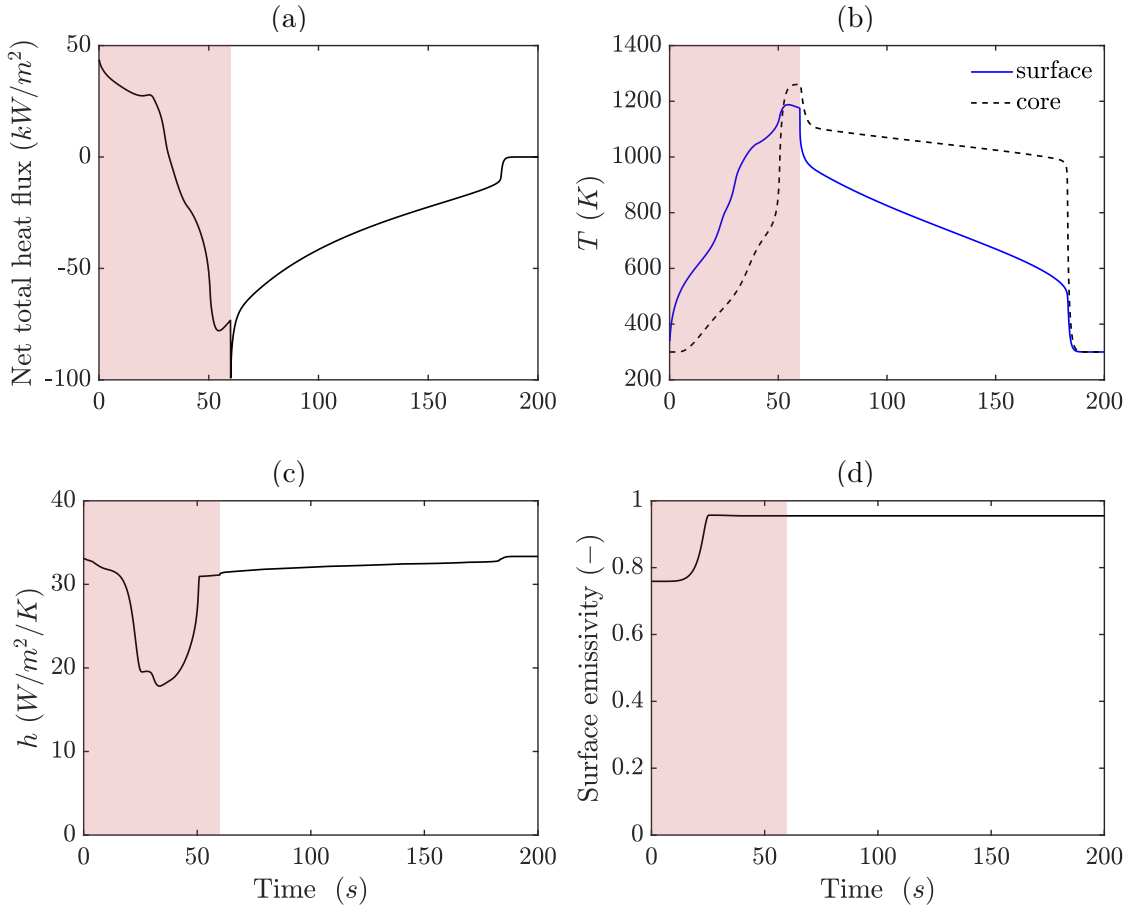


Figure 5.7: Response of a 10 mm particle to an external irradiation of $G = 60 \text{ kW/m}^2$ for 60 s, and ambient air flow at $u_g = 1 \text{ m/s}$: a) the net total heat flux; b) the surface and core temperatures; c) the convective heat transfer coefficient; d) the surface emissivity. The duration of the external irradiation is highlighted in red.

different sizes to different combinations of simultaneous convective and radiative heat loads, as well as to evaluate the respective weights of the convective and the radiative contributions using PIHF_{conv} and PIHF_{rad}, respectively.

We define the PIHF as a combination of the convective and the radiative

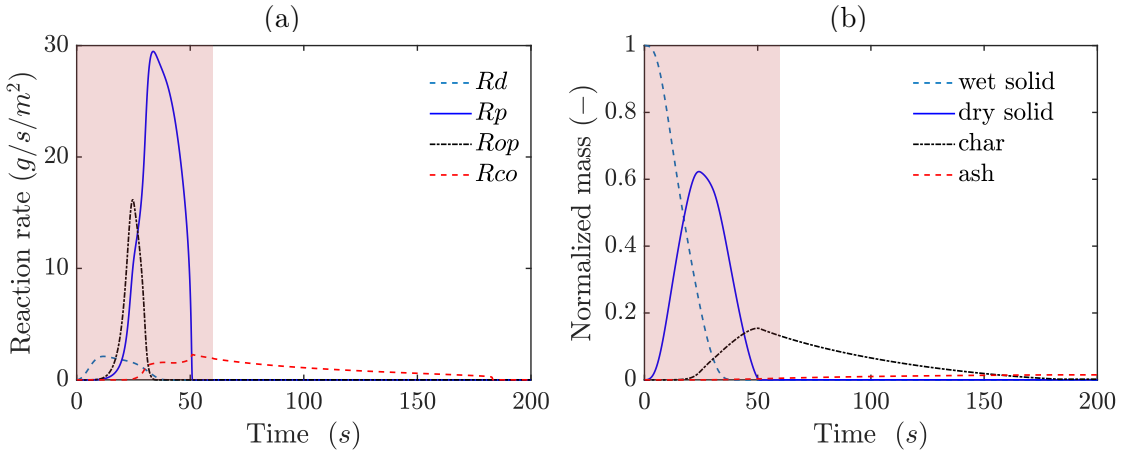


Figure 5.8: Response of a 10 mm particle to an external irradiation of $G = 60 \text{ kW/m}^2$ for 60 s, and ambient air flow at $u_g = 1 \text{ m/s}$: a) the reaction rates of R_d - R_{op} ; b) the normalized solid constituent mass. The duration of the external irradiation is highlighted in red.

contributions such that

$$\text{PIHF} = \begin{cases} \text{PIHF}_{conv} + \text{PIHF}_{rad} & \text{for } 0 \leq t \leq \tau_{\text{PIHF}} \\ \text{PIHF}_0 & \text{for } \tau_{\text{PIHF}} < t < t_{\text{end}} \end{cases} \quad (5.2)$$

where $\text{PIHF}_{conv} = h \times T_g$, $\text{PIHF}_{rad} = \epsilon_{p,surf} \times G$, τ_{PIHF} is the residence time (the duration) of an external heat source such as a flame, t_{end} the particle lifetime (or the total simulation time), and where PIHF_0 is evaluated at an ambient level such that

$$\text{PIHF}_0 = \epsilon_{p,surf} \times G_0 + h \times T_{g,0}, \quad (5.3)$$

where $T_{g,0}$ is the ambient temperature ($T_{g,0} \approx 300 \text{ K}$) and where G_0 is the ambient irradiance ($G_0 = \sigma T_{g,0}^4$).

In order to determine the degree completeness of the thermal degradation process, we integrate the mass reaction rates over the particle lifetime and we

normalize them by the corresponding theoretical mass of the solid constituent that is expected to be consumed to get a value between 0 and 1, where 0 indicates no consumption at all, and 1 indicates complete consumption. We calculate the degree of completion of the drying (E_{Rd}), the pyrolysis (E_{Rp+Rop}) and the char oxidation (E_{Rco}) reactions as follows:

$$\begin{aligned} E_{Rd} &= \frac{\int_0^\infty \int_{V_p} \dot{m}_{Rd}''' dV dt}{m_{ws}|_{t=0}} \\ E_{Rp+Rop} &= \frac{\int_0^\infty \int_{V_p} (\dot{m}_{Rp}''' + \dot{m}_{Rop}''') dV dt}{m_{ws}|_{t=0} \times E_{Rd} \times \eta_{ds,Rd}} \\ E_{Rco} &= \frac{\int_0^\infty \int_{V_p} \dot{m}_{Rco}''' dV dt}{(m_{ws}|_{t=0} \times E_{Rd} \times \eta_{ds,Rd}) \times E_{Rp+Rop} \times \eta_{c,Rp}} \end{aligned} \quad (5.4)$$

where \dot{m}_{Rd}''' , \dot{m}_{Rp}''' , \dot{m}_{Rop}''' and \dot{m}_{Rco}''' are the volumetric mass reaction rates for the drying, thermal pyrolysis, oxidative pyrolysis, and char oxidation reactions, respectively, discussed in section 2.2, and where $m_{ws}|_{t=0}$ is the initial mass of the wet solid before thermal degradation.

We now turn to a discussion about the 2-D maps that we generated using the above information. The 2-D maps are generated to cover a range of conditions corresponding to PIHF between 10 and 120 kW/m^2 , and gas velocity u_g between 0 and 5 m/s . The PIHF here can be entirely convective, entirely radiative, or a combination of both. Each point on the map is obtained from a simulation of the PBR model with input values of the PIHF, u_g , and τ_{PIHF} . Each simulation runs long enough until either the particle is completely consumed or a steady state condition is achieved. Note that as the wind velocity increases, the convective transfer coefficient h increases, and some regions on the map may have a value of PIHF below ($PIHF_0$). These regions are grayed out on the map as they correspond to unwanted conditions

of cooling below ambient level.

5.3.1 Effect of the particle size

5.3.1.1 Maps of small particles (2 mm diameter) heated for a long duration ($\tau_{\text{PIHF}} = 120\text{ s}$)

Figures 5.9a, 5.9b and 5.9c show 2-D maps of the variation of the degree of completion of the drying reaction (E_{Rd}), the pyrolysis reactions (E_{Rp+Rop}) and the char oxidation reaction (E_{Rco}), respectively, for a 2 mm diameter pine wood particle exposed to different combinations of PIHF and u_g for $\tau_{\text{PIHF}} = 120\text{ s}$. Figure 5.10a presents the corresponding maps of the peak pyrolysis rate (i.e., the peak rate of production of gaseous fuel from the thermal and oxidative pyrolysis reactions Rp and Rop). The threshold pyrolysis rate for flaming ignition is indicated by the iso-contour of 1 g/s/m^2 . The corresponding duration of the pyrolysis phase is shown in Fig. 5.10b.

Our first observation from these maps is that despite continuous heating at a fairly long period of $\tau_{\text{PIHF}} = 120\text{ s}$, some combinations of PIHF and u_g are not able to achieve either ignition (activation) or completion of the drying, pyrolysis and char oxidation processes. For example, Fig. 5.10a shows that there exists a region where the particle did not ignite at all even at a high PIHF of $\sim 80 - 100\text{ kW/m}^2$ (the region to the left of the 1 g/s/m^2 iso-contour). At very low wind speeds ($u_g \approx 0$), there is no loss of heat due to convective cooling, and the particle is always heated by the PIHF. Therefore, nearly all considered PIHF conditions near $u_g \approx 0$ achieve

complete drying, flaming ignition, and complete consumption. As u_g increases, the PIHF required to achieve flaming ignition increases to compensate for the increased loss of heat from the particle to the ambient gas associated with the high convective transfer. For instance, the minimum PIHF required for flaming ignition at 2.5 m/s estimated by the model is $\sim 50 \text{ kW/m}^2$, while the minimum PIHF required for flaming ignition at 5 m/s estimated by the model is $\sim 95 \text{ kW/m}^2$.

Figure 5.10b shows that the pyrolysis duration in the cases that achieved complete pyrolysis is not constant and is ranging between ~ 5 to ~ 20 seconds. We find that this duration depends on both the PIHF and the wind speed u_g at least for this small particle. The shortest pyrolysis duration is achieved at the highest PIHF but at low to moderate wind speeds. We also find that, because of the effect of the coupling between the exothermic oxidative reactions, the particle temperature, and the wind velocity, the peak rate of pyrolysis is achieved at high PIHF and high u_g values as seen in Fig. 5.10a. Therefore, it seems that the conditions of peak pyrolysis rate do not guarantee the fastest pyrolysis.

Figures 5.11a and 5.11b show maps of the maximum temperature achieved at any depth inside the particle during the entire thermal degradation process, and the maximum temperature of the particle core during the residence time τ_{PIHF} , respectively. While increasing the wind speed promotes the diffusion of oxygen into the particle which may increase the rate of the exothermic char oxidation and the overall particle temperature, it is not evident in Fig. 5.11a that the peak temperature increases monotonically with wind speed. For instance, if we consider a PIHF of 80 W/m^2 , the peak particle temperature increases from $\sim 1200 \text{ K}$ at wind speeds

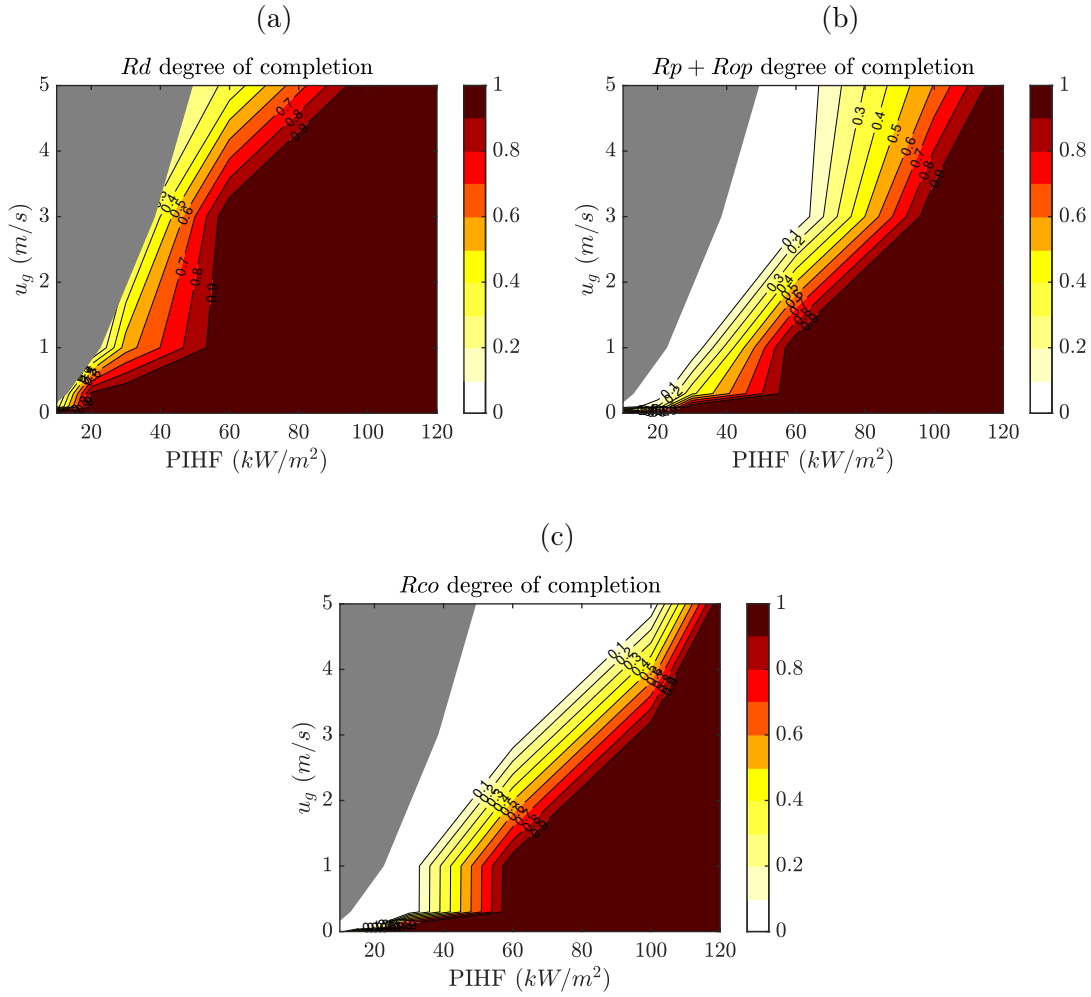


Figure 5.9: Maps of a 2 mm pine wood particle for $\tau_{\text{PIHF}} = 120 \text{ s}$: a) degree of completion of the drying reaction Rd ; b) degree of completion of the pyrolysis reaction $Rp+Rop$; c) degree of completion of the char oxidation reaction Rco . The gray zone indicates $\text{PIHF} < \text{PIHF}_0$.

below 0.5 m/s to $\sim 1350 \text{ K}$ at a wind speed around 1 – 2 m/s , then it decreases to below 600 K at $u_g > 3 m/s$. This result shows that there is a trade-off at which the wind can bring more oxygen to the particle surface while avoiding excessive cooling.

By comparing the contours of the particle core temperature in Fig. 5.11b and

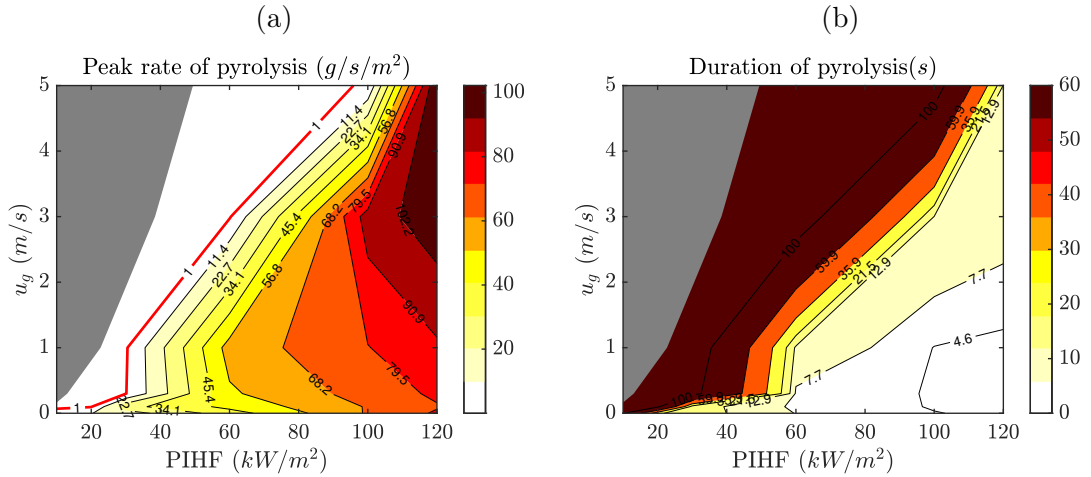


Figure 5.10: Maps of a 2 mm pine wood particle for $\tau_{\text{PIHF}} = 120 \text{ s}$: a) peak value of the pyrolysis rate; b) pyrolysis duration. The red solid iso-contour depicts the flaming threshold of 1 g/s/m^2 . The gray zone indicates $\text{PIHF} < \text{PIHF}_0$.

the contours of the degree of completeness of the char oxidation reaction shown in Fig. 5.9c, we find a correlation between the temperature achieved at the core of the particle at the end of the external heating period (i.e., τ_{PIHF}) and the degree of completeness of the self-sustained char oxidation. We will revisit this correlation later in this chapter as we try to establish a threshold of the particle core temperature required to achieve complete smoldering.

5.3.1.2 Maps of large particles (20 mm diameter) heated for a long duration ($\tau_{\text{PIHF}} = 120 \text{ s}$)

Figure 5.12 shows the maps of the degree of completion of thermal degradation of 20 mm particle heated for $\tau_{\text{PIHF}} = 120 \text{ s}$. Consistent with the maps of the smaller

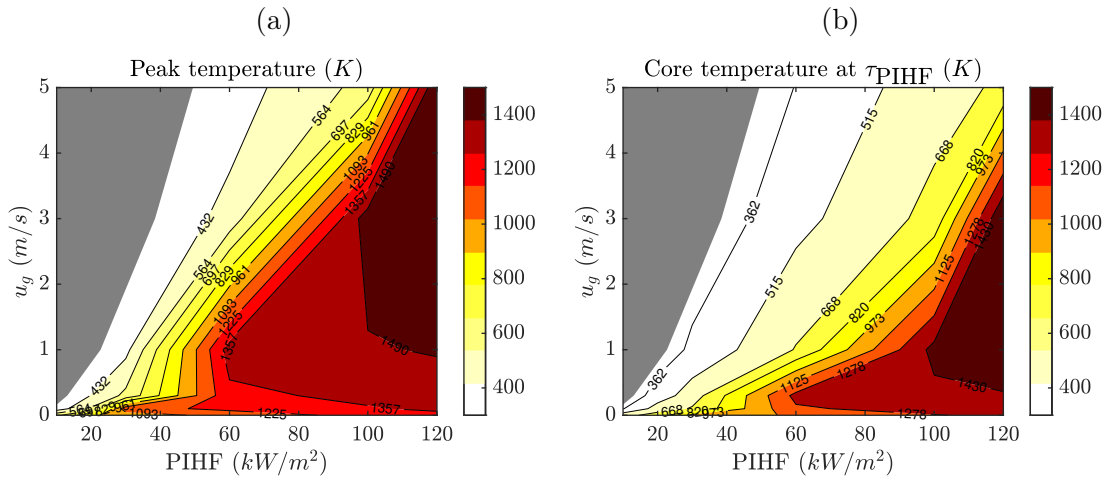


Figure 5.11: Maps of a 2 mm pine wood particle for $\tau_{\text{PIHF}} = 120$ s: a) the peak particle temperature Rd ; b) the temperature at the core of the particle at $t = \tau_{\text{PIHF}}$. The gray zone indicates $\text{PIHF} < \text{PIHF}_0$.

particle discussed in the previous section, we also found for this larger particle some regions of PIHF and u_g at which incomplete drying, pyrolysis, or char oxidation is achieved. However, in contrast to smaller particles, the effect of u_g on the degree of completion of the thermal degradation process in larger particles is significantly reduced except at very low wind speeds ($u_g < 0.25 \text{ m/s}$) where a strong effect of u_g on the degree of completion of the char oxidation is evident. This can be explained by the correlation between the wind speed u_g , the particle effective diameter, and the convective transfer coefficient h responsible for both heat and mass transfer discussed earlier in Fig. 2.3. As discussed in Chapter 2, the effect of increasing the wind velocity on increasing the convective transfer to the particles is much lower in larger particles than that in smaller ones due to differences in the surface area to volume ratio and differences in the aerodynamics of the flow between small and large

particles.

Figure 5.12c suggests that this large particle will experience complete consumption to ash at any values of PIHF > 60 kW/m² under the constraint of $u_g > 0.25m/s$ if heated for at least 120 s.

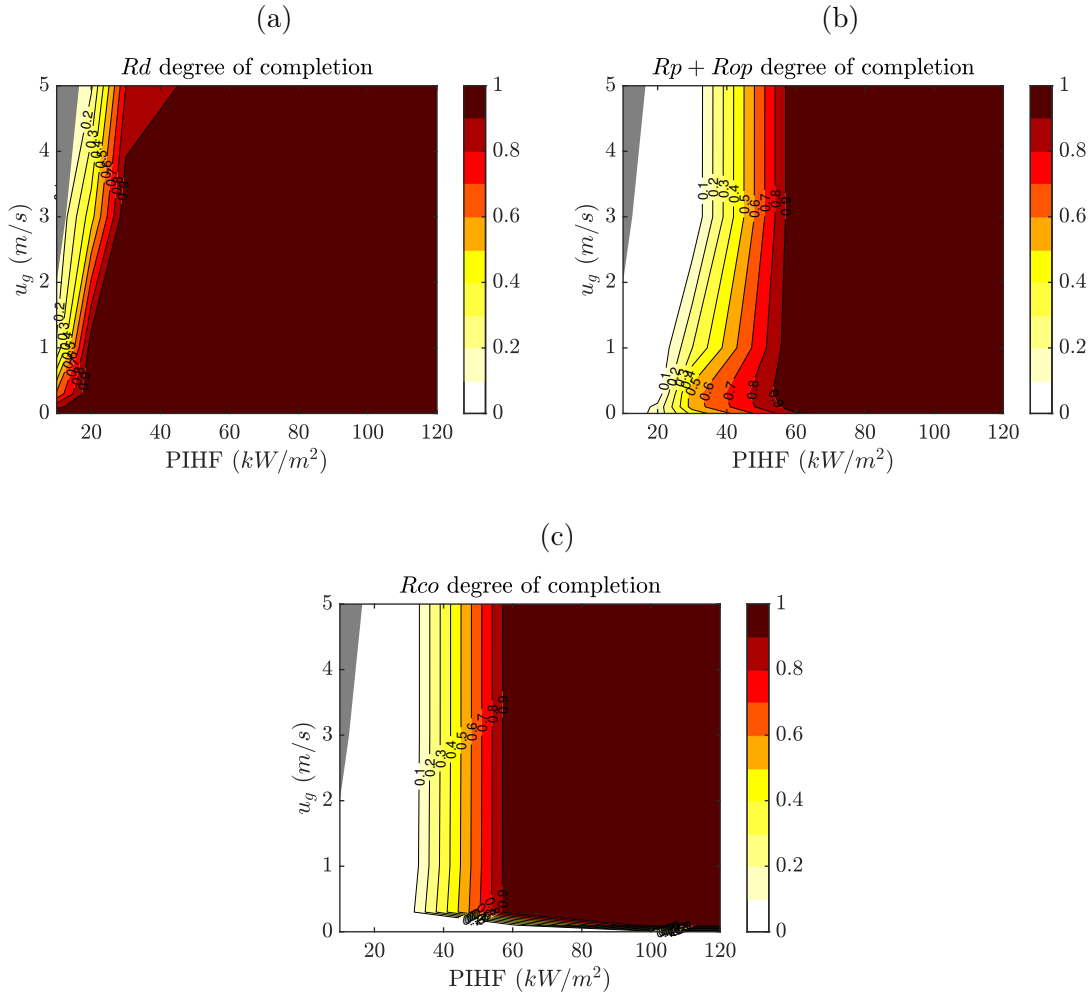


Figure 5.12: Maps of a 20 mm pine wood particle for $\tau_{\text{PIHF}} = 120$ s: a) degree of completion of the drying reaction Rd ; b) degree of completion of the pyrolysis reaction $Rp+Rop$; c) degree of completion of the char oxidation reaction Rco .

Figures 5.13a and 5.13b show the peak rate of pyrolysis and the total duration

of the pyrolysis process for this 20 mm particle, respectively. Consistent with our previous discussion, we see that the minimum PIHF required to achieve flaming ignition is weakly dependent on u_g and is on the order of $\sim 30 \text{ kW/m}^2$. However, as seen in Fig. 5.12b, this PIHF does not guarantee the completion of the pyrolysis process. Figure 5.13b suggests that there are regions that show the extinction of the pyrolysis process in which the pyrolysis duration is less than $\tau_{\text{PIHF}} = 120 \text{ s}$ but $E_{R_p+R_{op}}$ is less than one. Also, Fig. 5.13b depicts that the conditions for the fastest pyrolysis coincide with those of peak pyrolysis, and the fastest complete pyrolysis is achieved in $\sim 83 \text{ s}$.

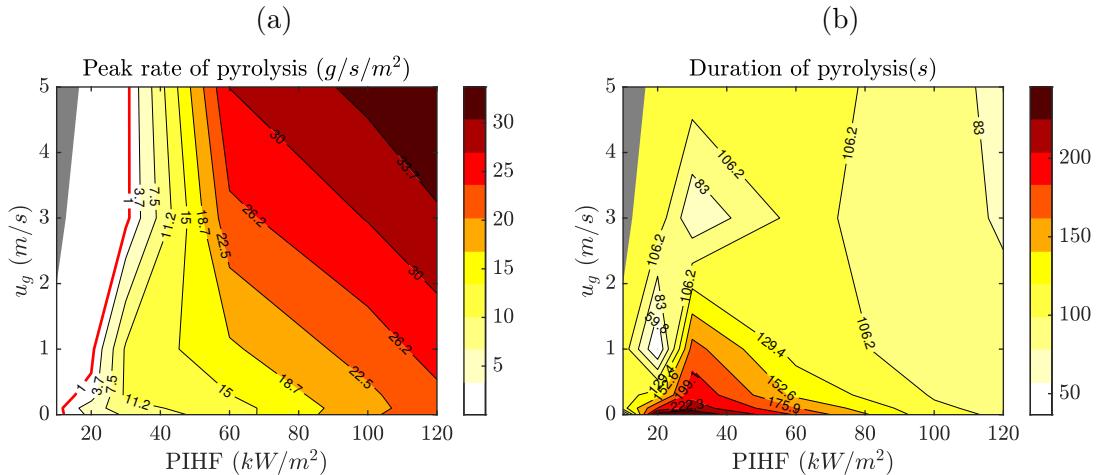


Figure 5.13: Maps of a 20 mm pine wood particle for $\tau_{\text{PIHF}} = 120 \text{ s}$: a) peak value of the pyrolysis rate; b) pyrolysis duration. The red solid iso-contour highlights the flaming threshold of 1 g/s/m^2 .

The maps of the peak temperature of the 20 mm particle and the temperature at its core at the end of the heating residence time are shown in Fig. 5.14a and 5.14b, respectively. Unlike the smaller particle case shown earlier, we see in Fig.

[5.14a](#) that the peak particle temperature increases monotonically with the PIHF and is very weakly dependent on u_g . The maximum temperature achieved in the particle that features complete thermal degradation through pyrolysis and char oxidation is $\sim 1300\text{ K}$. Also. Fig. [5.14b](#) suggests that the core temperature has to reach $\sim 700\text{ K}$ for this large particle to achieve complete consumption to ash.

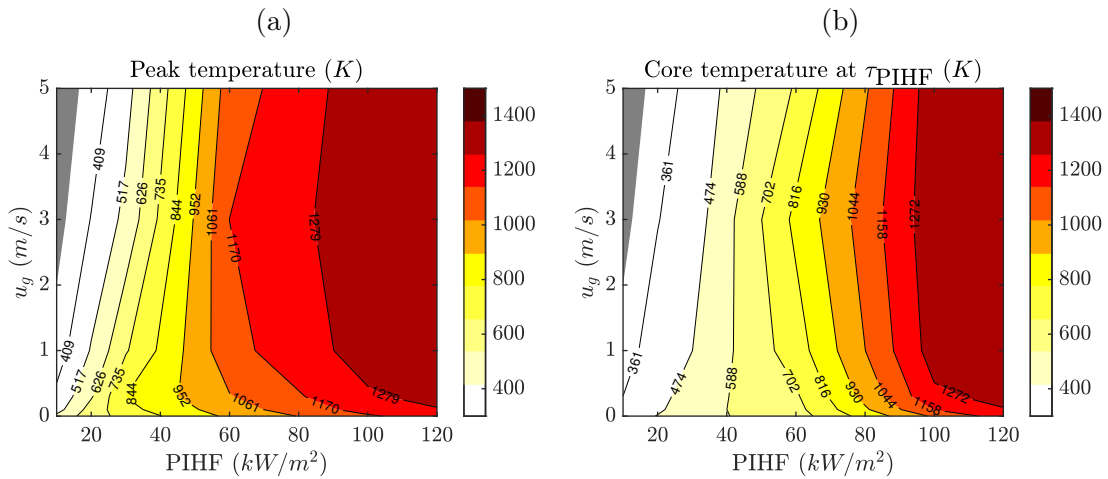


Figure 5.14: Maps of a 20 mm pine wood particle for $\tau_{PIHF} = 120\text{ s}$: a) the peak particle temperature Rd ; b) the temperature at the core of the particle at $t = \tau_{PIHF}$.

5.3.2 Effect of the residence time (τ_{PIHF})

We discuss in this section the influence of the duration of heating or the residence time (τ_{PIHF}) on the behavior of the particle. Our emphasis here is on the variation of the degree of completion of thermal degradation of small (2 mm diameter) and large (20 mm diameter) particles at different residence times and heating conditions.

Figures [5.15](#) present the maps of the degree of completion of the pyrolysis

and char oxidation reactions for a 2 mm particle subjected to different values of PIHF for a duration of either 5, 15 or 30 seconds. The corresponding maps of the peak particle temperature and the particle core temperature at the end of the residence time (τ_{PIHF}) are presented in Fig. 5.16. The results from these maps are of great interest as they quantify the significance of the residence time on the particle behavior. These results show that at a low residence time of $\tau_{\text{PIHF}} = 5\text{ s}$ and except for values of $\text{PIHF} > 100\text{ kW/m}^2$ and $u_g < 1\text{ m/s}$, the 2 mm particle may not ignite or sustain thermal degradation. For instance, at moderate conditions (e.g., $\text{PIHF} \sim 60\text{ kW/m}^2$ and $u_g \sim 1\text{ m/s}$), the degree of completion of the pyrolysis reactions is only 10% and no char oxidation is activated at a residence time of $\tau_{\text{PIHF}} = 5\text{ s}$. This can be explained by the characteristic response time of the particle discussed earlier, which estimates the time required to increase the particle's exposed surface temperature to a certain threshold value, in addition to the response time, there is an additional time required for heat to diffuse into the particle and to allow the endothermic pyrolysis reaction to consume the particle.

Figures 5.17 and 5.18 present similar maps but for a larger particle (20 mm diameter). We see from the results of these maps that due to the increase in the particle's thermal inertia and its response time, this particle does not exhibit any complete thermal degradation except at a residence of $\tau_{\text{PIHF}} \geq 60\text{ s}$. In the case of $\tau_{\text{PIHF}} = 60\text{ s}$ and $\text{PIHF} > 100\text{ kW/m}^2$, this large particle receives enough heat for long enough time such that its core temperature reaches values on the order of 500 K at $t = \tau_{\text{PIHF}} = 60\text{ s}$, and it undergoes complete consumption. We believe that the completion of the pyrolysis is strongly related to the exothermic char oxidation

process because once the external heating is stopped, the endothermic pyrolysis can not sustain itself unless the particle temperature is maintained at a high level which can only be achieved through the exothermic oxidation process.

5.3.3 Threshold value of the particle core temperature for complete smoldering

As discussed in the previous section, the residence time τ_{PIHF} is very critical to determine the degree of complete consumption of the particle, and this residence time is correlated to the temperature achieved inside the particle. We believe that in order for the exothermic char oxidation to be self-sustained, the particle core temperature must be at a much higher value than ambient at the end of the external heating period in order to avoid excessive losses of heat from regions near the particle surface and regions near the particle core, and hence to avoid extinction of the char oxidation.

We used data from maps generated for 2, 10, and 20 mm particles heated for $\tau_{\text{PIHF}} = 15, 30, 60$ and $120\ s$ to generate the scatter plot, presented in Fig. 5.19, which shows the variation of the degree of completion of the char oxidation reaction with the core temperature achieved at the end of the external heating period (i.e., at $t = \tau_{\text{PIHF}}$). While there is a certain level of scatter in the results, Fig. 5.19 confirms that high core temperatures lead to a complete char oxidation reaction (i.e., complete fuel consumption and conversion to ash) and suggests that there is a critical core temperature of $\sim 700\ K$ above which the particle will support self-sustained

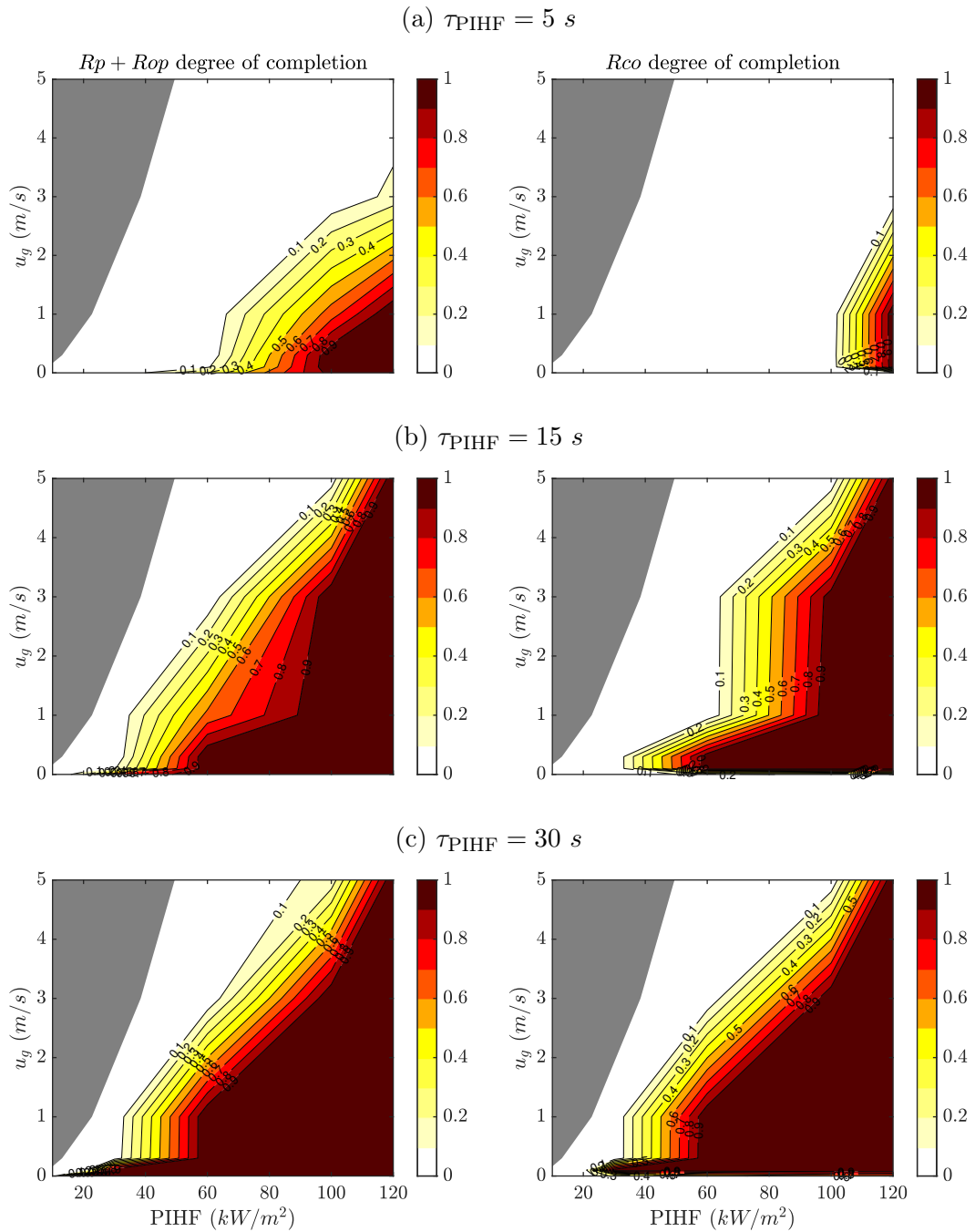


Figure 5.15: Maps of the degree of completion of pyrolysis (left) and the degree of completion of char oxidation (right) for a 2 mm pine wood particle heated for different periods: a) $\tau_{\text{PIHF}} = 5 \text{ s}$, b) $\tau_{\text{PIHF}} = 15 \text{ s}$, and c) $\tau_{\text{PIHF}} = 30 \text{ s}$.

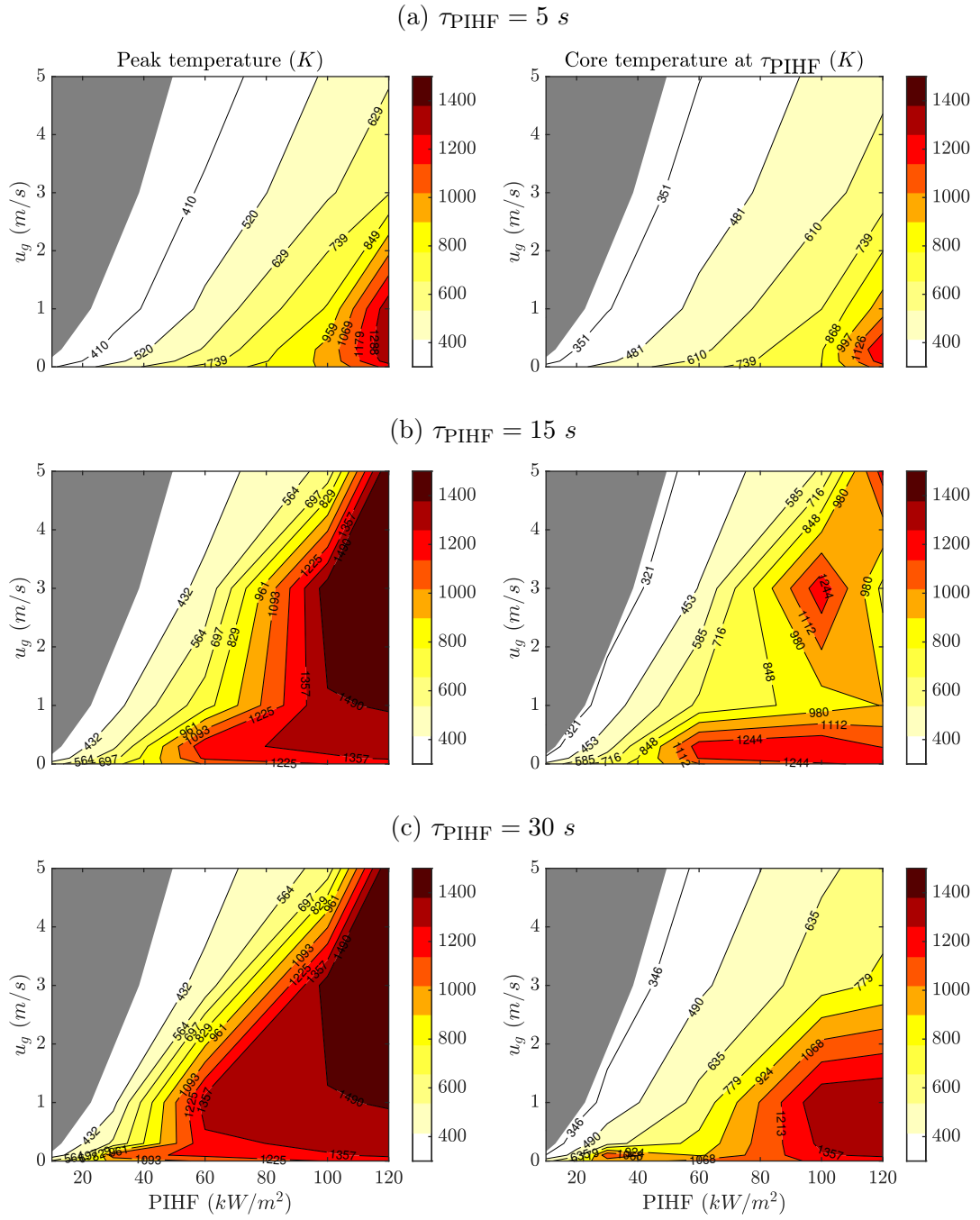


Figure 5.16: Maps of the particle peak temperature (left), and the particle core temperature at the end of the heating period (right) for a 2 mm pine wood particle heated for different periods: a) $\tau_{\text{PIHF}} = 5 \text{ s}$, b) $\tau_{\text{PIHF}} = 15 \text{ s}$, and c) $\tau_{\text{PIHF}} = 30 \text{ s}$.

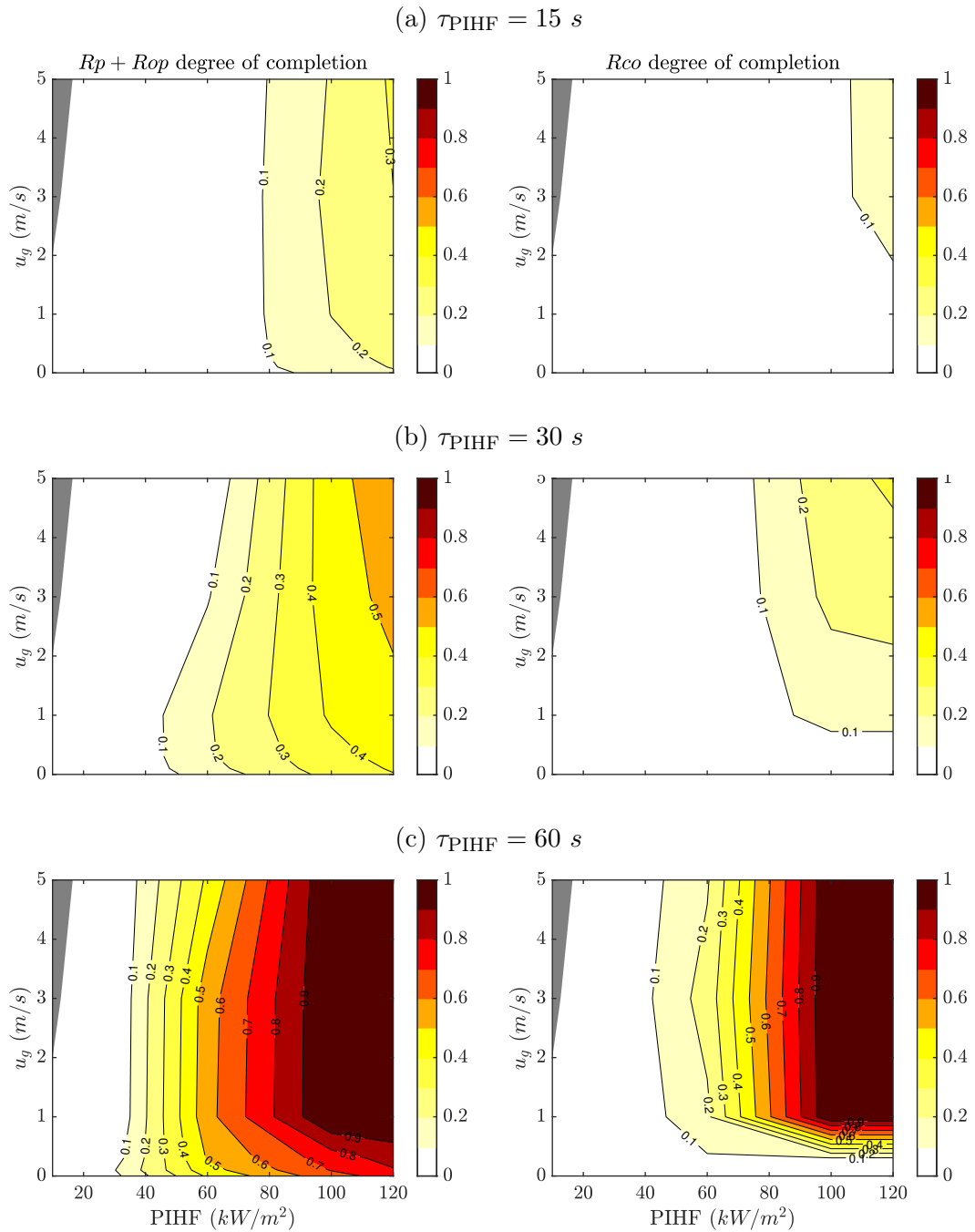


Figure 5.17: Maps of the degree of completion of pyrolysis (left) and the degree of completion of char oxidation (right) for a 20 mm pine wood particle heated for different periods: a) $\tau_{\text{PIHF}} = 15 \text{ s}$, b) $\tau_{\text{PIHF}} = 30 \text{ s}$, and c) $\tau_{\text{PIHF}} = 60 \text{ s}$.

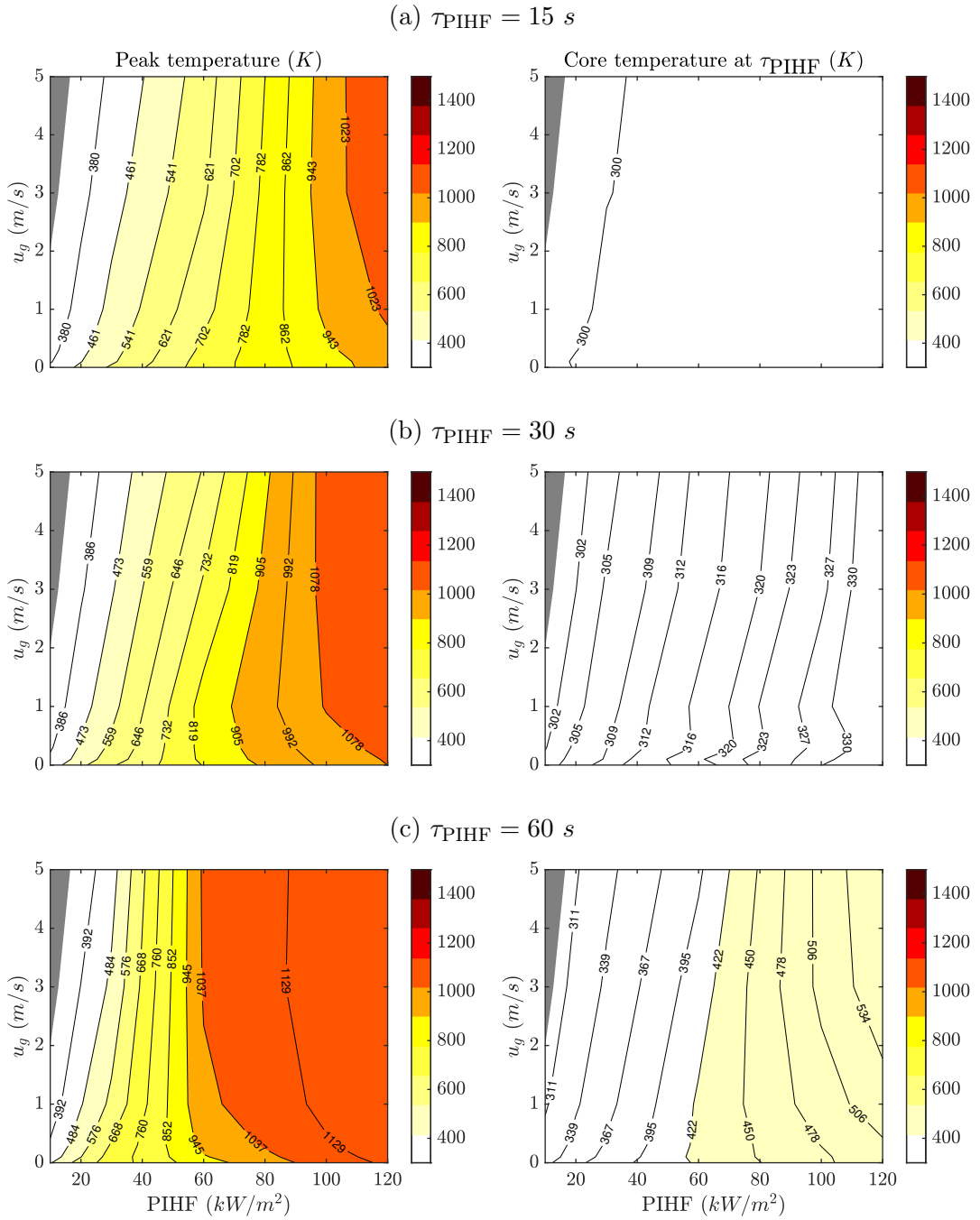


Figure 5.18: Maps of the particle peak temperature (left), and the particle core temperature at the end of the heating period (right) for a 20 mm pine wood particle heated for different periods: a) $\tau_{\text{PIHF}} = 15 \text{ s}$, b) $\tau_{\text{PIHF}} = 30 \text{ s}$, and c) $\tau_{\text{PIHF}} = 60 \text{ s}$.

smoldering.

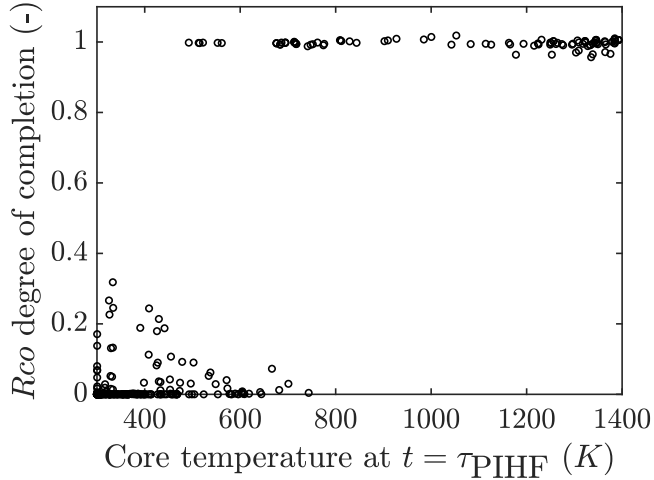


Figure 5.19: Scatter plot of the char oxidation degree of completion against the particle core temperature achieved at the time corresponding to the end of the heating duration τ_{PIHF} .

This chapter presented simulations of small and large biomass particles exposed to prescribed steady or oscillatory external heat loading conditions. These conditions represent situations in wildland fires in which a flame is spreading over a vegetation fuel bed and heating the solid fuel elements at certain intensity and residence time. The chapter was divided into two parts: the first part discussed the effect of oscillations in the external heating conditions on the particle behavior in terms of the start of pyrolysis, mass loss rate, and burnout; and the second part discussed the behavior of the particle under given conditions of external heating and gas flow

velocity using 2-D maps that describe the degree of completion of pyrolysis and char oxidation, the particle temperature as well as the pyrolysis rate and duration.

The results of the first part suggest that, in most cases, even when temperature and mass loss rate oscillations are strong, the particle features a quasi-linear response in which the net effect of oscillations remains small and the mean particle behavior is well represented by a simulation without oscillations in the external heating conditions. A different behavior is observed in the case of unsteady convective heating when the external gas velocity fluctuates in phase with the external gas temperature. In this case, the particle features a non-linear response that leads to a net effect of the oscillations in the form of an augmented heat transfer, higher particle temperatures, higher values of the pyrolysis mass loss rate, and shorter burnout times.

The results of the second part suggest that the particle behavior is not dependent only on its size or the external heating intensity but also strongly on the flame residence time (or the duration of the external heating phase). The 2-D maps show that the degree of completion of thermal degradation of small particles (on the order of 1 mm) exhibits a strong dependence on both the intensity of the external heating (the PIHF) as well as the external gas velocity, while larger particles (on the order of 1 cm) exhibit less sensitivity to changes in the external gas velocity and their behavior is mainly controlled by the PIHF. The maps also highlight the significance of the residence time and show quantitatively the conditions required to achieve complete thermal degradation as the residence time increases or decreases. The results suggest that there is a critical core temperature of $\sim 700\ K$ above which the particle will

support self-sustained smoldering. These maps are important to interpret more complex scenarios of spreading fire and to determine conditions at which spread or no spread is expected or the degree of fuel consumption when designing prescribed burns.

6 Simulations of Fire Spread in Engineered Cardboard Fuel Beds

6.1 Overview

Line fires are attractive configurations to study wildland fire behavior because they spread in only one direction which makes the analysis of the flame structure relatively simple through the rate of spread (ROS), the flaming zone depth, and the flame residence time. Our primary objective in this chapter is to evaluate the new modeling capability by comparing simulation results of global fire behavior in terms of flame structure, ROS, and flame residence time against the experimental measurements and observations obtained from the fire spread experiments conducted at the Fire Sciences Laboratory [36, 99]. Our secondary objective is to bring fundamental insights into the local conditions at the particle level during fire propagation in fuel beds of different packing ratios.

We consider here fuel beds made of laser-cut cardboard strips that are oriented vertically and are arranged at certain separation distances in axial and lateral directions to achieve a given fuel packing ratio [36] (the total volume of the solid particles inside the fuel bed divided by the total volume of the fuel bed region). Each

individual fuel particle represents a single cardboard strip that has a certain thickness, width, and height. Note these cardboard strips have homogeneous properties, unlike the corrugated cardboard which is made of multiple layers and separators. The fire spread over these fuel beds was studied experimentally at the Missoula Fire Sciences Laboratory on either an inclined surface (Fig. 6.1a) or inside a wind tunnel (Figs. 6.1b and 6.1c). In contrast to bench-scale fuel beds made of matchsticks or toothpicks, these configurations feature the spread of continuous flames that cover several arrays of particles as opposed to the spread of discontinuous flames that are attached to only one particle. More importantly, these configurations show typical features observed in actual wildland fires such as the coherent peak and trough flame structures [99], as well as the glowing zones that correspond to a transition from flaming to smoldering combustion.

6.2 Numerical configuration

6.2.1 Computational domain and fuel bed setup

The simulations correspond to the experiments that were conducted inside the wind tunnel facility at the Missoula Fire Sciences Laboratory. A schematic of the wind tunnel facility is shown in Fig. 6.2. As shown in Fig. 6.2, the tunnel flow system is not simple. The inflow to the tunnel is supplied through a large room (noted as the combustion laboratory in Fig 6.2). The tunnel exit is not directly open to the ambient and the outflow can be recirculated to the inlet chamber after passing across a conditioning section. The test section has a 3 m square cross-section. The

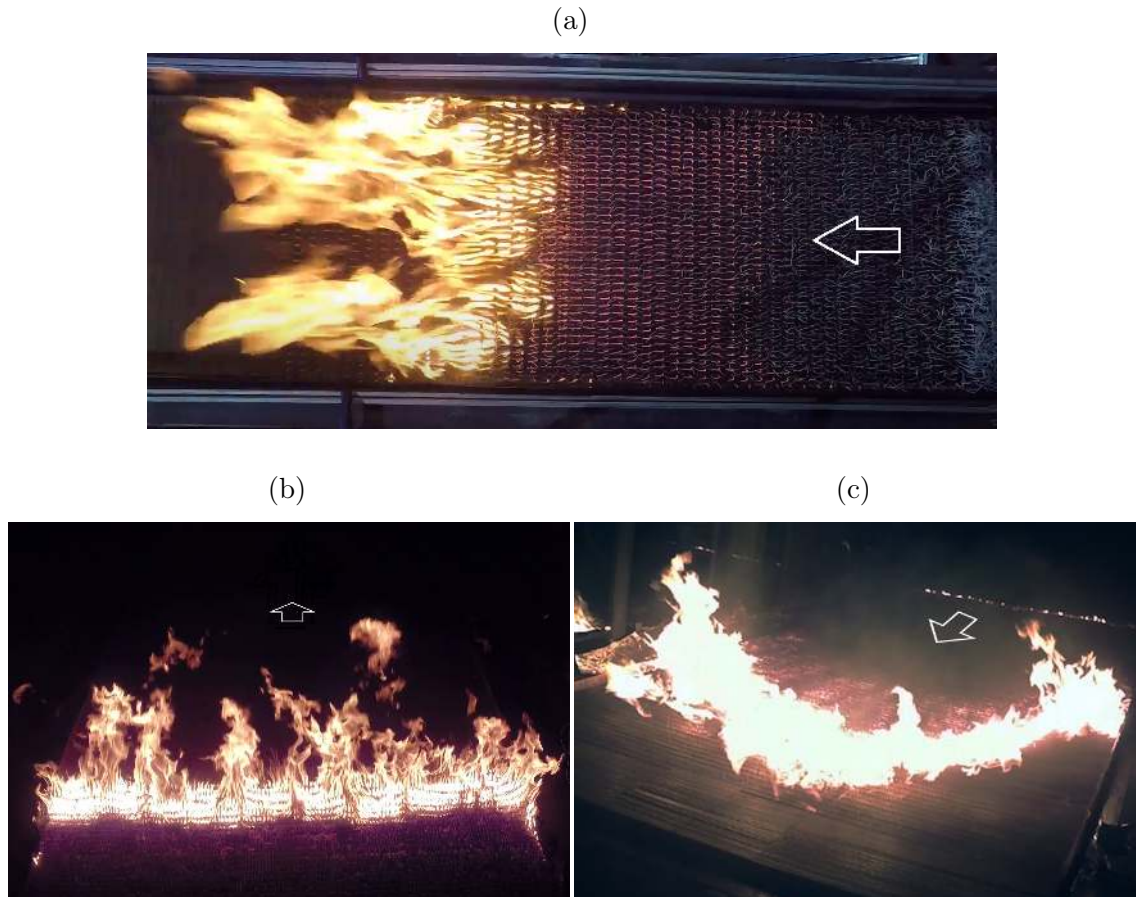


Figure 6.1: Images from the experimental burns of fire spread in cardboard fuel beds conducted at the Missoula Fire Sciences Laboratory (courtesy of Dr. Mark Finney):
 a) top view of an experiment conducted on an inclined surface, featuring flaming and glowing zones; b) back view of a buoyancy-dominated fire experiment in the wind tunnel (Burn 53), featuring a uniform flame front with peak and trough structures; c) isometric view of the wind-dominated fire in the wind tunnel at high speed (Burn 67), featuring flaming and glowing zones as well as a curved flame front.

fuel bed extends to a length of 8 m. There is approximately 5 m straight extension downstream of the fuel bed after which the flow is turned 90 degrees twice until it either exits the facility or enters the conditioning section for recirculation. The tunnel provides a laminar flow except along the bottom surface where a trip-fence is placed at approximately 6.4 m upstream of the fuel bed to promote a transition to turbulent boundary layer [104].

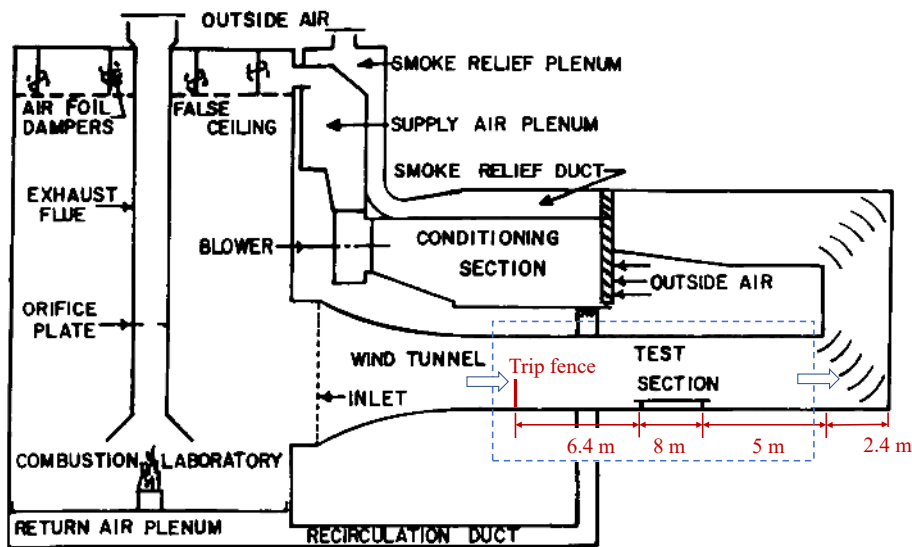


Figure 6.2: Schematic of the wind tunnel facility at Missoula Fire Sciences Laboratory (adapted from Ref. [105]). The dimensions on the image are obtained from private communication with Dr. Mark Finney. The blue dashed box contours the simulated region.

Because simulating the entire flow system of the wind tunnel is not computationally efficient, we simulate only the test section highlighted by the blue dashed rectangle shown in Fig. 6.2. The computational domain that we constructed to replicate the test section of the wind tunnel is displayed in Fig. 6.3. The computational

domain has a total length of 14 m and a square cross-section of $3 \times 3\text{ m}^2$. The fuel bed starts from $x = 0$ to $x = 8\text{ m}$ and spans the entire tunnel width. Note that the fuel bed width in the experimental setup was slightly different where there was a small gap between the wind tunnel side walls and the edges of the fuel bed, and lateral baffles made of paper and coated with flame retardant were used to prevent lateral entrainment. In order to mimic the effect of the trip fence that promotes boundary layer transition from laminar to turbulent, we added a trip wire at 0.5 m downstream of the domain inlet that spans the entire tunnel width. The trip wire has a height of 2.5 cm and a width of 5 cm . This technique has been used in previous studies of wind-driven flames [106]. The implication of the trip wire on the velocity and turbulence intensity profiles will be discussed later.

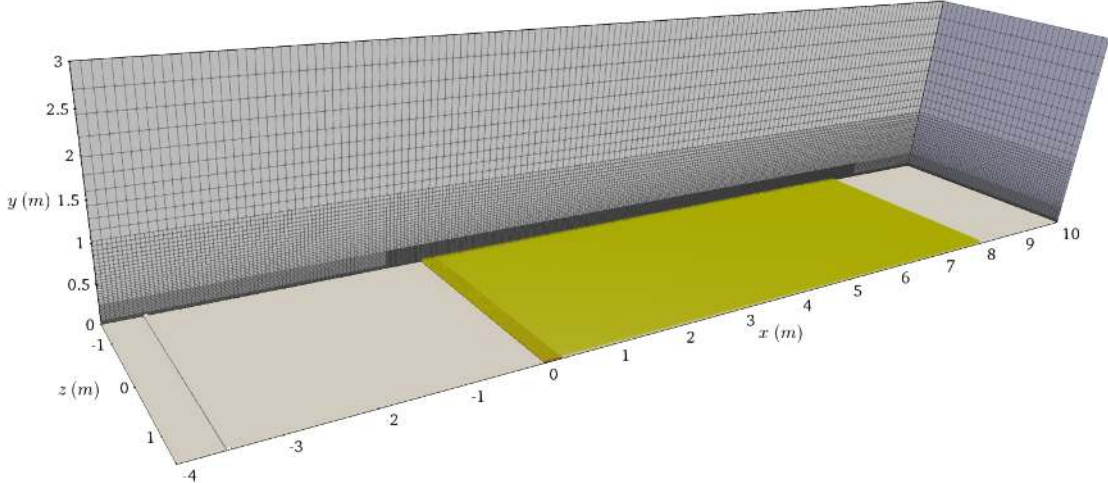


Figure 6.3: The computational domain used in the simulations of the cardboard fire spread. The fuel bed is colored in yellow.

We consider two experimental burns named burn 53 (Fig. 6.1b) and burn 67 (Fig. 6.1c). These two burns correspond to a buoyancy-dominated flame under a low

wind speed of 0.335 m/s and a wind-dominated flame under a high wind speed of 1.34 m/s , respectively. The two burns were designed to achieve approximately the same fire line intensity (i.e., the rate of heat release due to homogeneous gas-phase combustion per unit length of the fireline). Therefore, the height and the packing of the fuel bed are different between the two burns.

Table 6.1 shows a summary of the data corresponding to Burn 53 and Burn 67. The data include the geometric parameters of the fuel bed, the observed flame structure and ROS, the theoretical estimations of the fire intensity using the Byram expression, and an estimate of Byram's convection number. The theoretical intensity is estimated by

$$\dot{Q}'_{fire} = m''_{fuel} \times \text{ROS} \times \Delta H_F \quad (6.1)$$

where \dot{Q}'_{fire} is the fire line intensity, and where m''_{fuel} is the fuel loading defined as

$$m''_{fuel} = \chi_{consumption} \times \eta_{ds,Rd} \times (1 - \eta_{c,Rp}) \times \beta_s \times \rho_p \quad (6.2)$$

where $\chi_{consumption}$ is the degree of complete consumption of the fuel bed ($\chi_{consumption}$ is assumed to be 1). The Byram's convection number N_C is defined as

$$N_C = \frac{2 \dot{Q}'_{fire} g}{\rho_\infty c_{p,\infty} T_\infty (u_\infty - \text{ROS})^3} \quad (6.3)$$

where \dot{Q}'_{fire} is the fire intensity, g the gravitational acceleration, ρ_∞ , $c_{p,\infty}$ and T_∞ the mass density, heat capacity (at constant pressure), and temperature of ambient air, respectively, and where u_∞ the magnitude of the cross-wind velocity. The calculated Byram numbers are $N_C = 241.1$ and 4.3 for Burn 53 and Burn 67, respectively. These numbers indicate that Burn 53 belongs to the Buoyancy-dominated fire regime

as $N_C \gg 1$ and Burn 67 belongs to the wind-dominated fire regime as N_C is close to 1.

In addition to the simulations of Burn 53 and Burn 67, we consider additional simulations that correspond to fuel beds of different packing ratios ranging from 0.0071 to 0.0246. These packing ratios are achieved by changing the axial separation distance between the fuel particles. The particles in these simulations have a thickness of 0.001397 m, a width of 0.0015 m, and a height of 0.0508 m. The variation of the packing ratio with the axial separation distance is shown in Fig. 6.4. The lateral separation distance is fixed at 0.0097 m in these cases. A script was developed to position the cardboard sticks inside the fuel bed considering these separation distances.

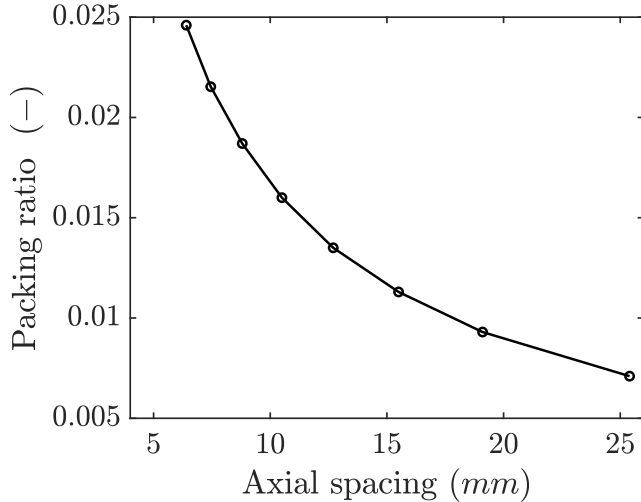


Figure 6.4: Variation of the fuel bed packing ratio with the axial spacing between particle arrays.

Table 6.1: Conditions of Burn 53 and Burn 67.

Quantity	Burn 53	Burn 67
Particle thickness in x-dir (m)	0.001397	0.001397
Particle width in z-dir (m)	0.00231	0.00127
Axial separation in x-dir (m)	0.03016	0.04604
Lateral separation in z-dir (m)	0.012954	0.00635
Fuel bed height (m)	0.1016	0.0508
Packing ratio β_s (-)	0.0067	0.0049
Wind speed (m/s)	0.335	1.34
Moisture content (%)	6	6
Observed flame zone depth (m)	0.36	0.45
Observed flame height (m)	0.5	0.4
Fuel loading m''_{fuel} (kg/m ²)	0.35	0.13
Observed ROS (m/min)	1.82 ± 0.14	6.01 ± 1.24
Theoretical intensity \dot{Q}'_{fire} (kW/m)	123	149
Byram number N_C (-)	241.1	4.3

6.2.2 Computational mesh resolution

As shown in Table 6.1, the characteristic length-scales of the experimental burns are the fuel bed height $\sim 0.05 - 0.1$ m, the flame height, and flame zone depth ~ 0.5 m. There is an additional length-scale associated with the radiation penetration $\delta_{rad} = 4/(\beta_s \sigma_p)$. The smallest radiation penetration length is estimated to be ~ 0.1 m. All these length-scales have to be resolved by the computational grid.

The computational grid is a multi-block structured mesh with three refinement zones (Fig. 6.3). The grid cell size in the vicinity of the fuel bed zone (from $x = -0.5$ to 8.5 m) and between $y = 0$ to $y = 0.25\text{ m}$ elevation is $\Delta x = \Delta z = 25\text{ mm}$ and $\Delta y = 6.25\text{ mm}$. Then, the cell size from $y = 0.25$ to $y = 1\text{ m}$ elevation is doubled and stretched in the $y-$ direction. Similarly, the grid size above $y = 1\text{ m}$ elevation is doubled and stretched in the $y-$ direction. The computational grid upstream and downstream of the fuel bed is stretched in the $x-$ direction when moving away from the fuel bed zone. The total number of grid cells in the baseline mesh resolution is ~ 2.4 million cells. Note that the fuel shallowest fuel bed height is resolved by 8 cells, the flame zone depth is resolved by 20 cells, and the smallest radiation penetration length is resolved by 4 grid cells.

Regarding the angular discretization used in the solution of the MRTE, we use a total number of 144 solid angles to resolve the $4\pi\text{ sr}$ angular space.

In order to check the sensitivity of the solution to the computational grid resolution, a computational domain with a refined mesh resolution of cell sizes equal to half of that of the baseline mesh is constructed. The total number of cells in the refined mesh is ~ 19 million cells.

As mentioned earlier, the fuel bed height is resolved with at least 8 cells, and the cardboard particles are discretized in the vertical y -direction. Note that this method allows resolving of the spatial variations through the fuel bed height as each portion of the cardboard particle is exposed to different gas conditions, but the conduction of heat through the axial direction is still ignored due to the one-dimensional assumption used in the PBR model. Each portion of the cardboard

particles is modeled in the PBR model using 1-D rectangular particles. The mesh resolution inside each particle is $25 \mu m$. The total number of simulated cardboard particles ranges from approximately 0.8 to 2.2 million particles depending on the fuel packing.

6.2.3 Boundary conditions

As mentioned earlier, the tunnel flow system is complex, particularly, in the case of buoyancy-dominated fires because of the possible interaction between the smoke and the tunnel ceiling that leads to a smoke layer spreading toward the tunnel inlet. This phenomenon is known in tunnel fires as *back-layering* and the distance which the smoke travels upstream is known as the *back-layering length* (see Ref. [107]). Previous studies have shown that the back-layering length is dependent on the fire intensity, the tunnel height, and the wind speed. We estimate the back-layering length in Burn 53 to be greater than $100 m$ using the correlations of Hu et al. [107]. We also estimate no back-layering in Burn 67. Moreover, the wind velocity was measured under cold flow conditions and no measurements were taken during the actual burn. However, we expect that the flow velocity measured in cold flow can be different from the one in the burning case due to the back-layering effect and the fire-induced flow.

We tested different combinations of the inlet boundary conditions: 1) a velocity-driven system with a prescribed inlet velocity and, and 2) a pressure-driven system with a prescribed inlet total pressure. The domain exit boundary is treated as

an outflow to ambient pressure with no reverse flow allowed (a wave-transmissive treatment at the exit boundary is also applied for the buoyancy-dominated burn). The top and the bottom of the tunnel are treasured as no-slip adiabatic walls. The side walls of the tunnel are treated as periodic boundaries. Ignition is achieved using a slot burner that extends between $x = 0$ to $x = 0.2\text{ m}$. The burner provides a gaseous fuel at a flow rate of 0.01 m/s and a temperature of 1400 K and is activated for at least 10 seconds.

6.2.4 Sub-models

We use in all simulations the PGRF radiation model with a radiant fraction of 0.24 which represents the average value of the measurements of Zeng et al. obtained from corrugated cardboard flames [108]. We use the WALE model for SGS turbulent fluctuations.

6.2.5 Computational cost

The time-step is controlled using a Courant–Friedrichs–Lewy condition and is of the order of $\sim 0.001\text{ s}$. The radiation field is updated every 10 time-steps. The simulations are carried out on a distributed-memory parallel cluster using Message Passing Interface (MPI) technique. The average computational cost of 60 seconds of fire spread using the baseline mesh is $\sim 31\text{ kCPU hours}$ using 128 processors. The computational cost associated with the fine mesh resolution is $\sim 150\text{ kCPU hours}$ using 300 processors.

6.3 Fire behavior in Burn 53 and Burn 67

6.3.1 Flow field at cold flow

We conducted simulations under cold flow conditions in order to verify the effect of the trip wire and to obtain a turbulent flow condition before ignition. Figure 6.5 shows the instantaneous flow field inside the wind tunnel at the cold flow conditions corresponding to Burn 53 and Burn 67, respectively. The contours show a turbulent flow structure that evolves downstream of the trip wire. The cold flow simulations were run long enough to achieve a quasi-steady flow field and to calculate the mean flow quantities.

The mean velocity profiles at different locations upstream and downstream of the leading edge of the cardboard bed are shown in Figs. 6.6a and 6.6b for the low-velocity and the high-velocity cases, respectively. The corresponding profiles of the root-mean-square velocity are shown in Figs. 6.7a and 6.7b. The boundary layer profiles display variations as moving from the entrance region upstream of the cardboard fuel bed to downstream locations, due to the presence of the cardboard particles. The profiles of the root-mean-square velocity indicate that the boundary layer upstream of the fuel bed is turbulent as a result of the trip wire. The estimated turbulent intensity is $\sim 5 - 15\%$, which is very close to the cold flow measurements provided by the U.S Forest Service internal report that characterizes the turbulent intensity of the wind tunnel [104]. Inside and above the fuel bed, the flow is strongly affected by the presence of the cardboard particles, and the turbulent intensity

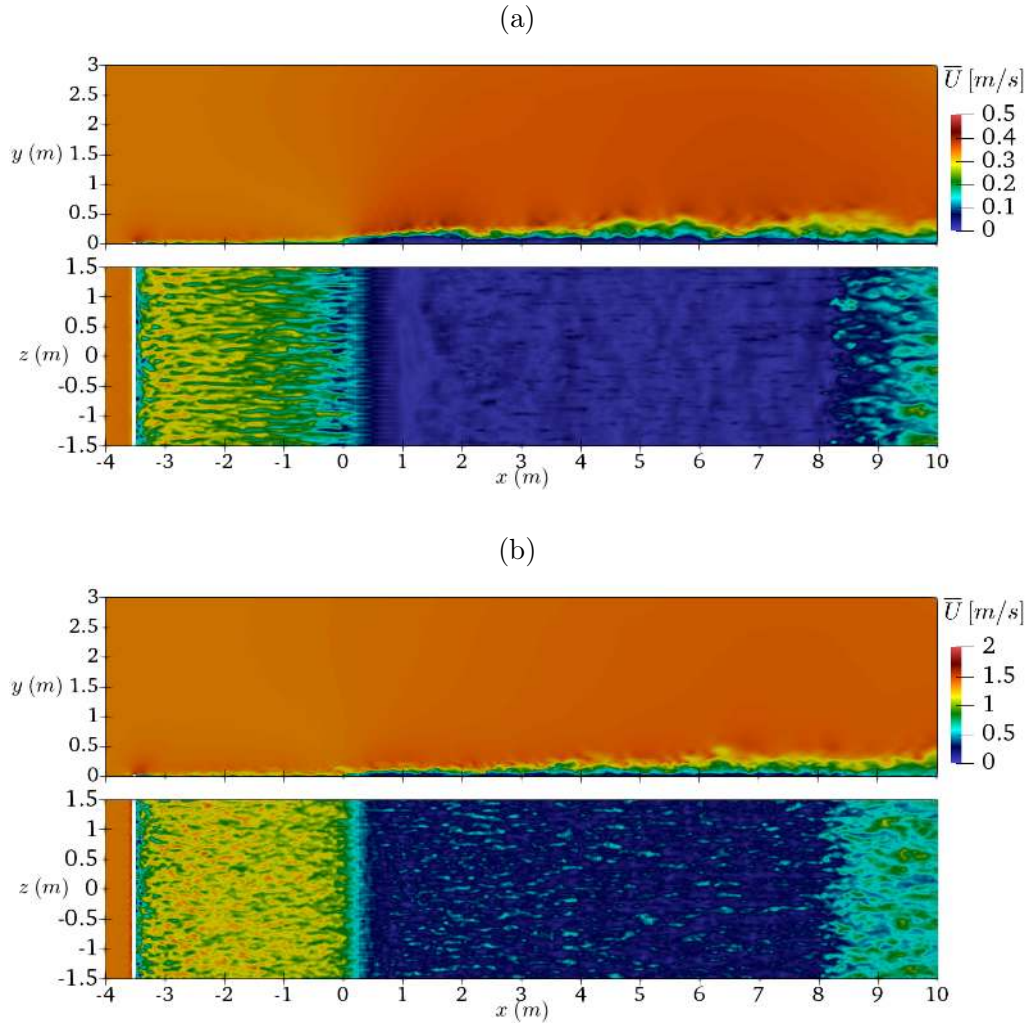


Figure 6.5: Contours of the velocity magnitude at the vertical center-plane of the wind tunnel (top slice) and at a horizontal plane at $y = 0.025\text{ m}$ elevation (bottom slice). The contours correspond to cold flow simulations of a) Burn 53 and b) Burn 67.

reaches levels higher than 15%.

In order to assess the vertical grid resolution at the wall, we calculate $\Delta y_w^+ = \sqrt{|\tau_w|/\rho_w} \Delta y_w / \nu_w$, where τ_w is the wall shear stress, ρ_w and ν_w are the density and the kinematic viscosity at the wall, and where Δy_w is the elevation of the first cell

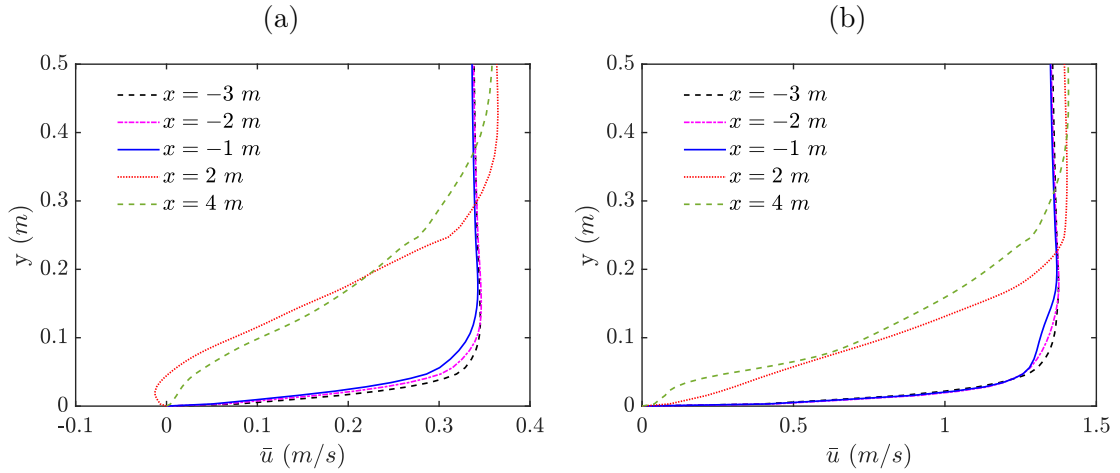


Figure 6.6: Profiles of the mean velocity at different locations in the streamwise direction in a) the low-velocity case (Burn 53), and b) the high-velocity case (Burn 67).

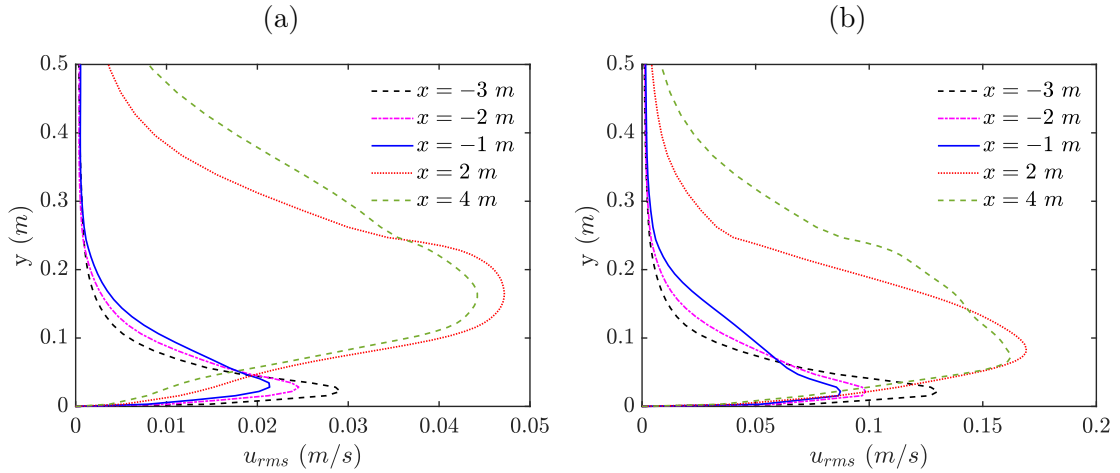


Figure 6.7: Profiles of the root-mean-square velocity. See the caption of Fig. 6.6.

center above the wall. Figure 6.8 displays the variations of the instantaneous and the mean values of Δy_w^+ at different streamwise locations. The results of Fig. 6.8 indicate that Δy_w^+ changes from ~ 3 upstream of the fuel bed to ~ 1 inside the fuel

bed in the low-velocity case (Burn 53), which suggests that this case is wall-resolved. The high-velocity case (Burn 67) shows variations of Δy_w^+ from ~ 10 upstream of the fuel bed to ~ 5 inside the fuel bed, which suggests that this case may not be wall-resolved. The expected inaccuracies in the wall shear stress upstream of the fuel bed are not believed to be a concern for the simulation of fire behavior within the cardboard bed.

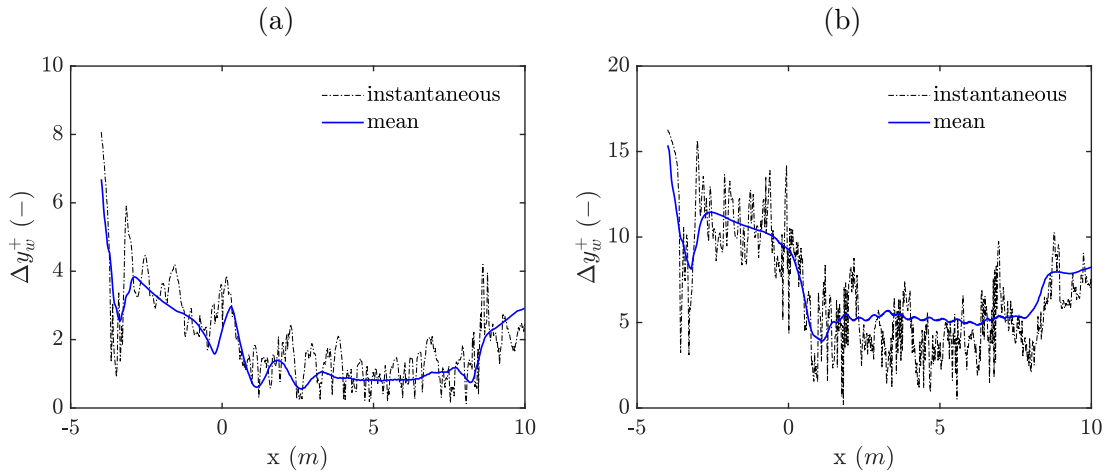


Figure 6.8: Streamwise variation of Δy_w^+ in: a) the low-velocity case; b) the high-velocity case. The dashed line represents instantaneous values and the solid line represents mean values. The cardboard fuel bed starts at $x = 0$.

6.3.2 Flow field during combustion

We now discuss the tunnel flow field during an active burn. Particularly, we would like to highlight the issue of back-layering in simulations of buoyancy-dominated fires in wind tunnels. We performed simulations of Burn 53 and Burn 67 with either prescribed inlet velocity or prescribed total pressure. We found that in

the case of Burn 67, the choice of the boundary condition has no effect on the flow field as the wind speed is high enough to push all the plume to exit the domain. As shown in Fig. 6.9, the tunnel flow is well-controlled and is uni-directional. Therefore, this case is more favorable and is considered for further investigations regarding the effect of the fuel packing ratio on fire behavior.

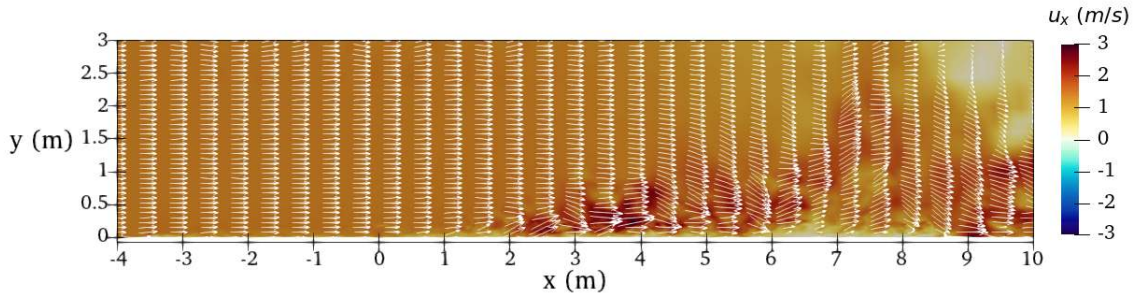


Figure 6.9: Tunnel flow field in the case of wind-dominated fire (Burn 67). Contours of the axial velocity in the tunnel mid-plane. The velocity vectors are scaled by velocity magnitude.

In the case of a buoyancy-dominated fire (Burn 53), we found that the flow field is very sensitive to the choice of the inlet boundary condition. Figures 6.10a and 6.10b shows a plume traveling in the negative x-direction towards the inlet boundary, as well as a plume that travels in the positive x-direction towards the outlet boundary. The plume is recirculating at the inlet boundary in the case of the prescribed inlet velocity boundary (Fig. 6.10a), but the magnitude of the incoming flow velocity is unchanged as it remains equal to the prescribed value. On the other hand, the plume is able to escape from the inlet boundary in the case of a prescribed total pressure (Fig. 6.10b), and no recirculation is observed in the inlet zone. The

magnitude of the incoming velocity in this case is dependent on the pressure balance and may deviate from that measured at cold flow. We will present in the following the implication of these choices on the ROS predictions of the fire.

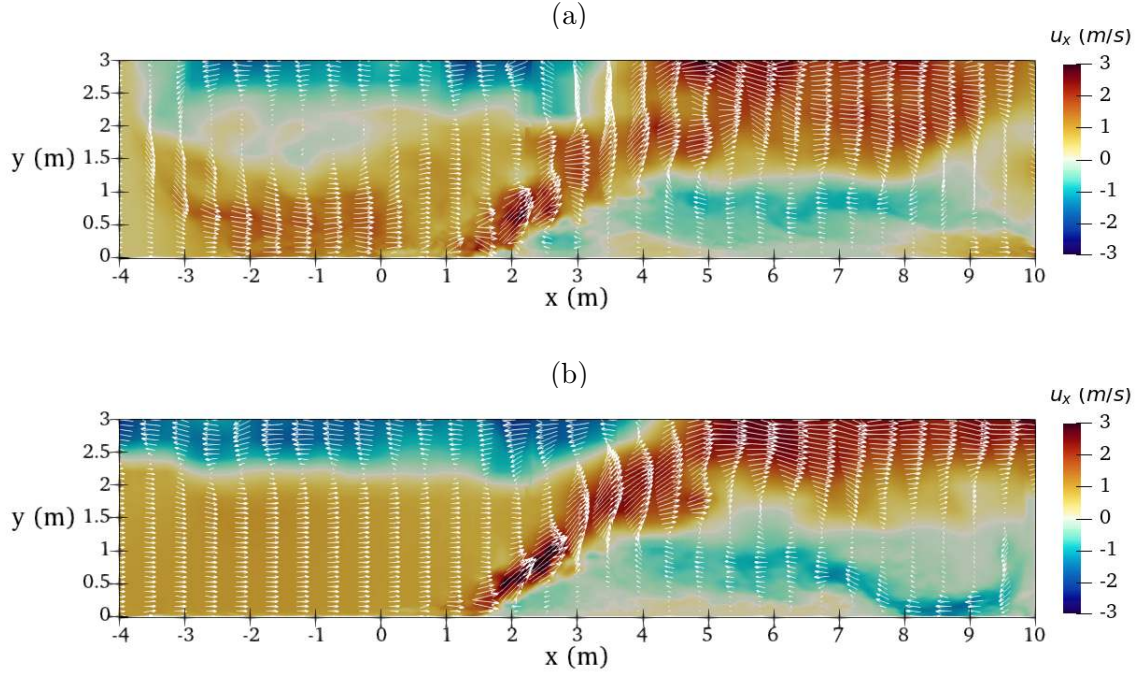


Figure 6.10: Tunnel flow field in the case of a buoyancy-dominated fire (Burn 53) with a) a prescribed inlet velocity, b) a prescribed total pressure. See the caption of Fig. 6.9.

6.3.3 Flame structure

As shown in Figs. 6.1b and 6.1c, the experimental flame structure of Burn 53 features a buoyancy-dominated flame that is slightly tilted forward, and has a quasi-linear fire front with flame peaks and troughs. The experimental flame structure of Burn 67 features a wind-dominated flame that is strongly tilted towards the fuel

bed, and has a slightly curved front that is not perfectly linear despite the special treatment made in the experiments at the fuel bed sides to mimic an asymptotic line fire. A 3-D view of the simulated flame structure of Burn 53 and Burn 67 is displayed in Figs. 6.11a and 6.11b, respectively. As seen in Fig. 6.11a, the simulation of Burn 53 features the same flame peaks and troughs as those observed in the experiments. We also see in Fig. 6.11a some effect of these peaks and troughs on the mass loss rate of the fuel bed. The simulation of Burn 67 displayed in Fig. 6.11b shows a flaming zone of hot luminous gases followed by a glowing zone of smoldering particles, similar to that seen in the experiments (Fig. 6.1c). The simulations, however, show a perfectly uniform line fire as a result of the use of periodic boundary conditions.

Table 6.2 shows also a quantitative comparison between the simulated flame structure in terms of flame height and flame zone depth against those measured visually. The flame height is estimated in the simulations as the maximum elevation where the volumetric heat release rate from the gas-phase combustion is above a threshold value of 1 kW/m^3 . Similarly, the flame front is estimated in the simulations as the maximum downstream distance where the volumetric heat release rate from the gas-phase combustion is above a threshold value of 1 kW/m^3 . The flaming and smoldering zone depths are estimated based on the particle states described in section 2.2.6. The visually measured flaming zone depth in Burn 53 (Burn 67) is 0.36 m (0.45 m). The simulations predict a slightly longer flaming zone depth of 0.56 m for Burn 53 and 0.64 m for Burn 67. The simulations also predict longer flame heights than those observed in the experiments. The observed flame height in Burn 53 is 0.5 m and the simulated value is 0.8 m . The observed flame height in

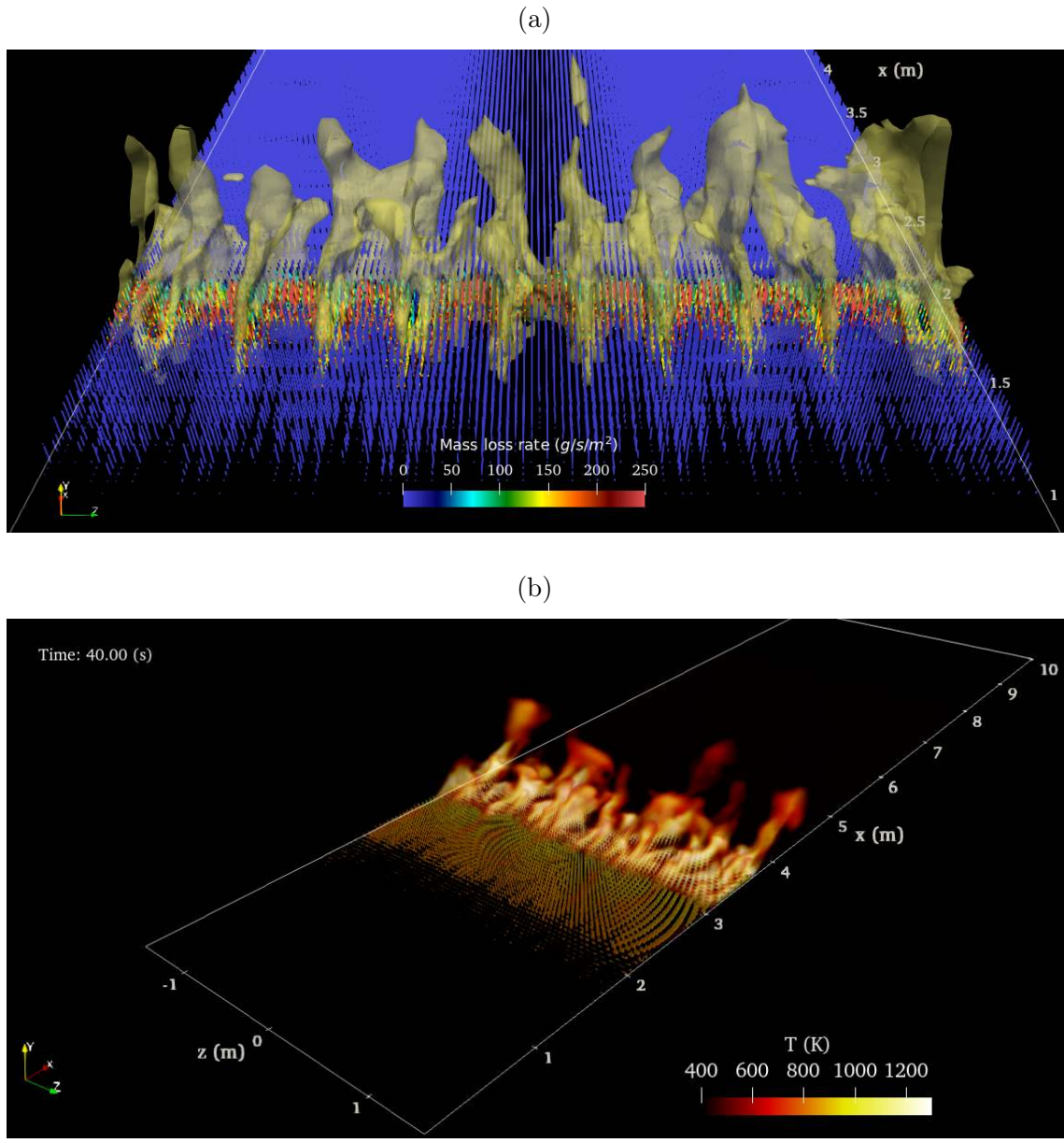


Figure 6.11: A 3-D rendering of the simulated fires: a) back view of Burn 53 showing the iso-surface of hot gases at $1000\text{ }K$ and the cardboard particles colored by the mass loss rate (fire spreads into the page); b) isometric view of Burn 67 showing the iso-volume of hot gases $> 550\text{ }K$ and the cardboard particles colored by their surface temperature (fire spreads from left to right).

Burn 67 is 0.4 m while the simulated value is 0.6 m .

Table 6.2: Characteristics of Burn 53 and Burn 67. A comparison between observed and simulated quantities.

Quantity	Burn 53		Burn 67	
	Observed	Simulated	Observed	Simulated
ROS (m/min)	1.82	2.27	6.01	5.71
Intensity-gas (kW/m)	123	137	149	125
Intensity-solid (kW/m)	-	63	-	54
Residence time (s)	9	10.4	4	5.4
Flaming zone depth (m)	0.36	0.56	0.45	0.63
Flame height (m)	0.5	0.8	0.4	0.6

6.3.4 Fire intensity and rate of spread

The global behavior of Burn 53 and Burn 67 in terms of the rate of spread and the fire line intensity is shown if Fig. 6.12. Figure 6.12a shows the time evolution of the pyrolysis front (defined as the furthest downstream location at which the particle is flaming according to the criterion established in section 2.2.6). The rate of spread is obtained from the slope of these curves. The measured rate of spread is also plotted for comparison. Qualitatively, the evolution of the pyrolysis front agrees well with the estimated evolution obtained from the measured rate of spread. A quantitative comparison is shown in Table 6.2. The average measured rate of spread in Burn 53 is $1.82\text{ m}/\text{min}$ while the simulated value is ($2.27\text{ m}/\text{min}$) which is $\sim 25\%$ larger. The average measured rate of spread in Burn 67 is $6.01\text{ m}/\text{min}$ and the corresponding simulated value is $5.71\text{ m}/\text{min}$. The simulations here underestimate

the rate of spread by only $\sim -5\%$. We believe that these deviations are acceptable given the experimental uncertainty and the complexity of the problem.

Figure 6.12b shows the time evolution of the fire intensity obtained from the gas-phase combustion. Note that consistent with the experimental objective, both Burn 53 and Burn 67 have approximately the same intensity (137 kW/m for Burn 53 and 125 kW/m for Burn 67) despite Burn 67 having a much higher rate of spread. We also estimate that there is an additional 30% of the heat release rate due to the smoldering of the solid particles.

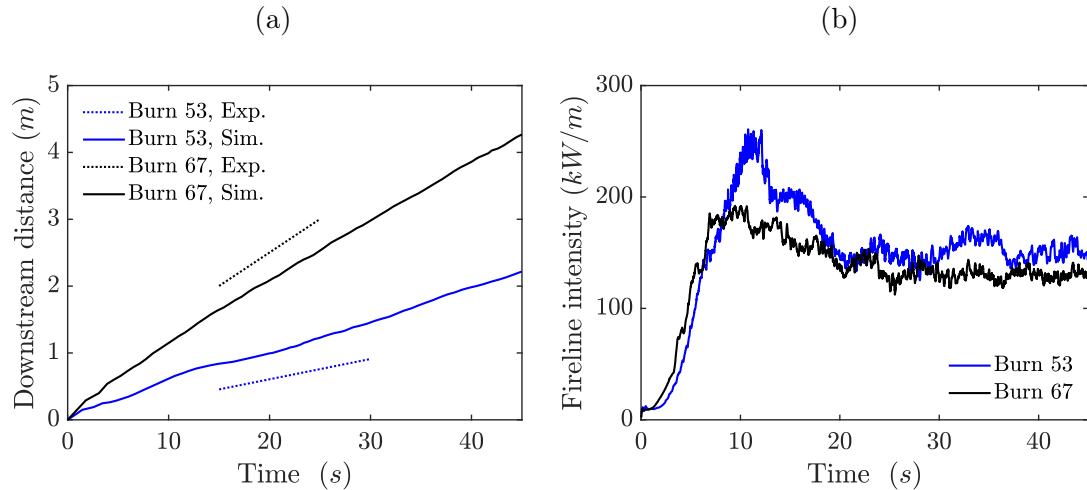


Figure 6.12: Global fire behavior of Burn 53 and Burn 67 in terms of a) rate spread, and b) fire line intensity. The dashed lines represent the slope from the measured rate of spread.

The implication of the boundary condition choices on the rate of spread of the simulated fires is shown in Fig. 6.13. The results show that the estimated ROS from the simulations is relatively insensitive to the choices of the inlet velocity or the total pressure boundary or the choice of the treatment of the lateral walls of the tunnel.

Because of the advantages associated with a uniform fire front, we prefer to employ periodic boundaries at lateral sides in the rest of the simulations presented in this dissertation.

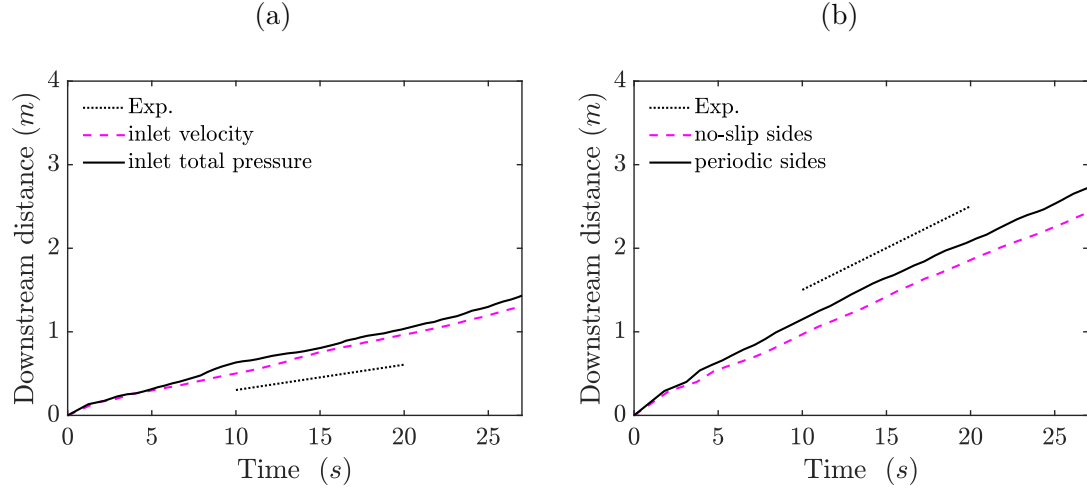


Figure 6.13: Time evolution of the pyrolysis front obtained from simulations with different boundary conditions: a) effect of inlet boundary in Burn 53; b) effect of the side walls on Burn 67.

The impact of the grid resolution on the fire propagation in Burn 67 is presented in Fig. 6.14. The estimated difference in the rate of spread obtained from the simulation with the baseline mesh choice and a simulation with the refined mesh is within $\sim 10\%$. Since these differences are relatively small and due to the large computational cost associated with the refined mesh, the baseline mesh choice is deemed adequate.

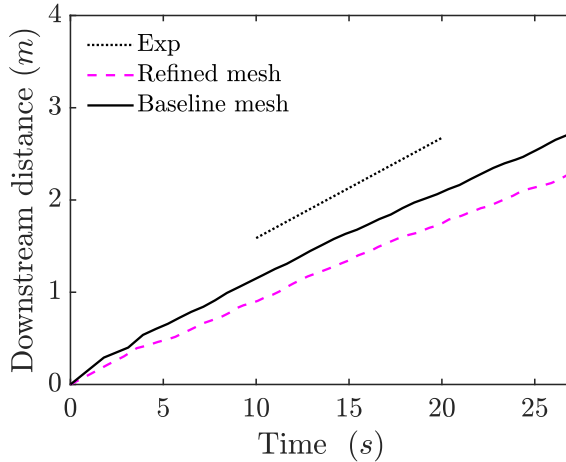


Figure 6.14: Time evolution of the pyrolysis front obtained from simulations with the baseline mesh and a refined mesh.

6.3.5 Local particle viewpoint

We present in this section additional diagnostics related to the gas conditions around an individual particle and the particle's thermal degradation behavior as a response to the external gas conditions. Figure 6.15 shows the gas temperature, the gas velocity, the oxygen mass fraction as well as the irradiation at $x = 3\text{ m}$, $z = 0$, at the top of the fuel bed obtained from the simulation of Burn 67. The temperature, the velocity, and the oxygen mass fraction in the gas show strong fluctuations associated with the turbulent instabilities of the buoyant flame. Consistent with experimental observations, the temperature of the gas in Fig. 6.15a fluctuates between 1200 K down to 400 K during the flame spread. The velocity at the top of the fuel bed shown in Fig. 6.15b increases/decreases around the nominal wind speed of 1.34 m/s due to flame-induced flow acceleration/deceleration. The oxygen mass fraction shown in

Fig. 6.15c starts at ambient value and then fluctuates significantly between ambient value to nearly zero when the flame passes at that location. The local irradiation shown if Fig. 6.15d starts from ambient value then increases gradually up to a peak of 60 kW/m^2 as the flame approaches the probe location. Note that the irradiation exhibits lower fluctuations than other quantities discussed earlier. This is because this irradiation represents the absorption and emission contributions from both the gas as well as the solid particles.

The response of the particle located at $x = 3 \text{ m}$, $z = 0$ is shown in Fig. 6.16. Note that we are reporting the variations at the top of the fuel bed (i.e., the upper portion of the particle). We will discuss in the next chapter the possible variations that may occur inside much deeper fuel beds.

The temperature evolution at the surface and the core of the particle is shown in Fig. 6.16a. Although the particle has a relatively small thickness, there are some differences between the particle surface temperature and the particle core temperature, particularly during the mass loss activity between $t = 30 \text{ s}$ to $t = 40 \text{ s}$. The particle temperature reaches about 900 K at approximately $t = 35 \text{ s}$ which is aligned with the peak MLR activity (Fig. 6.16c). The particle heats further to reach a temperature level above 1200 K . The peak temperature corresponds to the start of ash formation (Fig. 6.16b). Note that the particle surface temperature and the MLR exhibit some oscillations due to oscillations in the local gas conditions (see the discussion of the particle response to oscillatory conditions presented in Chapter 5).

The convective and radiation heat fluxes at the particle surface are shown in Fig. 6.16d. Note that these heat fluxes are dependent on the external gas conditions

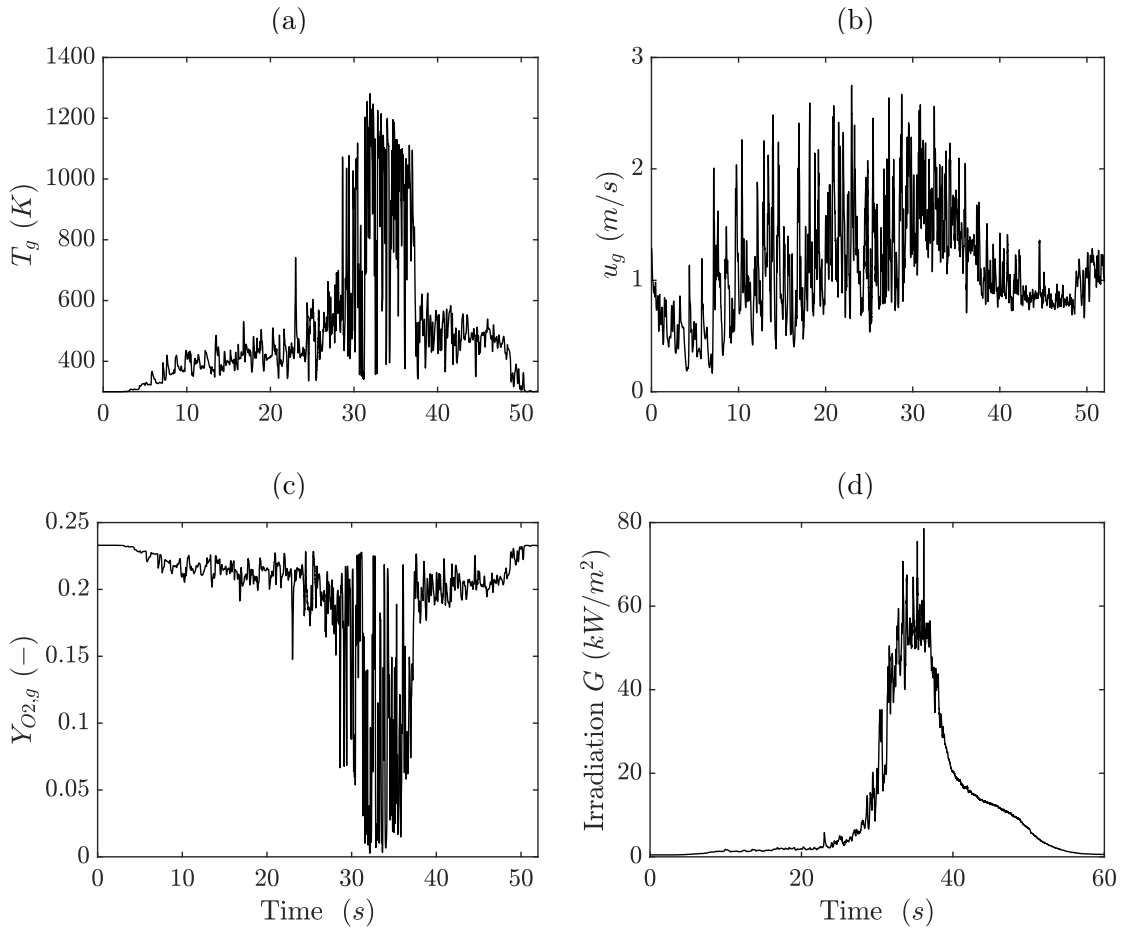


Figure 6.15: Local viewpoint of the gas conditions in Burn 67 at the top of the particle located at $x = 3\text{ m}$, $z = 0$: a) local gas temperature, b) local gas velocity, c) local oxygen mass fraction; and d) local irradiation.

as well as the particle response. Therefore, we see positive heat fluxes when the heat is transferred from the hot gases to the particle, followed by negative heat fluxes when the particle loses heat to the cold gas that is left after the flame has passed. We also see strong oscillations in the convective heat flux due to oscillations in both the velocity and the temperature of the surrounding gas (see Chapter 5).

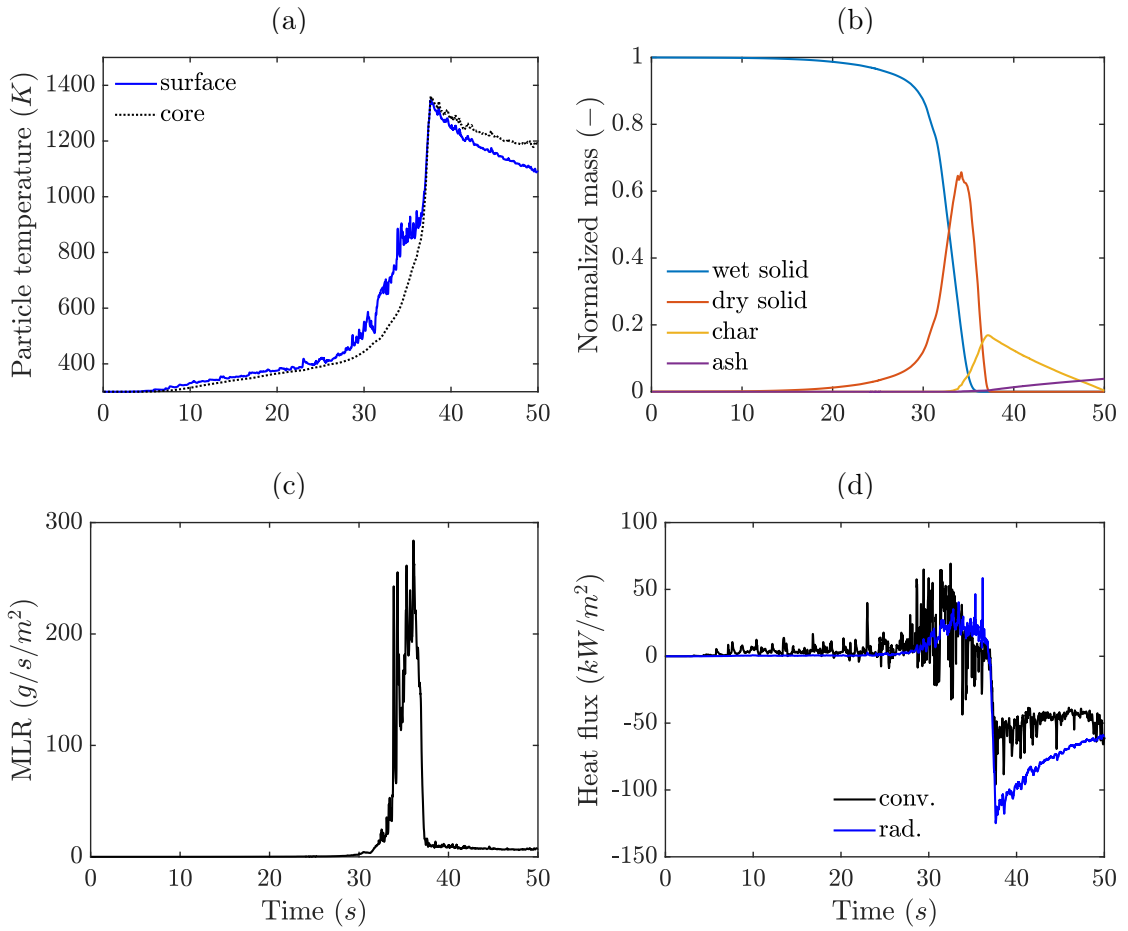


Figure 6.16: The behavior of the particle located at $x = 3\text{ m}$, $z = 0$ in Burn 67: a) particle surface and core temperature, b) particle constituents masses, c) particle mass loss rate; and d) net heat flux at the particle's exposed surface.

6.4 The Pseudo Incident Heat Flux (PIHF)

As shown in Fig. 6.16d and discussed in Chapter 5, the heat flux signals exhibit variations that are dependent on the instantaneous particle response, and we can not draw conclusions easily based on these signals. Therefore, we use the PIHF to analyze the convective and radiative contributions in external heating. Figures 6.17a

and 6.17b show the convective and radiative portions of the PIHF extracted from Burn 53 and Burn 67, respectively. Note that we generally remove the value of PIHF corresponding to ambient conditions ($\text{PIHF}_0 = \epsilon_{\text{surf}} G_0 + h T_{g,0}$, where $T_{g,0} = 300 \text{ K}$ is the ambient temperature and G_0 is its corresponding irradiation). The quantity $\text{PIHF} - \text{PIHF}_0$ starts at zero and then gradually increases as the hot gases approach the measurement location. We see that the convective part starts increasing in Burn 67 at a much earlier time than that of Burn 53 because of the higher wind speed that tends to tilt the flame towards the fuel bed. We also see that there is a mixed mode of heating with both convection and radiation. However, convective heating is slightly higher and occurs earlier than radiative heating. Integrating these signals over time reveals that 60% of the PIHF is due to convection and 40% of the PIHF is due to radiation in Burn 53 and Burn 67. These ratios indicate the significance of the convective heating for these small particles. We will discuss in the following chapter the respective weights of convection and radiation for other particle sizes.

6.5 The flame residence time

We discuss in this section possible ways to estimate the flame residence time. According to the description of Finney et al. [36], the residence time is estimated experimentally from the spline smoothing of the temperature signal obtained from a thermocouple (a preheat zone is defined from the first crossing of the 350°C to where the spline reaches its peak, then the burning phase continues until the spline drops again to below 350°C). We applied this technique to our simulation data

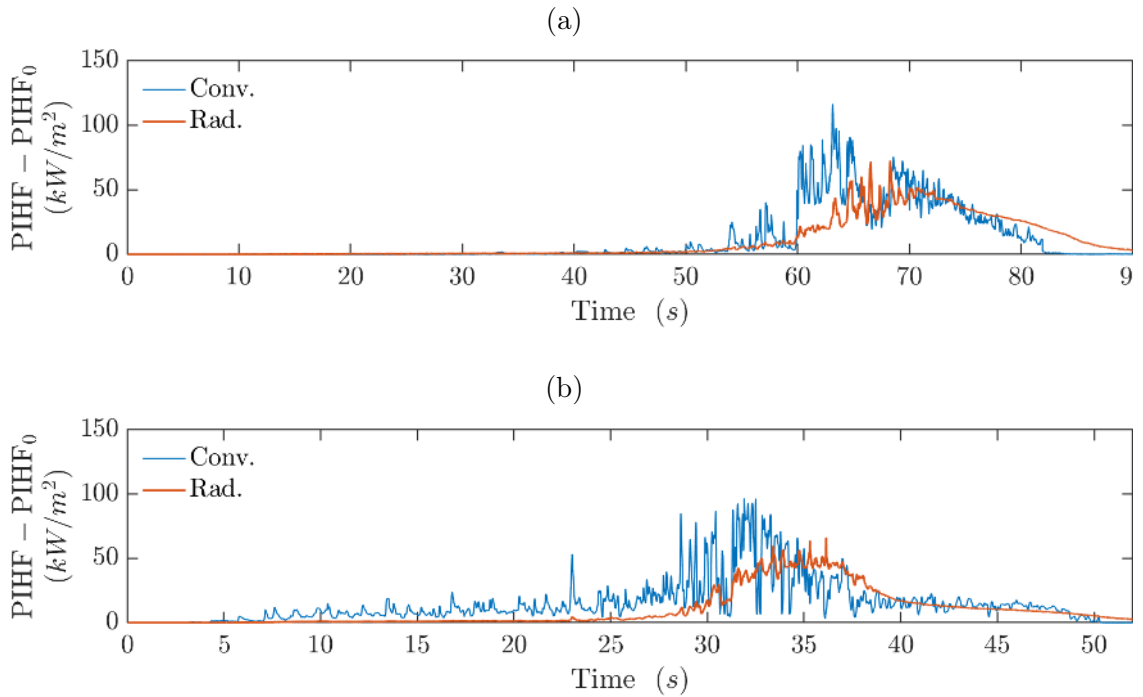


Figure 6.17: The convective and radiation contributions to the pseudo incident heat flux (PIHF) extracted at the top of the fuel bed at $x = 3 \text{ m}$, $z = 0$ in a) Burn 53, and b) Burn 67.

by first extracting the temperature of the gas at a certain location, then applying a cubic smoothing spline fit using the MATLAB function *csaps* with a smoothing parameter of 0.5. Figure 6.18a shows our application of this technique using the gas temperature data obtained from the Burn 67 simulation.

Figure 6.18b provides the model description of the flaming and glowing times of a single particle following the criteria described in section 2.2.6. We also propose an alternative residence time based on the intense PIHF define as the duration at which $\text{PIHF} - \text{PIHF}_0$ is greater than 10% of its peak value (Fig. 6.18c). This new quantity allows us to consider the heating duration of both convective and radiative

contributions.

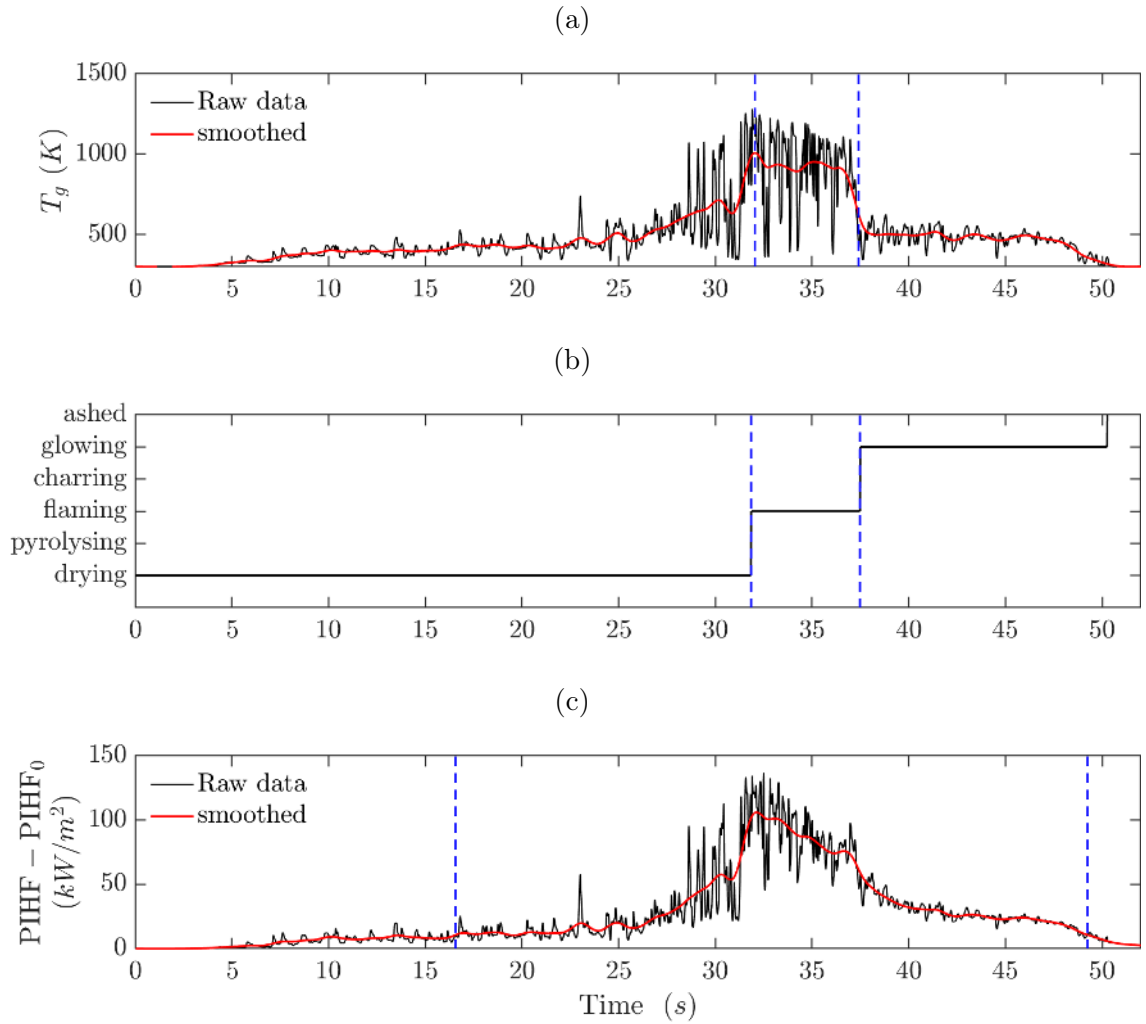


Figure 6.18: Flame residence time based on a) gas temperature, b) particle flaming duration, and c) duration of intense PIHF. The red solid line is a spline fit of the raw data. The vertical dashed blue lines delimit the start and the end of the residence time. The data correspond to the particle located at $x = 3\text{ m}$, $z = 0$ in Burn 67.

6.6 Fire behavior variation with the fuel bed packing

6.6.1 Global fire behavior

We discuss in this section the results obtained from simulations of fire spread in cardboard fuel beds with different fuel packing. As described earlier, the packing ratio β_s is varied between 0.0071 and 0.0246 by changing the axial spacing between the particles. The wind speed is kept similar to Burn 67 at 1.34 m/s to achieve a well-controlled flow field in the tunnel and to avoid uncertainties associated with the back-layering effect.

Figure 6.19 shows a 3-D view of the flaming zone obtained from simulations with different packing ratios. The flaming zone is determined by the flaming particles that produce a gaseous fuel at a rate greater than 1 g/s/m^2 (see section 2.2.6). Our first observation from these views is that the flaming zone depth increases with the packing ratio. Our second observation is the existence of a coherent wavy structure at the tail of the flaming zone that becomes more evident at a high packing ratio. We believe that this wavy structure is related to buoyant instabilities that interact with the smoldering zone.

In terms of quantitative behavior, Fig. 6.20 shows the variation of the fire line intensity, the ROS, the flame zone depth, and the flame height for different packing ratios. A linear fit of the simulated data is included in the plots. Figure 6.20a shows a comparison between the simulated fire intensity and the one calculated from Byram's expression. The simulated fire intensity shows a linear increase with the

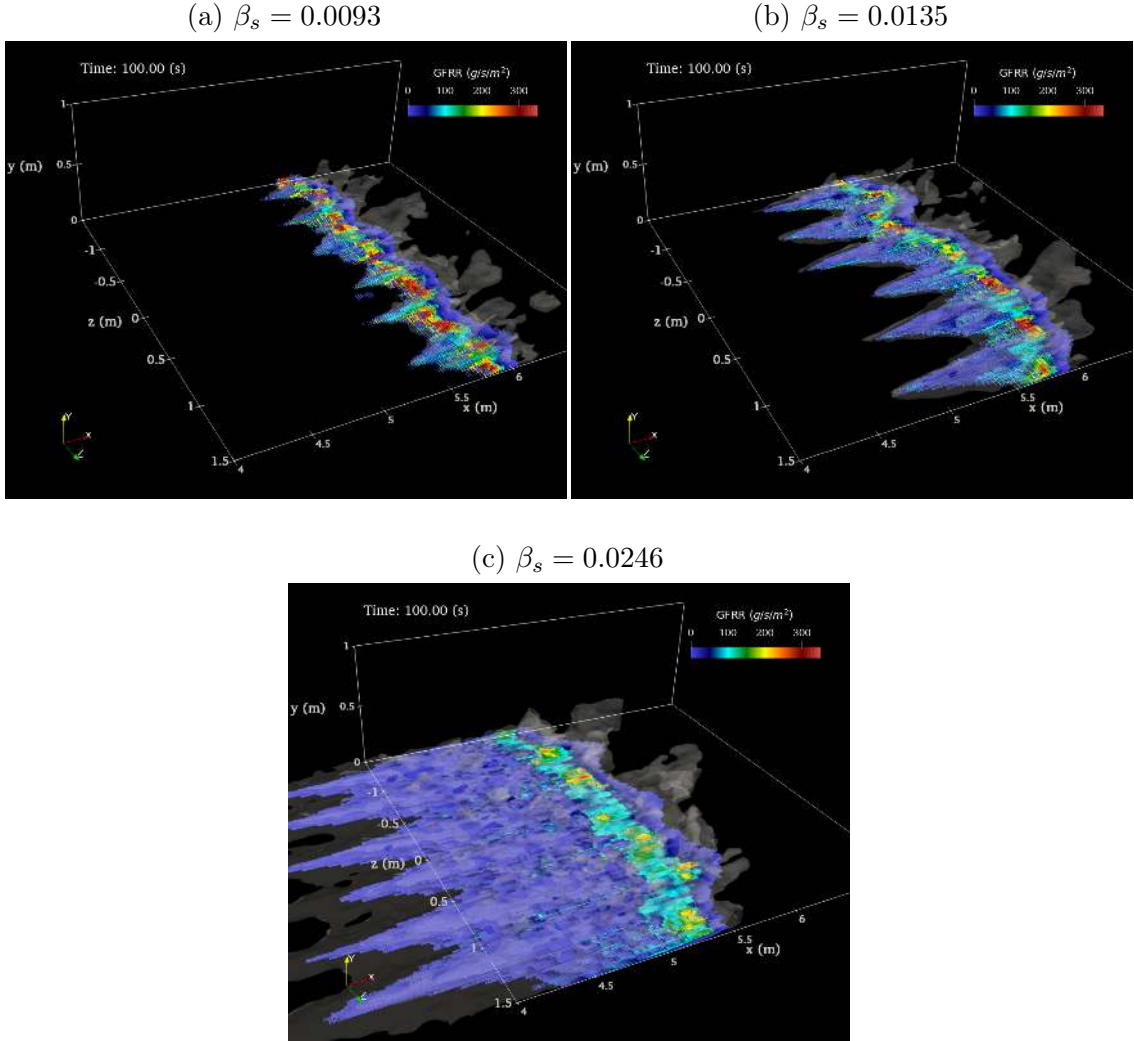


Figure 6.19: A 3-D rendering of the flaming zone variation with the packing ratio β_s .

The flaming particles are colored by the gaseous fuel release rate (GFRR) (i.e., the production rate of fuel from the pyrolysis reactions R_p and R_{op}). The hot gases at $1000\text{ }K$ are represented by the white iso-surface.

packing ratio. There is a relatively small deviation between the simulated intensities and the corresponding values obtained from Byram's expression. The simulated flame zone depth also shows a linear increase with the packing ratio (Fig. 6.20b).

The flame zone depth increases from $\sim 0.5\text{ m}$ at the lowest packing ratio to above $\sim 2\text{m}$ in the case with the highest packing ratio. The simulated ROS (Fig. 6.20c) shows a slight decrease as the fuel packing increases. Also, the flame height shows a slight increase as the packing ratio increases as indicated in Fig. 6.20d.

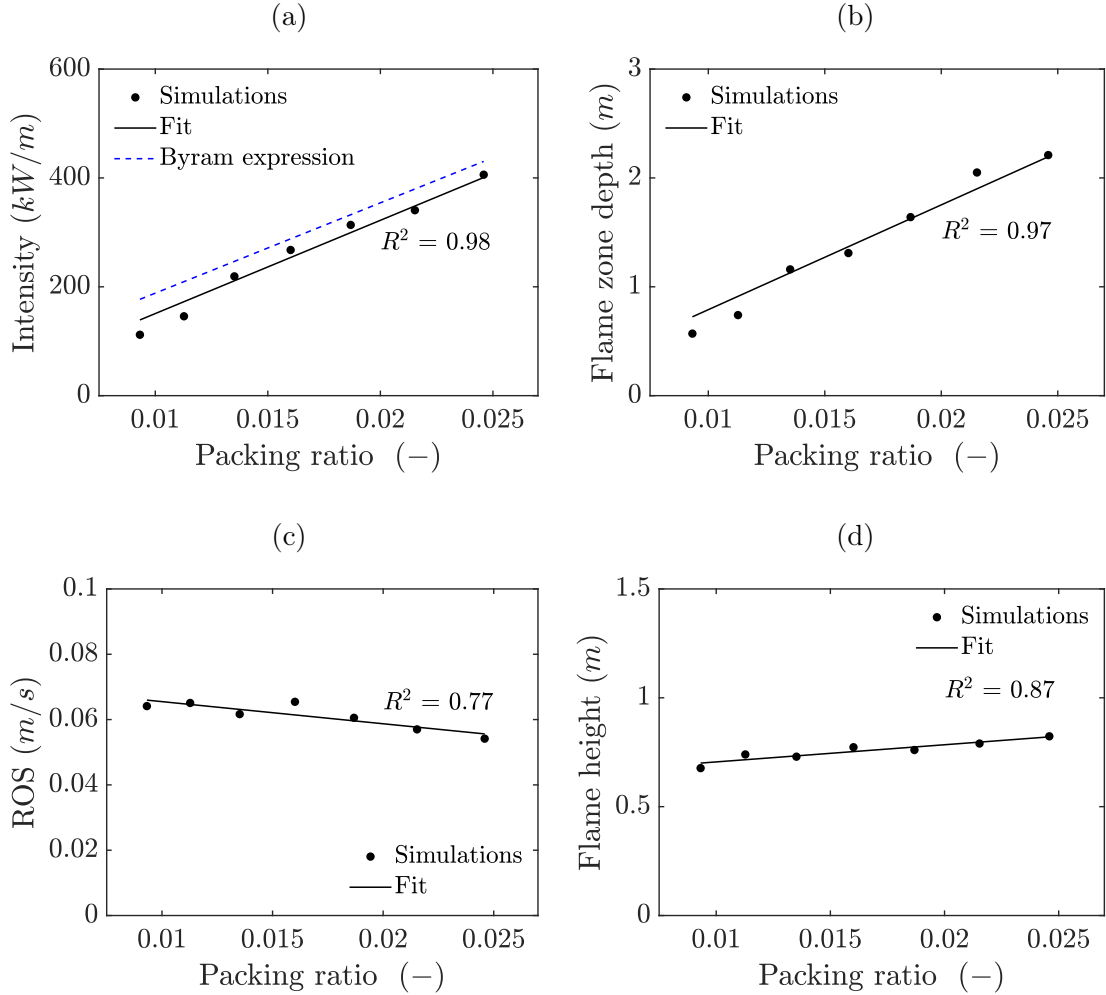


Figure 6.20: Variations of the a) fire intensity, b) the flame zone depth, c) the fire rate of spread, and d) the flame height with the fuel bed packing ratio. The symbols represent the simulated cases and the solid line represents a linear fit to the simulated data.

6.6.2 Local particle viewpoint

Figure 6.21 shows the behavior of 36 particles located between $3 \leq x \leq 4 \text{ m}$ and $0 \leq z \leq 1.5 \text{ m}$. The axial and lateral distances between these particles are 0.2 m and 0.25 m , respectively. The results of Fig. 6.21 feature some variation in the behavior of individual particles across different locations in the fuel bed. These variations are due to the interaction between the turbulent flame instabilities (represented by the flame peaks and troughs discussed earlier) and the solid fuel bed, which cause certain locations in the fuel bed to burn faster than others. We account for these variations in the following discussion about the residence time by calculating the average quantities from the 36 locations as well as estimating the standard deviations.

Figure 6.22 shows the variation of the residence time of the simulated fires obtained using the definitions discussed in section 6.5. The estimated residence times are obtained from the 36 locations discussed earlier. The results presented in Fig. 6.22 suggest that, despite some variations across the 36 locations as indicated by the vertical bars, the average residence time obtained from all definitions increases linearly with the increase in the fuel packing ratio, but at different rates. This indicates that the particles in the densely packed bed burn slower and are exposed to external heating for a longer duration than those in the loosely packed beds. Also, the results of Fig. 6.22b show that the residence time based on the PIHF duration is much larger than the other two definitions based on the particle burning time or the experimental method for gas temperature. This is because the PIHF accounts for

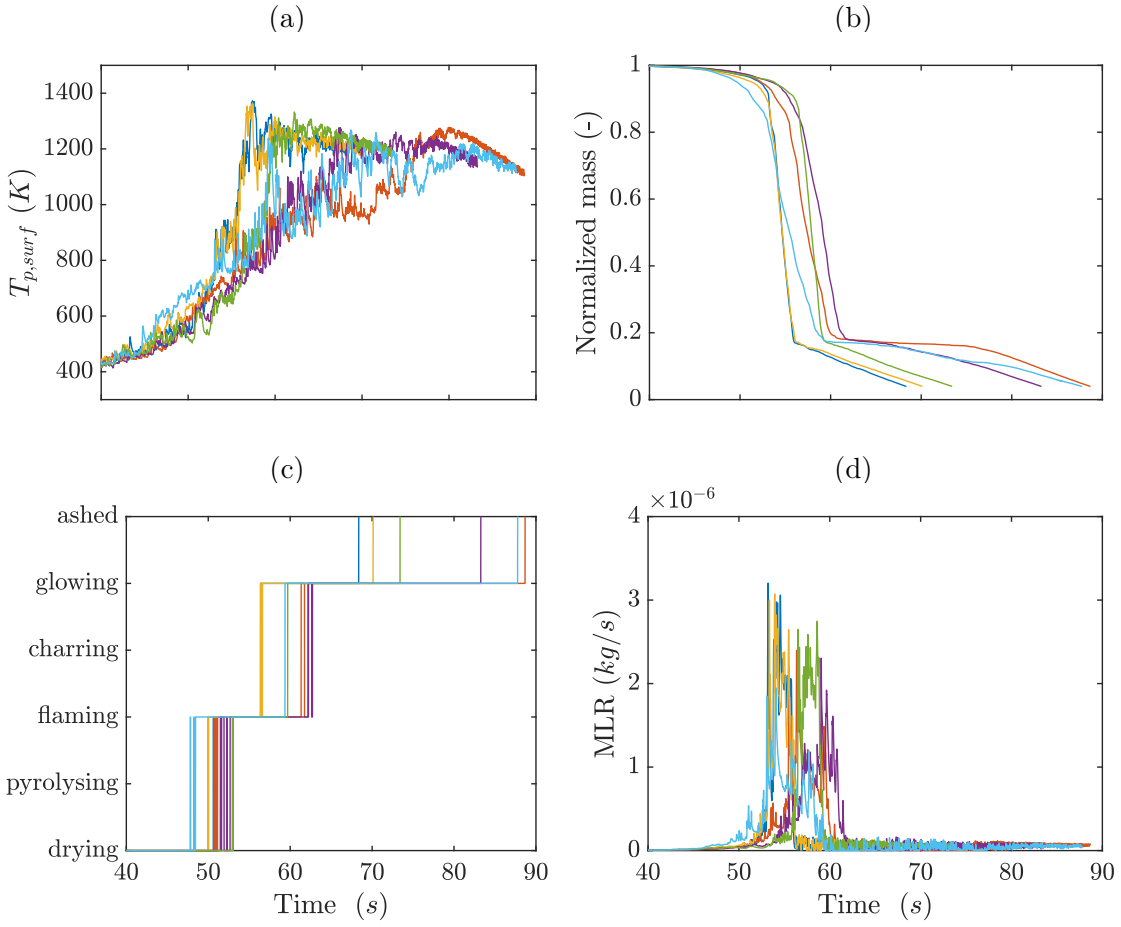


Figure 6.21: The behavior of 36 particles in Burn 67, starting from $x = 3 \text{ m}$, $z = 0$ and separated by 0.2 m in the x -direction and 0.25 m in the z -direction: a) particle surface temperature, b) normalized particle masses, c) particle state, and d) particle mass loss rate.

the external preheating period by convection or radiation before flame arrival, as well as the external heat that comes from the nearby glowing particles late in the thermal degradation process. Lastly, the results of Fig. 6.22c reveal that the average simulated residence time obtained from the gas temperature method is in very good agreement with the empirical equation proposed by Finney et al. [2], which was

obtained by fitting the experimental measurements taken from similar configurations.

This equation shows a linear dependence of the residence time τ_r on the fuel packing ratio as follows [2]

$$\tau_r = 566\beta_s + 4894/\sigma_p + 4.6m''_{fuel} \quad (6.4)$$

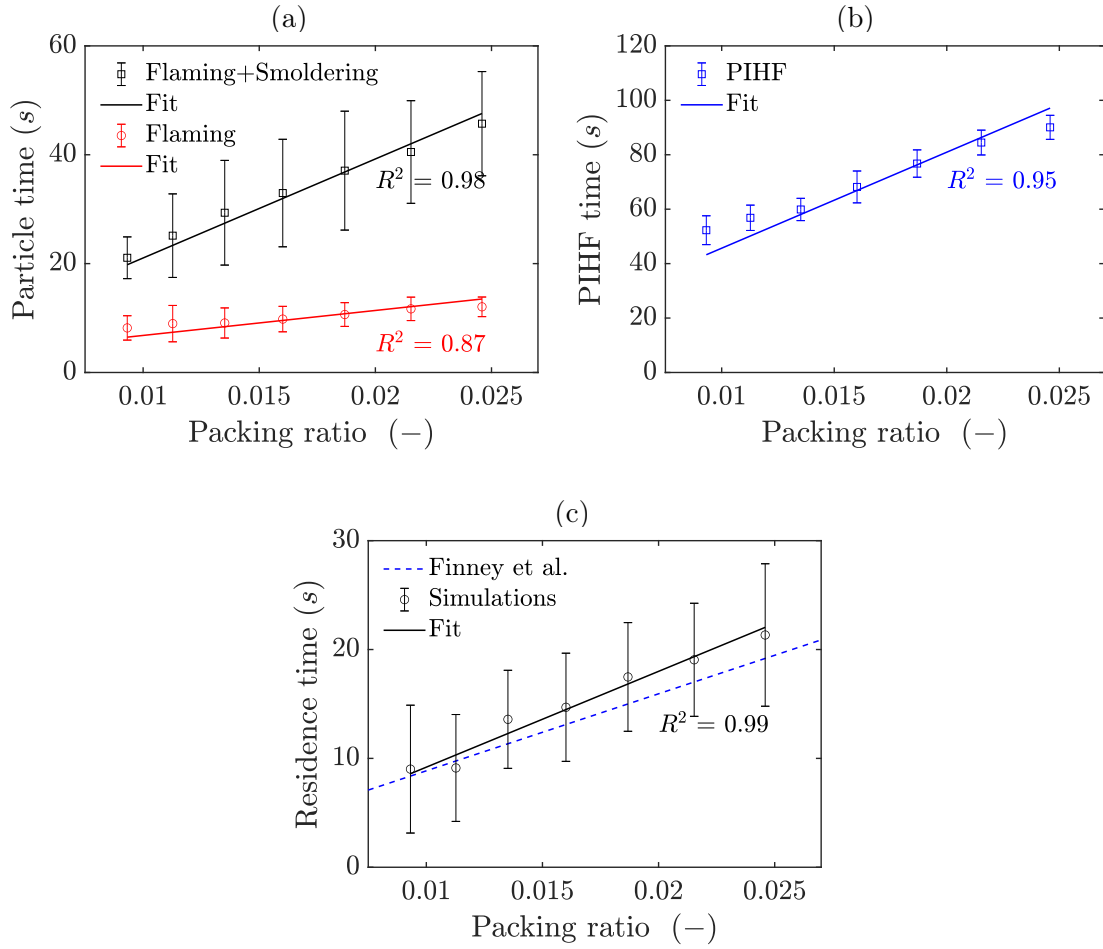


Figure 6.22: Variation of the residence time with the packing ratio: a) the particle flaming and smoldering times, b) the PIHF time, and c) the flame residence time based on the gas temperature. The symbols represent the average of 36 particles, the bars represent the standard deviation, and the solid lines represent linear fit. The dashed blue line represents the experimental fit of Finney et al. [2].

6.7 Summary

This chapter presented simulations of fire spread in loosely and densely packed fuel beds comprised of discrete cardboard sticks. The simulations correspond to past wind tunnel fire experiments that have been conducted at the Missoula Fire Sciences Laboratory.

The first part of the chapter focused on evaluating the newly developed modeling capability in predicting the structure and the behavior of two experimental burns that belong to either a buoyancy-dominated fire regime or a wind-dominated fire regime. The simulated fires were in very good agreement with the experimental measurements of the ROS and observations of the flame structure. The simulated buoyancy-dominated fire featured a peak and trough structure similar to that observed experimentally. Also, the wind-dominated fire featured a flaming front followed by a glowing zone similar to that observed experimentally. In terms of quantitative measures, the difference between the measured ROS and the simulated value was within $\sim 5\%$ in the wind-dominated fire, while a higher difference of $\sim 25\%$ was obtained in the buoyancy-dominated fire.

The second part of this chapter discussed the change in fire behavior due to changes in the fuel packing. The simulations showed similar trends as those observed experimentally where the residence time was found to increase linearly with the increase in the fuel packing ratio with strong scaling. Also, the ROS was found to slightly decrease with the increase in the packing ratio.

7 Simulations of Fire Spread in Idealized Uniform and Mixed Size Pine Wood Fuel Beds

7.1 Overview

This chapter presents a study of fire spread in idealized uniform fuel beds of mono-dispersed cylindrical-shaped pine wood sticks of 2 mm diameter and in fuel beds that feature a mixed-size patch comprised of small and larger particles (10 or 20 mm diameter). The mixed-size patch is inserted in a limited region within the uniform bed to avoid disruption of the main fire front. The configurations presented in this chapter represent asymptotic line fires that are spreading over flat terrain in an open field under prescribed wind velocities.

As suggested in past studies (e.g. Ref. [106]), the structure of the line fires is controlled by Byram's convection number N_C [109]. The literature suggests that a buoyancy-dominated fire regime occurs when $N_C > 1$, while a wind-dominated fire regime occurs when $N_C < 1$. Note that the fire intensity \dot{Q}'_{fire} is directly proportional to the ROS and the fuel loading per unit surface area m''_{fuel} . The fuel loading is a function of the fuel bed characteristics (i.e., the packing ratio, the particle mass density, and the fuel bed height).

We present in this chapter two configurations that correspond to either the buoyancy-dominated regime or the wind-dominated regime. The emphasis in this study is on the behavior of individual particles in terms of the degree of complete consumption, the transition from flaming to smoldering, and the respective weights of convective and radiative heating.

7.2 Numerical configuration

Careful attention is paid while choosing the configuration parameters (i.e., the fire intensity, the wind speed, and the fuel bed characteristics) in order to simulate configurations corresponding to either the buoyancy-dominant regime or the wind-dominant regime. We modified a MATLAB script, that has been previously developed by Dr. Arnaud Trouv 's research group for calculating the ROS based on the Rothermel model, to iteratively estimate Byram's convection number N_C based on inputs of the wind profile and the fuel bed characteristics. The Rothermel model estimates the ROS based on the following: 1) a rate of fuel consumption that has been determined from empirical correlations as a function of the surface area to volume ratio of the fuel particles and the packing ratio of the fuel bed, 2) the fuel load defined as the mass of fuel per unit square area, and 3) the heat required to ignite the fuel which was evaluated analytically for cellulosic fuels as a function of the fuel moisture. More details about the Rothermel model inputs can be found in Ref. [110]. The flame height was estimated using the empirical correlation of Yuana and Cox [111].

After iterating on different variations of the wind speed and the fuel bed characteristics, we converged at a configuration that has a 0.4 m high fuel bed of 2 mm diameter cylindrical pine wood sticks arranged at a packing ratio of $\beta_s = 0.005$ (a fuel loading of 0.7581 kg/m^2). The fuel bed is subjected to a cross-wind at either 1 or 5 m/s nominal speed evaluated at 2 m elevation. The estimated ROS using the Rothermel model is 0.098 m/s at 1 m/s wind speed and is 0.33 m/s at 5 m/s wind speed. The corresponding Byram's convection numbers are 66 and 1.2 , respectively. A summary of the configuration parameters for the uniform pine wood fuel bed simulations is presented in table 7.1.

Table 7.1: Design parameters of the buoyancy-dominated and wind-dominated line fires in the uniform pine wood fuel bed.

Parameter	Buoyancy-dominated	Wind-dominated
Wind speed $u_2\text{ m (m/s)}$	$1 \pm 10\%$	$5 \pm 10\%$
Domain size (m^3)	$52 \times 40 \times 15$	$152 \times 40 \times 40$
Fuel bed height (m)	0.4	0.4
FMC (%)	5	5
Packing ratio β_s (-)	0.005	0.005
Particle diameter (mm)	2	2
Fuel loading $m''_{fuel}\text{ (kg/m}^2)$	0.76	0.76
Rothermel ROS (m/s)	0.088	0.34
Theoretical $\dot{Q}'_{fire}\text{ (MW/m)}$	0.79	3.02
Byram number N_C (-)	66.08	1.24
Empirical flame height (m)	2.9	7.1

7.2.1 Computational domain and fuel bed setup

Figure 7.1 shows a 3-D representation of the computational domain including the fuel bed and the computational grid cells. As shown in Fig. 7.1, the domain has a flat terrain and a square cross-section of $40 \times 40 \text{ m}^2$. The domain inlet is placed at $x = -2 \text{ m}$ and the domain outlet extends to a distance of up to 152 m downstream of the inlet to allow for the wind-dominated line fire to establish and achieve a quasi-steady propagation. Preliminary tests show that a shorter domain that extends to a length of only 52 m and width of 16 m is sufficient for the buoyancy-dominated line fire.

As shown in Fig. 7.1a, the baseline configuration has a uniform fuel bed comprised of cylindrical-shaped pine wood sticks of 2 mm diameter and 0.4 m height. The 2 mm pine wood sticks are oriented vertically and are packed in the uniform fuel bed that extends from $x = -0.5 \text{ m}$ to the domain outlet and spans the entire domain width. The number of physical pine wood sticks is selected to achieve a packing ratio of $\beta_s = 0.005$ in the uniform fuel bed (more details about the number of computational particles that represent the physical sticks are presented later).

In addition to the configuration with the uniform fuel bed, we simulated another configuration that has a mixed-size patch comprised of large (10 or 20 mm diameter) pine wood sticks in addition to the small ones. As shown in Fig. 7.1b, the mixed-size patch in the computational domain of the wind-dominated fire extends between $38 \leq x \leq 42 \text{ m}$. The mixed-size patch in the computational domain of the buoyancy-dominated fire extends between $18 \leq x \leq 22 \text{ m}$. The larger pine wood

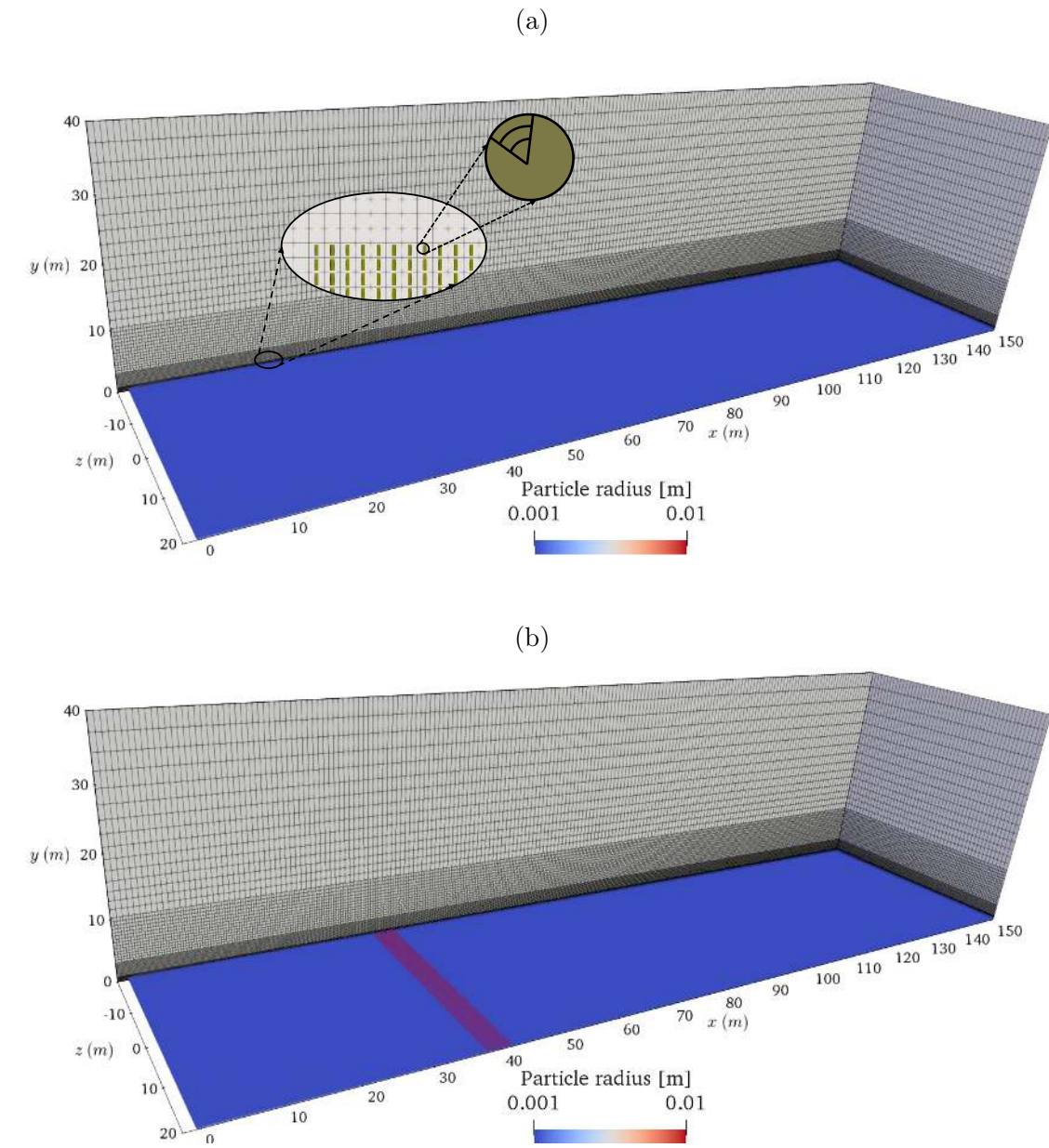


Figure 7.1: A 3-D view of the computational domain used in the simulations of fire spread in pine wood fuel beds: a) the uniform fuel bed with 2 mm particles ($\beta_s = 0.005$); b) the fuel bed with a patch of mixed small/large particles ($D_p = 2$ and 10 or 20 mm) located at $38 \leq x \leq 42$ m ($\beta_s = 0.0068$ or 0.012).

sticks (the ones with 10 or 20 mm diameter) are separated by 0.2 m (edge-to-edge) in the axial and the transverse directions (i.e., x- and z-directions, respectively), while the arrangement of the smaller particles is not changed in the mixed-size patch and is similar to the uniform bed. The packing ratio in the mixed-size patch is 0.0068 when the larger particles of 10 mm diameter are used and is 0.012 when the larger particles of 20 mm diameter are used.

7.2.2 Computational mesh resolution

As shown in table 7.1, the estimated characteristic length-scales of the fires of interest are the 0.4 m fuel bed height and a flame height of $\sim 3 - 8 m$. In addition to these length-scales, there is a radiation penetration length-scale that is estimated to be $\sim 0.4 m$. The computational grid is designed to resolve all these length-scales.

The baseline computational configuration shown in Fig. 7.1 has 3 refinement regions and a far-field region. Region-1 extends from the ground to 0.8 m elevation and features the highest grid resolution with cubic cells of 10 cm size; Region-2 exists between 0.8 and 3 m elevation and features cubic grid cells with a resolution that is twice that used in Region-1; Region-3 exists between 3 and 10 m elevation and features cubic grid cells with a resolution that is twice that used in Region-2; and finally, the far-field region exists above 10 m elevation and features a stretched grid.

To study grid convergence, two additional computational grids are tested by increasing or decreasing the grid resolution in Region-1 by a factor 2 (i.e., a finer resolution of 5 cm cubic or a coarser resolution of 20 cm cubic cells). The number

of grid cells in the larger domain for wind-dominated fires is 7,362,500 cells (the coarser mesh has 1,045,000 cells and the finer mesh has 57,969,000 cells). The reduced domain that is used in the simulations of the buoyancy-dominated fire has 1,007,500 cells (the coarser mesh has 143,000 cells and the finer mesh has 7,822,100 cells).

The pine wood sticks are distributed inside the fuel bed region such that a certain number of physical particles is placed inside each computational grid cell to achieve the desired packing ratio of 0.005 (e.g., the baseline computational grid with the 10 cm resolution has 16 particles per computational grid cell). A single cylindrical-shaped computational particle is used to represent multiple particles that exist within the same computational grid cell of the fuel bed region. The height of each cylindrical computational particle is distributed over multiple cells in order to resolve the variations inside the fuel bed depth. Each cylindrical particle is resolved using 25 μm resolution axisymmetric cylindrical shells (40 shells for the 2 mm diameter particle). We also tested the impact of this choice by increasing or decreasing the particle grid resolution by a factor of 2.

The total number of computational particles in the larger domain for wind-dominated fires is 2,408,000 particles (the domain with a coarser mesh has 301,200 particles and the one with a finer mesh has 19,257,600 particles). The reduced domain that is used in the simulations of the buoyancy-dominated fire has 323,200 particles (the corresponding domain with a coarser mesh has 40,480 particles and the one with a finer mesh has 2,583,040 particles).

Lastly, the angular space used in the solution of the MRTE is discretized using

144 solid angles following the study presented in Chapter 4.

7.2.3 Boundary conditions

Regarding the boundary conditions, the external wind velocity is imposed at the west boundary of the computational domain using the classical power-law atmospheric boundary layer profile given by [112]

$$u(z) = u_{ref} (z/z_{ref})^{(1/7)} \quad (7.1)$$

where z_{ref} is the reference elevation ($= 2\text{ m}$) and u_{ref} is the nominal velocity at the reference elevation ($= 1$ or 5 m/s). Turbulence fluctuations are introduced to the mean inlet velocity profile using temporal sinusoidal oscillations that include a randomly generated spatial noise to represent 10% fluctuations.

The ground surface ($y = 0$) is treated with a no-slip condition and is assumed to be adiabatic (i.e., no heat loss to the ground underneath the fuel bed). Periodic boundary conditions are used on lateral sides to mimic a quasi-infinite domain. The top and east boundaries are treated as open boundaries with free inlet/outlet flow. Because the domain size is large, hydrostatic effects may become significant. These effects are accounted for by using the *prghTotalHydrostaticPressure* boundary condition from the OpenFOAM library. The reference height and pressure used in this boundary condition are 40 m and 100864.31 Pa , respectively.

A slot burner that extends from $-0.5 \leq x \leq 0\text{ m}$ is flush mounted to the floor underneath the fuel bed and is used to ignite the fuel bed. Ignition of the fuel bed is achieved by injecting gaseous fuel at 0.01 m/s and 1600 K for a duration of 10 s .

7.2.4 Sub-models

The WALE model is used to calculate the subgrid-scale turbulent quantities and the PGRF radiation approach is used with a global radiant fraction of 0.35. This value is selected based on the study of turbulent buoyant sooting fire flames in ambient air (see Chapter 4).

7.2.5 Computational cost

The flow time-step is controlled using a Courant–Friedrichs–Lewy condition and is on the order of $\sim 0.004\text{ s}$. The particle time-step is different and is dependent on the local particle behavior (see A.3). The particle time-step is ranging between 0.0002 and 0.004 s. The MRTE is solved every 10 flow time-steps to update the radiation field.

The simulations are carried out on a distributed-memory parallel cluster using Message Passing Interface (MPI) techniques. The simulation of 60 seconds of the fire spread using the baseline configuration requires approximately 25 kCPU hours using 200 processors (the configuration with finer mesh requires ~ 330 kCPU hours to simulate 60 seconds of flow time). The simulations presented here typically run for at least 300 seconds of fire spread.

7.3 Fire spread in the uniform fuel bed

We discuss in this section the results obtained from the simulations of the buoyancy-dominated and the wind-dominated fire spread in the uniform fuel bed.

7.3.1 Global fire behavior

Figure 7.2a shows the time-dependent propagation of the wind-dominated fire downstream of the ignition burner obtained from the simulations as well as from the Rothermel model. The flame back and front are estimated in the simulations using the rearmost and foremost points in the domain at which the volumetric heat release rate is greater than a threshold value of 1 kW/m^3 . The pyrolysis back and front are determined based on the rearmost and foremost particle that has a "flaming" state based on the criteria established in Section 2.2.6. Similarly, the smoldering back and front are determined based on the rearmost and foremost particle that has a "glowing" state. The corresponding time evolution of the simulated fire intensity is shown in Fig. 7.2b.

A first examination of Figs. 7.2a and 7.2b suggests that the fire exhibits a damping behavior in the transient phase shortly after ignition until reaching a quasi-steady state. For instance, during the first 60 seconds, the fire intensity profile shows an increase to a peak of $\sim 3 \text{ MM/m}$, followed by a decrease to $\sim 1 \text{ MW/m}$ then an increase to a peak of $\sim 4 \text{ MW/m}$ followed by a decrease to $\sim 3 \text{ MW/M}$. The wind-dominated fire achieves a steady propagation rate and a quasi-steady intensity after about 150 s from the time of ignition. Figure 7.2a also shows that the fire can be identified by three zones: a flame zone with a flame front located the furthest downstream; a pyrolysis zone with a pyrolysis front that is $\sim 5 \text{ m}$ upstream of the flame front; a smoldering zone that is $\sim 1.5 \text{ m}$ upstream of the pyrolysis front. The results of Fig. 7.2a depict that the three zones are not expanding nor contracting and

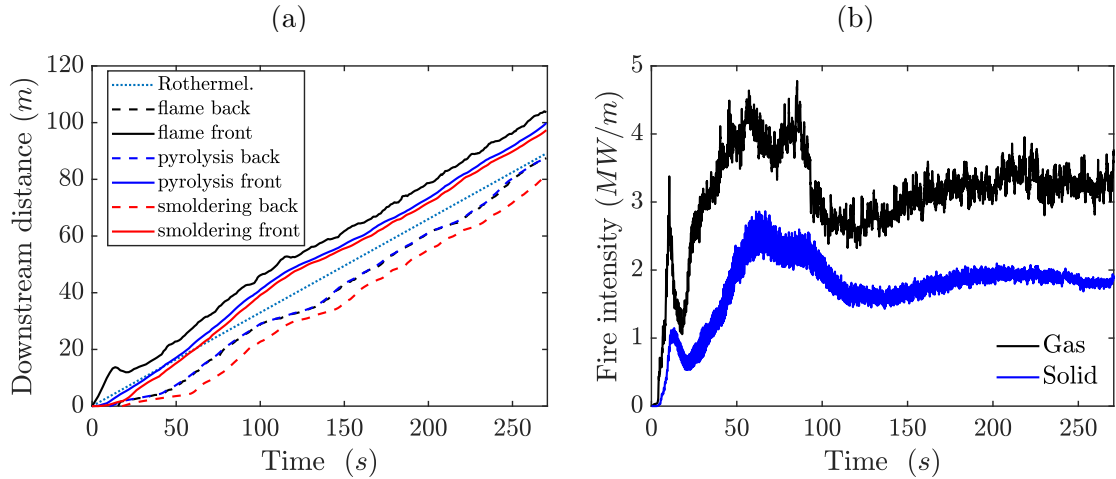


Figure 7.2: Propagation of the wind-dominated fire in the uniform bed: a) time evolution of the simulated flame, pyrolysis and smoldering zones (solid and dashed lines) and the estimated spread from Rothermel model (dotted line); b) time evolution of the simulated fire intensity from homogeneous gas-gas reactions (black line) and from heterogeneous solid-gas reactions (blue line).

are only moving at the same rate. We also notice from the results that there are not many differences between the fire propagation estimated using the Rothermel model and the fire propagation estimated from the simulations in this wind-dominated fire.

Figure 7.2b shows that the simulated intensity can be divided into two parts: a first part that comes from the exothermic homogeneous combustion of the gaseous volatiles with ambient air (referred to as gas), and a second part that comes from the exothermic heterogeneous reactions corresponding to oxidative pyrolysis and char oxidation (referred to as solid). The simulation results indicate that the solid contribution to the fire intensity in this wind-dominated fire is significant and is approximately half of that from the homogeneous gas-phase combustion.

The time evolution of the propagation rate and the intensity of the buoyancy-dominated fire are plotted in Figs. 7.3a and 7.3b. Similar to the wind-dominated fire, we see some overshoot in the spread rate and the fire intensity soon after ignition, followed by damped oscillations until a quasi-steady state is achieved. However, the simulated buoyancy-dominated fire features a much slower propagation rate.

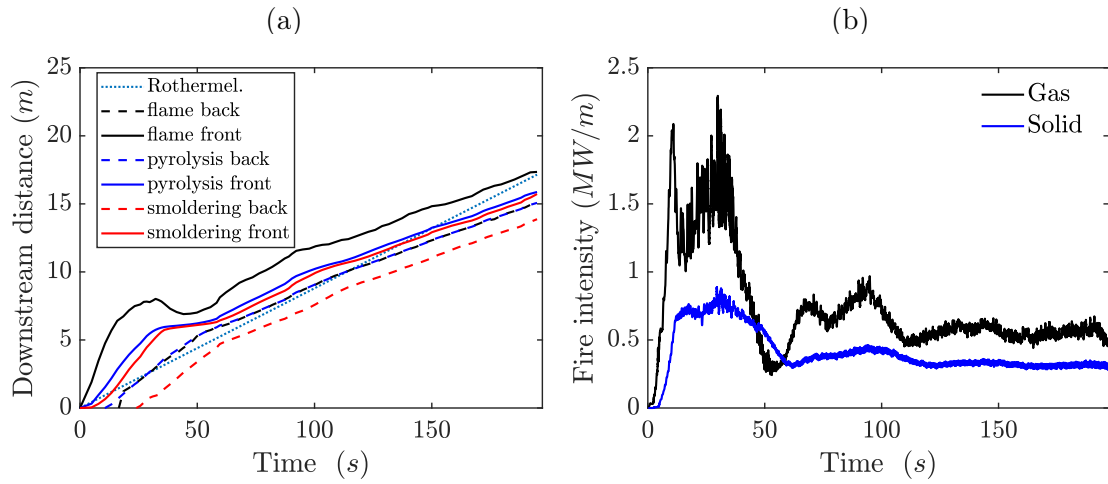


Figure 7.3: Global behavior of the buoyancy-dominated fire in the uniform bed at 1 m/s external wind speed. See the caption of Fig. 7.2

In terms of quantitative evaluation, the quasi-steady values of the rate of spread, the fireline intensity, and the characteristic flame dimensions obtained from the simulations of the buoyancy-dominate and the wind-dominated fires are reported in Table 7.2. The simulated ROS is ~ 0.066 and $\sim 0.37 \text{ m/s}$ in the buoyancy-dominated and the wind-dominated fires. These values are comparable to those estimated by the Rothermel model (0.088 and 0.34 m/s , respectively). The simulation results also show comparable fire intensities with theoretical values based on Byram's expression. The simulated fire intensity are 0.56 and 3.26 MW/m , for the buoyancy-dominated

and the wind-dominated cases respectively, while the corresponding theoretical fire intensity are 0.79 and 3.02 MW/m , respectively. Note that these intensities are obtained from the flaming combustion mode only. The simulations estimate that the total intensity based on both the flaming and smoldering combustion modes is higher and $\sim 55\%$ should be added due to the exothermic reactions that occur inside the particles.

Table 7.2: Simulated parameters of the buoyancy-dominated and wind-dominated line fires in the uniform pine wood fuel bed.

Parameter	Buoyancy-dominated	Wind-dominated
ROS (m/s)	0.066 ± 0.014	0.37 ± 0.066
Intensity (gas) (MW/m)	0.56 ± 0.035	3.26 ± 0.14
Intensity (solid) (MW/m)	0.31 ± 0.031	1.84 ± 0.058
Flame height (m)	3.2	5.6
Flaming zone depth (m)	0.42	1.5
MLR activity zone depth (m)	1.62	9.5

7.3.2 The structure of the fire

Figures 7.4 and 7.5 show a 3-D visualization of the simulated wind-dominated and buoyancy-dominated fires, respectively. The visualization includes a rendering of the hot gasses produced from the homogeneous gas-phase reaction as well as the hot pine wood particles that exhibit pyrolysis and smoldering. As seen in Figs. 7.4 and 7.5, the simulated fires feature the classical peak and trough structures that result from buoyant instabilities. These structures are believed to affect the

burning rate of the solid fuel bed as some parts of the fuel are exposed to increased or decreased heating due to spatial disturbances in the flame structure. Figure 7.6 shows a snapshot of the pine wood particles colored by their burning state. Because the fire is well established at this time, the footprint of the fire on the solid particles can be clearly seen by the non-uniformity in the transverse structure of the pyrolysis and smoldering zones. This non-uniformity is attributed to the flame peak and trough structures mentioned earlier.

In terms of quantitative measures, the simulated fire has a mean flame height of $\sim 3.2\text{ m}$ in the buoyancy-dominated case and $\sim 5.6\text{ m}$ in the wind-dominated case. The depth of the flaming zone extracted from Fig. 7.6 is 0.42 m in the buoyancy-dominated fire and 1.5 m in the wind-dominated fire. We also see that the simulated fires feature a smoldering zone behind the flaming zone that is relatively long. We estimate that the length of the combined zone of reaction activity to be 1.62 m in the buoyancy-driven fire and 9.5 m in the wind-dominated fire.

7.3.3 Sensitivity to the grid resolution

We present below a discussion about the sensitivity of the solution to the choice of the grid resolution in both the gas-phase and the fuel particle.

Figure 7.7 shows the time evolution of the pyrolysis front, the fire intensity obtained from the homogeneous gas-phase combustion, and the fire intensity obtained from the heterogeneous particle reactions. These data are obtained from simulations of the buoyancy-dominated fire conducted in computational domains with grid

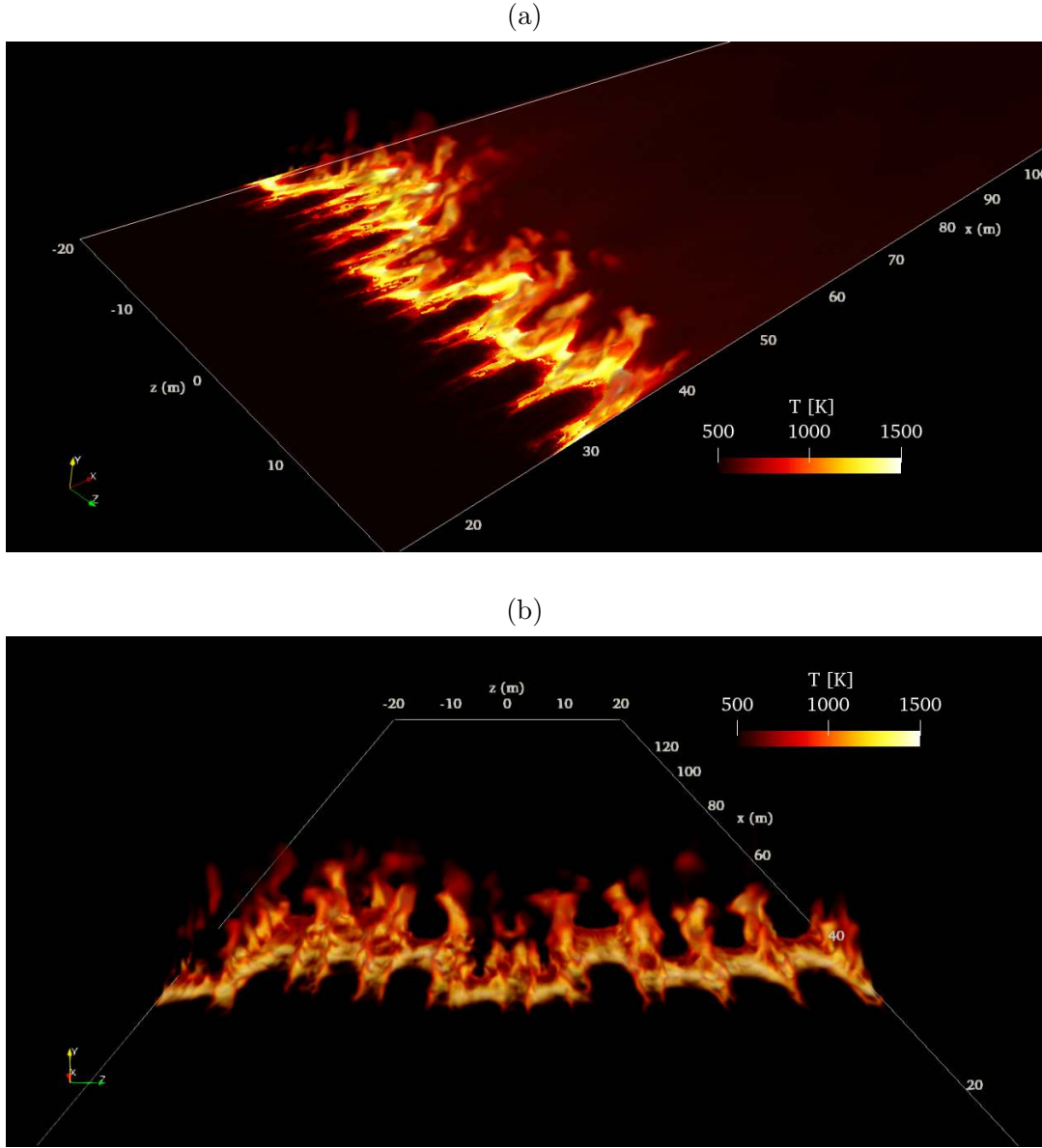


Figure 7.4: Visualization of the wind-dominated fire in the uniform bed: a) isometric view (fire spreads from left to right) of; b) back view of the hot gases only (fire spreads into the page). The hot gases in (a) and (b) are rendered by an iso-volume of $T > 550 \text{ K}$ and colored by the gas temperature. The glowing solid particles in (a) are colored by their surface temperature.

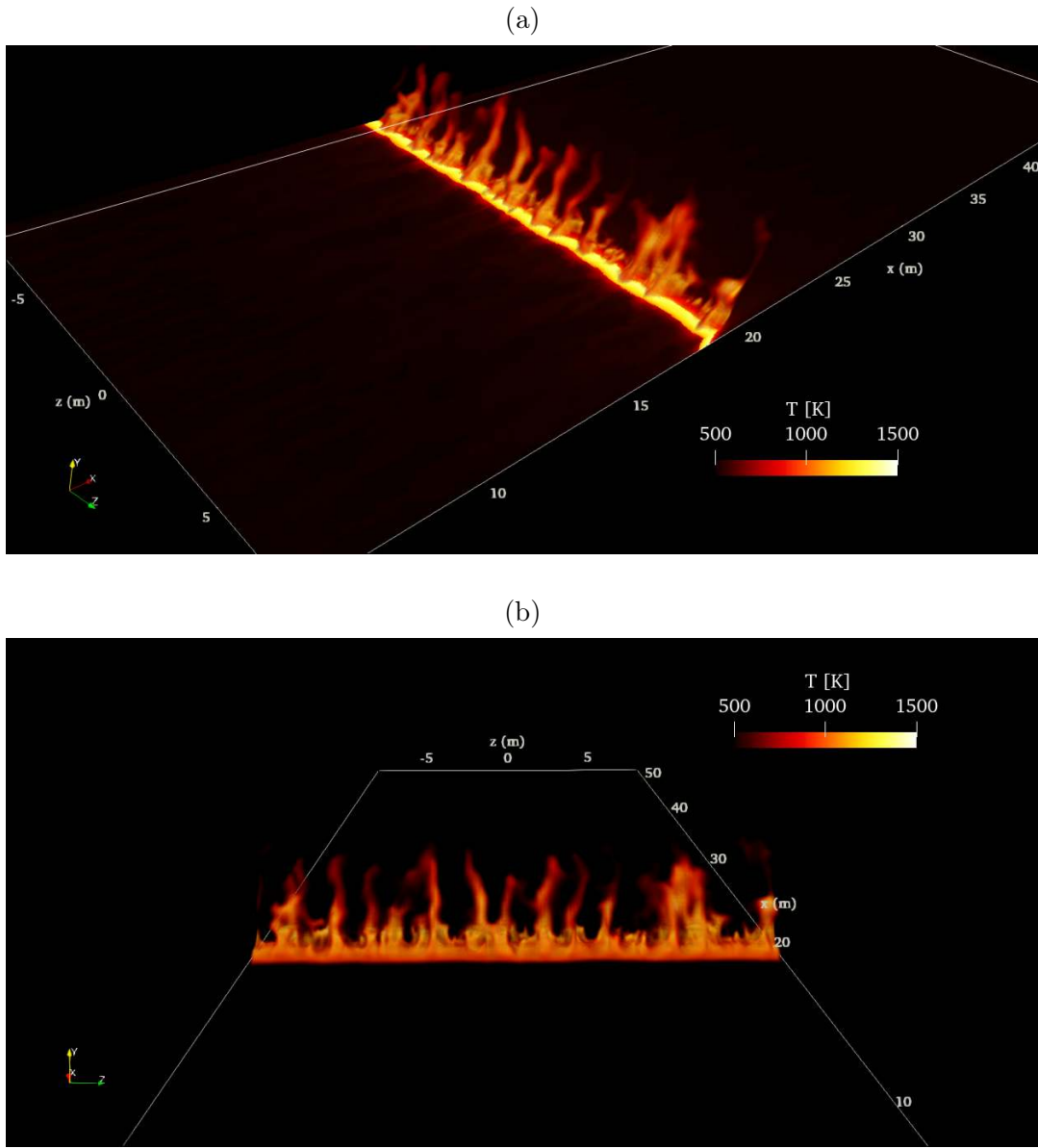
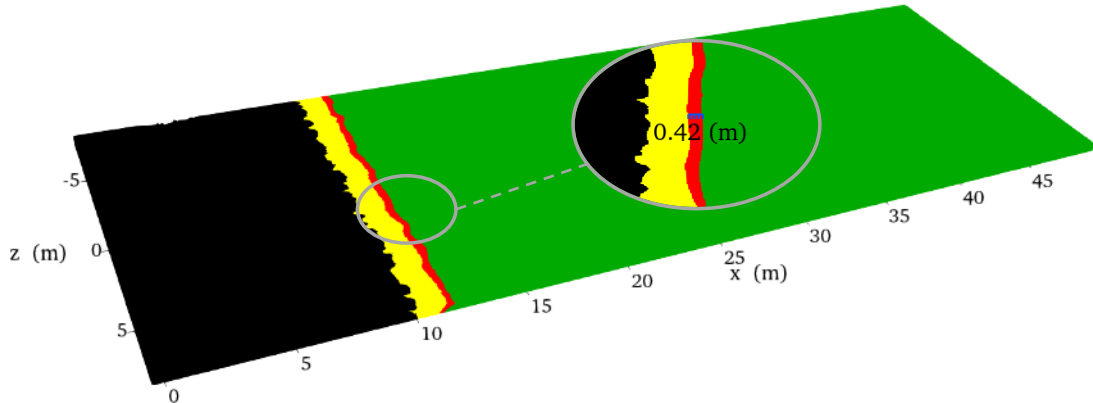


Figure 7.5: Visualization of the buoyancy-dominated fire in the uniform bed: a) isometric view (fire spreads from left to right) of; b) back view of the hot gases only (fire spreads into the page). The hot gases in (a) and (b) are rendered by an iso-volume of $T > 550 \text{ K}$ and colored by the gas temperature. The glowing solid particles in (a) are colored by their surface temperature.

(a) The buoyancy-dominated fire



(b) The wind-dominated fire

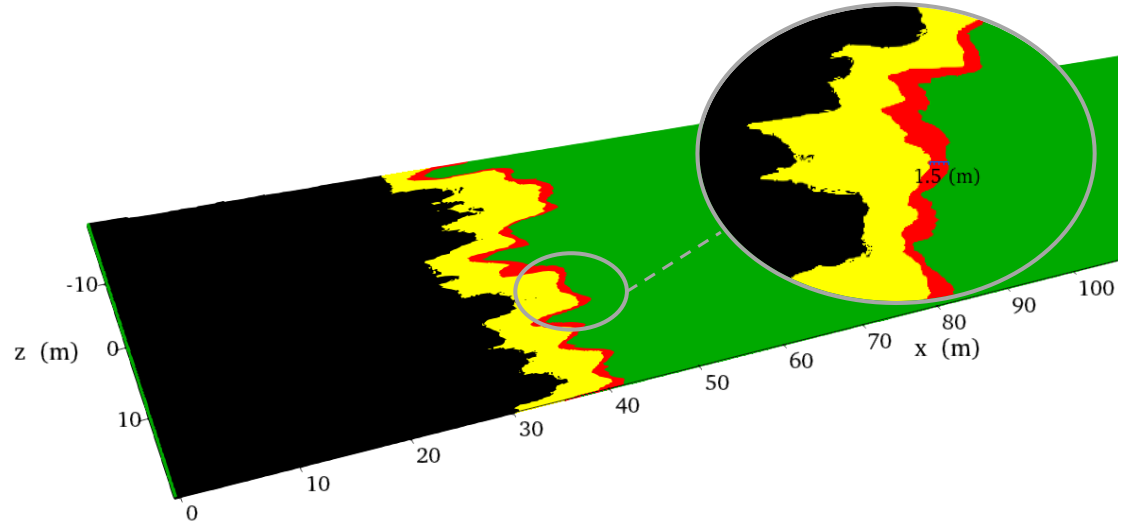


Figure 7.6: Visualization of the solid particles colored by their respective burning state. The unburned particles are colored in green, the burned particles are colored in black, the flaming particles are colored red, and the smoldering particles are colored in yellow.

resolutions of 20, 10, or 5 cm. The results presented in Fig. 7.7 show that, excluding some transient shift, the differences between the results at a quasi-steady state become minimal as one goes from a resolution of 10 cm to 5 cm which suggests

that the solutions are grid-converged in the buoyancy-dominated fire. Similarly, the results of the wind-dominated fire presented in Fig. 7.8 show that the solutions obtained using grid resolutions of either 20 cm or 10 cm have small differences at quasi-steady state, which suggests also grid convergence in the wind-dominated fire.

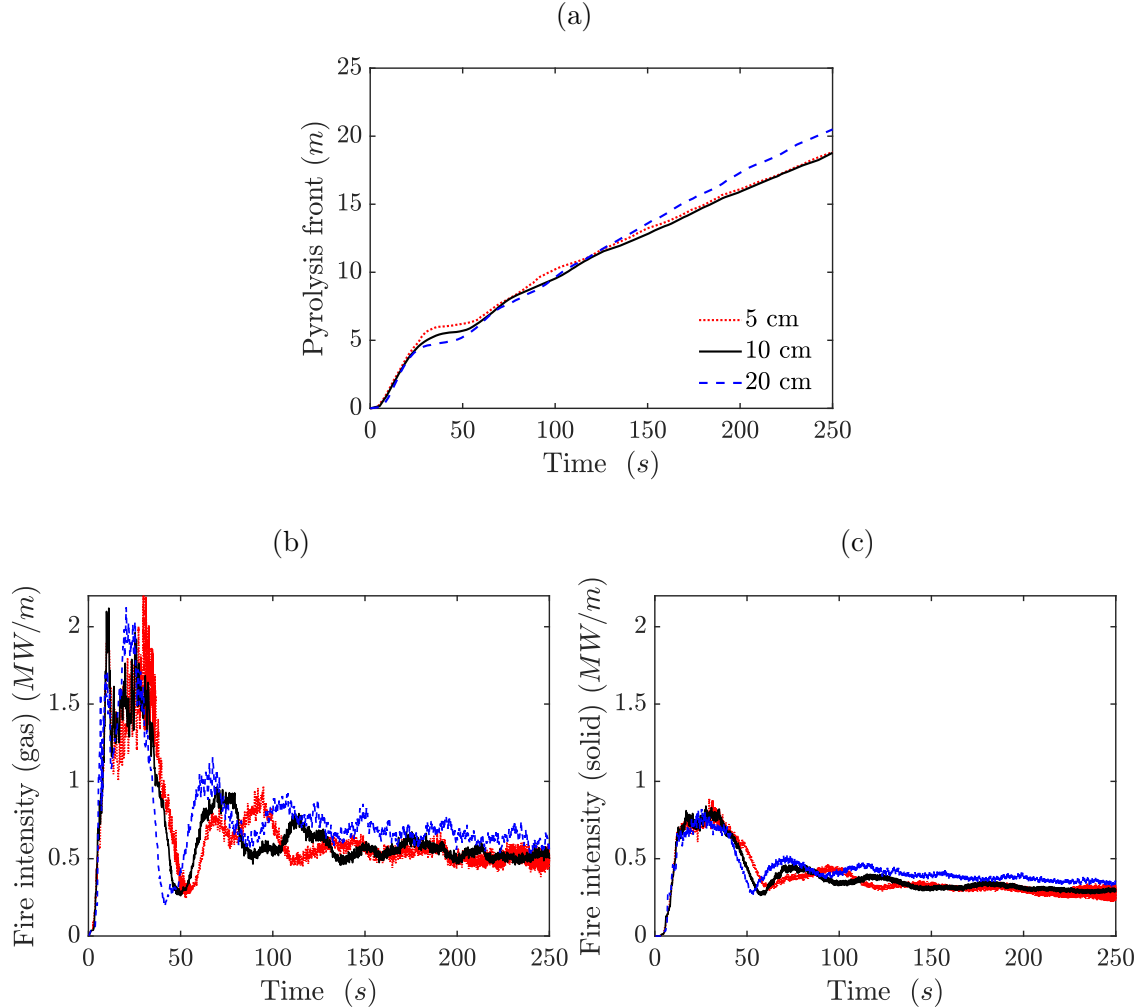


Figure 7.7: Global fire behavior in the buoyancy-dominated fire predicted using three grid resolutions of the gas-phase: a) pyrolysis front, b) fire intensity from homogeneous gas phase combustion, and c) fire intensity from heterogeneous particle reactions. The particle resolution is fixed at 25 μm .

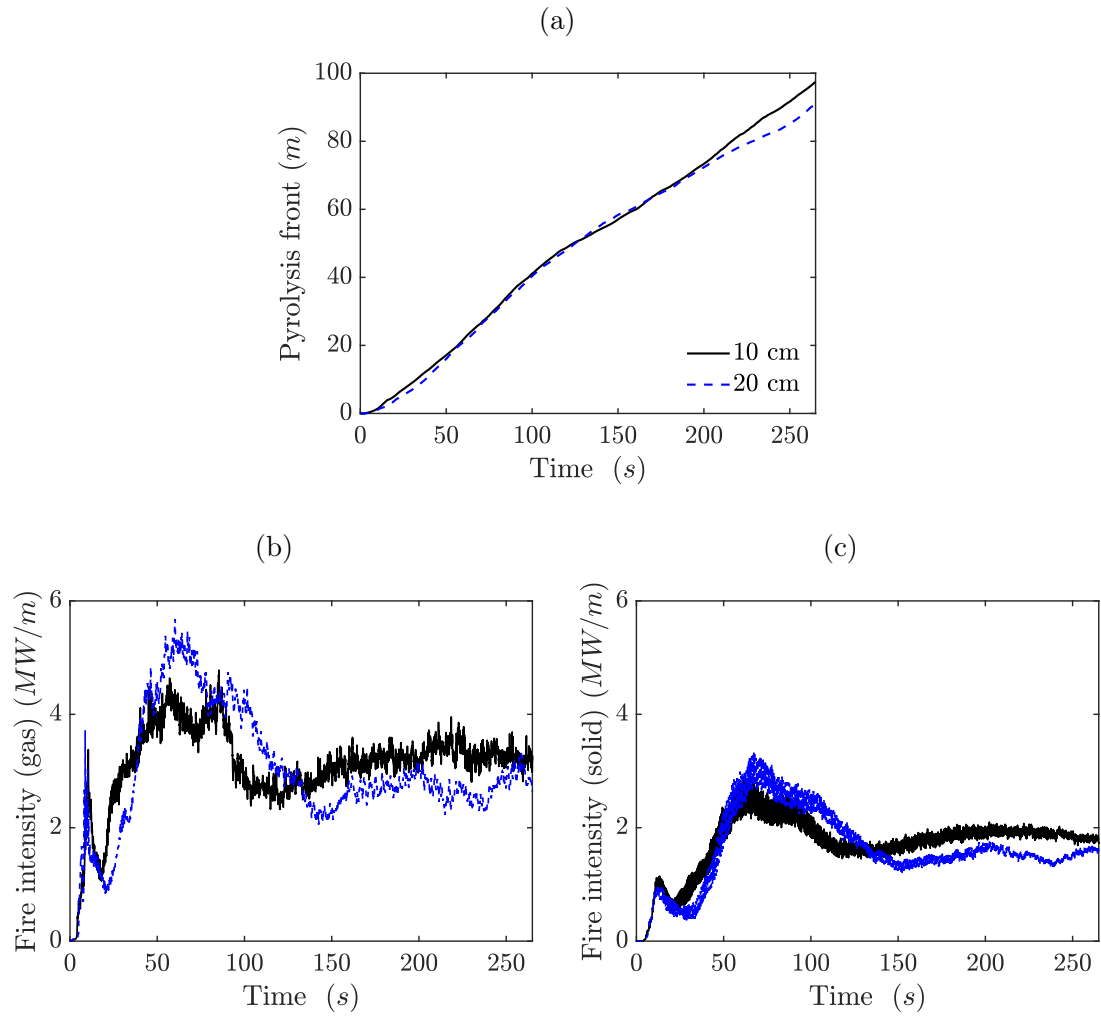


Figure 7.8: Global fire behavior in the wind-dominated fire predicted using three grid resolutions of the gas-phase. See the caption of Fig. 7.7

A similar comparison between the fire behavior obtained with particle resolutions of 10, 25, and $50 \mu\text{m}$ is presented in Fig. 7.9. The results show a minimal effect of the particle resolution on global fire behavior. Thus, a particle resolution of $50 \mu\text{m}$ can be accepted. In terms of local particle behavior, Fig. 7.10 shows the time evolution of the mass and the temperature at the core of a particle located at 20 m downstream of the ignition burner. The results of Fig. 7.10 show very minor

differences between the solution obtained with particle grid resolutions of 25 and $10 \mu\text{m}$, and slightly larger differences at a resolution of $50 \mu\text{m}$.

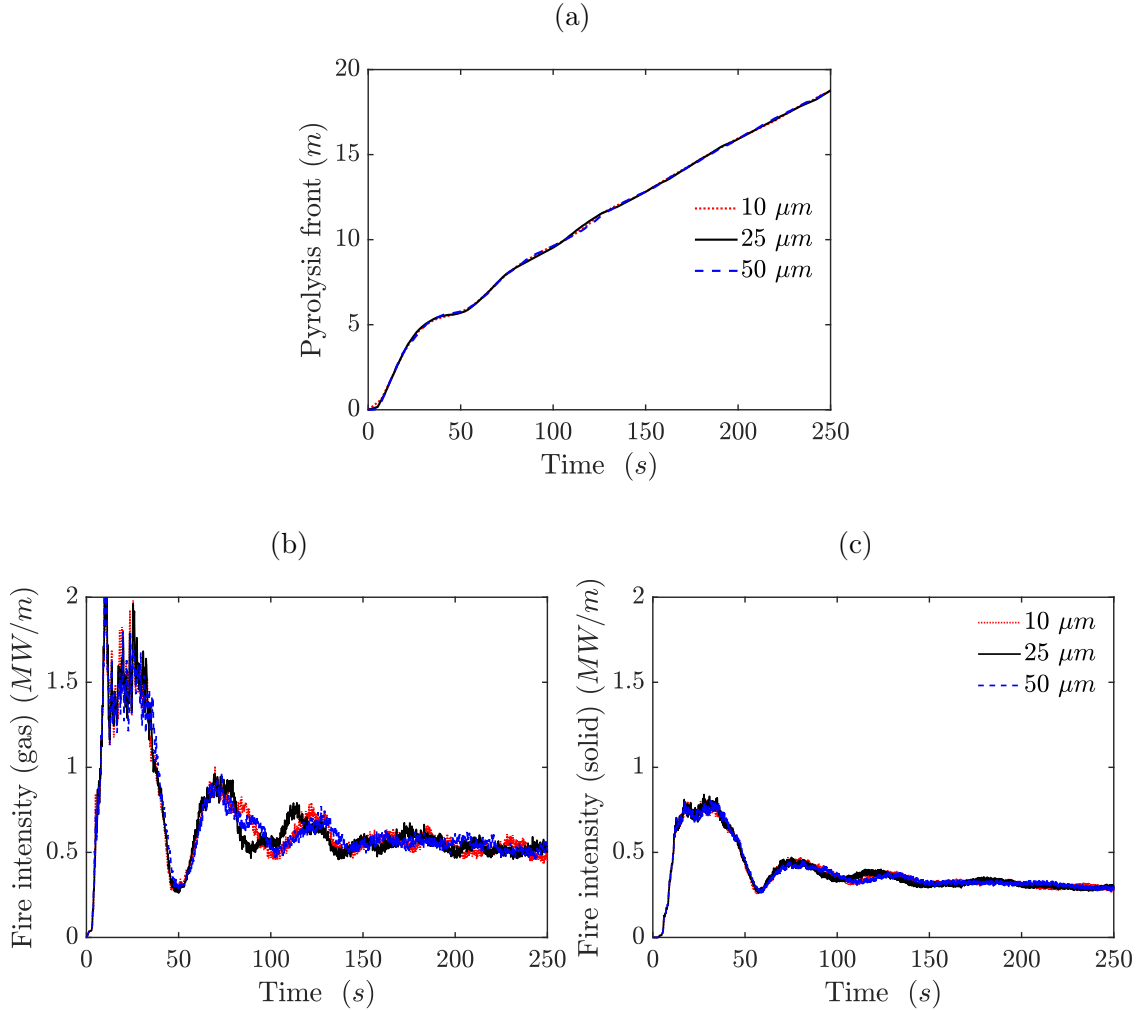


Figure 7.9: Global fire behavior in the buoyancy-dominated fire predicted using three mesh resolutions of the particles. The gas-phase resolution is 10 cm .

According to the tests presented in this section, the choices of gas-phase grid resolution of 10 cm and particle resolution of $25 \mu\text{m}$ are deemed adequate and are adopted in the rest of the simulations presented in this chapter.

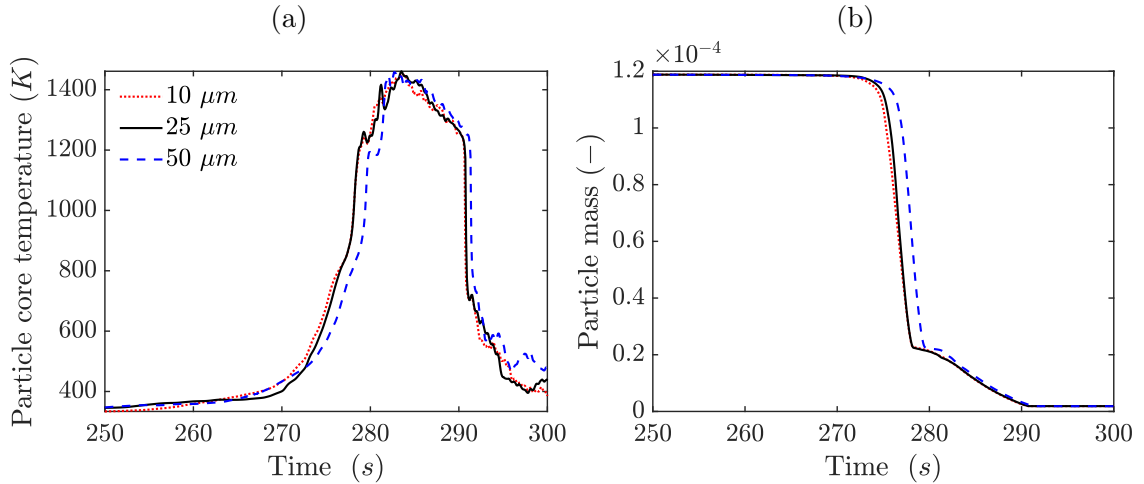


Figure 7.10: Behavior of the particle located 20 m downstream of the ignition burner in the buoyancy-dominated fire in terms of a) the temperature at the core of the particle; b) the particle mass. The results are obtained using three mesh resolutions of the particles, and a gas-phase resolution of 10 cm .

7.4 Fire spread in the mixed-size fuel patch

We discuss here the results of the configurations that feature a mixed-size patch of small and large particles (see Fig. 7.1b). We present below results from 4 combinations: either a mixed-size patch of 2 mm and 10 mm particles or a mixed-size patch of 2 mm and 20 mm particles in either a wind-dominated fire at 5 m/s nominal wind speed or a buoyancy dominated fire at 1 m/s nominal wind speed.

Figure 7.11 describes the fire spread in a case that features complete consumption of the small and large particles by transitioning from flaming to smoldering. The images correspond to a sequence of snapshots taken at different times during the wind-dominated fire propagation across the mixed-size patch of 2 and 10 mm

diameter pine wood particles. At $t = 115\text{ s}$, the flame approaches the mixed-size patch located at $38 \leq x \leq 42\text{ m}$ and ignites the small and large particles. At $t = 150\text{ s}$, the main flame completely crosses the patch leaving behind a glowing zone and some traces of flaming particles. At $t = 210\text{ s}$, the main flame moves further downstream, while the larger particles in the patch are still glowing. The larger particles then complete the thermal degradation process through smoldering.

7.4.1 Variations with the fuel bed height

Because this fuel bed is not shallow and the pine wood sticks are relatively tall (0.4 m high), we anticipate some variations to occur through the fuel bed depth (i.e., variations across the particle height). As described earlier, the height of the cylindrical pine wood particle is distributed over multiple cells, and its surface is exposed to different surrounding gas conditions at different elevations. The objective of this section is to evaluate the variations of thermal degradation across the particle height and to select a reference height, that is representative of the average particle behavior, for further analyses.

Figure 7.12a shows the time variation of the temperature at the core of the 20 mm diameter particle obtained from the lower, middle, and upper parts of the particle. The particle is located near the centerline of the mixed-size patch (i.e., at $x = 40\text{ m}$, $z = 0$ in the wind-dominated fire). The corresponding time variations of the mass of each part is shown in Fig. 7.12b (this mass is non-dimensional and is normalized by the initial mass in each part). The results of Fig. 7.12a show

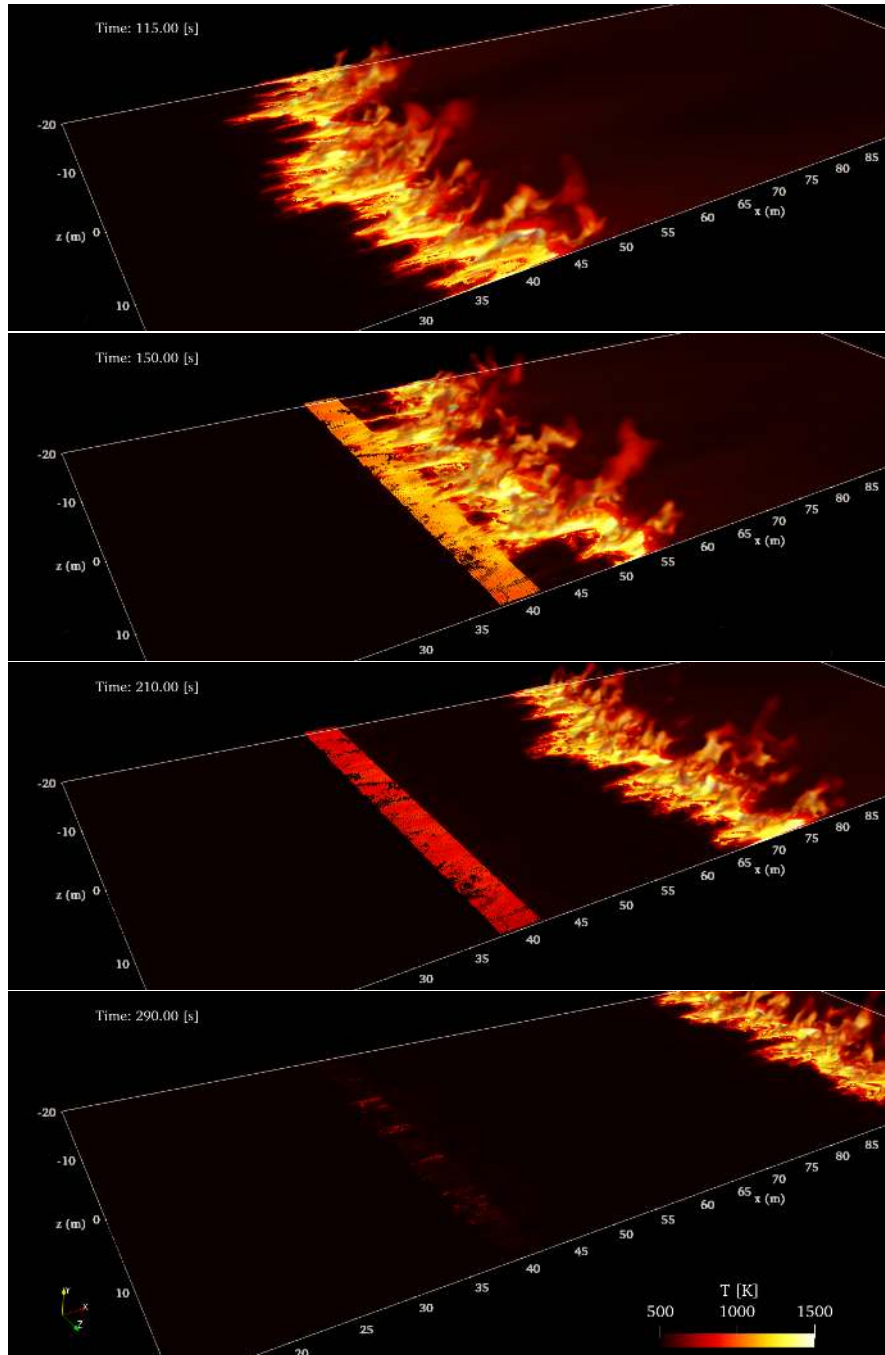


Figure 7.11: Snapshots of the wind-dominated fire while spreading across the mixed-size patch of 2 and 10 mm particles. The flame is rendered by an iso-volume of gases at $T_g > 550 K$. The solid particles are colored by their surface temperature.

that the upper part of this 20 mm particle increases steadily from ambient up to $\sim 700\text{ K}$ then rapidly increases from $\sim 800\text{ K}$ to $\sim 1100\text{ K}$. The middle and lower parts, however, exhibit an increase in the core temperature up to only $\sim 500\text{ K}$ followed by a slow cool down indicating that these parts received less heat. As a result, the residual mass of the upper part decreases to levels below 10% as indicated in Fig. 7.12b. However, the residual mass of the middle and lower parts stay at only 60 – 70%. These results suggest that the upper part of the particle burns differently than the rest of the particle and that the middle part of the particle is more representative of the average particle behavior.

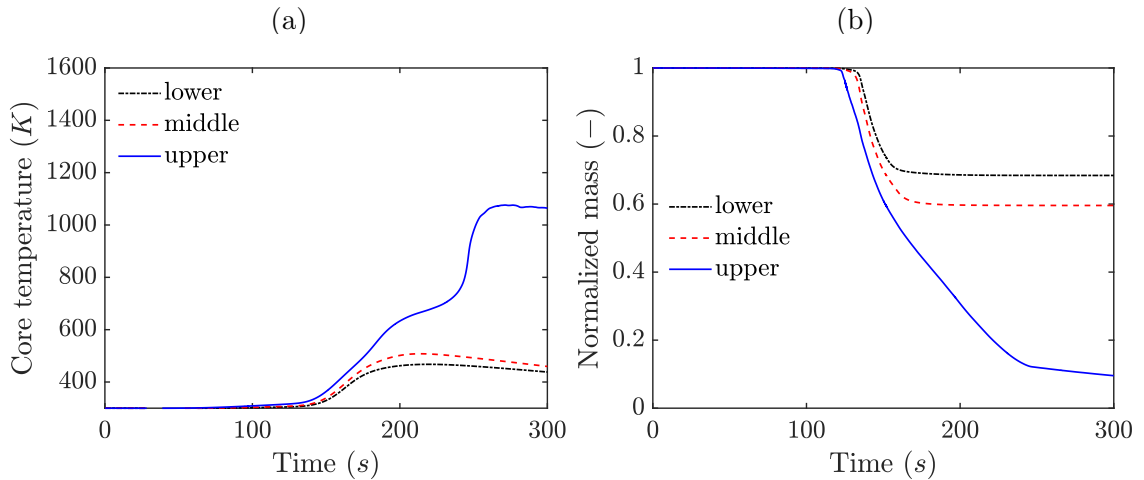


Figure 7.12: The variation of a) the core temperature and b) the normalized mass of the lower, middle and upper parts of the 20 mm diameter particle located at $x = 40\text{ m}, z = 0$ in the mixed-size patch of the wind-dominated fire.

As shown in Figs. 7.13a and 7.13b, the 10 mm particle exhibits much less variation in thermal degradation with respect to its height in this wind-dominated fire. The lower and the middle parts show very similar behavior with a very slight

shift in the temperature rise and mass consumption. The upper part shows a faster increase in temperature and mass consumption. But overall, the lower, middle, and upper parts of this small particle exhibit complete consumption. In the following, we expand our analysis by considering the behavior at mid-elevation of the fuel bed as a reference.

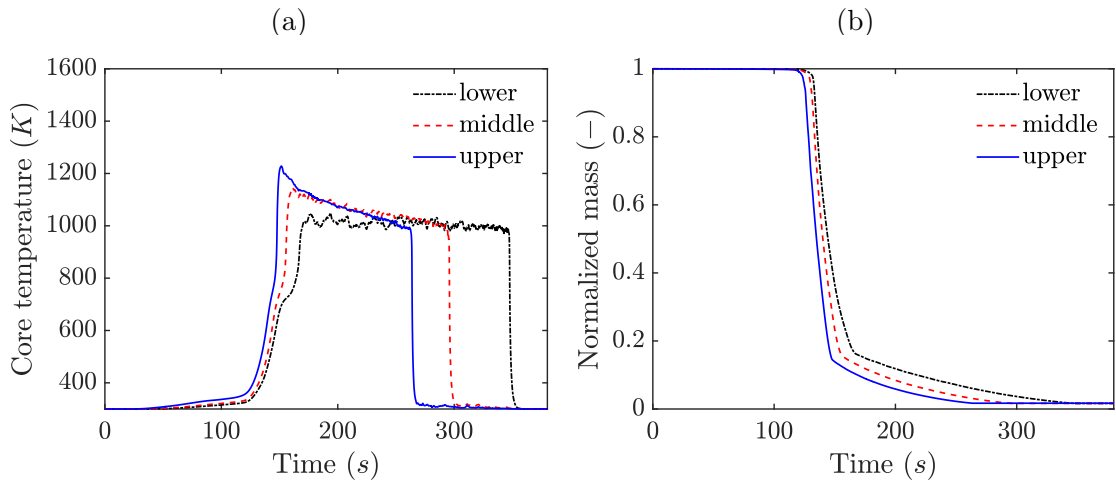


Figure 7.13: The variation of a) the core temperature and b) the normalized mass of the lower, middle and upper parts of the 10 mm diameter particle located at $x = 40\ m, z = 0$ in the mixed-size patch of the wind-dominated fire.

7.4.2 Local gas conditions at mid-elevation of the fuel bed

The temporal evolution of the external conditions experienced by individual particles is presented in Fig. 7.14. These conditions correspond to the position at the mid-elevation of the mixed-size patch (i.e., at $y = 0.2\ m$) and at $x = 40\ m, z = 0$. The data in Fig. 7.14a show that the temperature of the gas at this location increases slowly from ambient temperature to approximately $500\ K$ at $t \approx 115\ s$ (which

corresponds to the flame arrival time). This increase in the temperature is attributed to plume transport from the upstream hot gases to this location, which can cause preheating to the particles at an earlier time before flame contact. At $t \approx 150$ s, the gas temperature shows a significant rise indicating a flame ignition. The gas temperature increases further up to a peak of ~ 1200 K. The gas temperature also features some fluctuations with a magnitude of ~ 300 K. The local irradiation presented in Fig. 7.14b shows a similar profile as the gas temperature but with no increase before the flame ignition at $t \approx 115$ s, which suggests that the radiation here is limited to the flame zone only.

As shown in Fig. 7.14c, the temporal evolution of the oxygen concentration in the local gas is approximately the opposite of the gas temperature. The oxygen concentration drops rapidly from the ambient level to very low values at $t \approx 115$ s as it gets consumed by the gas-phase combustion with the volatiles produced by pyrolysis. It also shows some fluctuations when the flame is spreading across this location until it recovers back to the ambient level. This behavior suggests that the particles are still exposed to some oxygen, but at a reduced level, during the flaming combustion.

The velocity of the gas presented in Fig. 7.14d is around 1 m/s before the flame arrives at this location. This value is much lower than the nominal wind velocity of 5 m/s specified at 2 m elevation because of the lower elevation of the fuel bed and also because of the drag effects inside the fuel bed. The gas velocity increases to a peak of around 2 m/s during flame spread across this location due to the buoyancy effects induced by the hot gases. The gas velocity also features some

turbulent fluctuations that are present before, during, and after the flame crossing.

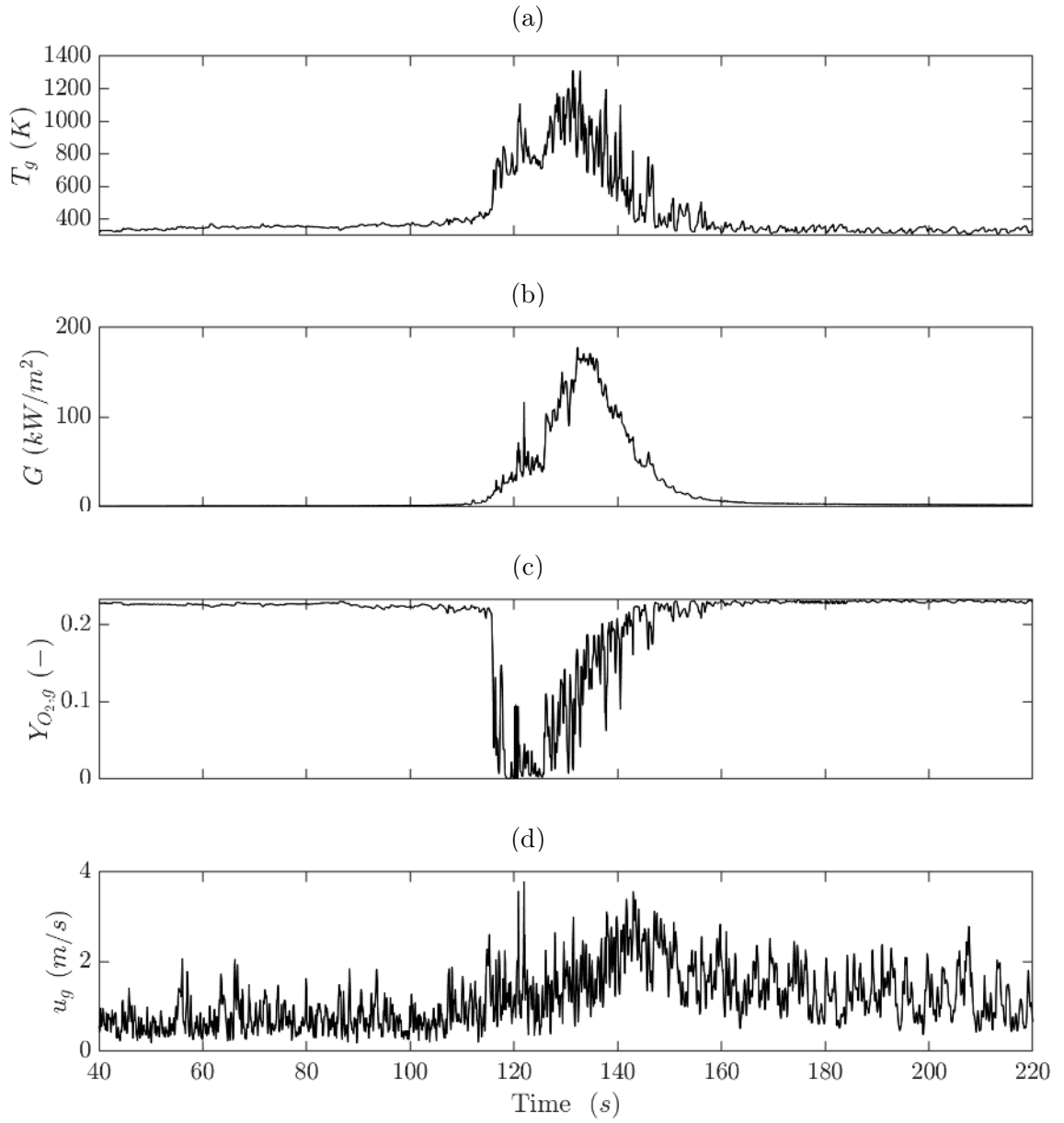


Figure 7.14: External conditions around the particle evaluated at $x = 40 \text{ m}$, $y = 0.2 \text{ m}$, $z = 0$ position in the wind-dominated fire: a) local gas temperature; b) local irradiation; c) local oxygen mass fraction; d) local gas velocity.

7.4.3 Particle behavior in the wind-dominated fire

Figure 7.15 shows the time evolution of the temperature of the surface and the core of the small particle (2 mm diameter) and the large particles (10 or 20 mm diameter) in the mixed-size patch during the wind-dominated fire spread. The mass loss rate and the mass of solid constituents (wet solid, dry solid, char, and ash) are shown in Figs. 7.16 and 7.17, respectively. We see from these figures that the profiles of temperature, MLR, and constituents mass are very similar for the 2 mm particle in the mixed-size patch when larger particles of either 10 mm or 20 mm diameter are inserted.

The results of Fig. 7.15 suggest that the 2 mm particle is thermally-thin as no significant difference is observed between its surface and core temperatures. The 2 mm particle's surface and core temperatures rapidly increase from 400 K at $t \approx 115$ s to about 1400 K in less than ~ 50 seconds. Examining the profiles of MLR and the constituent masses of this 2 mm particle in Fig. 7.16 indicates that this particle undergoes complete thermal degradation through pyrolysis and char oxidation, and shows that this particle experiences a complete transformation of wet solid into dry solid, dry solid into char and char into ash. The final mass consumption of this 2 mm particle is listed in Table 7.3 and is $\sim 99.9\%$, which is very close to the theoretical consumption of 99.98% that is calculated for this pine wood based on the ash yield (i.e., the non-combustible minerals).

The particle surface and core temperatures in the case of the 10 or 20 mm particles are different as indicated in Fig. 7.15, and there is a time lag between

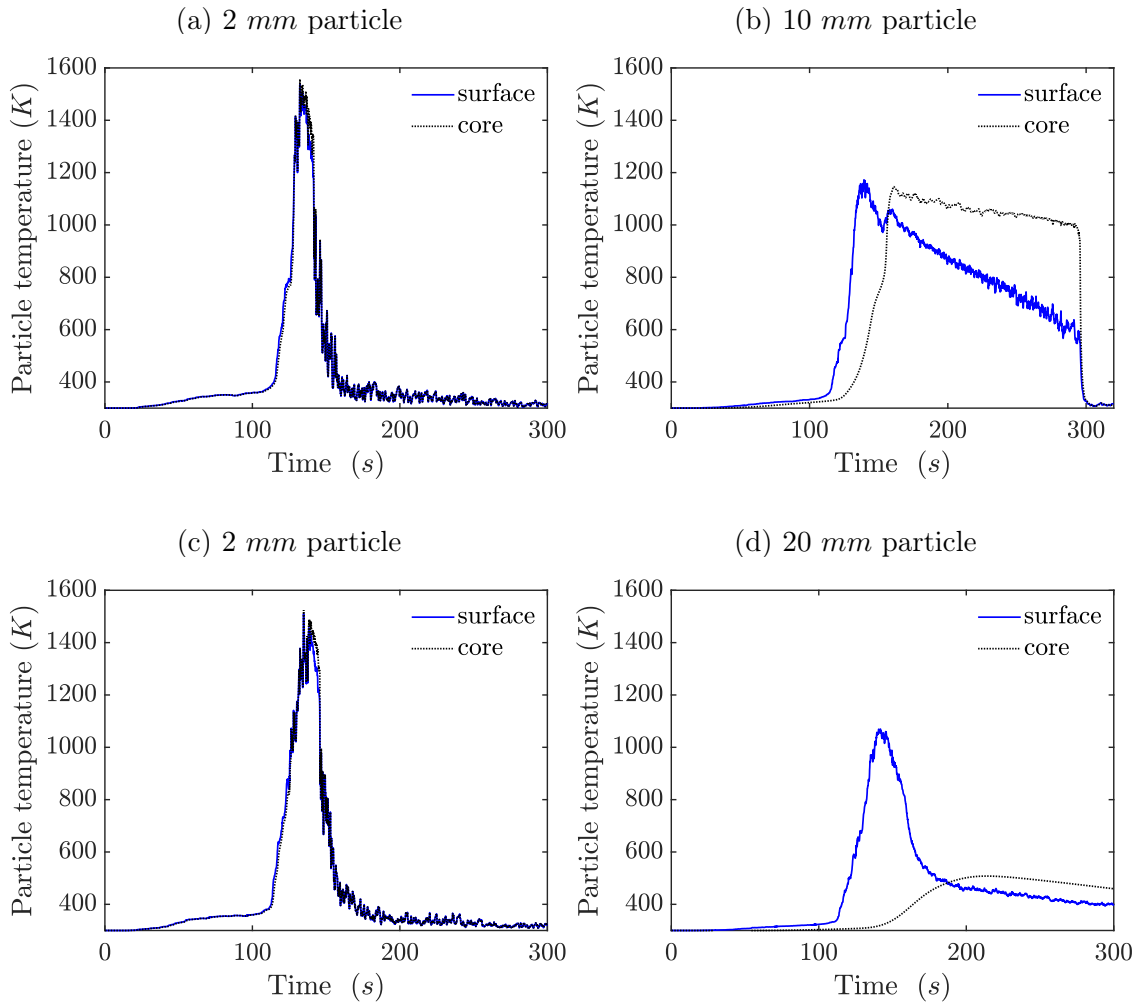


Figure 7.15: Time variation of the surface and core temperatures of the particles in the mixed-size patch with 2 mm and 10 mm particles (a, b), and in the mixed-size patch with the 2 mm and 20 mm particles (c, d). The data correspond to particles located at $x = 40\text{ m}$, $y = 0.2\text{ m}$, $z = 0$ in the wind-dominated fire.

the two associated with the time required for heat to reach the particle core. For instance, the core of the 10 mm particle reaches a temperature of $600 - 700\text{ K}$ approximately 20 seconds after the particle surface has reached this temperature. The core of the 20 mm particle, however, never exceeds $\sim 500\text{ K}$ due to either low

intensity of external heating or short heating time. We will elaborate more on this in the following discussion.

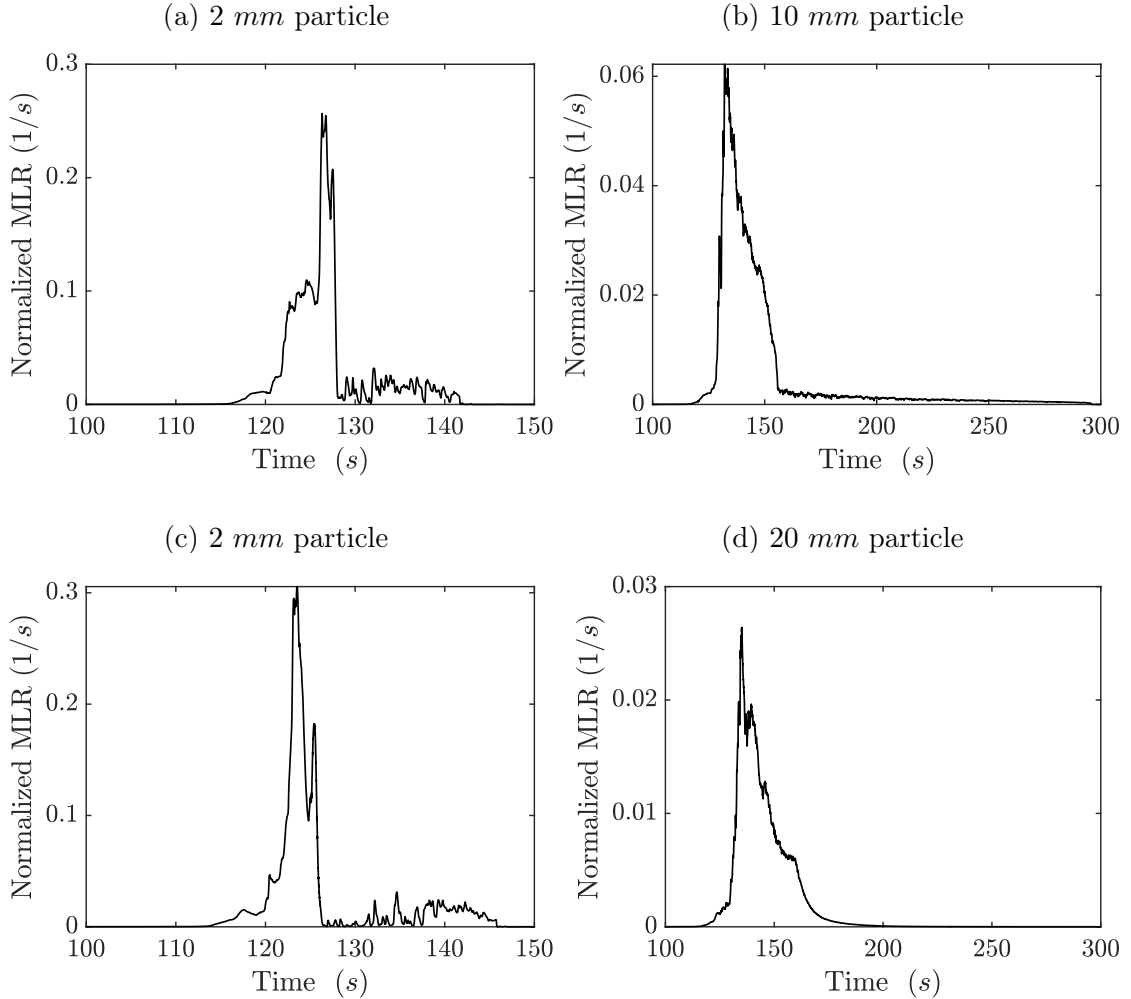


Figure 7.16: Time variation of the normalized mass loss rate of particles in mixed-size patch of the wind-dominated fire. See caption of Fig. 7.15.

Further examination of the MLR and the masses of the solid constituents of the 10 and 20 mm particles in Figs. 7.16 and 7.17 indicates that the core of the 10 mm particle reaches a sufficiently high temperature for the smoldering reaction to reach self-sustained condition (i.e., a transition from flaming to self-sustained smoldering).

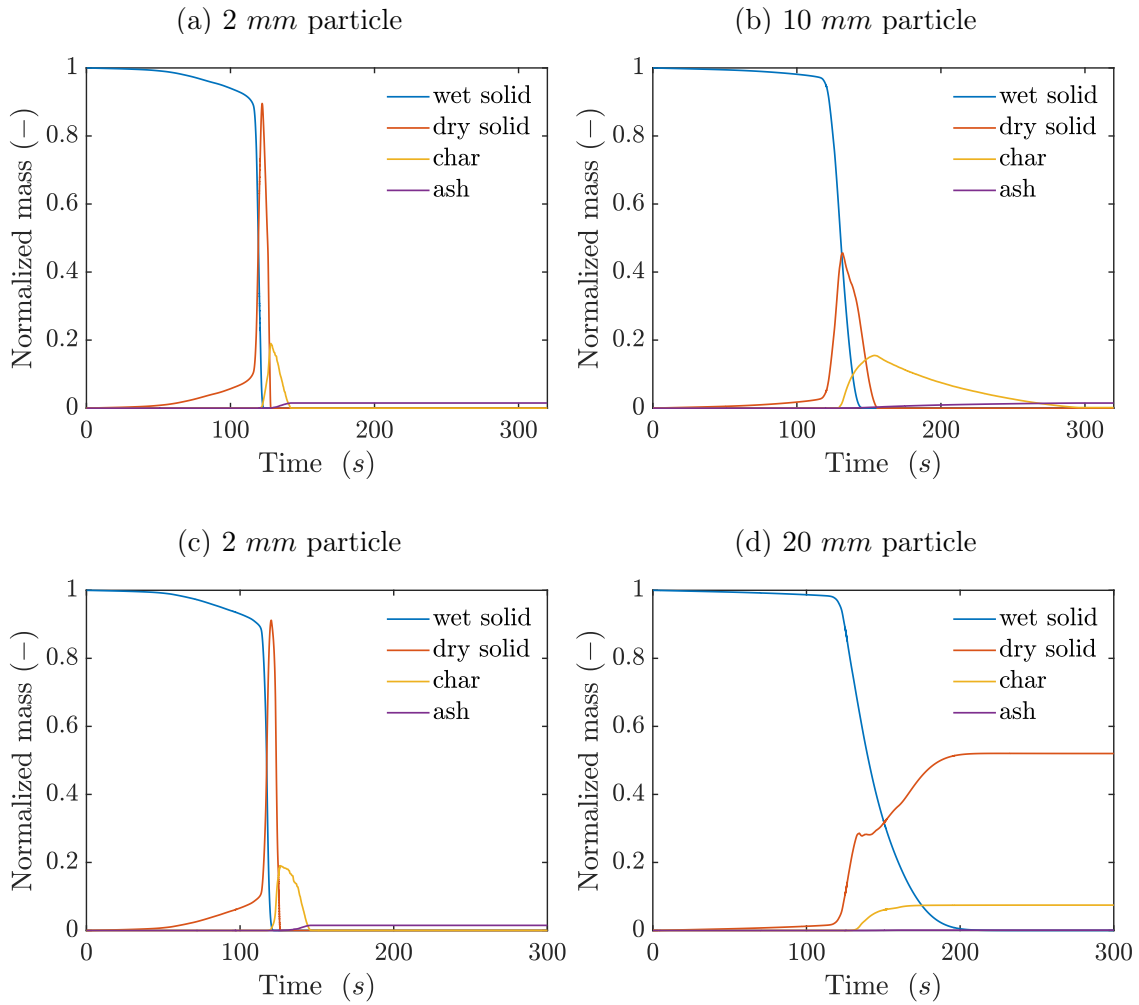


Figure 7.17: Time variation of the normalized solid constituents masses of particles in mixed-size patch of the wind-dominated fire. See caption of Fig. 7.15.

The transition from flaming to smoldering, as indicated by the change in slope of the MLR curve of the 10 mm particle in Fig. 7.16, begins at a time equal to ≈ 160 seconds, and it is seen at this time that the core temperature has already reached 700 K (the threshold core temperature for self-sustained smoldering established in Chapter 5). This behavior leads the 10 mm particle to complete consumption (complete conversion from dry solid to char and from char to ash with both flaming

and self-sustained smoldering). The MLR of the 20 mm particle does not show the same behavior as that of the 10 mm particle as it rapidly drops to zero. Thus, the 20 mm particle undergoes only partial consumption (with no or limited smoldering). Table 7.3 indicates that 99.8% of the 10 mm particle is consumed, but only 41% of the 20 mm particle is consumed in this wind-dominated fire.

In order to explore the variations inside the particle that feature self-sustained smoldering, we present in Fig. 7.18 the spatial profiles inside the 10 mm diameter particle at two instants of time representing the end time of the flaming phase and the mid-time of the self-sustained smoldering phase. The profiles in Fig. 7.18a indicate the high temperature achieved inside the particle which reaches values above 1000 K at these two instances of time. The displacement of the char oxidation reaction from the surface of the particle to the core region where char is transformed into ash is displayed in Figs. 7.18b and 7.18d. The corresponding profiles of oxygen mass fraction inside the pores of the particle are shown in Fig. 7.18c. These profiles show that the oxygen is diffusing from the gas phase surrounding the particle into the particle and that the char oxidation is sustained by this oxygen diffusion and is oxygen diffusion limited. These spatial profiles indicate that there is no oxygen mass in the core of the particle as all oxygen that diffuses into the particle is consumed by the char oxidation reaction.

The spatial profiles of the temperature, oxygen mass fraction, volume fractions of char and ash, and the char oxidation rate of the 20 mm particle at similar times as those presented for the 10 mm particle are shown in Fig. 7.19. As seen in the profiles at $t = 160\ s$, there is still a dry solid that has not been converted to char

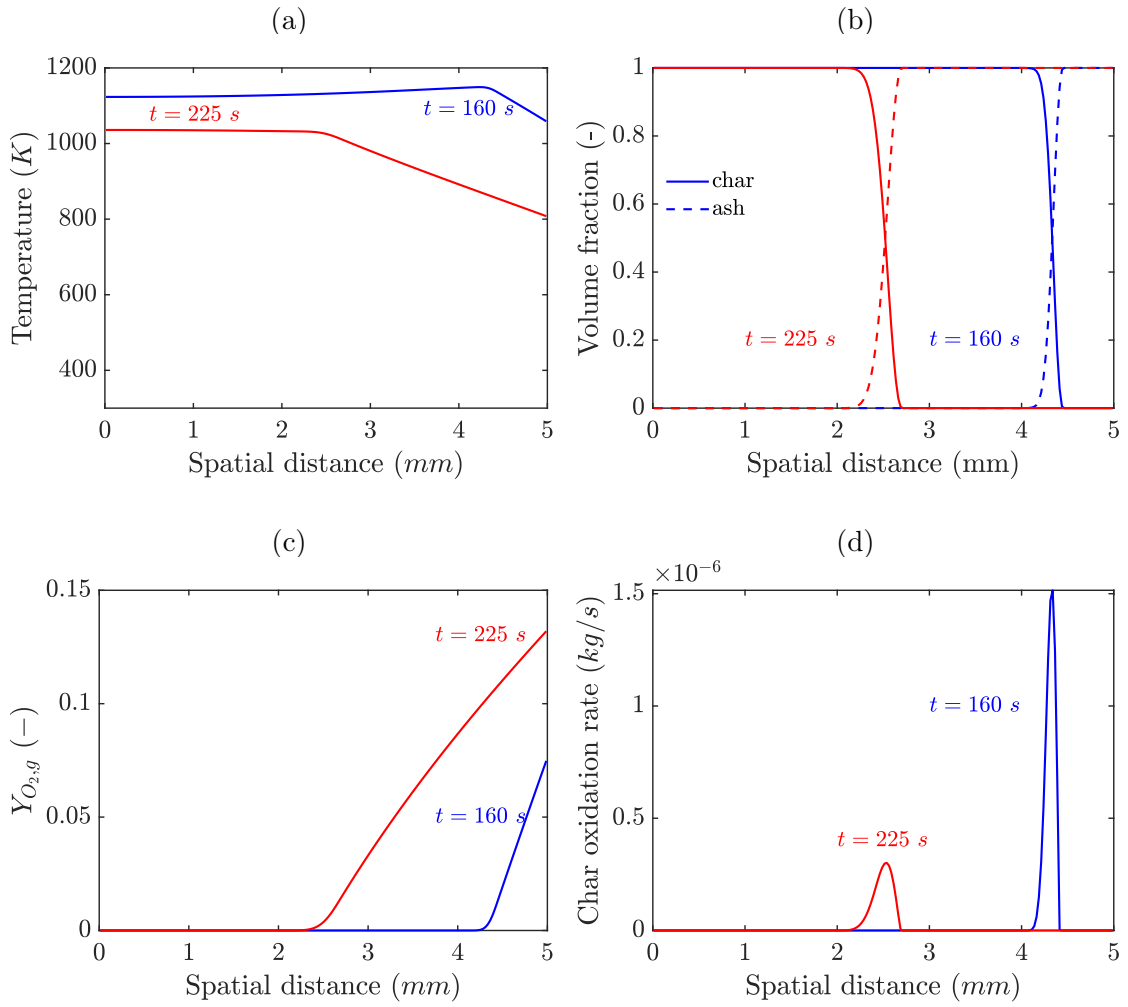


Figure 7.18: Spatial distribution of: a) temperature; b) volume fraction of char and ash; c) oxygen mas fraction; d) char oxidation reaction rate inside the 10 mm particle located at $x = 40 \text{ m}$, $y = 0.2 \text{ m}$, $z = 0$ in the mixed-size patch of the wind-dominated fire.

at the core of the particle, and the conversion from char to ash occurs in a limited region near the particle surface where char, oxygen and high enough temperature ($\sim 700 \text{ K}$) coexist. The temperature at the core of the particle is below 400 K and increases to only $\sim 500 \text{ K}$ at a later time ($t = 225 \text{ s}$). As a result, the char oxidation

ceases at $t = 225$ s despite high oxygen levels reached inside the particle.

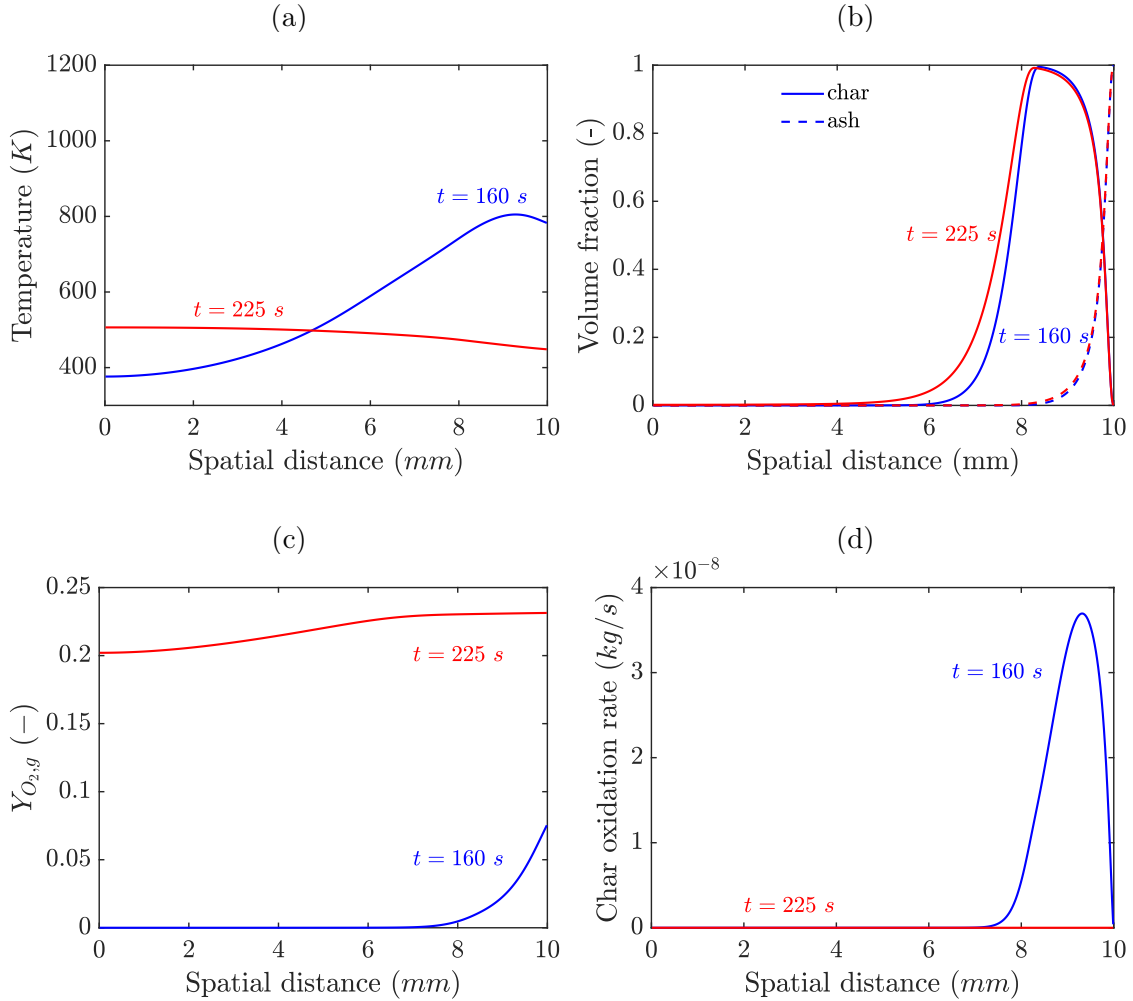


Figure 7.19: Spatial distributions inside the 20 mm particle. See the caption of Fig. 7.18.

7.4.4 Particle behavior in the buoyancy-dominated fire

Unlike the previous cases in which the flame is buoyancy-dominated, the cases discussed here belong to the buoyancy-dominated regime at 1 m/s nominal wind speed. Figure 7.20 shows the time variation of the solid constituents mass of the

2, 10, and 20 mm particles in the mixed-size fuel patch. Consistent with the wind-dominated fire, the results show that the 2 mm particle still exhibits complete thermal degradation and conversion into ash at this buoyancy-dominated fire. The data of Table 7.3 show that 99.9% of the particle is consumed. On the other hand, neither the 10 nor the 20 mm particles show complete consumption at this wind speed. The 10 mm particle shows partial thermal degradation with 69.6% mass consumption, whereas the 20 mm particle shows only 19% mass consumption. The underlying physics behind the differences between the behavior of the particle in the wind-dominated and the buoyancy-dominated regimes are explored in the following discussion.

7.4.5 The Pseudo Incident Heat Flux (PIHF)

Figure 7.21 shows the total net heat flux ($\dot{q}_{g \rightarrow s}''$) as well as the convective component (\dot{q}_{conv}'') and the radiative component (\dot{q}_{rad}'') of the 2 and 10 mm particles located at $x = 40\text{ m}$, $y = 0.2\text{ m}$, $z = 0$ in the mixed-size patch of the wind-dominated fire. For completeness, the mathematical formulae of these heat fluxes are given below

$$\begin{aligned}\dot{q}_{g \rightarrow s}'' &= \dot{q}_{conv}'' + \dot{q}_{rad}'' \\ \dot{q}_{conv}'' &= h(T_{g,\infty} - T_{p,surf}) , \quad \dot{q}_{rad}'' = \epsilon_{p,surf}(G - \sigma T_{p,surf}^4)\end{aligned}\tag{7.2}$$

The results of Fig. 7.21 show that these heat fluxes start from positive values that correspond to a heating phase, then decrease to negative values that correspond to a cooling phase once the particle reaches higher temperatures than the surrounding

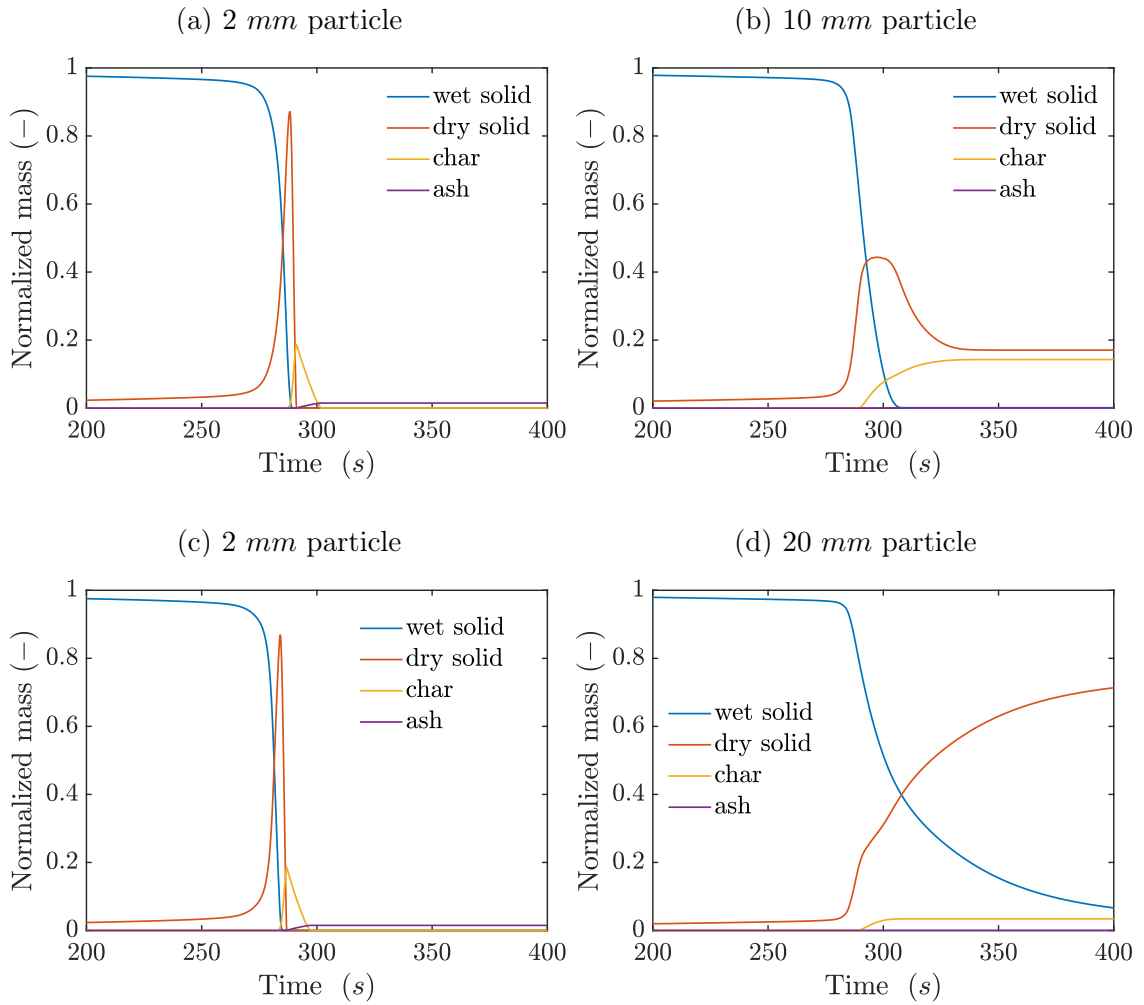


Figure 7.20: Time variation of the normalized solid constituents masses of particles in the mixed-size patch with 2 mm and 10 mm particles (a, b), and in the mixed-size patch with the 2 mm and 20 mm particles (c, d). The data correspond to particles located at $x = 40\text{ m}$, $y = 0.2\text{ m}$, $z = 0$ in the buoyancy-dominated fire.

gas and the flame moves away from the particle. While the net heat flux is a physically meaningful quantity, it is complex to interpret because it exhibits changes from positive to negative values depending not only on the external heat loading but also on the response of the particle itself.

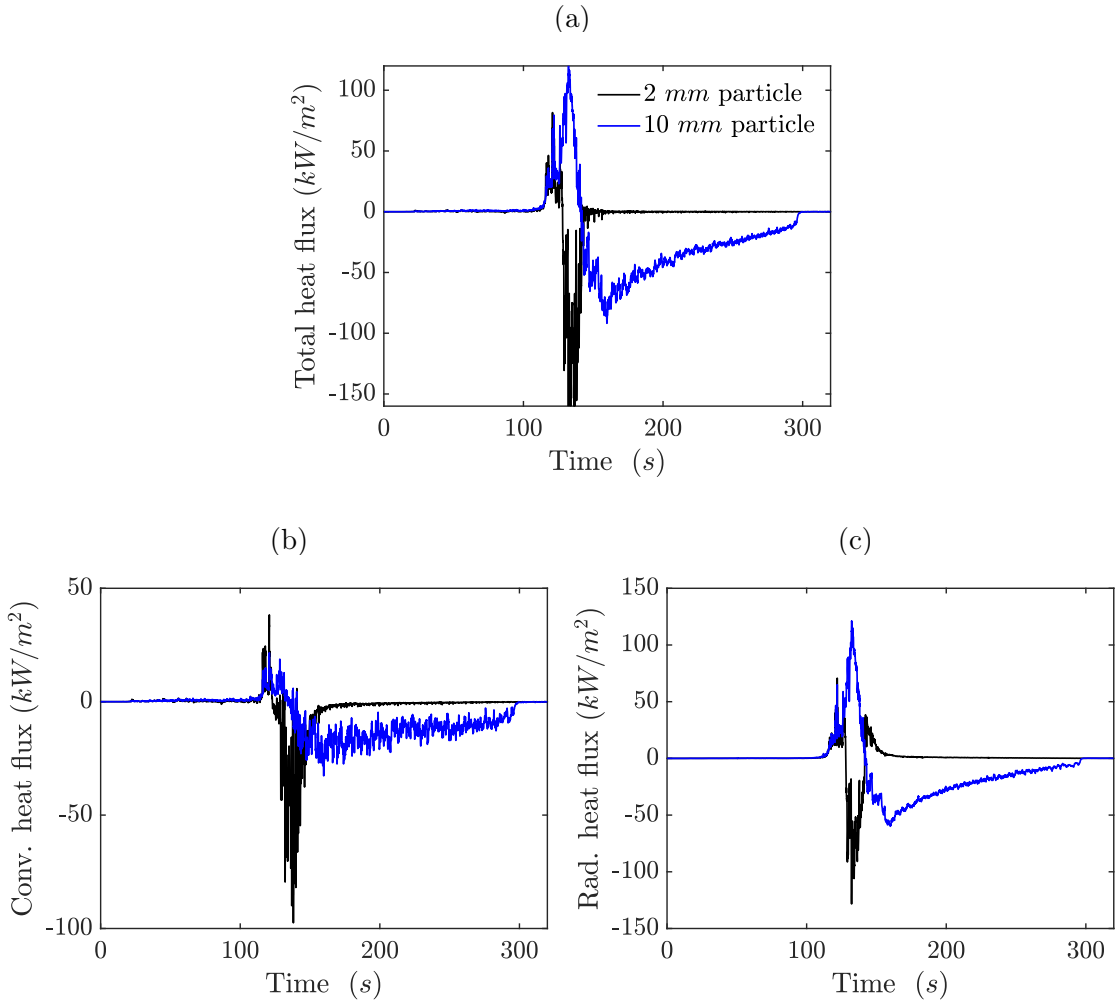


Figure 7.21: Time variation of the a) total heat flux, b) convective heat flux, and c) radiative heat flux at the surface of the 2 and 10 mm particles located at $x = 40 m, z = 0$ in the mixed-size patch of the wind-dominated fire. The heat fluxes are evaluated at mid-elevation.

In order to differentiate and identify the contribution of the external heating without the particle response, we use the PIHF (already introduced in previous sections), which accounts for the part of the net heat flux that represents external quantities only. This allows us to identify the magnitude as well as the duration of

the external thermal load. The PIHF can be constructed from the net heat flux of the particle as follows

$$\begin{aligned} \text{PIHF} &= \text{PIHF}_{conv} + \text{PIHF}_{rad} \\ \text{PIHF}_{conv} &= h T_g = \dot{q}_{conv}'' + h T_p \\ \text{PIHF}_{rad} &= \epsilon_{p,surf} G = \dot{q}_{rad}'' + \epsilon_{p,surf} \sigma T_p^4 \end{aligned} \quad (7.3)$$

Figure 7.22 shows the time variations of PIHF obtained for the 10 mm particle located at $x = 40\text{ m}$, $y = 0.2\text{ m}$, $z = 0$ in the mixed-size patch of the wind-dominated fire. In order to remove the contribution of the cold gases, we subtract the PIHF evaluated at room temperature (PIHF_0) from the PIHF. Furthermore, we define the duration of the intense external heating (τ_{PIHF}) as the duration when $\text{PIHF} - \text{PIHF}_0$ is greater than 10% of its peak value. We compute the time integral of the PIHF that is equivalent to the net energy that the PIHF carries during τ_{PIHF} , and we use it to obtain an equivalent quasi-steady value of the intense PIHF. We also calculate the average velocity during τ_{PIHF} using an arithmetic mean of the velocity profile. A summary of these quantities calculated for the 2, 10, and 20 mm particles in the mixed-size patch of the wind-dominated and the buoyancy-dominated fires is presented in Table 7.3.

Figures 7.23 and 7.24 display the convective and the radiate contributions to the PIHF. For the 2 mm particle, the results show that this small particle is exposed to a mixed mode of heat transfer with both convection and radiation at the approximately same level in the wind-dominated fire (see Fig. 7.23) and slightly lower convection in the buoyancy dominated fire (see Fig. 7.24). A quantitative

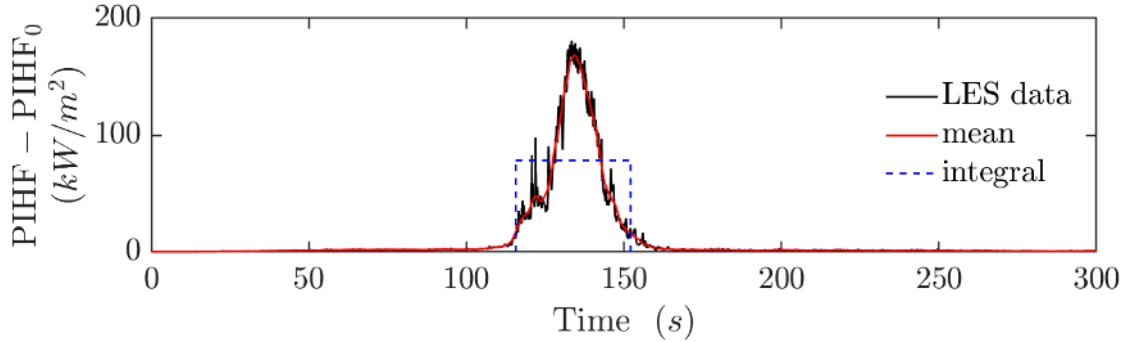


Figure 7.22: Time variation of the instantaneous values of the PIHF (black solid line), the moving average (red solid line), and the time integral of the intense PIHF of the 10 mm particle located at $x = 40\text{ m}$, $y = 0.2\text{ m}$, $z = 0$ position in the wind-dominated fire.

Table 7.3: Summary of the simulation results corresponding to particles in the mixed-size patch located at $x = 40\text{ m}$, $y = 0.2\text{ m}$, $z = 0$ position.

	Buoyancy-dominated			Wind-dominated		
Particle diameter (mm)	2	10	20	2	10	20
Mass consumption (%)	99.9%	69.6%	19%	99.9%	99.8%	41%
PIHF duration τ_{PIHF} (s)	37.5	37.1	32.4	37.5	36.5	44.3
Mean velocity u_g (m/s)	0.74	0.73	0.74	1.75	1.75	1.48
Intense PIHF (kW/m^2)	54.2	48.1	49.1	97	78.2	67.6
Convective contribution (%)	34.7%	15.6%	10.9%	43.8%	21.8%	15.2%
Radiative contribution (%)	65.3%	84.4%	89.1%	56.2%	78.2%	84.8%

measure of the respective weights of convection and radiation shown in Table 7.3 indicates that 34.7% of the PIHF of the 2 mm particle is due to convection in the buoyancy-dominated, and it increases to 43.8% in the wind-dominated fire.

On the other hand, the results of Figs. 7.23 and 7.24 show that the contribution of convection is very small for the larger particles in the mixed-size patch in both the wind-dominated fire and the buoyancy-dominated fire. The results of Table 7.3 suggest that these particles are exposed to a single mode of heat transfer dominated by radiation with a contribution of convection of only 10 – 20% of the PIHF. This result is of great interest as it highlights that the impact of convective heating is much reduced for larger particles, which may limit their ability to ignite and sustain thermal degradation [12, 99].

7.4.6 Interpretation of the particles' behavior using the quasi-steady 2-D maps

In order to interpret the particle behavior in the mixed-size patch during the fire spread, we present in Fig. 7.25 2-D maps of the degree of completion of the char oxidation reaction that are constructed for 2, 10, and 20 mm particles exposed to variations of the PIHF and u_g , and for specific durations of τ_{PIHF} close to the value reported in Table 7.3. We added points on the maps (the blue symbols) to represent the conditions estimated in Table 7.3. These points on the maps show trends that are consistent with the simulated fire in the mixed-size patch. For a residence time of $\tau_{\text{PIHF}} \sim 37.5 s$ for the 2 mm particle and PIHF of 54 or 95 kW/m^2 and $u_g = 0.74$ or 1.75 m/s (see Table 7.3), the 2-D maps in Figs. 7.25a and 7.25b suggest that the 2 mm particles are fully consumed under these conditions. For a residence time of $\tau_{\text{PIHF}} \sim 37 s$ and PIHF value for the 10 mm particle of 48 kW/m^2 and $u_g = 0.73 m/s$

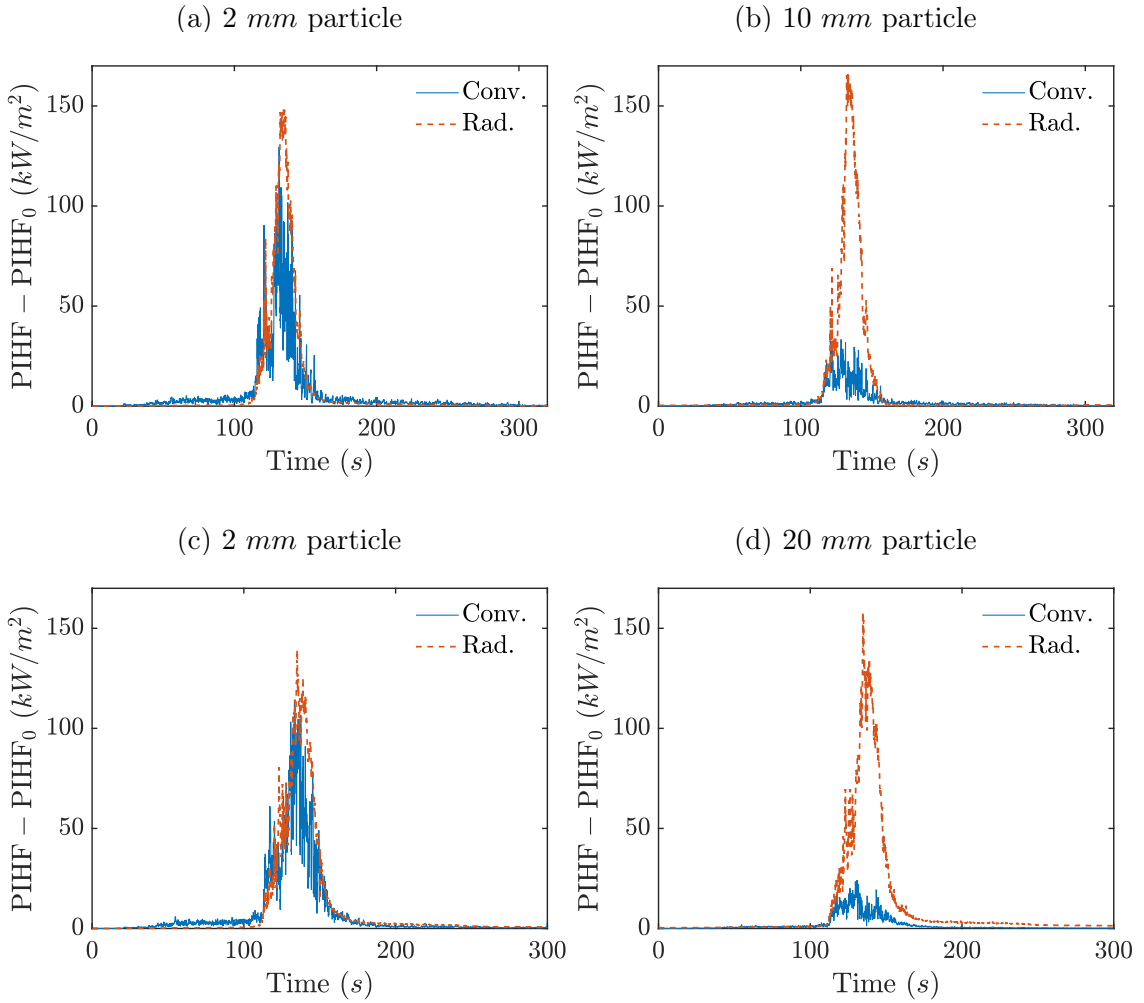


Figure 7.23: Time variation of the convective and the radiative components of the PIHF of particles in mixed-size patch of the wind-dominated fire. See caption of Fig. 7.15.

in the buoyancy dominated fire (see Table 7.3), the maps in Figs. 7.25c and 7.25d suggest that the 10 mm particle are in the partially consumed zone. The maps also show that the case of the wind-dominated fire with $\text{PIHF} = 78.2 \text{ kW/m}^2$ and $u_g = 1.75 \text{ m/s}$ is in the full consumption zone at $\tau_{\text{PIHF}} = 45 \text{ s}$ and is on the edge of this zone at $\tau_{\text{PIHF}} = 30 \text{ s}$; for the 20 mm particle, the maps in Figs. 7.25e and

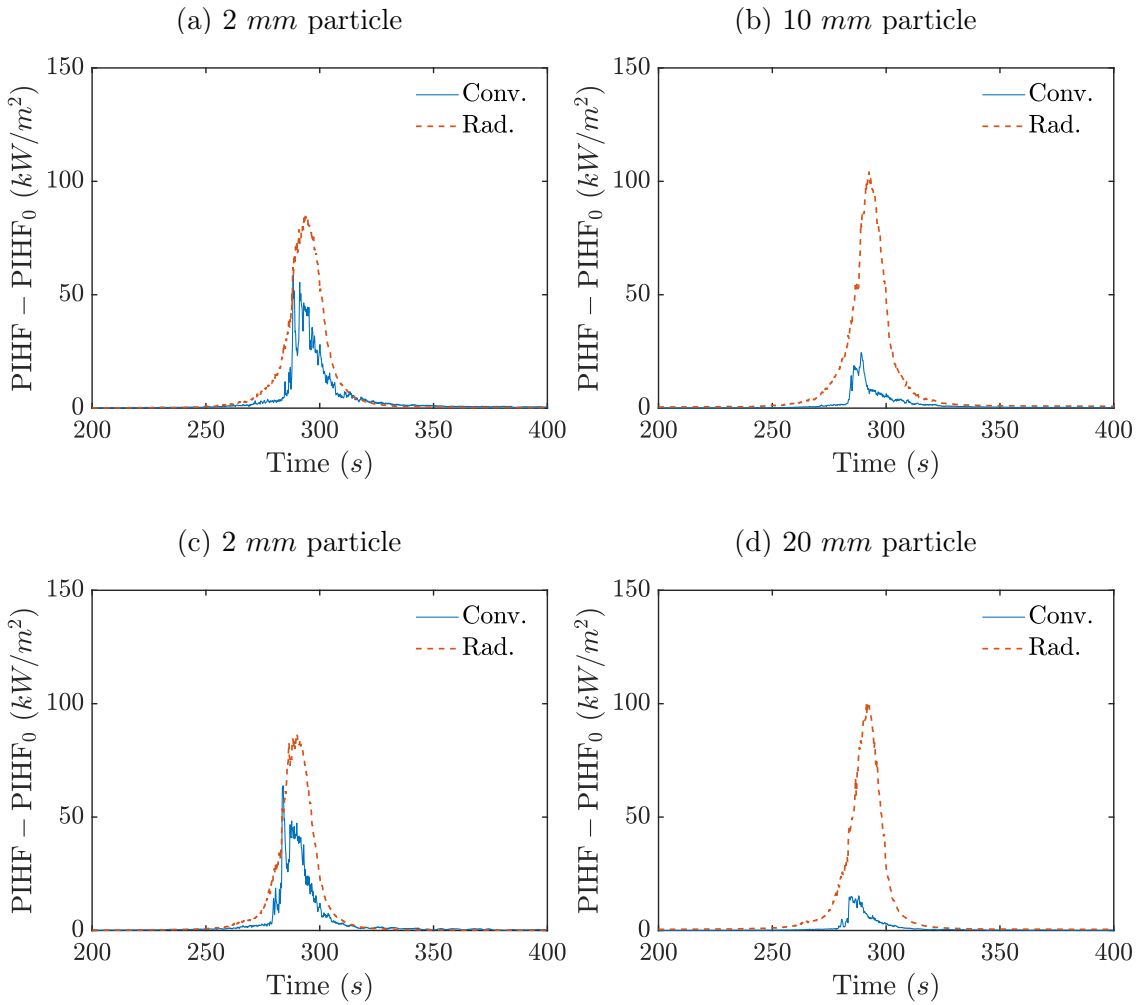


Figure 7.24: Time variation of the convective and the radiative components of the PIHF of particles in mixed-size patch of the buoyancy-dominated fire. See caption of Fig. 7.20.

7.25f indicate that the points corresponding to the conditions listed in Table 7.3 are very far from the full consumption zone at $\tau_{\text{PIHF}} = 30 \text{ s}$, and are slightly closer at $\tau_{\text{PIHF}} = 45 \text{ s}$. Overall, these results show the sensitivity of the particle behavior to the residence time and the intensity of the PIHF.

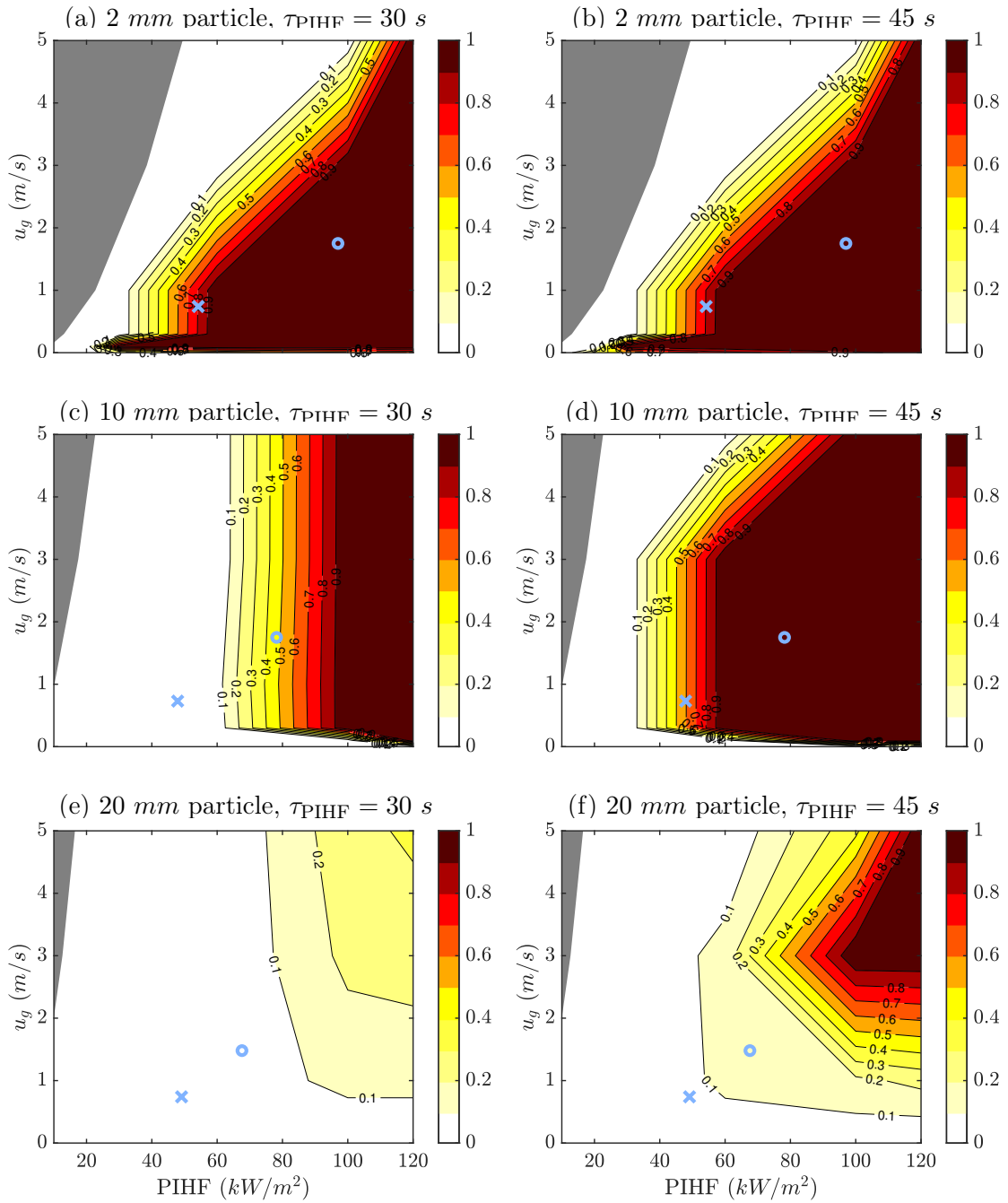


Figure 7.25: Maps of *Rco* degree of completion for 2 mm particles (a,b), 10 mm particles (c,d), and 20 mm particles (e,f). The cross symbol represents conditions from the buoyancy-dominated fire listed in Table 7.3. The circles represent similar conditions from the wind-dominated fire.

7.5 Summary

This chapter presented simulations of fire spread in idealized fuel beds that feature a mixed-size patch of small and large particles. The simulations used sub-millimeter-scale spatial resolution in the solid biomass solver and centimeter-scale spatial resolution in the gas phase solver and thereby resolving the exchanges of mass, momentum, and heat associated with pyrolysis, combustion, radiation, and flow at flame and vegetation scales. The simulations featured successful fire spread over a uniform fuel bed comprised of cylindrical pine wood particles with a diameter of 2 mm at two wind conditions, 1 or 5 m/s, corresponding to a buoyancy-dominated fire regime and a wind-dominated fire regime, respectively. The particles in the uniform fuel bed were found to be completely consumed and converted into ash during flame propagation at the two nominal wind speeds. A mixed-size patch of small and large particles was inserted in a limited region within the uniform bed to avoid disruption of the main fire front. Both the 2 and 10 mm radius particles experienced complete consumption in the mixed-size patch in the wind-dominated fire, with the 10 mm particles featuring a transition from flaming to smoldering combustion which lasts for approximately 150 seconds after the main flame front has passed. These particles showed partial consumption in the buoyancy-dominated fire. Increasing the larger particle size to 20 mm in the mixed-size patch showed that these particles exhibit very limited thermal degradation and no or limited transition from flaming to smoldering. Further inspection of the results indicated that the small particles in the mixed-size patch were exposed to a mixed mode of heat transfer of

convection and radiation of approximately equal weight, whereas the larger particles were exposed to a radiation-dominated heat transfer with a convective contribution of less than 20%. Lastly, the behavior of the particles in the mixed-size patch was explained in terms of changes in the flame residence time and in the intensity of the PIHF through comparisons with maps generated from simulations of single-particle behavior. The present comparison between the behavior of isolated biomass particles and the behavior of the same particles positioned inside vegetation beds emphasized the importance of the PIHF and its duration as the main controlling factors in wildland fire spread.

8 Conclusion and Future Directions

The development of a physics-based computational capability that models the coupling between solid-phase and gas-phase processes that control the dynamics of flame spread in wildland fire problems was the main objective of this dissertation. The approach presented in Chapter 2 focused on resolving processes occurring at flame and vegetation scales, including the formation of flammable vapors from porous biomass vegetation, combustion of these fuel vapors with ambient air, turbulent flow due to heat release and buoyant acceleration, and thermal feedback to the solid biomass. The coupled solver developed, called PBRFoam, was based on the Computational Fluid Dynamics library OpenFOAM and an in-house stand-alone C++ Particle Burning Rate (PBR) solver that used a one-dimensional porous medium formulation to model the thermal degradation of solid biomass particles. Each porous particle was described as a system with a solid phase and a gas phase, which allowed for a detailed treatment of the particle-to-external-gas outflow of volatile mass and the external-gas-to-particle diffusion of oxygen mass; this detailed treatment is required to account for in-depth oxidative pyrolysis and char oxidation. The governing equations of mass, momentum, and energy conservation inside each control volume of the porous particle were solved numerically using an implicit approach that

treated convection and diffusion through a second-order, Crank-Nicolson method and chemical reaction through a first-order, backward Euler method. This PBR solver included an implicit iterative scheme, an adaptive time-stepping technique (for speed, stability, and robustness), and a re-meshing capability (for deforming particles due to swelling or shrinking). The coupling between the solid- and the gas-phases was carried out at the sub-grid level where source terms were added to the governing equations of the gas-phase to account for the exchange of mass, momentum, and energy. A Multi-phase Radiative Transfer Equation (MRTE) was included to account for the radiation absorption and emission due to the presence of solid biomass particles. The development work presented in this dissertation also included modifying the Eddy Dissipation Model (EDM) to account for flame zones at which the mixing is controlled by laminar diffusing; as well as an implementation of a coupled soot-radiation model based on the Laminar Smoke Pint (LSP) concept and the Weighted-Sum-of-Gray-Gases (WSGG) approach.

In Chapter 3, a series of tests and evaluations were presented to verify the developed models using simplified configurations where exact analytical solutions could be obtained. The tests included verification of the in-depth heat conduction in thick rectangular-, cylindrical- and spherical-shaped solids, momentum exchange between the gas-phase and the solid fuel bed, pressure-velocity coupling, multi-phase radiative transfer, and in-depth radiation heat transfer inside the fuel bed. These tests showed that the model can adequately be used to simulate fire spread scenarios including moving glowing firebrands or self-sustained smoldering in a fuel bed driven only by radiation. Additionally, the chapter provided calibration tests of the thermal

degradation model for cardboard and pine wood using simulations of micro-scale TGA experiments in inert and oxidative environments, followed by an evaluation of the PBR model's ability to predict the thermal degradation of thick samples. The results showed that the calibrated model predicts well the thermal degradation at both micro- and bench-scales. The chapter also discussed the ability of the PBR model to simulate particles that feature a volume change. These simulations showed that the choice of the model input parameters such as the residual yield, the constituents density, or the porosity impacts the particle volume change during thermal degradation. This suggests the need for additional data from experiments showing the evolution of volume during thermal degradation in order to evaluate further the model input parameters. Future work should also aim at applying this modeling capability to model the transport of glowing firebrands and the possible spotting ignition.

In Chapter 4, the focus was on evaluating the ability of gas-phase combustion and radiation models to predict thermal feedback in two pool fire configurations. This study of pool fires was viewed as an intermediate but essential step toward modeling more complex fire configurations that feature flame spread. The two canonical pool fire configurations that were evaluated in this study corresponded to a non-sooting methanol pool fire and a sooting buoyancy-driven turbulent ethylene burner. The objective of the study was to evaluate the accuracy of the combustion and radiation models to predict the flame structure and the thermal feedback in these non-sooting and sooting flames. The numerical results in terms of flame structure, temperature fields, and thermal feedback were found to range from fair to very good

agreement with experimental measurements. In particular, the results related to a quantification of the thermal feedback were of particular interest. The results suggested that thermal feedback was estimated within 25% error using the PGRF modeling approach in non-sooting and sooting flames. The simulations suggested that the WSGG model is accurate and superior to the baseline PGRF model. Using the WSGG model, predictions of the radiative heat flux near the pool surface are found to compare well with the measurement. In addition, the simulated value of the global radiant fraction was close to the experimental value. Simulations with both PGRF and WSGG suggest that 75 – 80% of the thermal feedback was due to radiative heat transfer in the non-sooting pool fire. On the other hand, the simulations with WSGG show a significant dependence on soot radiation in the sooting flame, which emphasizes the need for an accurate estimation of the soot field. The results also suggest the need for more accurate modeling of soot at the subgrid level where soot formation/oxidation rates are under-resolved by LES grid cells. The predictions using the PGRF modeling approach were close to that of the WSGG in the sooting flame, where both were spatially off by a maximum of $\sim 25\%$ from the experimental measurements. This level of accuracy is encouraging and suggests that the PGRF approach is adequate to model spreading fires. However, future work should address the implication of using the more elaborate WSGG model in spreading fires.

Simulations of small and large biomass particles exposed to prescribed steady or oscillatory external gas conditions were presented in Chapter 5. The first part discussed the effect of oscillations in the external gas conditions on the pyrolysis of

thin, thick, charring, and non-charring particles, while the second part discussed 2-D maps of the behavior of the flaming and smoldering particles under quasi-steady external heating and gas flow conditions that were present for a limited residence time. The results of the first part suggested that in most scenarios when the heat feedback is dominated by oscillatory radiative heating or when the heat feedback is dominated by oscillatory convection but oscillations in the flow velocity do not exist, the particle featured a quasi-linear response in which the presence of oscillations in the external gas conditions did not significantly affect the overall particle behavior in terms of peak mass loss rate and ignition and burnout out. In this case, it was concluded that the particle behavior can be predicted using quasi-steady external gas conditions. However, in cases where strong oscillations in both the external gas velocity and the temperature co-existed, the simulations showed that the particle featured a non-linear response where the effect of oscillations resulted in faster ignition and short burnout times. The results of the second part suggested that the particle behavior was strongly dependent on the flame residence time and a quantity called the Pseudo Incident Heat Flux that represents the external heating due to convection and radiation. The 2-D maps showed also that the burning behavior of small particles is very sensitive to the external gas velocity, whereas larger particles were found to be less sensitive. The results also suggested that there is a critical core temperature of $\sim 700\text{ K}$ above which the particle will support self-sustained smoldering. These maps are important to interpret more complex scenarios of spreading fire and to determine conditions at which spread or no spread is expected or the degree of fuel consumption.

Simulations of fire spread in loosely and densely packed fuel beds comprised of discrete cardboard sticks were presented in Chapter 6. The simulations corresponded to wind tunnel fire experiments conducted at the Missoula Fire Sciences Laboratory. The first part of the chapter focused on evaluating the newly developed modeling capability in predicting the structure and behavior of two experimental burns belonging to either a buoyancy-dominated fire regime or a wind-dominated fire regime. The simulated fires featured peak and trough flame structures that were a result of buoyant instabilities as well as flaming and glowing zones that were a result of homogeneous combustion in the gas-phase as well as heterogeneous combustion in the solid-phase. Despite some uncertainties and complexities of the flow structure in the wind tunnel during combustion, particularly in buoyancy-dominated fires, the simulated ROS was within $\sim 5 - 25\%$ of the experimental measurements. The second part of the chapter discussed the change in fire behavior due to changes in fuel packing, with the simulations showing a linear increase in residence time with increasing fuel packing and a slight decrease in ROS with increasing packing ratio. Ongoing work aims at evaluating quantitatively the variations of the local conditions in the vicinity of the particles near ignition with changes in the fuel packing.

In Chapter 7, a computational study of fire spread in idealized fuel beds comprised of cylindrical-shaped pine wood sticks was conducted. This configuration corresponded to an idealized field-scale experiment in which the fire spread in relatively larger domains of several tens of meters. The simulations showed successful fire spread over a uniform fuel bed comprised of particles with a diameter of 2 mm at two wind conditions, 1 and 5 m/s , corresponding to a plume-dominated fire regime

and a wind-driven fire regime, respectively. The particles in the uniform fuel bed were completely consumed and converted into ash during flame propagation at the two nominal wind speeds. Simulations were also conducted to study the degree of fuel consumption in a mixed biomass patch comprised of small (2 mm diameter) and large particles (10 or 20 mm diameter). The mixed patch was inserted in a limited region within the uniform bed to avoid disruption of the main fire front. Both the 2 and 10 mm particles showed complete consumption in the mixed patch in the wind-dominated fire, with the 10 mm particles experiencing a transition from flaming to smoldering combustion which lasts long after the main flame front has passed. The larger 20 mm particles showed incomplete consumption and no or limited transition from flaming to smoldering at the two nominal wind speeds. The plume-dominated fires showed that only the 2 mm particles experienced complete consumption, whereas the larger particles experienced very limited consumption. Insights into the local conditions in the vicinity of the particle were presented. The PIHF quantity was used to identify and differentiate between different modes of heating to the particle surface. The results showed that the small particles experienced a mixed mode of heat transfer of both convection and radiation that was adequate to support complete consumption, whereas the larger particles were exposed to radiation-dominated heat transfer with a very limited convective contribution of less than 20% of the incident heat. The behavior of the particles in the mixed-size patch was explained in terms of changes in the flame residence time and the intensity of the PIHF through comparisons with maps generated from simulations of single particle behavior. The study emphasized the importance of the PIHF and its duration (i.e., the residence time) as the main

controlling factors in wildland fire spread.

Lastly, this work has made several contributions:

- the developed computational tools are modular and reusable as they employ the advantages of Object-Oriented Programming (OOP) and open-sourcing to provide a clear interface for other programmers or users to use the code for further development or new simulation studies
- the study of thermal feedback presented in Chapter 4 was published in Combustion and Flame [86]
- the study of biomass particle response to unsteady external gas conditions presented in Chapter 5 was published in Fire Safety Journal [43]
- a journal article about the proposed modification to the EDM model to account for laminar diffusion, presented in Appendix B, is in preparation
- the studies of fire spread in cardboard and pine wood fuel beds presented in Chapters 6 and 7 are still in progress and two journal articles are in preparation

Appendix A: Numerical Algorithms of the Particle Burning Rate Model (PBR)

This appendix describes the numerical algorithms implemented in our in-house object-oriented C++ solver of the Particle Burning Rate Model (PBR). We model each porous particle as a system with a solid phase and a gas phase, which allows for a detailed treatment of the particle-to-external-gas outflow of volatile mass and the external-gas-to-particle diffusion of oxygen mass; this detailed treatment is required to account for in-depth oxidative pyrolysis and char oxidation. We consider here thermally-thick and composition-thick particles featuring in-depth variations of temperature and composition. The particle geometry is modeled as a rectangular slab, cylindrical or spherical.

Rectangular slabs are assumed to be symmetric and have a half-volume $V_p = A_{rect}\delta$, where A_{rect} is the surface area of the exposed surface of the particle and δ the half-thickness. Cylindrical-shaped particles have a volume $V_p = \pi R_p^2 L_{cyl}$, where R_p is the radius of the particle and L_{cyl} is the length of the cylinder. Spherical-shaped particles have a volume $V_p = 4/3\pi R_p^3$, where R_p is the radius of the particle.

The particle is discretized into an ensemble of computational cells introduced to describe variations of heat and mass in the direction normal to the exposed surface

of the particle. In that case, ΔV denotes the volume of a given computational cell. For rectangular slabs, each cell is a rectangular slab with a center located at $x_{C,i}$, a right-boundary located at $x_{R,i}$, and a thickness Δx_i (see Fig. A.1(a) and Table A.1); $x = 0$ is the location of the center of the particle; $x = \delta$ is the location of the exposed surface. For cylindrical-shaped (spherical-shaped) particles, each cell is a cylindrical (spherical) shell with a center located at $r_{C,i}$, a right-boundary located at $r_{R,i}$, and a thickness Δr_i (see Fig. A.1(b) and Table A.1); $r = 0$ is the location of the center of the particle; $r = R_p$ is the location of the exposed surface.

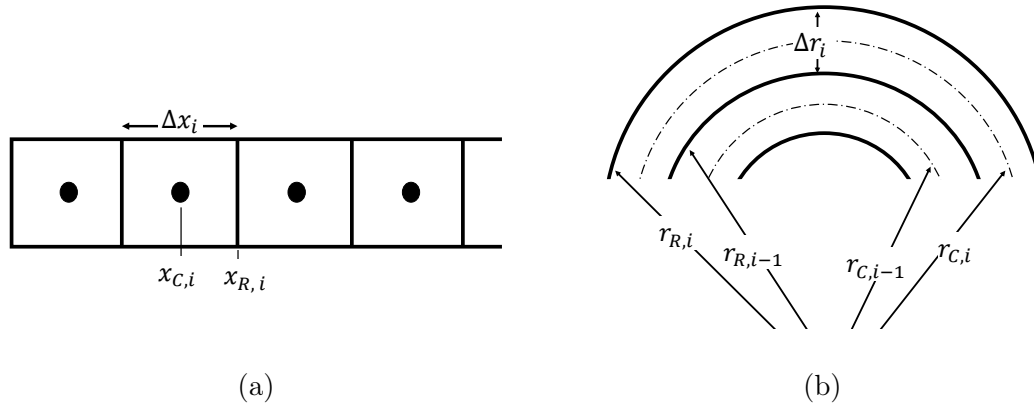


Figure A.1: One-dimensional computational mesh for particles with: (a) rectangular slab geometry; (b) cylindrical or spherical geometry

Table A.1: Definition of the mesh parameters. In these expressions, A_{rect} is the exposed surface area of rectangular particles, and L_{cyl} is the length of the cylindrical-shaped particles. The subscript C refers to the center of the cell; the subscript R refers to its right-boundary.

	Rectangular particles	Cylindrical particles	Spherical particles
Coordinate of the cell right-boundary	$x_{R,i} = x_{R,i-1} + \Delta x_i$	$r_{R,i} = r_{R,i-1} + \Delta r_i$	$r_{R,i} = r_{R,i-1} + \Delta r_i$
Coordinate of the cell center	$x_{C,i} = \frac{x_{R,i} + x_{R,i-1}}{2}$	$r_{C,i} = \frac{r_{R,i} + r_{R,i-1}}{2}$	$r_{C,i} = \frac{r_{R,i} + r_{R,i-1}}{2}$
Cell volume	$\Delta V_i = A_{rect} \times \Delta x_i$	$\Delta V_i = \pi(r_{R,i}^2 - r_{R,i-1}^2)L_{cyl}$	$\Delta V_i = \frac{4}{3}\pi(r_{R,i}^3 - r_{R,i-1}^3)$
Surface area of the cell right-boundary	$S_i^+ = A_{rect}$	$S_i^+ = 2\pi r_{R,i} \times L_{cyl}$	$S_i^+ = 4\pi r_{R,i}^2$
Surface area of the cell left-boundary	$S_i^- = A_{rect}$	$S_i^- = 2\pi r_{R,i-1} \times L_{cyl}$	$S_i^- = 4\pi r_{R,i-1}^2$

[!ht]

A.1 Discretization of the governing equations

A.1.1 Solid-phase mass conservation equations

We first re-write Eq. 2.17 as follows:

$$\frac{\partial}{\partial t}(X_{ws}\Delta V)_i = -\frac{(K_{Rd})_i}{\rho_{ws,bulk}} \quad (\text{A.1})$$

where $K_{Rd} = (\dot{m}_{Rd}''' \Delta V)$, and where the subscript i designates the index of the computational cell ($1 \leq i \leq N$, with N the total number of computational cells).

$$\frac{\partial}{\partial t}(X_{ds}\Delta V)_i = \frac{\eta_{ds,Rd}(K_{Rd})_i}{\rho_{ds,bulk}} - \frac{(K_{Rp})_i}{\rho_{ds,bulk}} - \frac{(K_{Rop})_i}{\rho_{ds,bulk}} \quad (\text{A.2})$$

where $K_{Rp} = (\dot{m}_{Rp}''' \Delta V)$ and $K_{Rop} = (\dot{m}_{Rop}''' \Delta V)$.

$$\frac{\partial}{\partial t}(X_c\Delta V)_i = \frac{\eta_{c,Rp}(K_{Rp})_i}{\rho_{c,bulk}} + \frac{\eta_{c,Rop}(K_{Rop})_i}{\rho_{c,bulk}} - \frac{(K_{Rco})_i}{\rho_{c,bulk}} \quad (\text{A.3})$$

where $K_{Rco} = (\dot{m}_{Rco}''' \Delta V)$.

$$\frac{\partial}{\partial t}(X_a\Delta V)_i = \frac{\eta_{a,Rco}(K_{Rco})_i}{\rho_{a,bulk}} \quad (\text{A.4})$$

Equations A.1-A.4 are integrated in time using a semi-implicit iterative method in which $(\Delta V)_i$ is frozen and treated as equal to its value at the previous time step and the factors K_{Rj} , $1 \leq j \leq 4$, are treated as equal to their values at the new time step and at the previous iteration; we use the following expressions:

$$(X_{ws}\Delta V)_i^{(n+1,iter+1)} = \frac{(X_{ws}\Delta V)_i^{(n)}}{1 + \Delta t \times \frac{(K_{Rd})_i^{(n+1,iter)}}{\rho_{ws,bulk} \times \max((X_{ws}\Delta V)_i^{(n+1,iter)}, \epsilon)}} \quad (\text{A.5})$$

where the superscripts (n) and $(n + 1)$ designate quantities evaluated at the previous and new time steps, respectively, and the superscripts $(iter)$ and $(iter + 1)$ designate quantities evaluated at the new time step $(n + 1)$ and at the previous and new iterations, respectively. The parameter ϵ is a small number introduced in the formulation to avoid dividing by 0.

$$(X_{ds}\Delta V)_i^{(n+1,iter+1)} = \frac{(X_{ds}\Delta V)_i^{(n)} + \Delta t \times \frac{\eta_{ds,Rd}(K_{Rd})_i^{(n+1,iter)}}{\rho_{ds,bulk}}}{1 + \Delta t \times \frac{((K_{Rp})_i^{(n+1,iter)} + (K_{Rop})_i^{(n+1,iter)})}{\rho_{ds,bulk} \times \max((X_{ds}\Delta V)_i^{(n+1,iter)}, \epsilon)}} \quad (\text{A.6})$$

$$(X_c\Delta V)_i^{(n+1,iter+1)} = \frac{(X_c\Delta V)_i^{(n)} + \Delta t \times \frac{(\eta_{c,Rp}(K_{Rp})_i^{(n+1,iter)} + \eta_{c,Rop}(K_{Rop})_i^{(n+1,iter)})}{\rho_{c,bulk}}}{1 + \Delta t \times \frac{(K_{Rco})_i^{(n+1,iter)}}{\rho_{c,bulk} \times \max((X_c\Delta V)_i^{(n+1,iter)}, \epsilon)}} \quad (\text{A.7})$$

$$(X_a\Delta V)_i^{(n+1,iter+1)} = (X_a\Delta V)_i^{(n)} + \Delta t \times \frac{\eta_{a,Rco}(K_{Rco})_i^{(n+1,iter)}}{\rho_{a,bulk}} \quad (\text{A.8})$$

The new total volume of the cell can now be calculated as:

$$(\Delta V)_i^{(n+1,iter+1)} = \sum_{k=ws,ds,c,a} (X_k\Delta V)_i^{(n+1,iter+1)} \quad (\text{A.9})$$

The composition vector $(X_{ws}, X_{ds}, X_c, X_a)$ is then obtained from the following ratios:

$$(X_k)_i^{(n+1,iter+1)} = \frac{(X_k\Delta V)_i^{(n+1,iter+1)}}{(\Delta V)_i^{(n+1,iter+1)}}, \quad k = ws, ds, c, a \quad (\text{A.10})$$

And the porosity is finally updated:

$$(\bar{\psi})_i^{(n+1,iter+1)} = \sum_{k=ws,ds,c,a} \psi_k (X_k)_i^{(n+1,iter+1)} \quad (\text{A.11})$$

These expressions are solved until convergence is achieved.

A.1.2 The temperature equation

We start from Eq. 2.37:

$$(\rho c)_{eff} \frac{\partial T_p}{\partial t} \Delta V + \dot{m}_\zeta'' \bar{c}_{p,g} \frac{\partial T_p}{\partial \zeta} \Delta V = \frac{1}{\phi} \frac{\partial}{\partial \zeta} (k_{eff} \phi \frac{\partial T_p}{\partial \zeta}) \Delta V + \dot{q}_{hrr}''' \Delta V \quad (\text{A.12})$$

where $(\rho c)_{eff}$ and k_{eff} are effective gas-solid properties, $(\rho c)_{eff} = \bar{\rho}_s \bar{c}_s (1 - \bar{\psi}) + \bar{\rho}_g \bar{c}_{p,g} \bar{\psi}$ and $k_{eff} = \bar{k}_s (1 - \bar{\psi}) + \bar{k}_g \bar{\psi}$. We adopt a classical finite volume formulation and re-write the above equation as follows:

$$\begin{aligned} & (\rho c)_{eff,i} \frac{\partial (T_p)_i}{\partial t} \Delta V_i + \left(\bar{c}_{p,g} \frac{\bar{K}}{\nu_g} \right)_i \left(-\frac{\partial p}{\partial \zeta} \frac{\partial T_p}{\partial \zeta} \right)_i \Delta V_i \\ &= -S_i^- f_i^- + S_i^+ f_i^+ + (\dot{q}_{hrr}')_i \Delta V_i \quad (\text{A.13}) \end{aligned}$$

where the pressure and temperature gradients in the convective term of the equation are estimated using an upwind scheme, where S_i^- and S_i^+ are the surface areas of the left and right boundaries of the computational cell ΔV_i (see Table A.1), and where f_i^- and f_i^+ represent the heat fluxes due to conduction (and possibly due to radiation across the pores of the particle) at these boundaries:

$$\begin{aligned} & \left(-\frac{\partial p}{\partial \zeta} \frac{\partial T_p}{\partial \zeta} \right)_i = H((p_{i-1} - p_i), 0) \times H((p_i - p_{i+1}), 0) \times \left(-\frac{\partial p}{\partial \zeta} \frac{\partial T_p}{\partial \zeta} \right)_{\zeta=\zeta_{R,i-1}} \quad (\text{A.14}) \\ & + H((p_i - p_{i-1}), 0) \times H((p_{i+1} - p_i), 0) \times \left(-\frac{\partial p}{\partial \zeta} \frac{\partial T_p}{\partial \zeta} \right)_{\zeta=\zeta_{R,i}} \end{aligned}$$

where H is the Heaviside step function, $H(x) = 0$ if $x \leq 0$, $H(x) = 1$ if $x > 0$.

$$\begin{aligned} f_i^- &= \left(k_{eff} \frac{\partial T_p}{\partial \zeta} \right)_{\zeta=\zeta_{R,i-1}} \\ f_i^+ &= \left(k_{eff} \frac{\partial T_p}{\partial \zeta} \right)_{\zeta=\zeta_{R,i}} \quad (\text{A.15}) \end{aligned}$$

Equation A.12 is integrated in time using an implicit approach that treats convection and diffusion through a second-order, Crank-Nicolson method and chemical reaction through a first-order, backward Euler method. The quantities $(\rho c)_{eff,i}$, $(\bar{c}_{p,g}\bar{K}/\nu_g)_i$, $k_{eff,i}$, and the mesh coordinates/geometry are frozen and treated as equal to their values at the previous time step:

$$\begin{aligned}
 & (\rho c)_{eff,i}^{(n)} \frac{(T_p)_i^{(n+1,iter+1)} - (T_p)_i^{(n)}}{\Delta t} (\Delta V)_i^{(n)} \\
 & + \frac{1}{2} \left(\frac{\bar{K}}{\nu_g} \bar{c}_{p,g} \right)_i^{(n)} \left(-\frac{\partial p}{\partial \zeta} \frac{\partial T_p}{\partial \zeta} \right)_i^{(n+1,iter+1)} (\Delta V)_i^{(n)} \\
 & + \frac{1}{2} \left(\frac{\bar{K}}{\nu_g} \bar{c}_{p,g} \right)_i^{(n)} \left(-\frac{\partial p}{\partial \zeta} \frac{\partial T_p}{\partial \zeta} \right)_i^{(n)} (\Delta V)_i^{(n)} \\
 & = \frac{1}{2} (-S_i^- f_i^- + S_i^+ f_i^+)^{(n+1,iter+1)} + \frac{1}{2} (-S_i^- f_i^- + S_i^+ f_i^+)^{(n)} \\
 & + \left((\dot{q}_{hrr,+}''')_i^{(n+1,iter)} + (\dot{q}_{hrr,-}''')_i^{(n+1,iter)} \right) (\Delta V)_i^{(n)} \tag{A.16}
 \end{aligned}$$

where $(\dot{q}_{hrr}''')_i^{(n+1,iter)}$ has been decomposed into positive and negative components,

$$(\dot{q}_{hrr}''')_i^{(n+1,iter)} = (\dot{q}_{hrr,+}''')_i^{(n+1,iter)} + (\dot{q}_{hrr,-}''')_i^{(n+1,iter)}, \text{ with } \dot{q}_{hrr,+}''' \geq 0 \text{ and } \dot{q}_{hrr,-}''' \leq 0,$$

where also $(S_i^- f_i^-)$ and $(S_i^+ f_i^+)$ are evaluated at $\zeta = \zeta_{R,i-1}$ and $\zeta = \zeta_{R,i}$, respectively:

$$\begin{aligned}
 (S_i^- f_i^-)^{(n+1,iter+1)} &= (S_i^-)^{(n)} \frac{k_{eff,i}^{(n)} + k_{eff,i-1}^{(n)}}{2} \frac{(T_p)_i^{(n+1,iter+1)} - (T_p)_{i-1}^{(n+1,iter+1)}}{\zeta_{C,i}^{(n)} - \zeta_{C,i-1}^{(n)}} \\
 (S_i^- f_i^-)^{(n)} &= (S_i^-)^{(n)} \frac{k_{eff,i}^{(n)} + k_{eff,i-1}^{(n)}}{2} \frac{(T_p)_i^{(n)} - (T_p)_{i-1}^{(n)}}{\zeta_{C,i}^{(n)} - \zeta_{C,i-1}^{(n)}} \\
 (S_i^+ f_i^+)^{(n+1,iter+1)} &= (S_i^+)^{(n)} \frac{k_{eff,i+1}^{(n)} + k_{eff,i}^{(n)}}{2} \frac{(T_p)_{i+1}^{(n+1,iter+1)} - (T_p)_i^{(n+1,iter+1)}}{\zeta_{C,i+1}^{(n)} - \zeta_{C,i}^{(n)}} \\
 (S_i^+ f_i^+)^{(n)} &= (S_i^+)^{(n)} \frac{k_{eff,i+1}^{(n)} + k_{eff,i}^{(n)}}{2} \frac{(T_p)_{i+1}^{(n)} - (T_p)_i^{(n)}}{\zeta_{C,i+1}^{(n)} - \zeta_{C,i}^{(n)}} \tag{A.17}
 \end{aligned}$$

and where the pressure and temperature gradients in the convective terms of the

temperature equation are expressed as:

$$\begin{aligned}
\left(-\frac{\partial p}{\partial \zeta} \frac{\partial T_p}{\partial \zeta} \right)_i^{(n+1,iter+1)} &= H((p_{i-1}^{(n)} - p_i^{(n)}), 0) \times H((p_i^{(n)} - p_{i+1}^{(n)}), 0) \times \frac{p_{i-1}^{(n)} - p_i^{(n)}}{\zeta_{C,i}^{(n)} - \zeta_{C,i-1}^{(n)}} \\
&\times \frac{(T_p)_i^{(n+1,iter+1)} - (T_p)_{i-1}^{(n+1,iter+1)}}{\zeta_{C,i}^{(n)} - \zeta_{C,i-1}^{(n)}} \\
&+ H((p_i^{(n)} - p_{i-1}^{(n)}), 0) \times H((p_{i+1}^{(n)} - p_i^{(n)}), 0) \times \frac{p_i^{(n)} - p_{i+1}^{(n)}}{\zeta_{C,i+1}^{(n)} - \zeta_{C,i}^{(n)}} \\
&\times \frac{(T_p)_{i+1}^{(n+1,iter+1)} - (T_p)_i^{(n+1,iter+1)}}{\zeta_{C,i+1}^{(n)} - \zeta_{C,i}^{(n)}} \tag{A.18}
\end{aligned}$$

$$\begin{aligned}
\left(-\frac{\partial p}{\partial \zeta} \frac{\partial T_p}{\partial \zeta} \right)_i^{(n)} &= H((p_{i-1}^{(n)} - p_i^{(n)}), 0) \times H((p_i^{(n)} - p_{i+1}^{(n)}), 0) \times \frac{p_{i-1}^{(n)} - p_i^{(n)}}{\zeta_{C,i}^{(n)} - \zeta_{C,i-1}^{(n)}} \\
&\times \frac{(T_p)_i^{(n)} - (T_p)_{i-1}^{(n)}}{\zeta_{C,i}^{(n)} - \zeta_{C,i-1}^{(n)}} \\
&+ H((p_i^{(n)} - p_{i-1}^{(n)}), 0) \times H((p_{i+1}^{(n)} - p_i^{(n)}), 0) \times \frac{p_i^{(n)} - p_{i+1}^{(n)}}{\zeta_{C,i+1}^{(n)} - \zeta_{C,i}^{(n)}} \\
&\times \frac{(T_p)_{i+1}^{(n)} - (T_p)_i^{(n)}}{\zeta_{C,i+1}^{(n)} - \zeta_{C,i}^{(n)}} \tag{A.19}
\end{aligned}$$

After some straightforward algebraic manipulations, we finally get the following system of equations:

$$a_i (T_p)_{i-1}^{(n+1,iter+1)} + b_i (T_p)_i^{(n+1,iter+1)} + c_i (T_p)_{i+1}^{(n+1,iter+1)} = d_i \tag{A.20}$$

where a, b , and c are one-dimensional arrays representing the coefficients of a tri-diagonal matrix, and where d is an array corresponding to the right-hand side of the linear system of temperature equations. In the particle burning rate model, Eq. A.20 is solved using an efficient tri-diagonal matrix algorithm (Thomas algorithm). The coefficients a, b, c and d are defined as

$$\begin{aligned}
a_i &= -\frac{FO_L}{2} - \frac{CFL_L}{2} \\
b_i &= 1 + \frac{FO_L}{2} + \frac{FO_R}{2} + \frac{CFL_L}{2} - \frac{CFL_R}{2} - \frac{(\dot{q}_{hrr,-}''')_i^{(n+1,iter)} \Delta t}{(\rho c)_{eff,i}^{(n)} (T_p)_i^{(n+1,iter)}} \\
c_i &= -\frac{FO_R}{2} + \frac{CFL_R}{2} \\
d_i &= \left(\frac{FO_L}{2} + \frac{CFL_L}{2} \right) (T_p)_{i-1}^{(n)} + \left(1 - \frac{FO_L}{2} - \frac{FO_R}{2} - \frac{CFL_L}{2} + \frac{CFL_R}{2} \right) (T_p)_i^{(n)} \\
&\quad + \left(\frac{FO_R}{2} - \frac{CFL_R}{2} \right) (T_p)_{i+1}^{(n)} + \frac{(\dot{q}_{hrr,+}''')_i^{(n+1,iter)} \Delta t}{(\rho c)_{eff,i}^{(n)}} \tag{A.21}
\end{aligned}$$

where FO_L and FO_R are Fourier numbers (also called von Neumann numbers):

$$\begin{aligned}
FO_L &= \Delta t \times \left(\frac{k_{eff,i} + k_{eff,i-1}}{2 (\rho c)_{eff,i}} \times \frac{S_i^-}{\Delta V_i (\zeta_{C,i} - \zeta_{C,i-1})} \right)^{(n)} \\
FO_R &= \Delta t \times \left(\frac{k_{eff,i+1} + k_{eff,i}}{2 (\rho c)_{eff,i}} \times \frac{S_i^+}{\Delta V_i (\zeta_{C,i+1} - \zeta_{C,i})} \right)^{(n)} \tag{A.22}
\end{aligned}$$

and where CFL_L and CFL_R are Courant–Friedrichs–Lewy (CFL) numbers:

$$\begin{aligned}
CFL_L &= \Delta t \times \left(\frac{\bar{c}_{p,g}}{(\rho c)_{eff}} \frac{\bar{K}}{\nu_g} \right)_i^{(n)} \times H((p_{i-1}^{(n)} - p_i^{(n)}), 0) \times H((p_i^{(n)} - p_{i+1}^{(n)}), 0) \\
&\quad \times \frac{p_{i-1}^{(n)} - p_i^{(n)}}{(\zeta_{C,i}^{(n)} - \zeta_{C,i-1}^{(n)})^2} \\
CFL_R &= \Delta t \times \left(\frac{\bar{c}_{p,g}}{(\rho c)_{eff}} \frac{\bar{K}}{\nu_g} \right)_i^{(n)} \times H((p_i^{(n)} - p_{i-1}^{(n)}), 0) \times H((p_{i+1}^{(n)} - p_i^{(n)}), 0) \\
&\quad \times \frac{p_i^{(n)} - p_{i+1}^{(n)}}{(\zeta_{C,i+1}^{(n)} - \zeta_{C,i}^{(n)})^2} \tag{A.23}
\end{aligned}$$

The boundary condition at the center of the particle (at $\zeta = 0$) corresponds to a zero-gradient symmetry condition: $FO_L = 0$, $CFL_L = 0$. The boundary condition at the exposed surface of the particle (at $\zeta = \delta$ or R_p , see Fig. A.2), corresponds to a prescribed heat flux condition: $FO_R = 0$, $CFL_R = 0$, $b_i = b_N$ and $d_i = d_N$, where b_N and d_N are given by:

$$\begin{aligned}
b_N &= 1 + \frac{FO_L}{2} + \frac{CFL_L}{2} - \frac{(\dot{q}_{hrr,-}''')_N^{(n+1,iter)} \Delta t}{(\rho c)_{eff,N}^{(n)} (T_p)_N^{(n+1,iter)}} \\
&\quad + \Delta t \left(\frac{S_N^+}{(\rho c)_{eff,N} (\Delta V)_N} \right)^{(n)} \left(\frac{h + h_{rad}}{1 + Bi} \right)^{(n)} \\
d_N &= \left(\frac{FO_L}{2} + \frac{CFL_L}{2} \right) (T_p)_{N-1}^{(n)} + \left(1 - \frac{FO_L}{2} - \frac{CFL_L}{2} \right) (T_p)_N^{(n)} \\
&\quad + \frac{(\dot{q}_{hrr,+}''')_N^{(n+1,iter)} \Delta t}{(\rho c)_{eff,N}^{(n)}} + \Delta t \left(\frac{S_N^+}{(\rho c)_{eff,N} (\Delta V)_N} \right)^{(n)} \left(\frac{h T_{g,\infty} + \epsilon_{p,surf} G}{1 + Bi} \right)^{(n)} \quad (\text{A.24})
\end{aligned}$$

with N the index of the computational cell that is adjacent to the exposed surface of the particle. In these expressions for b_N and d_N , the surface heat flux is written as:

$$\begin{aligned}
\dot{q}_{g \rightarrow s}'' &= h(T_{g,\infty} - T_{p,surf}) + \epsilon_{p,surf}(G - \sigma T_{p,surf}^4) \\
&= h(T_{g,\infty} - T_{p,surf}) + \epsilon_{p,surf}G - h_{rad}T_{p,surf} \quad (\text{A.25})
\end{aligned}$$

where h_{rad} is the effective radiation heat transfer coefficient, $h_{rad} = \epsilon_{p,surf}\sigma \times T_{p,surf}^3$, where $\epsilon_{p,surf}$ is the total surface emissivity and is calculated as a weighted material property, $\epsilon_{p,surf} = \sum_{k=ws,ds,c,a} (\epsilon_k X_k)$, with ϵ_k the surface emissivity of individual species k , and where the surface temperature $T_{p,surf}$ is obtained from a condition expressing continuity of the heat flux at $\zeta = \delta$ or R_p :

$$h(T_{g,\infty} - T_{p,surf}) + \epsilon_{p,surf}G - h_{rad}T_{p,surf} = k_{eff,N} \frac{T_{p,surf} - (T_p)_N}{\zeta_{R,N} - \zeta_{C,N}} \quad (\text{A.26})$$

with $\zeta_{R,N} = \delta$ or R_p . We get:

$$T_{p,surf} = \frac{(T_p)_N + (h T_{g,\infty} + \epsilon_{p,surf} G) \times (\zeta_{R,N} - \zeta_{C,N}) / k_{eff,N}}{1 + Bi} \quad (\text{A.27})$$

$$\dot{q}_{g \rightarrow s}'' = \frac{h(T_{g,\infty} - (T_p)_N) + \epsilon_{p,surf}G - h_{rad}(T_p)_N}{1 + Bi} \quad (\text{A.28})$$

where Bi is a Biot number,

$$Bi = (h + h_{rad})(\zeta_{R,N} - \zeta_{C,N})/k_{eff,N} \quad (\text{A.29})$$

Equation A.20 is solved until convergence is achieved.

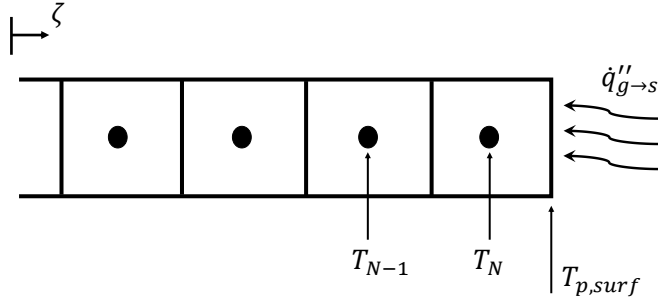


Figure A.2: Thermal boundary condition at the exposed surface of the particle.

A.1.3 The gas-phase oxygen mass equation

We start from Eq. 2.26 and first re-write the equation to give it a mathematical form similar to that found in the temperature equation:

$$(\bar{\rho}_g \bar{\psi}) \frac{\partial Y_{g,O_2}}{\partial t} \Delta V + \dot{m}_\zeta'' \frac{\partial Y_{g,O_2}}{\partial \zeta} \Delta V = \frac{1}{\phi} \frac{\partial}{\partial \zeta} (\phi \bar{\psi} \bar{\rho}_g \bar{D}_g \frac{\partial Y_{g,O_2}}{\partial \zeta}) \Delta V - \dot{m}_{O_2}''' \Delta V \quad (\text{A.30})$$

where $\dot{m}_{O_2}''' = (\eta_{O_2,Rop} \dot{m}_{Rop}''' + \eta_{O_2,Rco} \dot{m}_{Rco}''' + \dot{m}_{sg}''' Y_{g,O_2})$. We then adopt a classical finite volume formulation and re-write the equation as follows:

$$\begin{aligned} (\bar{\rho}_g \bar{\psi})_i \frac{\partial (Y_{g,O_2})_i}{\partial t} \Delta V_i + \left(\frac{\bar{K}}{\nu_g} \right)_i \left(- \frac{\partial p}{\partial \zeta} \frac{\partial Y_{g,O_2}}{\partial \zeta} \right)_i \Delta V_i \\ = -S_i^- f_i^- + S_i^+ f_i^+ - (\dot{m}_{O_2}''')_i \Delta V_i \quad (\text{A.31}) \end{aligned}$$

where the pressure and oxygen mass fraction gradients in the convective term of the equation are estimated using an upwind scheme, where S_i^- and S_i^+ are the surface

areas of the left and right boundaries of the computational cell ΔV_i (see Table A.1), and where f_i^- and f_i^+ represent the oxygen mass fluxes due to diffusion at these boundaries:

$$\begin{aligned} \left(-\frac{\partial p}{\partial \zeta} \frac{\partial Y_{g,O_2}}{\partial \zeta} \right)_i &= H((p_{i-1} - p_i), 0) \times H((p_i - p_{i+1}), 0) \times \left(-\frac{\partial p}{\partial \zeta} \frac{\partial Y_{g,O_2}}{\partial \zeta} \right)_{\zeta=\zeta_{R,i-1}} \\ &\quad + H((p_i - p_{i-1}), 0) \times H((p_{i+1} - p_i), 0) \times \left(-\frac{\partial p}{\partial \zeta} \frac{\partial Y_{g,O_2}}{\partial \zeta} \right)_{\zeta=\zeta_{R,i}} \end{aligned} \quad (\text{A.32})$$

$$\begin{aligned} f_i^- &= \left(\bar{\psi} \bar{\rho}_g \bar{D}_g \frac{\partial Y_{g,O_2}}{\partial \zeta} \right)_{\zeta=\zeta_{R,i-1}} \\ f_i^+ &= \left(\bar{\psi} \bar{\rho}_g \bar{D}_g \frac{\partial Y_{g,O_2}}{\partial \zeta} \right)_{\zeta=\zeta_{R,i}} \end{aligned} \quad (\text{A.33})$$

Equation A.31 is integrated in time using an implicit approach that treats convection and diffusion through a second-order, Crank-Nicolson method and chemical reaction through a first-order, backward Euler method. The quantities $(\bar{\rho}_g \bar{\psi})_i$, $(\bar{K}/\nu_g)_i$, $(\bar{\psi} \bar{\rho}_g \bar{D}_g)_i$, and the mesh coordinates/geometry are frozen and treated as equal to their values at the previous time step:

$$\begin{aligned} (\bar{\rho}_g \bar{\psi})_i^{(n)} &\frac{(Y_{g,O_2})_i^{(n+1,iter+1)} - (Y_{g,O_2})_i^{(n)}}{\Delta t} (\Delta V)_i^{(n)} \\ &+ \frac{1}{2} \left(\frac{\bar{K}}{\nu_g} \right)_i^{(n)} \left(-\frac{\partial p}{\partial \zeta} \frac{\partial Y_{g,O_2}}{\partial \zeta} \right)_i^{(n+1,iter+1)} (\Delta V)_i^{(n)} \\ &+ \frac{1}{2} \left(\frac{\bar{K}}{\nu_g} \right)_i^{(n)} \left(-\frac{\partial p}{\partial \zeta} \frac{\partial Y_{g,O_2}}{\partial \zeta} \right)_i^{(n)} (\Delta V)_i^{(n)} \\ &= \frac{1}{2} (-S_i^- f_i^- + S_i^+ f_i^+)^{(n+1,iter+1)} \\ &+ \frac{1}{2} (-S_i^- f_i^- + S_i^+ f_i^+)^{(n)} - (\dot{m}_{O_2}'''_i)^{(n+1,iter)} (\Delta V)_i^{(n)} \end{aligned} \quad (\text{A.34})$$

where $(S_i^- f_i^-)$ and $(S_i^+ f_i^+)$ are evaluated at $\zeta = \zeta_{R,i-1}$ and $\zeta = \zeta_{R,i}$, respectively:

$$\begin{aligned}
& \left(S_i^- f_i^- \right)^{(n+1,iter+1)} \\
&= (S_i^-)^{(n)} \frac{(\bar{\psi} \bar{\rho}_g \bar{D}_g)_i^{(n)} + (\bar{\psi} \bar{\rho}_g \bar{D}_g)_{i-1}^{(n)}}{2} \frac{(Y_{g,O_2})_i^{(n+1,iter+1)} - (Y_{g,O_2})_{i-1}^{(n+1,iter+1)}}{\zeta_{C,i}^{(n)} - \zeta_{C,i-1}^{(n)}} \\
& \left(S_i^- f_i^- \right)^{(n)} = (S_i^-)^{(n)} \frac{(\bar{\psi} \bar{\rho}_g \bar{D}_g)_i^{(n)} + (\bar{\psi} \bar{\rho}_g \bar{D}_g)_{i-1}^{(n)}}{2} \frac{(Y_{g,O_2})_i^{(n)} - (Y_{g,O_2})_{i-1}^{(n)}}{\zeta_{C,i}^{(n)} - \zeta_{C,i-1}^{(n)}} \\
& \left(S_i^+ f_i^+ \right)^{(n+1,iter+1)} \\
&= (S_i^+)^{(n)} \frac{(\bar{\psi} \bar{\rho}_g \bar{D}_g)_{i+1}^{(n)} + (\bar{\psi} \bar{\rho}_g \bar{D}_g)_i^{(n)}}{2} \frac{(Y_{g,O_2})_{i+1}^{(n+1,iter+1)} - (Y_{g,O_2})_i^{(n+1,iter+1)}}{\zeta_{C,i+1}^{(n)} - \zeta_{C,i}^{(n)}} \\
& \left(S_i^+ f_i^+ \right)^{(n)} = (S_i^+)^{(n)} \frac{(\bar{\psi} \bar{\rho}_g \bar{D}_g)_{i+1}^{(n)} + (\bar{\psi} \bar{\rho}_g \bar{D}_g)_i^{(n)}}{2} \frac{(Y_{g,O_2})_{i+1}^{(n)} - (Y_{g,O_2})_i^{(n)}}{\zeta_{C,i+1}^{(n)} - \zeta_{C,i}^{(n)}} \quad (\text{A.35})
\end{aligned}$$

and where the pressure and oxygen mass fraction gradients in the convective terms of the equation are expressed as:

$$\begin{aligned}
& \left(-\frac{\partial p}{\partial \zeta} \frac{\partial Y_{g,O_2}}{\partial \zeta} \right)_i^{(n+1,iter+1)} = H((p_{i-1}^{(n)} - p_i^{(n)}), 0) \times H((p_i^{(n)} - p_{i+1}^{(n)}), 0) \\
& \quad \times \frac{p_{i-1}^{(n)} - p_i^{(n)}}{\zeta_{C,i}^{(n)} - \zeta_{C,i-1}^{(n)}} \times \frac{(Y_{g,O_2})_i^{(n+1,iter+1)} - (Y_{g,O_2})_{i-1}^{(n+1,iter+1)}}{\zeta_{C,i}^{(n)} - \zeta_{C,i-1}^{(n)}} \\
& \quad + H((p_i^{(n)} - p_{i-1}^{(n)}), 0) \times H((p_{i+1}^{(n)} - p_i^{(n)}), 0) \\
& \quad \times \frac{p_i^{(n)} - p_{i+1}^{(n)}}{\zeta_{C,i+1}^{(n)} - \zeta_{C,i}^{(n)}} \times \frac{(Y_{g,O_2})_{i+1}^{(n+1,iter+1)} - (Y_{g,O_2})_i^{(n+1,iter+1)}}{\zeta_{C,i+1}^{(n)} - \zeta_{C,i}^{(n)}} \quad (\text{A.36})
\end{aligned}$$

$$\begin{aligned}
\left(-\frac{\partial p}{\partial \zeta} \frac{\partial Y_{g,O_2}}{\partial \zeta} \right)_i^{(n)} &= H((p_{i-1}^{(n)} - p_i^{(n)}), 0) \times H((p_i^{(n)} - p_{i+1}^{(n)}), 0) \\
&\times \frac{p_{i-1}^{(n)} - p_i^{(n)}}{\zeta_{C,i}^{(n)} - \zeta_{C,i-1}^{(n)}} \times \frac{(Y_{g,O_2})_i^{(n)} - (Y_{g,O_2})_{i-1}^{(n)}}{\zeta_{C,i}^{(n)} - \zeta_{C,i-1}^{(n)}} \\
&+ H((p_i^{(n)} - p_{i-1}^{(n)}), 0) \times H((p_{i+1}^{(n)} - p_i^{(n)}), 0) \\
&\times \frac{p_i^{(n)} - p_{i+1}^{(n)}}{\zeta_{C,i+1}^{(n)} - \zeta_{C,i}^{(n)}} \times \frac{(Y_{g,O_2})_{i+1}^{(n)} - (Y_{g,O_2})_i^{(n)}}{\zeta_{C,i+1}^{(n)} - \zeta_{C,i}^{(n)}} \quad (\text{A.37})
\end{aligned}$$

After some straightforward algebraic manipulations, we finally get the following system of equations:

$$a_i (Y_{g,O_2})_{i-1}^{(n+1,iter+1)} + b_i (Y_{g,O_2})_i^{(n+1,iter+1)} + c_i (Y_{g,O_2})_{i+1}^{(n+1,iter+1)} = d_i \quad (\text{A.38})$$

where a, b , and c are one-dimensional arrays representing the coefficients of a tri-diagonal matrix, and where d is an array corresponding to the right-hand side of the linear system of oxygen mass fraction equations. In the PBR, Eq. A.38 is solved using an efficient tri-diagonal matrix algorithm (Thomas algorithm). The coefficients a, b, c and d are defined as:

$$\begin{aligned}
a_i &= -\frac{FO_L}{2} - \frac{CFL_L}{2} \\
b_i &= 1 + \frac{FO_L}{2} + \frac{FO_R}{2} + \frac{CFL_L}{2} - \frac{CFL_R}{2} + \frac{(\dot{m}_{O_2}''')_i^{(n+1,iter)} \Delta t}{(\bar{\rho}_g \bar{\psi})_i^{(n)} (Y_{g,O_2})_i^{(n+1,iter)}} \\
c_i &= -\frac{FO_R}{2} + \frac{CFL_R}{2} \\
d_i &= \left(\frac{FO_L}{2} + \frac{CFL_L}{2} \right) (Y_{g,O_2})_{i-1}^{(n)} + \left(1 - \frac{FO_L}{2} - \frac{FO_R}{2} - \frac{CFL_L}{2} + \frac{CFL_R}{2} \right) (Y_{g,O_2})_i^{(n)} \\
&+ \left(\frac{FO_R}{2} - \frac{CFL_R}{2} \right) (Y_{g,O_2})_{i+1}^{(n)} \quad (\text{A.39})
\end{aligned}$$

where FO_L and FO_R are Fourier numbers:

$$\begin{aligned}
FO_L &= \Delta t \times \left(\frac{(\bar{\psi} \bar{\rho}_g \bar{D}_g)_i + (\bar{\psi} \bar{\rho}_g \bar{D}_g)_{i-1}}{2(\bar{\psi} \bar{\rho}_g)_i} \times \frac{S_i^-}{\Delta V_i (\zeta_{C,i} - \zeta_{C,i-1})} \right)^{(n)} \\
FO_R &= \Delta t \times \left(\frac{(\bar{\psi} \bar{\rho}_g \bar{D}_g)_{i+1} + (\bar{\psi} \bar{\rho}_g \bar{D}_g)_i}{2(\bar{\psi} \bar{\rho}_g)_i} \times \frac{S_i^+}{\Delta V_i (\zeta_{C,i+1} - \zeta_{C,i})} \right)^{(n)}
\end{aligned} \quad (\text{A.40})$$

and where CFL_L and CFL_R are Courant–Friedrichs–Lewy (CFL) numbers:

$$\begin{aligned}
CFL_L &= \Delta t \times \left(\frac{1}{(\bar{\rho}_g \bar{\psi})} \frac{\bar{K}}{\nu_g} \right)_i^{(n)} \times H((p_{i-1}^{(n)} - p_i^{(n)}), 0) \times H((p_i^{(n)} - p_{i+1}^{(n)}), 0) \\
&\quad \times \frac{p_{i-1}^{(n)} - p_i^{(n)}}{(\zeta_{C,i}^{(n)} - \zeta_{C,i-1}^{(n)})^2} \\
CFL_R &= \Delta t \times \left(\frac{1}{(\bar{\rho}_g \bar{\psi})} \frac{\bar{K}}{\nu_g} \right)_i^{(n)} \times H((p_i^{(n)} - p_{i-1}^{(n)}), 0) \times H((p_{i+1}^{(n)} - p_i^{(n)}), 0) \\
&\quad \times \frac{p_i^{(n)} - p_{i+1}^{(n)}}{(\zeta_{C,i+1}^{(n)} - \zeta_{C,i}^{(n)})^2}
\end{aligned} \quad (\text{A.41})$$

The boundary condition at the center of the particle (at $\zeta = 0$) corresponds to a zero-gradient symmetry condition: $FO_L = 0$, $CFL_L = 0$. The boundary condition at the exposed surface of the particle (at $\zeta = \delta$ or R_p , see Fig. A.2), corresponds to a prescribed mass flux condition: $FO_R = 0$, $CFL_R = 0$, $b_i = b_N$ and $d_i = d_N$, where b_N and d_N are given by:

$$\begin{aligned}
b_N &= 1 + \frac{FO_L}{2} + \frac{CFL_L}{2} + \frac{(\dot{m}_{O_2}''')_N^{(n+1,iter)}}{(\bar{\rho}_g \bar{\psi})_N^{(n)} (Y_{g,O_2})_N^{(n+1,iter)}} \\
&\quad + \Delta t \left(\frac{S_N^+}{(\bar{\rho}_g \bar{\psi})_N \Delta V_N} \right)^{(n)} \left(\frac{h_{mass}}{1 + Bi} \right)^{(n)} \\
d_N &= \left(\frac{FO_L}{2} + \frac{CFL_L}{2} \right) (Y_{g,O_2})_{N-1}^{(n)} + \left(1 - \frac{FO_L}{2} - \frac{CFL_L}{2} \right) (Y_{g,O_2})_N^{(n)} \\
&\quad + \Delta t \left(\frac{S_N^+}{(\bar{\rho}_g \bar{\psi})_N \Delta V_N} \right)^{(n)} \left(\frac{h_{mass} \times Y_{g,O_2,\infty}}{1 + Bi} \right)^{(n)}
\end{aligned} \quad (\text{A.42})$$

with N the index of the computational cell that is adjacent to the exposed surface of the particle. In these expressions for b_N and d_N , the surface oxygen mass flux is

written as:

$$\dot{m}_{g \rightarrow s, O_2}'' = h_{mass}(Y_{g,O_2,\infty} - Y_{g,O_2,surf}) \quad (\text{A.43})$$

where the surface oxygen mass fraction $Y_{g,O_2,surf}$ is obtained from a condition expressing continuity of the mass flux:

$$h_{mass}(Y_{g,O_2,\infty} - Y_{g,O_2,surf}) = (\bar{\psi} \bar{\rho}_g \bar{D}_g)_N \frac{Y_{g,O_2,surf} - (Y_{g,O_2})_N}{\zeta_{R,N} - \zeta_{C,N}} \quad (\text{A.44})$$

with $\zeta_{R,N} = \delta$ or R_p . We get:

$$Y_{g,O_2,surf} = \frac{Bi \times Y_{g,O_2,\infty} + (Y_{g,O_2})_N}{1 + Bi} \quad (\text{A.45})$$

$$\dot{m}_{g \rightarrow s, O_2}'' = \frac{h_{mass}(Y_{g,O_2,\infty} - (Y_{g,O_2})_N)}{1 + Bi} \quad (\text{A.46})$$

where Bi is a Biot number,

$$Bi = \frac{h_{mass}(\zeta_{R,N} - \zeta_{C,N})}{(\bar{\psi} \bar{\rho}_g \bar{D}_g)_N} \quad (\text{A.47})$$

Equation A.38 is solved until convergence is achieved.

A.1.4 The pressure equation

In the particle burning rate model, information on pressure is required in order to calculate the mass flux given by Darcy's law. We adopt a classical finite volume formulation and re-write Eq. 2.32 as follows:

$$\frac{\partial}{\partial t} \left(\frac{M_g}{RT_p} p \bar{\psi} \Delta V \right)_i = -S_i^- f_i^- + S_i^+ f_i^+ + (\dot{m}_{sg}''')_i \Delta V_i \quad (\text{A.48})$$

where the molecular weight M_g is assumed to be known and is assumed to be constant, where using the local thermal equilibrium assumption, T_g has been replaced by T_p ,

where S_i^- and S_i^+ are the surface areas of the left and right boundaries of the computational cell ΔV_i (see Table A.1), and where f_i^- and f_i^+ represent the pressure diffusion term at these boundaries:

$$\begin{aligned} f_i^- &= \left(\frac{\bar{K}}{\nu_g} \frac{\partial p}{\partial \zeta} \right)_{\zeta=\zeta_{R,i-1}} \\ f_i^+ &= \left(\frac{\bar{K}}{\nu_g} \frac{\partial p}{\partial \zeta} \right)_{\zeta=\zeta_{R,i}} \end{aligned} \quad (\text{A.49})$$

Tests have shown that the evolution of pressure is often quasi-steady and that a balance between the diffusion and reaction terms on the right-hand side of the pressure equation is quickly established. In the following, we assume quasi-steady behavior for pressure and consider this assumption as a simplification that brings stability and robustness to the solution algorithm; we write:

$$0 = -S_i^- f_i^- + S_i^+ f_i^+ + (\dot{m}_{sg}'''_i) \Delta V_i \quad (\text{A.50})$$

Equation A.50 is integrated in time using an implicit approach that treats diffusion and chemical reaction through a first-order, backward Euler method. The quantities $(\bar{K}/\nu_g)_i$ and the mesh coordinates/geometry are frozen and treated as equal to their values at the previous time step:

$$0 = (-S_i^- f_i^- + S_i^+ f_i^+)^{(n+1,iter+1)} + (\dot{m}_{sg}'''_i)^{(n+1,iter)} (\Delta V)_i^{(n)} \quad (\text{A.51})$$

where $(S_i^- f_i^-)$ and $(S_i^+ f_i^+)$ are evaluated at $\zeta = \zeta_{R,i-1}$ and $\zeta = \zeta_{R,i}$, respectively:

$$\begin{aligned} (S_i^- f_i^-)^{(n+1,iter+1)} &= (S_i^-)^{(n)} \frac{(\frac{\bar{K}}{\nu_g})_i^{(n)} + (\frac{\bar{K}}{\nu_g})_{i-1}^{(n)}}{2} \frac{p_i^{(n+1,iter+1)} - p_{i-1}^{(n+1,iter+1)}}{\zeta_{C,i}^{(n)} - \zeta_{C,i-1}^{(n)}} \\ (S_i^+ f_i^+)^{(n+1,iter+1)} &= (S_i^+)^{(n)} \frac{(\frac{\bar{K}}{\nu_g})_{i+1}^{(n)} + (\frac{\bar{K}}{\nu_g})_i^{(n)}}{2} \frac{p_{i+1}^{(n+1,iter+1)} - p_i^{(n+1,iter+1)}}{\zeta_{C,i+1}^{(n)} - \zeta_{C,i}^{(n)}} \end{aligned} \quad (\text{A.52})$$

After some straightforward algebraic manipulations, we finally get the following system of equations:

$$a_i p_{i-1}^{(n+1,iter+1)} + b_i p_i^{(n+1,iter+1)} + c_i p_{i+1}^{(n+1,iter+1)} = d_i \quad (\text{A.53})$$

where a, b , and c are one-dimensional arrays representing the coefficients of a tri-diagonal matrix, and where d is an array corresponding to the right-hand side of the linear system of pressure equations. In the PBR, Eq. A.53 is solved using an efficient tri-diagonal matrix algorithm (Thomas algorithm). The coefficients a, b, c and d are defined as:

$$\begin{aligned} a_i &= -\left(\frac{\left(\frac{\bar{K}}{\nu_g}\right)_i + \left(\frac{\bar{K}}{\nu_g}\right)_{i-1}}{2} \times \frac{S_i^-}{\zeta_{C,i} - \zeta_{C,i-1}} \right)^{(n)} \\ c_i &= -\left(\frac{\left(\frac{\bar{K}}{\nu_g}\right)_{i+1} + \left(\frac{\bar{K}}{\nu_g}\right)_i}{2} \times \frac{S_i^+}{\zeta_{C,i+1} - \zeta_{C,i}} \right)^{(n)} \\ b_i &= -a_i - c_i \\ d_i &= (\dot{m}_{sg}''')_i^{(n+1,iter)} (\Delta V)_i^{(n)} \end{aligned} \quad (\text{A.54})$$

The boundary condition at the center of the particle (at $\zeta = 0$) corresponds to a zero-gradient symmetry condition: $a_i = 0$; $b_i = -c_i$. The boundary condition at the exposed surface of the particle (at $\zeta = \delta$ or R_p , see Fig. A.2), corresponds to a prescribed pressure condition; a_N, b_N, c_N , and d_N are given by:

$$\begin{aligned} a_N &= -\left(\frac{\left(\frac{\bar{K}}{\nu_g}\right)_N + \left(\frac{\bar{K}}{\nu_g}\right)_{N-1}}{2} \times \frac{S_N^-}{\zeta_{C,N} - \zeta_{C,N-1}} \right)^{(n)} \\ b_N &= -a_N + \left(\left(\frac{\bar{K}}{\nu_g}\right)_N \times \frac{S_N^+}{\zeta_{R,N} - \zeta_{C,N}} \right)^{(n)} \\ d_N &= \left(\left(\frac{\bar{K}}{\nu_g}\right)_N \times \frac{S_N^+}{\zeta_{R,N} - \zeta_{C,N}} \right)^{(n)} \times p_\infty + (\dot{m}_{sg}''')_N^{(n+1,iter)} (\Delta V)_N^{(n)} \end{aligned} \quad (\text{A.55})$$

with N the index of the computational cell that is adjacent to the exposed surface of the particle.

Equation A.53 is solved until convergence is achieved.

A.2 Iterative scheme

As mentioned in the previous sections, the system of governing equations is solved using an implicit and iterative method for the time integration scheme. In order to guarantee stability and convergence, the iterative method is modified with the introduction of under-relaxation terms. These modifications are briefly described below.

Let us consider a generic time-dependent differential equation:

$$\frac{\partial q}{\partial t} = \text{RHS}(q) \quad (\text{A.56})$$

where q designates $(X_k \Delta V)$ (with $k = ws, ds, c, a$), T_p or Y_{g,O_2} (note that the under-relaxation treatment is not applied to the pressure equation because p is assumed to be quasi-steady).

Without under-relaxation, the discretization of the q -equation is:

$$\frac{q^{(n+1,iter+1)} - q^{(n)}}{\Delta t} = \text{RHS}(q^{(n+1,iter)}) \quad (\text{A.57})$$

With under-relaxation, the discretization of the q -equation is modified as follows:

$$\frac{q^{(n+1,iter+1)} - q^{(n)}}{\Delta t} = \text{RHS}(q^{(n+1,iter)}) + k(q^{(n+1,iter)} - q^{(n+1,iter+1)}) \quad (\text{A.58})$$

where k is a relaxation coefficient (with units of one over time). In the model, we use non-dimensional relaxation factors: $\lambda_q = (k\Delta t)$. Large values of λ_q correspond to strong under-relaxation conditions that promote stability but slow down convergence. In contrast, small values of λ_q correspond to weak under-relaxation conditions that may not guarantee stability but accelerate convergence. Baseline values of these factors that have been determined to provide accurate solutions are $\lambda_{X_k \Delta V} = 0$, $\lambda_{T_p} = 0.1$ and $\lambda_{Y_{g,O_2}} = 0.1$.

In the treatment of the equations for temperature and gaseous oxygen mass fraction (for which $\lambda_q \neq 0$), convergence is achieved in the iterative loop when the extra relaxation terms, that have been artificially introduced in the governing equations, have become negligible, i.e., when $\lambda_q \times |q^{(n+1,iter+1)} - q^{(n+1,iter)}| \ll |q^{(n+1,iter+1)} - q^{(n)}|$. We typically require $\lambda_q \times |q^{(n+1,iter+1)} - q^{(n+1,iter)}| < 0.01 \times |q^{(n+1,iter+1)} - q^{(n)}|$.

In the treatment of the equations for species mass and pressure (for which $\lambda_q = 0$), convergence is achieved in the iterative loop when changes in successive estimated values of $q^{(n+1)}$ have become negligible, i.e., when $|q^{(n+1,iter+1)} - q^{(n+1,iter)}| \ll 1$. We typically require $|q^{(n+1,iter+1)} - q^{(n+1,iter)}| < 0.01 \times \Delta q$, where Δq is a user-defined value for the maximum allowed variation in q during a single time step (see Section A.3 below).

A.3 Temporal discretization

The increment Δt used to advance the solution in time is chosen at the initial time based on estimates of the characteristic time scales of the problem. It

is then updated automatically based on criteria that require that the maximum variation in the values of temperature, solid-phase mole fractions, gas-phase oxygen mole fraction, and pressure during a single time step be less than user-defined thresholds, $\Delta T_{threshold}$, $\Delta X_{s,threshold}$, $\Delta Y_{g,O2,threshold}$ and $\Delta p_{threshold}$. Baseline values of these thresholds that have been determined to provide accurate solutions are $\Delta T_{threshold} = 0.1$ K, $\Delta X_{s,threshold} = 0.01$, $\Delta Y_{g,O2,threshold} = 0.01$ and $\Delta p_{threshold} = 0.1$ Pa. These values can be optimized through numerical tests.

Note that in the coupled fire spread simulation, the local time-step of a given particle should not exceed the time-step of the gas-phase which is controlled by the CFL number. Also, each individual particle in a fuel bed may have a different time-step depending on its state and the criterion described above (see Fig. A.3).

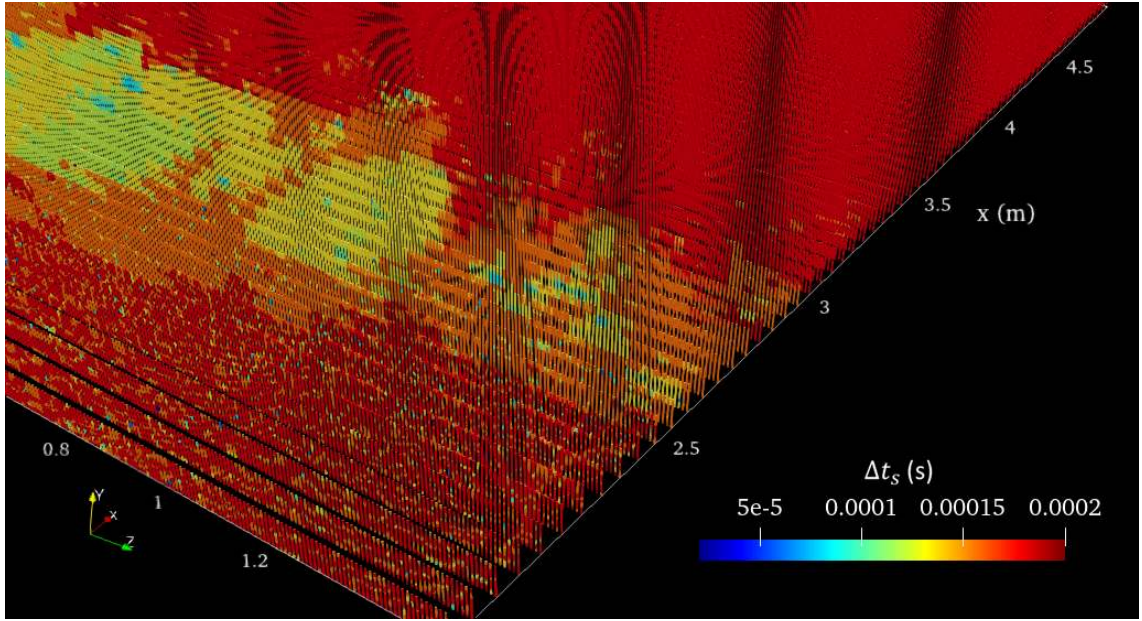


Figure A.3: 3D rendering of a fuel bed with discrete fuel particles colored by their corresponding time-step during fire spread.

A.4 Deforming mesh and re-meshing capabilities

The number of computational cells is determined at the initial time by setting a uniform grid spacing $\Delta\zeta_i^{(0)}$ (*e.g.*, $\approx 100 \mu\text{m}$). In general, the volume of particles changes due to reactions (*Rd*)-(*Rco*), and in special cases, the particle completely vaporizes and its size, δ or R_p , decreases to 0. There is a need to dynamically optimize the number of computational cells in order to save computational time and avoid difficulties associated with cells of vanishing size.

In response to this need, the PBR features a re-meshing capability. The different steps of the re-meshing algorithm are described below:

1. Update the number of computational cells $N^{(n)}$ using the new evaluation of the particle size (based on calculated cell volumes) with the objective to use a uniform grid spacing $\Delta X_i^{(n)}$ or $\Delta r_i^{(n)} \approx \Delta\zeta_i^{(0)}$. The algorithm also enforces a minimum of 5 computational cells.
2. Generate the new computational grid (*i.e.*, update the parameters of Table A.1 and get $\zeta_{R, i}^{(n+1)}$, $\zeta_{C, i}^{(n+1)}$, $S_i^{+(n+1)}$ and $S_i^{-(n+1)}$).
3. Interpolate the solution on the new computational grid. The particle burning rate model offers a choice between two methods. First, a simple linear interpolation method:

$$q_i^{(n+1)} = q_j^{(n+1)} + (q_{j+1}^{(n+1)} - q_j^{(n+1)}) \times \frac{\zeta_{C, i}^{(n+1)} - \zeta_{C, j}^{(n)}}{\zeta_{C, j+1}^{(n)} - \zeta_{C, j}^{(n)}}, \quad \zeta_{C, j}^{(n)} \leq \zeta_{C, i}^{(n+1)} \leq \zeta_{C, j+1}^{(n)}$$

where i and j are the indices of the coordinates of the new and old cell centers, respectively. And second, a more elaborate method. This second

method is based on a conjugate gradient algorithm that minimizes a cost function featuring the ζ -integral of the solution, and that thereby guarantees conservation of species mass and heat during the interpolation step.

Appendix B: Modified Eddy Dissipation Model for Diffusion Controlled Flames

This appendix presents our modified version of the Eddy Dissipation Model (EDM) that provides an accurate calculation of the heat release rate of under-resolved and well-resolved diffusion-controlled flames.

B.1 Model derivation

The classical EDM writes the heat release rate due to the combustion of a given fuel as follows [46]

$$\text{HRR} = \frac{\rho}{\tau_{EDM}} \times \min \left(Y_F, \frac{Y_{O_2}}{r_s} \right) \times \Delta H_c \quad (\text{B.1})$$

where ρ is the mass density, Y_F and Y_{O_2} is the mass fractions of fuel and oxygen, r_s the stoichiometric oxygen-to-fuel mass ratio, and where ΔH_c the heat of combustion.

We model the characteristic time-scale of the combustion process as the minimum between the diffusion and turbulent times

$$\tau_{EDM} = \min (\tau_{Turb}, \tau_{Diff}) \quad (\text{B.2})$$

with τ_{Turb} and τ_{Diff} being the characteristic time-scales of turbulent mixing and laminar diffusion, respectively.

We write the diffusion time-scale τ_{Diff} (s) as proportional to the mass diffusivity D (m^2/s) and the LES filter size Δ_{LES} (m):

$$\frac{1}{\tau_{Diff}} = C_{Diff} \times \frac{D}{\Delta_{LES}^2} \quad (\text{B.3})$$

We first develop a mathematical equation for the parameter C_{Diff} . Consider the simulation of a laminar counter-flow diffusion flame, the EDM gives the heat release rate per unit surface area of the flame (in units of $kg/s/m^2$) as

$$\text{HRRPUA} = \int_x \rho \min \left(Y_F, \frac{Y_{O_2}}{r_s} \right) \left(\frac{C_{Diff} D}{\Delta_{LES}^2} \right) \Delta H_c dx \quad (\text{B.4})$$

According to classical laminar diffusion flame theory, the fuel mass consumption rate may be expressed as the rate of fuel mass supply by molecular diffusion from the outer diffusive layer located on the fuel-side of the flame into the inner reactive sublayer [113, 114]. We require that the simulated value of HRRPUA is equal to the theoretical value given by laminar diffusion flame theory:

$$\text{HRRPUA}_{theory} = \rho_0 \sqrt{\frac{D_0}{2}} (Y_{F,1} + \frac{Y_{O_2,2}}{r_s}) \sqrt{\chi_{st}} \times \Delta H_c \quad (\text{B.5})$$

where ρ_0 and D_0 the values of the mass density and diffusivity in ambient air, respectively, where $Y_{F,1}$ and $Y_{O_2,2}$ are the values of the mass fractions of fuel and oxygen in the fuel and oxidizer supply streams, respectively, and where χ_{st} is the stoichiometric value of the scalar dissipation rate, $\chi = 2D |\nabla Z|^2$ with Z the mixture fraction, $Z = (Y_F - \frac{Y_{O_2}}{r_s} + \frac{Y_{O_2,2}}{r_s}) / (Y_{F,1} + \frac{Y_{O_2,2}}{r_s})$.

This leads to the following equation for C_{Diff} :

$$C_{Diff} = \frac{\rho_0 \sqrt{\frac{D_0}{2}} (Y_{F,1} + \frac{Y_{O_2,2}}{r_s}) \sqrt{\chi_{st}} \Delta_{LES}^2}{\int_x (\rho D) \min \left(Y_F, \frac{Y_{O_2}}{r_s} \right) dx} \quad (\text{B.6})$$

Next, we consider the case of well-resolved flames, $\Delta_{\text{LES}} \ll \delta_{\text{flame}}$, where δ_{flame} is the flame thickness. Under those conditions, the overlap region between fuel and oxygen (i.e., the region where the expression $\min\left(Y_F, \frac{Y_{O_2}}{r_s}\right)$ is not zero) is a small region located close Z_{st} and one can write:

$$\int_x (\rho D) \min\left(Y_F, \frac{Y_{O_2}}{r_s}\right) dx \approx \int_x (\rho D) \min\left(Y_F, \frac{Y_{O_2}}{r_s}\right) \frac{dZ}{\sqrt{\chi_{st}/2D}} \quad (\text{B.7})$$

This expression is independent of Δ_{LES} and can be estimated to scale like $1/\sqrt{\chi_{st}}$ (this is an approximation). This suggests that $C_{\text{Diff}} \sim \chi_{st} \Delta^2$.

Now we turn to the case of strongly under-resolved flames, $\delta_{\text{flame}} \ll \Delta_{\text{LES}}$. Under those conditions, because of numerical diffusion, the flame has a thickness $\delta_{\text{flame}} = (C_\Delta \Delta_{\text{LES}})$ with $C_\Delta = O(1)$. The profiles of Z , Y_F , and Y_{O_2} are approximately linear across the flame. We can approximate these profiles as follows:

$$Z(x) = \begin{cases} 0 & \text{for } x < x_0 \\ \frac{1}{(C_\Delta \Delta_{\text{LES}})}(x - x_0) & \text{for } x_0 \leq x \leq x_0 + (C_\Delta \Delta_{\text{LES}}) \\ 1 & \text{for } x_0 + (C_\Delta \Delta_{\text{LES}}) < x \end{cases} \quad (\text{B.8})$$

and

$$Y_F(Z) = Y_{F,1}Z \quad (\text{B.9})$$

$$Y_{O_2}(Z) = Y_{O_2,2}(1 - Z) \quad (\text{B.10})$$

Also, since the peak flame temperature is low in strongly under-resolved flames, we can assume that $T \sim T_0$.

Then we can write:

$$\begin{aligned}
\int_x (\rho D) \min \left(Y_F, \frac{Y_{O_2}}{r_s} \right) dx &\approx \rho_0 D_0 \int_0^1 \min \left(Y_F, \frac{Y_{O_2}}{r_s} \right) (C_\Delta \Delta_{\text{LES}}) dZ \\
&\approx \rho_0 D_0 (C_\Delta \Delta_{\text{LES}}) \times \left(\int_0^{Z_{st}} Y_{F,1} Z dZ + \int_{Z_{st}}^1 \frac{Y_{O_2,2}}{r_s} (1 - Z) dZ \right) \\
&\approx \rho_0 D_0 (C_\Delta \Delta_{\text{LES}}) \times \left(Y_{F,1} \frac{(Z_{st})^2}{2} + \frac{Y_{O_2,2}}{r_s} \left(\frac{1}{2} - Z_{st} + \frac{(Z_{st})^2}{2} \right) \right) \\
&= \frac{\rho_0 D_0 (C_\Delta \Delta_{\text{LES}})}{2} \frac{Y_{F,1} Y_{O_2,2}}{(r_s Y_{F,1} + Y_{O_2,2})} \quad (\text{B.11})
\end{aligned}$$

This leads to:

$$C_{\text{Diff}} = \frac{\rho_0 \sqrt{\frac{D_0}{2}} (Y_{F,1} + \frac{Y_{O_2,2}}{r_s}) \sqrt{\chi_{st}} \Delta_{\text{LES}}^2}{\frac{\rho_0 D_0 (C_\Delta \Delta_{\text{LES}})}{2} \frac{Y_{F,1} Y_{O_2,2}}{(r_s Y_{F,1} + Y_{O_2,2})}} \quad (\text{B.12})$$

which gives the final expression of the model parameter C_{Diff}

$$C_{\text{Diff}} = \frac{2}{C_\Delta \sqrt{2 D_0}} \times \frac{(r_s Y_{F,1} + Y_{O_2,2})^2}{r_s Y_{F,1} Y_{O_2,2}} \times \sqrt{\chi_{st}} \Delta_{\text{LES}} \quad (\text{B.13})$$

This expression suggests that $C_{\text{Diff}} \sim \sqrt{\chi_{st}} \Delta_{\text{LES}}$, and thereby suggests that C_{Diff} depends not only on the spatial resolution through δ_{LES} but also depends on local fuel-air mixing conditions through χ_{st} .

Note that for well-resolved flames, the value of χ_{st} can be evaluated from the gradient of the mixture fraction field. However, for under-resolved flames, this value can not be deduced from the computational field, and the application of equation B.13 requires additional modeling efforts. Since fire flames have moderate strains, one may use a representative value of $\chi_{st,\text{ref}} \approx 1 \text{ s}^{-1}$ in Eq. B.13. We show in the following the implications of using Eq. B.13 in different flames with known $\chi_{st,\text{ref}}$, and of using Eq. B.13 with a representative value of $\chi_{st,\text{ref}} \approx 1 \text{ s}^{-1}$.

B.2 Simulations of two-dimensional laminar counter-flow methane-air flames

In this section, we present two-dimensional simulations of laminar counter-flow methane/air diffusion flames under different mixing conditions associated with different values of χ_{st} . We first conducted well-resolved simulations (with a grid resolution of $0.5 \mu\text{m}$) using the single-step Arrhenius chemistry model provided by Westbrook and Dryer [115] where we varied the distance between the fuel and oxidizer nozzles and/or the injection velocity of both fuel and oxidizer to obtain different numerical configurations corresponding to different values of χ_{st} . We consider these cases as our benchmark for model validation.

Figure B.1 shows the variation of the heat release rate per unit surface area of the counter-flow diffusion flames at different mixing conditions represented by a range of χ_{st} between 0.07 and 21. The figure shows under-resolved simulations conducted using the proposed modification of the EDM represented by Eqs. B.2 and B.13. These simulations are labeled (EDM). We also present under-resolved simulations performed using EDM with optimized values of C_{Diff} that provide values of HRRPUA equal to those from the single-step Arrhenius chemistry. These simulations are labeled (True C_{Diff}) in Fig. B.1. We include additional simulations with a constant value of $C_{Diff} = 2.5$ for comparison.

The results of Fig. B.1 show that the HRRPUA predicted using the proposed model in under-resolved configurations is in excellent agreement with that of the

well-resolved single-step Arrhenius model. The maximum difference between the two is less than 20%. On the other hand, using a constant value of $C_{Diff} = 2.5$ leads to underpredicting the HRRPUA by an order of magnitude.

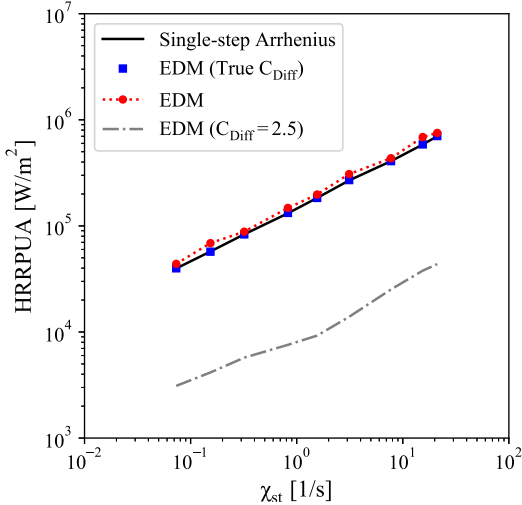


Figure B.1: Predictions of the heat release rate per unit surface area of counter-flow methane/air diffusion flames under different mixing conditions.

The profiles of mixture fraction and temperature in the under-resolved simulations are shown in Fig. B.2. In these cases, there are only 4 grid cells between the fuel and oxidizer nozzles, and the size of the grid cell depends on the distance between the fuel and oxidizer nozzles.

Figure B.3 shows the scatter of the predicted HRRPUA using EDM with a representative value of $\chi_{st} = 1 \text{ s}^{-1}$ in Eq. B.13. These points correspond to configurations at different mixing conditions that are resolved with $\Delta_{LES} = 0.25 \text{ cm}$ to 5 cm . The results show that the scatter is well aligned with the benchmark simulations with single-step Arrhenius chemistry. There is some deviation at very low values and very high values of χ_{st} attributed to the effect of the approximation

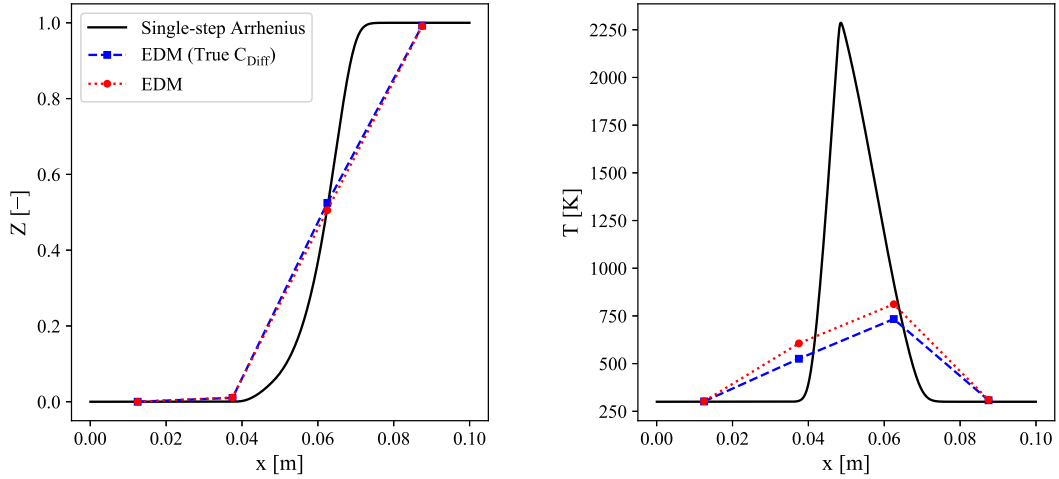


Figure B.2: Profiles of mixture fraction (left) and temperature (right) at the centerline distance between the fuel and oxidizer nozzles for an under-resolved flame using EDM and a well-resolved flame using single-step Arrhenius chemistry.

of using $\chi_{st} = 1 \text{ s}^{-1}$ in Eq. B.13 instead of the actual value at these points. The maximum deviation in the HRRPUA at these extreme points is about 60% which is deemed acceptable.

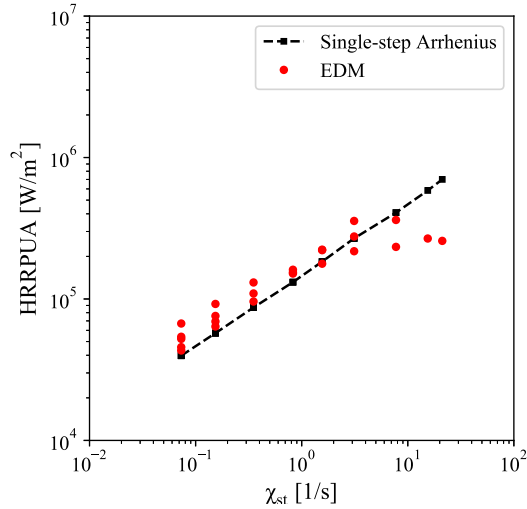


Figure B.3: Scatter of the estimated values of the HRRPUA using a representative value of $\chi_{st} = 1 \text{ s}^{-1}$ in Eq. B.13 .

Appendix C: Extension of the LSP Soot Model to LES Framework

This appendix summarizes our early work describing the formation and oxidation of soot in the LES framework using the Laminar Smoke Pint (LSP) soot model proposed by Yao et al. [47].

C.1 Conservation of soot mass

In the LES formulation, we write the Favre filtered transport equation of soot per unit volume of the multiphase fuel bed, ignoring thermophoresis and laminar diffusion, as

$$\begin{aligned} \frac{\partial}{\partial t} \left(\bar{\rho}(1 - \beta_s) \tilde{Y}_{soot} \right) + \frac{\partial}{\partial x_j} \left(\bar{\rho}(1 - \beta_s) \tilde{u}_j \tilde{Y}_{soot} \right) \\ = \frac{\partial}{\partial x_j} \left(D_{Turb} \frac{\partial \tilde{Y}_{soot}}{\partial x_j} \right) + \overline{\dot{\omega}_{sf}''' - \dot{\omega}_{so}'''} \end{aligned} \quad (\text{C.1})$$

where \tilde{Y}_{soot} is the soot mass fraction ($Y_{soot} \equiv m_{soot}/(m_g + m_{soot})$), and $\overline{\dot{\omega}_{sf}'''}$ and $\overline{\dot{\omega}_{so}'''}$ are the filtered soot formation and oxidation rates, respectively.

The volume fraction of soot is calculated from

$$\tilde{f}_v = \frac{\bar{\rho} \tilde{Y}_{soot}}{\rho_{soot}} \quad (\text{C.2})$$

where ρ_{soot} is the density of soot ($\sim 1800 \text{ kg/m}^3$).

Note that when soot modeling is active, additional terms related to $\overline{\dot{\omega}_{sf}'''}$ and $\overline{\dot{\omega}_{so}'''}$ are added to the governing equations of the gas-phase in order to account for the exchange of mass and energy between gaseous species and soot [116].

C.2 Soot formation and oxidation terms

The volumetric rates of soot formation and oxidation are given by Yao et al. [47] in units of ($kg/m^3 s$) as

$$\dot{\omega}_{sf}''' = \begin{cases} A_f \rho^2 \left(Y_{F,0} \frac{Z - Z_{st}}{1 - Z_{st}} \right) T^\gamma \exp(-T_a/T) & \text{if } Z_{so} \leq Z \leq Z_{sf} \\ 0 & \text{otherwise} \end{cases} \quad (\text{C.3})$$

$$\dot{\omega}_{so}''' = Y_{soot} \times \begin{cases} A_{soot} \rho^2 \left(A_{so} \frac{Y_{O_2}}{M_{O_2}} T^{1/2} \right) \exp(-E_{a,so}/RT) & \text{if } 0 \leq Z \leq Z_{sf} \\ 0 & \text{otherwise} \end{cases} \quad (\text{C.4})$$

where $T_a = 2000$ K, $\gamma = 2.25$, and $A_{soot} = 160,000$ m^2/kg , $A_{so} = 120$ and $E_{a,so} = 163,540$ J/mol.

The formation rate pre-exponential factor A_f is a fuel-dependent coefficient that is inversely proportional to the laminar smoke point height of the fuel $l_{sp, fuel}$ such that

$$\frac{A_{fuel}}{A_{C_2H_4}} = \frac{l_{sp, C_2H_4}}{l_{sp, fuel}} \quad (\text{C.5})$$

The soot inception mixture fraction limits Z_{so} and Z_{sf} are fuel dependent, and are estimated as

$$Z_{sf} = 2.5 Z_{st}, \quad Z_{so} = 1.25 Z_{st} \quad (\text{C.6})$$

C.3 Closure model for turbulent soot formation and oxidation rates

We assume that the subgrid-scale fluctuations of a given source term $\dot{\omega}'''(\eta)$ that is dependent on one scalar η can be described by a probability density function of the fluctuations of η , and the filtered source term can be expressed in LES framework as

$$\overline{\omega'''} = \bar{\rho} \int_0^1 \frac{\dot{\omega}'''(\eta)}{\rho(\eta)} \tilde{P}(\eta) d\eta \quad (\text{C.7})$$

where \tilde{P} is a presumed probability density function (PDF). In this work, we use a $\beta - \text{PDF}$ that can be deduced from the scalar $\tilde{\eta}$ and its subgrid-scale variance $\tilde{\eta}''^2$.

From the description of the soot formation and oxidation terms given in Eqs. C.3 and C.4, we see that the quantities $\dot{\omega}_{so}'''$ and $\dot{\omega}_{so}'''/Y_{soot}$ are expressed in terms of 4 variables: ρ , Z , T and Y_{O2} . Thus, we would need 4 joint PDFs to evaluate the filtered source terms which is not feasible.

In order to simplify the PDF integral, we assume that ρ and Y_{O2} can be written in terms of two independent variables, the mixture fraction Z and the temperature T , hence the soot formation and oxidation rates become dependent on only two variables Z and T . We write

$$\rho = \rho_\infty \left(\frac{M}{M_\infty} \right) \left(\frac{T_\infty}{T} \right) \quad (\text{C.8})$$

where M_∞ is the molecular weight of the oxidizer stream and $M = 1/\left(\frac{1-Z}{M_{oxidizer}} + \frac{Z}{M_{fuel}}\right)$, and where M_{fuel} is the molecular weight of the fuel. We also write

$$Y_{O2} = \begin{cases} Y_{O2,\infty} \times (1 - Z/Z_{st}) & , 0 \leq Z \leq C_Z Z_{st} \\ A \exp(-Z/B) & , Z > C_Z Z_{st} \end{cases} \quad (\text{C.9})$$

where $Y_{O_2,\infty}$ is the oxygen mass fraction in the oxidizer stream, $B = Z_{st}(1 - C_Z)$, $A = Y_{O_2,oxidizer}(1 - Z_0/Z_{st}) \exp(Z_0/B)$, Z_{st} the stoichiometric mixture fraction, and where C_Z is a model coefficient introduced to account for oxygen diffusion into the fuel-rich zone ($C_Z \approx 0.9$).

Now let us introduce a normalized temperature $\Theta = (T - T_\infty)/(T_{ad} - T_\infty)$, where T_∞ is the temperature of the oxidizer stream (i.e., the ambient) and T_{ad} is the adiabatic flame temperature of the stoichiometric mixture. Then we can write the filtered source terms as

$$\begin{aligned}\overline{\dot{\omega}_{sf}''''} &= \bar{\rho} \int_0^1 \int_0^1 \frac{\dot{\omega}_{sf}'''(Z, \Theta)}{\rho(Z, \Theta)} \tilde{P}(Z) \tilde{P}(\Theta) dZ d\Theta \\ \overline{\dot{\omega}_{so}''''} &= \bar{\rho} \int_0^1 \int_0^1 \frac{\dot{\omega}_{so}'''(Z, \Theta)}{\rho(Z, \Theta)} \tilde{P}(Z) \tilde{P}(\Theta) dZ d\Theta\end{aligned}\quad (\text{C.10})$$

As mentioned earlier, we use a presumed β -PDF approach that requires a knowledge of the subgrid-scale variance of the independent variables. Thus, we solve an additional transport equation for the variance of mixture fraction $\widetilde{Z''^2}$

$$\begin{aligned}\frac{\partial}{\partial t} \left(\bar{\rho} \widetilde{Z''^2} \right) + \frac{\partial}{\partial x_j} \left(\bar{\rho} \widetilde{u}_j \widetilde{Z''^2} \right) &= \frac{\partial}{\partial x_j} \left(\bar{\rho} (D + D_{Turb}) \frac{\partial \widetilde{Z''^2}}{\partial x_j} \right) \\ &\quad + 2 \bar{\rho} D_{Turb} \frac{\partial \widetilde{Z}}{\partial x_j} \frac{\partial \widetilde{Z}}{\partial x_j} - 2 \bar{\rho} \frac{\widetilde{Z''^2}}{\tau_{Turb}}\end{aligned}\quad (\text{C.11})$$

To get the subgrid-scale variance of the temperature, we assume a direct proportionality between the grid-resolved variance of mixture fraction and temperature and their subgrid-scale quantities such that

$$\frac{\sqrt{\Theta''^2}}{\widetilde{\Theta}} = C_\Theta \frac{\sqrt{Z''^2}}{\widetilde{Z}}\quad (\text{C.12})$$

where C_Θ is the proportionality factor (determined from LES to be $C_\Theta = 0.4$).

C.4 Integration of the probability density function

We calculate the integral $\int_0^1 F(Z) \tilde{P}(Z) dZ$ as

$$\begin{aligned} \int_0^1 F(Z) \tilde{P}(Z) dZ &= \int_0^1 F(Z) \frac{Z^{a-1} (1-Z)^{b-1}}{\int_0^1 Z^{a-1} (1-Z)^{b-1} dZ} dZ \\ &= \frac{\int_0^1 F(Z) Z^{a-1} (1-Z)^{b-1} dZ}{\int_0^1 Z^{a-1} (1-Z)^{b-1} dZ} \end{aligned} \quad (\text{C.13})$$

where

$$\begin{aligned} a &= \tilde{Z} \left[\frac{\tilde{Z}(1-\tilde{Z})}{\widetilde{Z''^2}} - 1 \right] \\ b &= (1-\tilde{Z}) \left[\frac{\tilde{Z}(1-\tilde{Z})}{\widetilde{Z''^2}} - 1 \right] \end{aligned} \quad (\text{C.14})$$

Finally, we adopt the algorithm proposed by Liu et al. [117], and we calculate the integral $\int_0^1 F(Z) \tilde{P}(Z) dZ$ in a pre-processing mode. We save it a lookup table that has two dimensions: \tilde{Z} and $\widetilde{Z''^2}$. We also generate a two-dimensional lookup table for the integral $\int_0^1 F(\Theta) \tilde{P}(\Theta) d\Theta$ that is dependent on $\tilde{\Theta}$ and $\widetilde{\Theta''^2}$.

Appendix D: Verification of the WSGG Model Implementation in OpenFOAM

We present in this section the verification of the WSGG approach for modeling radiation absorption and emission. As described in section 2.8.2, we split the MRTE (Eq. 2.87) into a finite number of spectral bands and we use either the polynomial fits of Bordbar et al. [74] (referred to as WSGG-Bordbar) or Cassol et al. [49] (referred to as WSGG-Cassol) to obtain the values of the absorption and weighting coefficients, κ_j and a_j , of the participating medium in each band. The model of Ref [74] that we implement here was originally designed for participating mixtures of H_2O/CO_2 at a wide range of molar ratios, while the model of Ref. [49] considered here was originally designed for participating mixtures of soot and H_2O/CO_2 at a molar ratio of 2.

In order to verify the implementation of these models in OpenFOAM, we consider a series of benchmark cases of radiation absorption and emission in a one-dimensional enclosure. The one-dimensional enclosure extends to a length $L = 1\text{ m}$ and contains a gaseous mixture of H_2O , CO_2 , N_2 , and soot. The enclosure is set at standard atmospheric pressure. The temperature and the volume fraction of the gases inside the enclosure are varied along the axial direction (i.e., x direction) to

obtain different radiation configurations. The left and right walls of the enclosure at $x = 0$ and $x = L$, respectively, are treated as black bodies at 400 K . We compare our numerical simulations conducted using the two implemented WSGG models to the Line-By-Line (LBL) solution that accounts for the spectral variation of the radiation properties of each gaseous species at all possible radiation wavelengths [49].

D.0.1 Radiation configuration 1

The first configuration has a sinusoidal distribution of temperature with $T(x) = 400 + 1400 \sin^2(2\pi x/L) K$, and a uniform distribution of gaseous species with volume fractions with $X_{H_2O} = 0.2$, $X_{CO_2} = 0.1$ and $X_{N_2} = 0.3$. No soot is considered in this case ($f_v = 0$). Note that this configuration considers a molar ratio of H_2O/CO_2 equals 2.

With the above conditions, the temperature of the mixture increases from 400 K near the walls to a maximum temperature of 1800 K at $x/L = 0.25$ and 0.75, and it then falls to 400 K at the center of the enclosure. Figure D.1 shows the simulated and the LBL solution of the axial distribution of the radiant power inside the enclosure. It can be seen that at the edges and the center of the enclosure, the radiant power is positive indicating a radiation absorption from the hot regions. The radiant power at $x/L = 0.25$ and 0.75 shows negative peaks at locations corresponding to the maximum temperature of the mixture. At such locations, the mixture is losing heat to the walls and the other cold regions in the enclosure. The results suggest that the two WSGG models are able to correctly predict the radiant power distribution and

are in very good agreement with the LBL solution.

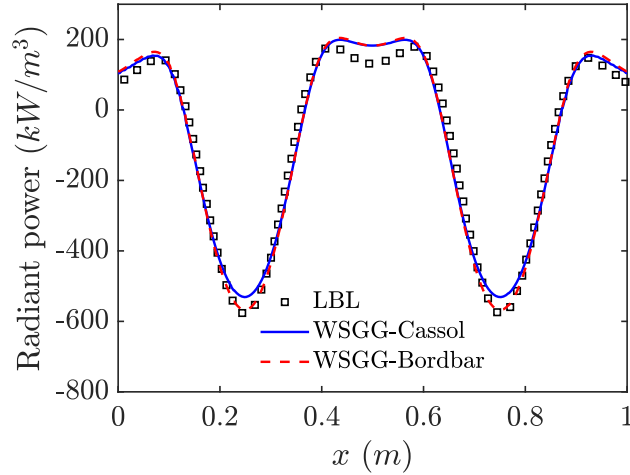


Figure D.1: Comparison between the numerical simulations (lines) and the LBL solution (symbols) of radiation configuration 1.

D.0.2 Radiation configuration 2

We now consider a second configuration in which the axial distribution of both temperature and gaseous species are non-uniform and following these distributions: $T(x) = 400 + 1400 \sin^2(\pi x/L)$, $X_{H_2O} = 0.2 \sin^2(2\pi x/L)$, $X_{CO_2} = 0.1 \cos^2(2\pi x/L)$, $X_{N_2} = 0.7$. This configuration shows a non-constant value of the molar ratio of H_2O/CO_2 that varies between 0 and infinity. Again, no soot is considered here ($f_v = 0$).

The axial distributions of the radiant power of this case obtained from our numerical simulations and the LBL solution are presented in Fig. D.2. The results of the two WSGG models show a satisfactory agreement with the LBL solution at different locations inside the enclosure. There is, however, a large deviation in the

results of Cassol's model near the center of the enclosure where the molar ratio of H_2O to CO_2 approaches zero. The simulation results overpredict the radiation power in this region owing to the fact that Cassol's model was designed based on a molar ratio of H_2O and CO_2 equals 2.

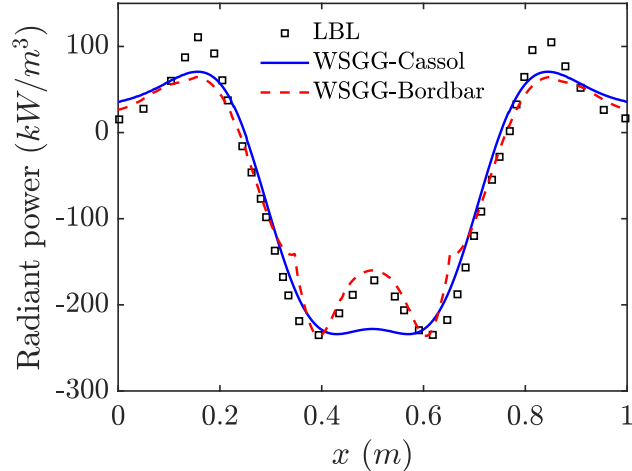


Figure D.2: Comparison between the numerical simulations (lines) and the LBL solution (symbols) of radiation configuration 2.

D.0.3 Radiation configuration 3

In the third configuration, we include soot to study its effect on the radiant power inside the enclosure. We consider here a uniform distribution of soot at $f_v(x) = 10^{-6}$. The distributions of temperature and volume fractions of CO_2 , H_2O , and N_2 are similar to those in radiation configuration 1. Figure D.3 presents a comparison between numerical simulations conducted using the two WSGG models and the LBL solution. The radiation power distribution obtained from the LBL solution indicates a significant increase in the high-temperature region (i.e., $x = 0.25$

and 0.75 m) compared to configuration 1 in response to the presence of soot. The peak radiant power increased from $\sim 600\text{ kW}/\text{m}^3$ in configuration 1 to $\sim 3000\text{ kW}/\text{m}^3$ in this configuration. This result suggests that radiation is dominated by soot. The simulation result obtained using Bordbar's model, which does not account for soot radiation, underestimates the peak radiant power by factor 5. On the other hand, the simulation result obtained using Cassol's model, which accounts for soot radiation, shows an acceptable agreement with the LBL solution. Note that the version of Cassol's model implemented here represents soot by only two gray gases. As pointed out in Ref. [49], a better agreement with the LBL solution can be achieved if soot is modeled by more gray gases.

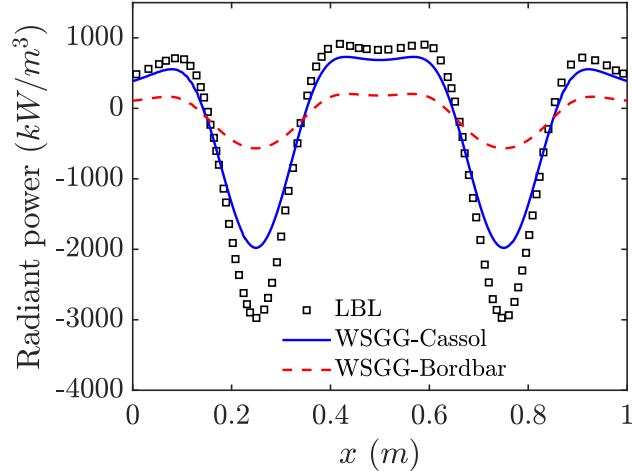


Figure D.3: Comparison between the numerical simulations (lines) and the LBL solution (symbols) of radiation configuration 3.

D.0.4 Radiation configuration 4

This final configuration corresponds to a more realistic case in which soot exists in a narrow region inside a flame. The radiation in this case is not dominated by soot in the entire flame region. We assume here a uniform distribution of temperature at $T(x) = 1100\text{ K}$. The distributions of H_2O and CO_2 are: $X_{H_2O}(x) = 0.2 \sin^2(2\pi x/L)$ and $X_{CO_2}(x) = 0.1 \sin^2(2\pi x/L)$. Under these conditions, the concentrations of H_2O and CO_2 are zero near the walls and the center of the enclosure, and are maximum near $x = 0.25$ and 0.75 m . We also consider soot to exist only between $x = 0.25$ and 0.75 m such that $f_v(x) = 10^{-6} \sin^2(2\pi(x - 0.25)/L)$ in that region, and $f_v = 0$ otherwise.

Figure D.4 presents the radiant power distribution obtained from numerical simulations conducted using Cassol's model and the LBL results. The plots show that the radiant power is negative along the entire enclosure indicating that the mixture is losing radiation to the cold walls. The radiant power shows a first peak near $x = 0.25$ and 0.75 m where the concentrations of H_2O and CO_2 are maximum. The radiant power then slightly decrease followed by a second peak at the center of the enclosure where the concentrations of H_2O and CO_2 are zero and the concentration of soot is maximum. The peak value of the radiant power obtained from the LBL solution at this region is about two times higher than at regions where the concentrations of H_2O and CO_2 are maximum.

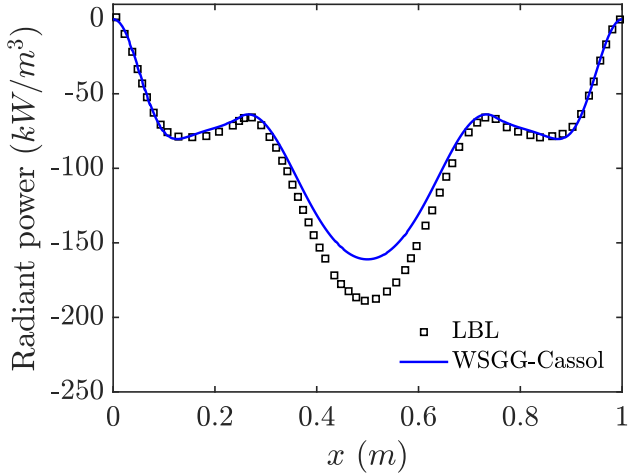


Figure D.4: Comparison between the numerical simulations (lines) and the LBL solution (symbols) of radiation configuration 4.

As shown in Fig. D.4, the simulation results obtained using the WSGG-Cassol model are in very good agreement with the LBL solution outside the soot region and are in acceptable agreement inside the soot region. The peak radiant power estimated by the WSGG model is $\sim 14\%$ lower than that estimated by the LBL solution. These error levels are similar to those obtained by Ref. [49] which suggests that the implementation of the WSGG model is free from coding errors.

Appendix E: Installation of PBRFoam on HPC Clusters and its Parallel Performance

E.1 Installation

The solver PBRFoam is uploaded on this GitHub repository:

<https://github.com/mmahmed15/PBRFoam>

This repository is private but access is granted upon request. The solver is built on OpenFOAM version 4.x build number: dev-8dafde6048ab, which we used for previous development in our group. The source files are saved in this repository:

https://github.com/mmahmed15/OpenFOAM_UMD.

Below are the steps to compile PBRFoam and OpenFoam version 4.x on the UMD cluster Zaratan [118] or Expanse cluster [119] located at the San Diego Supercomputer Center (SDSC) and supported by the NSF ACCESS program [120].

- Load the following modules

For Zaratan HPC cluster use:

```
1 module load gcc/8.4.0
2 module load openmpi/3.1.5
```

For Expanse HPC cluster use:

```
1 module load gcc/10.2.0
2 module load openmpi/4.0.4
```

- Download the source files in the home directory

```
1 cd ~
2 git clone https://github.com/mmahmed15/OpenFOAM_UMD.git
```

- Navigate to the compile directory and unzip the source files For Zaratan HPC cluster use:

```
1 cd OpenFOAM_UMD
2 unzip ThirdParty-dev.zip
3 unzip OpenFOAM-dev.zip
```

- add the following line to the end of the (\sim /.bashrc) file

```
1 source ~/OpenFOAM_UMD/OpenFOAM-dev/etc/bashrc
```

- then run the following command in the terminal

```
1 source ~/.bashrc
```

- Compile the third-party library

```
1 cd ~/OpenFOAM/ThirdParty-dev
2 ./Allwmake -j 8 >& log.Allwmake &
```

- Compile the OpenFOAM library using for example 8 cores

```
1 cd ~/OpenFOAM_UMD/ThirdParty-dev
2 ./Allwmake -j 6 >& log.Allwmake &
```

check for errors in the log.Allwmake file

- Compile the OpenFOAM library

```
1 cd ~/OpenFOAM_UMD/OpenFOAM-dev  
2 ./Allwmake -j 6 >& log.Allwmake &
```

check for errors in the log.Allwmake file

- Download the source files of PBRFOAM from this repository in the home directory

```
1 cd ~  
2 git clone https://github.com/mmahmed15/PBRFoam.git
```

- Navigate to the PBRFoam directory and compile the code

```
1 cd ~/PBRFOAM  
2 ./Allwmake -j 6 >& log.Allwmake &
```

check for errors in the log.Allwmake file

E.2 Parallel Performance

Parallelization is robust and integrated at a low level in the OpenFOAM library, so in general, new applications require no “parallel-specific” coding; they will run in parallel (efficiently) by default. Based on prior scaling studies, it appears that with a suitable setup, solvers based on the OpenFOAM CFD library can scale up to several 100s CPUs. We have recently (January 2023) performed a new series of parallel performance tests of PBRFoam on Expanse using simulations corresponding

to the configuration of fire spread in pine wood bed, with a computational grid of approximately 57 million cells and 19 million particles but computed with a variable number of cores. Figure E.1 shows very good scaling with respect to increasing the number of compute nodes.

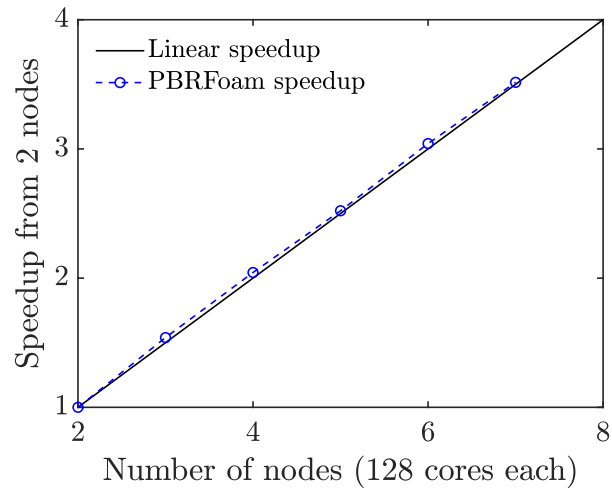


Figure E.1: Test of the scaling performance of PBRFoam on the HPC cluster Expanse.

Bibliography

- [1] National Interagency Fire Center. <https://www.nifc.gov/> (accessed May 2023).
- [2] Mark A Finney, Sara S McAllister, Jason M Forthofer, and Torben P Grumstrup. *Wildland fire behaviour: dynamics, principles and processes*. CSIRO publishing, 2021.
- [3] Smithsonian's National Zoo & Conservation Biology Institute. <https://nationalzoo.si.edu> (accessed May 2023).
- [4] Greenpeace International. <https://www.greenpeace.org> (accessed May 2023).
- [5] NASA Earth Observatory. <https://earthobservatory.nasa.gov/> (accessed May 2023).
- [6] Robert E Burgan. *Behave: fire behavior prediction and fuel modeling system, fuel subsystem*, volume 167. US Department of Agriculture, Forest Service, Intermountain Forest and Range Experiment Station, 1984.
- [7] Mark A Finney. *FARSITE, Fire Area Simulator—model development and evaluation*. Number 4. US Department of Agriculture, Forest Service, Rocky Mountain Research Station, 1998.
- [8] Chris Lautenberger. Wildland fire modeling with an eulerian level set method and automated calibration. *Fire Safety Journal*, 62:289–298, 2013.
- [9] Mark A Finney. An overview of flammmap fire modeling capabilities. In *Fuels management—how to measure success: conference proceedings*, volume 28, page 30. USDA Forest Service, Rocky Mountain Research Station, Fort Collins, CO, 2006.
- [10] Richard C Rothermel. *A mathematical model for predicting fire spread in wildland fuels*, volume 115. Intermountain Forest & Range Experiment Station, Forest Service, US Department of Agriculture, 1972.

- [11] Miguel G Cruz, Martin E Alexander, Andrew L Sullivan, James S Gould, and Musa Kilinc. Assessing improvements in models used to operationally predict wildland fire rate of spread. *Environmental Modelling & Software*, 105:54–63, 2018.
- [12] Mark A Finney, Jack D Cohen, Sara S McAllister, and W Matt Jolly. On the need for a theory of wildland fire spread. *International journal of wildland fire*, 22(1):25–36, 2012.
- [13] B Porterie, D Morvan, JC Loraud, and M Larini. Firespread through fuel beds: Modeling of wind-aided fires and induced hydrodynamics. *Physics of Fluids*, 12(7):1762–1782, 2000.
- [14] D Morvan and JL Dupuy. Modeling of fire spread through a forest fuel bed using a multiphase formulation. *Combustion and flame*, 127(1-2):1981–1994, 2001.
- [15] Dominique Morvan and Jean-Luc Dupuy. Modeling the propagation of a wildfire through a mediterranean shrub using a multiphase formulation. *Combustion and flame*, 138(3):199–210, 2004.
- [16] Dominique Morvan, Gilbert Accary, Sofiane Meradji, Nicolas Frangieh, and Oleg Bessonov. A 3D physical model to study the behavior of vegetation fires at laboratory scale. *Fire Safety Journal*, 101:39–52, 2018.
- [17] Kevin McGrattan, Simo Hostikka, Randall McDermott, Jason Floyd, Craig Weinschenk, and Kristopher Overholt. Fire dynamics simulator user’s guide. *NIST special publication*, 1019(6), 2013.
- [18] FireFOAM. <https://github.com/fireFoam-dev> (accessed May 2023).
- [19] Rodman Linn, Jon Reisner, Jonah J Colman, and Judith Winterkamp. Studying wildfire behavior using firetec. *International journal of wildland fire*, 11(4):233–246, 2002.
- [20] Rodman R Linn and Philip Cunningham. Numerical simulations of grass fires using a coupled atmosphere–fire model: basic fire behavior and dependence on wind speed. *Journal of Geophysical Research: Atmospheres*, 110(D13), 2005.
- [21] JM Canfield, RR Linn, JA Sauer, M Finney, and Jason Forthofer. A numerical investigation of the interplay between fireline length, geometry, and rate of spread. *Agricultural and Forest Meteorology*, 189:48–59, 2014.
- [22] William Mell, Mary Ann Jenkins, Jim Gould, and Phil Cheney. A physics-based approach to modelling grassland fires. *International Journal of Wildland Fire*, 16(1):1–22, 2007.

- [23] Marcos Vanella, Kevin McGrattan, Randall McDermott, Glenn Forney, William Mell, Emanuele Gissi, and Paolo Fiorucci. A multi-fidelity framework for wildland fire behavior simulations over complex terrain. *atmosphere*, 12(2):273, 2021.
- [24] Eric V Mueller, Nicholas S Skowronski, Kenneth L Clark, Michael R Gallagher, William E Mell, Albert Simeoni, and Rory M Hadden. Detailed physical modeling of wildland fire dynamics at field scale—an experimentally informed evaluation. *Fire Safety Journal*, 120:103051, 2021.
- [25] Terry L Clark, Janice Coen, and Don Latham. Description of a coupled atmosphere–fire model. *International Journal of Wildland Fire*, 13(1):49–63, 2004.
- [26] Jan Mandel, Jonathan D Beezley, and Adam K Kochanski. Coupled atmosphere–wildland fire modeling with wrf 3.3 and sfire 2011. *Geoscientific Model Development*, 4(3):591–610, 2011.
- [27] Janice L Coen, Marques Cameron, John Michalakes, Edward G Patton, Philip J Riggan, and Kara M Yedinak. Wrf-fire: coupled weather–wildland fire modeling with the weather research and forecasting model. *Journal of Applied Meteorology and Climatology*, 52(1):16–38, 2013.
- [28] Adam K Kochanski, Mary Ann Jenkins, Jan Mandel, Jonathan D Beezley, Craig B Clements, and Steven Krueger. Evaluation of wrf-sfire performance with field observations from the fireflux experiment. *Geoscientific Model Development*, 6(4):1109–1126, 2013.
- [29] Jean-Baptiste Filippi, Xavier Pialat, and Craig B Clements. Assessment of forefire/meso-nh for wildland fire/atmosphere coupled simulation of the fireflux experiment. *Proceedings of the Combustion Institute*, 34(2):2633–2640, 2013.
- [30] Jacques Henri Balbi, Frédéric Morandini, Xavier Silvani, Jean Baptiste Filippi, and Frédéric Rinieri. A physical model for wildland fires. *Combustion and Flame*, 156(12):2217–2230, 2009.
- [31] LIHTFire. <https://www.firelab.org/media/1010> (accessed May 2023).
- [32] Mark A Finney, Jason M Forthofer, Xinle Liu, John Burge, Matthias Ihme, Fei Sha, Yi-fan Chen, Jason Hickey, and John Anderson. Deep learning for high-resolution wildfire modeling. In Domingos X Viegas and Luis M Ribeiro, editors, *Advances in Forest Fire Research*, pages 136–141. Coimbra University Press, Coimbra, 2022.
- [33] M Vogel and FA Williams. Flame propagation along matchstick arrays. *Combustion Science and Technology*, 1(6):429–436, 1970.

- [34] MF Wolff, GF Carrier, and FE Fendell. Wind-aided firespread across arrays of discrete fuel elements. ii. experiment. *Combustion science and technology*, 77(4-6):261–289, 1991.
- [35] Giovanni Di Cristina, Nicholas S Skowronski, Albert Simeoni, Ali S Rangwala, and Seong-kyun Im. Flame spread behavior characterization of discrete fuel array under a forced flow. *Proceedings of the Combustion Institute*, 38(3):5109–5117, 2021.
- [36] Mark A Finney, Jason Forthofer, Isaac C Grenfell, Brittany A Adam, Nelson K Akafuah, and Kozo Saito. A study of flame spread in engineered cardboard fuelbeds; part i: Correlations and observations. In *Seventh International Symposium on scale modeling (ISSM-7)*, 2013.
- [37] Qianqian He, Naian Liu, Xiaodong Xie, Linhe Zhang, Yang Zhang, and Weidong Yan. Experimental study on fire spread over discrete fuel bed-part i: Effects of packing ratio. *Fire Safety Journal*, 126:103470, 2021.
- [38] Qianqian He, Naian Liu, Xiaodong Xie, Linhe Zhang, Jiao Lei, Yang Zhang, and Di Wu. Experimental study on fire spread over discrete fuel bed-part ii: Combined effects of wind and packing ratio. *Fire Safety Journal*, 128:103520, 2022.
- [39] Nicolas Frangieh, Gilbert Accary, Dominique Morvan, Sofiane Méradjji, and Oleg Bessonov. Wildfires front dynamics: 3d structures and intensity at small and large scales. *Combustion and flame*, 211:54–67, 2020.
- [40] Carmen Awad, Nicolas Frangieh, Thierry Marcelli, Gilbert Accary, Dominique Morvan, Sofiane Meradjji, Francois Joseph Chatelon, and Jean Louis Rossi. Numerical study of the moisture content threshold under prescribed burning conditions. *Fire Safety Journal*, 122:103324, 2021.
- [41] OpenFOAM. www.openfoam.org (accessed May 2023).
- [42] Salman Verma. *A Large Eddy Simulation Study of the Effects of Wind and Slope on the Structure of a Turbulent Line Fire*. PhD thesis, University of Maryland, College Park, 2019.
- [43] Mohamed Mohsen Ahmed and Arnaud Trouv . Simulations of the unsteady response of biomass burning particles exposed to oscillatory heat flux conditions. *Fire Safety Journal*, 120:103059, 2021.
- [44] Chris Lautenberger and Carlos Fernandez-Pello. A model for the oxidative pyrolysis of wood. *Combustion and Flame*, 156(8):1503–1513, 2009.
- [45] Hrvoje Jasak. Error analysis and estimation for the finite volume method with applications to fluid flows. 1996.

- [46] Bjørn F Magnussen and Bjørn H Hjertager. On mathematical modeling of turbulent combustion with special emphasis on soot formation and combustion. In *Symposium (international) on Combustion*, volume 16, pages 719–729. Elsevier, 1977.
- [47] Wei Yao, Jianping Zhang, Ali Nadjai, Tarek Beji, and Michael A Delichatsios. A global soot model developed for fires: Validation in laminar flames and application in turbulent pool fires. *Fire safety journal*, 46(7):371–387, 2011.
- [48] Ivan Sikic, Siaka Dembele, and Jennifer Wen. Non-grey radiative heat transfer modelling in les-cfd simulated methanol pool fires. *Journal of Quantitative Spectroscopy and Radiative Transfer*, 234:78–89, 2019.
- [49] Fabiano Cassol, Rogério Brittes, Francis HR França, and Ofodike A Ezekoye. Application of the weighted-sum-of-gray-gases model for media composed of arbitrary concentrations of h₂o, co₂ and soot. *International Journal of Heat and Mass Transfer*, 79:796–806, 2014.
- [50] Chris Lautenberger and Carlos Fernandez-Pello. Generalized pyrolysis model for combustible solids. *Fire Safety Journal*, 44(6):819–839, 2009.
- [51] Mohammed M Khan, John L De Ris, and Steve D Ogden. Effect of moisture on ignition time of cellulosic materials. *Fire Safety Science*, 9(9):167–178, 2008.
- [52] R Bruce Prime, Harvey E Bair, Sergey Vyazovkin, Patrick K Gallagher, and Alan Riga. Thermogravimetric analysis (tga). *Thermal analysis of polymers: Fundamentals and applications*, pages 241–317, 2009.
- [53] Stanislav I Stoliarov and Richard N Walters. Determination of the heats of gasification of polymers using differential scanning calorimetry. *Polymer Degradation and Stability*, 93(2):422–427, 2008.
- [54] Frank P Incropera, David P DeWitt, Theodore L Bergman, and Adrienne S Lavine. *Fundamentals of heat and mass transfer*, volume 6. Wiley New York, 1996.
- [55] S McAllister, M Finney, and J Cohen. Critical mass flux for flaming ignition of wood as a function of external radiant heat flux and moisture content. In *In: 7th US National Technical Meeting of the Combustion Institute; Georgia Institute of Technology, Atlanta, GA; 20-23 March 2011. 1: 1698-1704.*, pages 1698–1704, 2011.
- [56] JL Consalvi, B Porterie, and JC Loraud. A formal averaging procedure for radiation heat transfer in particulate media. *International Journal of Heat and Mass Transfer*, 45(13):2755–2768, 2002.
- [57] SW Churchill and M Bernstein. A correlating equation for forced convection from gases and liquids to a circular cylinder in crossflow. 1977.

- [58] S Whitaker. Forced convection heat transfer calculations for flow in pipes, past flat plate, single cylinder, and for flow in packed beds and tube bundles. *AIChE J*, 18:361–371, 1972.
- [59] Eric V Mueller, Michael R Gallagher, Nicholas Skowronski, and Rory M Hadden. Convective heat transfer in pine forest litter beds. *International Journal of Heat and Mass Transfer*, 195:123057, 2022.
- [60] Eric Victor Mueller. *LES modeling of flow through Vegetation with applications to wildland fires*. PhD thesis, Worcester Polytechnic Institute, 2012.
- [61] Andrea Defina and Anna Chiara Bixio. Mean flow and turbulence in vegetated open channel flow. *Water Resources Research*, 41(7), 2005.
- [62] Francis Henry Robertson. *An experimental investigation of the drag on idealised rigid, emergent vegetation and other obstacles in turbulent free-surface flows*. The University of Manchester (United Kingdom), 2016.
- [63] Nian-Sheng Cheng, Cai Ling Hui, Xikun Wang, and Soon Keat Tan. Laboratory study of porosity effect on drag induced by circular vegetative patch. *Journal of Engineering Mechanics*, 145(7):04019046, 2019.
- [64] Rui ML Ferreira, Miltiadis Gymnopoulos, Panayotis Prinos, Elsa Alves, and Ana M Ricardo. Drag on a square-cylinder array placed in the mixing layer of a compound channel. *Water*, 13(22):3225, 2021.
- [65] Steven J Ritchie, Kenneth D Steckler, Anthony Hamins, Thomas G Cleary, Jiann C Yang, and Takashi Kashiwagi. The effect of sample size on the heat release rate of charring materials. In *Fire Safety Science-Proceedings of the 5th International Symposium*, pages 177–188. Citeseer, 1997.
- [66] Richard E Lyon and Richard Walters. A microscale combustion calorimeter. Technical report, Federal Aviation Administration Washington DC Office of Aviation Research, 2002.
- [67] Robert J Kee, Fran M Rupley, and James A Miller. The chemkin thermodynamic data base. Technical report, Sandia National Lab.(SNL-CA), Livermore, CA (United States), 1990.
- [68] Malcolm W Chase and National Information Standards Organization (US). *NIST-JANAF thermochemical tables*, volume 9. American Chemical Society Washington, DC, 1998.
- [69] Franck Nicoud and Frédéric Ducros. Subgrid-scale stress modelling based on the square of the velocity gradient tensor. *Flow, turbulence and Combustion*, 62(3):183–200, 1999.

- [70] Won-Wook Kim and Suresh Menon. A new dynamic one-equation subgrid-scale model for large eddy simulations. In *33rd Aerospace Sciences Meeting and Exhibit*, page 356, 1995.
- [71] RS Barlow, AN Karpetis, JH Frank, and J-Y Chen. Scalar profiles and no formation in laminar opposed-flow partially premixed methane/air flames. *Combustion and flame*, 127(3):2102–2118, 2001.
- [72] William L Grosshandler. Radcal: a narrow band model for radiation. *Calculations in a Combustion Environment, NIST Technical Note*, 1402, 1993.
- [73] Michael F Modest. The weighted-sum-of-gray-gases model for arbitrary solution methods in radiative transfer. 1991.
- [74] Mohammad Hadi Bordbar, Gabriel Węcel, and Timo Hyppänen. A line by line based weighted sum of gray gases model for inhomogeneous co₂–h₂o mixture in oxy-fired combustion. *Combustion and flame*, 161(9):2435–2445, 2014.
- [75] Yi Wang, Prateep Chatterjee, and John L de Ris. Large eddy simulation of fire plumes. *Proceedings of the Combustion Institute*, 33(2):2473–2480, 2011.
- [76] Georgios Maragkos, S Verma, A Trouvé, and Bart Merci. Evaluation of openfoam’s discretization schemes used for the convective terms in the context of fire simulations. *Computers & Fluids*, 232:105208, 2022.
- [77] F. Moukalled, L. Mangani, and M. Darwish. The Finite Volume Method in Computational Fluid Dynamics: An advanced introduction with OpenFOAM® and Matlab. *Springer*, 2016.
- [78] Cengel A Yunus and Afshin Ghajar. *Heat and mass transfer: fundamentals and applications*. McGraw-Hill Education, 2015.
- [79] K McGrattan, S Hostikka, R McDermott, J Floyd, C Weinschenk, and K Overholt. *Fire Dynamics Simulator, Verification Guide*. National Institute of Standards and Technology, Gaithersburg, Maryland, USA, and VTT Technical Research Centre of Finland, Espoo, Finland, sixth edition, September 2013. Vol. 1: Mathematical Model; Vol. 2: Verification Guide; Vol. 3: Validation Guide Vol. 4: Software Quality Assurance. v, 55, 61, 124, 145, 203.
- [80] Andrés Anca-Couce, Nico Zobel, Anka Berger, and Frank Behrendt. Smouldering of pine wood: Kinetics and reaction heats. *Combustion and Flame*, 159(4):1708–1719, 2012.
- [81] Mark B McKinnon, Stanislav I Stolarov, and Artur Witkowski. Development of a pyrolysis model for corrugated cardboard. *Combustion and Flame*, 160(11):2595–2607, 2013.

- [82] M Semmes, X Liu, M McKinnon, S Stoliarov, and A Witkowski. A model for oxidative pyrolysis of corrugated cardboard. *Fire Safety Science*, 11:111–123, 2014.
- [83] Jorge Nocedal and Stephen J Wright. *Numerical optimization*. Springer, 2006.
- [84] Gregory J Fiola, Dushyant M Chaudhari, and Stanislav I Stoliarov. Comparison of pyrolysis properties of extruded and cast poly (methyl methacrylate). *Fire Safety Journal*, 120:103083, 2021.
- [85] T Kashiwagi, TJ Ohlemiller, and K Werner. Effects of external radiant flux and ambient oxygen concentration on nonflaming gasification rates and evolved products of white pine. *Combustion and Flame*, 69(3):331–345, 1987.
- [86] Mohamed M Ahmed and Arnaud Trouvé. Large eddy simulation of the unstable flame structure and gas-to-liquid thermal feedback in a medium-scale methanol pool fire. *Combustion and Flame*, 225:237–254, 2021.
- [87] A Brown, Morgan Bruns, M Gollner, J Hewson, Georgios Maragkos, A Marshall, R McDermott, Bart Merci, T Rogaume, and S Stoliarov. Proceedings of the first workshop organized by the iafss working group on measurement and computation of fire phenomena (macfp). *Fire safety journal*, 101:1–17, 2018.
- [88] MaCFP. <https://github.com/MaCFP/macfp-db> (accessed May 2023).
- [89] EJ Weckman and AB Strong. Experimental investigation of the turbulence structure of medium-scale methanol pool fires. *Combustion and Flame*, 105(3):245–266, 1996.
- [90] Anthony Hamins, SJ Fischer, Takashi Kashiwagi, ME Klassen, and JP Gore. Heat feedback to the fuel surface in pool fires. *Combustion Science and Technology*, 97(1-3):37–62, 1994.
- [91] Sung Chan Kim, Ki Yong Lee, and Anthony Hamins. Energy balance in medium-scale methanol, ethanol, and acetone pool fires. *Fire safety journal*, 107:44–53, 2019.
- [92] E. J. Weckman and A. Sobiesiak. The oscillatory behaviour of medium-scale pool fires. *Proc. Combust. Inst.*, 22:1299–1310, 1988.
- [93] B. M. Cetegen and T. A. Ahmed. Experiments on the periodic instability of buoyant plumes and pool fires. *Combust. Flame*, 93:157–184, 1993.
- [94] Tao Ren, Michael F Modest, and Somesh Roy. Monte carlo simulation for radiative transfer in a high-pressure industrial gas turbine combustion chamber. *Journal of Engineering for Gas Turbines and Power*, 140(5), 2018.
- [95] Dong Zeng, Prateep Chatterjee, and Yi Wang. The effect of oxygen depletion on soot and thermal radiation in buoyant turbulent diffusion flames. *Proceedings of the Combustion Institute*, 37(1):825–832, 2019.

- [96] Gang Xiong, Dong Zeng, Pratikash P Panda, and Yi Wang. Laser induced incandescence measurement of soot in ethylene buoyant turbulent diffusion flames under normal and reduced oxygen concentrations. *Combustion and Flame*, 230:111456, 2021.
- [97] Xingyu Ren, Dong Zeng, Yi Wang, Gang Xiong, Gaurav Agarwal, and Michael Gollner. Temperature measurement of a turbulent buoyant ethylene diffusion flame using a dual-thermocouple technique. *Fire Safety Journal*, 120:103061, 2021.
- [98] V Novozhilov, Behdad Moghtaderi, DF Fletcher, and JH Kent. Computational fluid dynamics modelling of wood combustion. *Fire safety journal*, 27(1):69–84, 1996.
- [99] Mark A Finney, Jack D Cohen, Jason M Forthofer, Sara S McAllister, Michael J Gollner, Daniel J Gorham, Kozo Saito, Nelson K Akafuah, Brittany A Adam, and Justin D English. Role of buoyant flame dynamics in wildfire spread. *Proceedings of the National Academy of Sciences*, 112(32):9833–9838, 2015.
- [100] B Mike Wotton, James S Gould, W Lachlan McCaw, N Phillip Cheney, and Stephen W Taylor. Flame temperature and residence time of fires in dry eucalypt forest. *International Journal of Wildland Fire*, 21(3):270–281, 2011.
- [101] Xavier Silvani, Frédéric Morandini, and Jean-François Muzy. Wildfire spread experiments: Fluctuations in thermal measurements. *International communications in heat and mass transfer*, 36(9):887–892, 2009.
- [102] Xavier Silvani and Frédéric Morandini. Fire spread experiments in the field: temperature and heat fluxes measurements. *Fire Safety Journal*, 44(2):279–285, 2009.
- [103] Horatio Scott Carslaw and John Conrad Jaeger. Conduction of heat in solids. *Conduction of heat in solids*, 1947.
- [104] Cyle Wold. *Air Flow Characterization of the Missoula Fire Lab. Low Speed Wind Tunnel Using a TSI IFA 300 Hot Wire Anemometer*. Missoula Fire Sciences Laboratory, US Forest Service, US Department of Agriculture, 2022.
- [105] Richard C Rothermel and Hal E Anderson. *Fire spread characteristics determined in the laboratory*, volume 30. Intermountain Forest & Range Experiment Station, Forest Service, US Department of Agriculture, 1966.
- [106] Salman Verma, Mohamed Ahmed, and Arnaud Trouvé. *The Structure of Line Fires at Flame Scale*, page 35–62. Cambridge University Press, 2022.
- [107] LH Hu, Ran Huo, and Wan Ki Chow. Studies on buoyancy-driven back-layering flow in tunnel fires. *Experimental Thermal and Fluid Science*, 32(8):1468–1483, 2008.

- [108] Dong Zeng, Marcons Chaos, Mohammed M Khan, and Sergey B Dorofeev. Radiation characteristics of corrugated cardboard flames. *Fire Safety Science*, 11:97–110, 2014.
- [109] Frank A Albini. A model for the wind-blown flame from a line fire. *Combustion and Flame*, 43:155–174, 1981.
- [110] Patricia L Andrews et al. *The Rothermel surface fire spread model and associated developments: A comprehensive explanation*. United States Department of Agriculture, Forest Service, Rocky Mountain Research Station, 2018.
- [111] Li-Ming Yuana and G Cox. An experimental study of some line fires. *Fire Safety Journal*, 27(2):123–139, 1996.
- [112] JO Counihan. Adiabatic atmospheric boundary layers: a review and analysis of data from the period 1880–1972. *Atmospheric Environment (1967)*, 9(10):871–905, 1975.
- [113] GF Carrier, FE Fendell, and FE Marble. The effect of strain rate on diffusion flames. *SIAM Journal on Applied Mathematics*, 28(2):463–500, 1975.
- [114] Thierry Poinsot and Denis Veynante. *Theoretical and numerical combustion*. RT Edwards, Inc., 2005.
- [115] Charles K Westbrook and Frederick L Dryer. Simplified reaction mechanisms for the oxidation of hydrocarbon fuels in flames. *Combustion science and technology*, 27(1-2):31–43, 1981.
- [116] YR Sivathanu and JP Gore. Coupled radiation and soot kinetics calculations in laminar acetylene/air diffusion flames. *Combustion and Flame*, 97(2):161–172, 1994.
- [117] F Liu, H Guo, GJ Smallwood, ÖL Gülder, and MD Matovic. A robust and accurate algorithm of the β -pdf integration and its application to turbulent methane-air diffusion combustion in a gas turbine combustor simulator. *International journal of thermal sciences*, 41(8):763–772, 2002.
- [118] The UMD cluster Zaratan. <https://hpcc.umd.edu/hpcc/zaratan.html> (accessed May 2023).
- [119] The SDSC cluster Expanse. https://www.sdsc.edu/support/user_guides/expanse.html (accessed May 2023).
- [120] NSF ACCESS program. <https://access-ci.org/> (accessed May 2023).